

Copyright Warning & Restrictions

The copyright law of the United States (Title 17, United States Code) governs the making of photocopies or other reproductions of copyrighted material.

Under certain conditions specified in the law, libraries and archives are authorized to furnish a photocopy or other reproduction. One of these specified conditions is that the photocopy or reproduction is not to be “used for any purpose other than private study, scholarship, or research.” If a user makes a request for, or later uses, a photocopy or reproduction for purposes in excess of “fair use” that user may be liable for copyright infringement,

This institution reserves the right to refuse to accept a copying order if, in its judgment, fulfillment of the order would involve violation of copyright law.

Please Note: The author retains the copyright while the New Jersey Institute of Technology reserves the right to distribute this thesis or dissertation

Printing note: If you do not wish to print this page, then select “Pages from: first page # to: last page #” on the print dialog screen

The Van Houten library has removed some of the personal information and all signatures from the approval page and biographical sketches of theses and dissertations in order to protect the identity of NJIT graduates and faculty.

ABSTRACT

DEVELOPMENT OF NOVEL MASS SPECTROMETRIC METHODS FOR REACTION SCREENING, OLIGOSACCHARIDE DETECTION AND NITROSAMINE QUANTITATION

by
Qi Wang

Benefitting from its high detection sensitivity and specificity, mass spectrometry (MS) has become a powerful technique in academia and industry. The aim of this dissertation study is to develop new mass spectrometric methods for organic reaction screening, detection of oligosaccharide/glycan in complex matrices, and nitrosamine absolute quantitation.

First, an electrochemistry/mass spectrometry (EC/MS) platform is built to generate an *N*-cyclopropylaniline radical cation electrochemically and to monitor its reactivity toward alkenes, which leads to the discovery of a new redox neutral reaction of intermolecular [3 + 2] annulation of *N*-cyclopropylanilines and alkenes. Net redox neutral electrosynthesis is quite rare in synthetic organic electrochemistry. Taking full advantage of the online EC/MS platform as a screening tool which only uses 50 nmol of substrates, a large scale electrosynthesis for 4-chloro-*N*-(2-phenylcyclopentyl)aniline in 128 mg is successfully conducted in an electrochemical cell. Such an EC/MS screening of reaction may expedite the discovery of other novel redox neutral electrochemical reactions.

Second, conventional MS-based analytical methods for carbohydrates are time-consuming because of offline sample pretreatment to remove matrix which suppresses MS signal. A fast and sensitive MS-based oligosaccharide characterization strategy is developed, termed desalting paper spray mass spectrometry (DPS-MS), that uses a piece of triangular paper (10 mm × 5 mm, height × base) for both carbohydrate desalting and

subsequent ionization for analysis of various oligosaccharide types of analytes in complex nonvolatile buffers (Tris-HCl, PBS, and HEPES), and glycosyltransferases (GT) reaction products. This new analytical method is not only fast (<5 min per sample) and straightforward but is also highly sensitive (LOD of 1.1 nM for β -cyclodextrin). Furthermore, DPS-MS quantitative analysis of acceptor sugars in GT reactions control samples afford a slight deviation (6.5%~11.6%) from theoretical values. This vital result shows excellent potential for onsite, high-throughput characterization of GT activities and carbohydrate diagnostics by DPS-MS.

Third, *N*-Nitrosamines, possible carcinogenic substrates, are recently found in the sartan family of drugs and led to drug recalls. Their detection and quantification are therefore of significant importance for human health. Although many literature quantitation papers reported, they focused on simple nitrosamines, relying on the use of standards. Nevertheless, quantitation of nitrosamines directly derived from drug molecules with a complicated structure is not explored, due to the grand challenge of lacking standards that are difficult and expensive to synthesize. A novel absolute quantitation approach for *N*-nitrosamines using coulometric mass spectrometry (CMS) based on Faraday's Law is explored. In this approach, reductive conversion of *N*-nitrosamines into electrochemically active hydrazines is accomplished using zinc as a reductant under acidic conditions and hydrazines are then easily quantified using CMS, without using standards.

**DEVELOPMENT OF NOVEL MASS SPECTROMETRIC METHODS FOR
REACTION SCREENING, OLIGOSACCHARIDE DETECTION, AND
NITROSAMINE QUANTITATION**

by
Qi Wang

**A Dissertation
Submitted to the Faculty of
New Jersey Institute of Technology
in Partial Fulfillment of the Requirements for the Degree of
Doctor of Philosophy in Chemistry**

Department of Chemistry and Environmental Science

May 2022

Copyright © 2022 by Qi Wang

ALL RIGHTS RESERVED

APPROVAL PAGE

**DEVELOPMENT OF NOVEL MASS SPECTROMETRIC METHODS FOR
REACTION SCREENING, OLIGOSACCHARIDE DETECTION, AND
NITROSAMINE QUANTITATION**

Qi Wang

Dr. Hao Chen, Dissertation Advisor Date
Professor of Chemistry and Environmental Science, NJIT

Dr. Zeyuan Qiu, Committee Member Date
Professor of Chemistry and Environmental Science, NJIT

Dr. Alexei Khalizov, Committee Member Date
Associate Professor of Chemistry and Environmental Science, NJIT

Dr. Yuanwei Zhang, Committee Member Date
Assistant Professor of Chemistry and Environmental Science, NJIT

Dr. Sagnik Basuray, Committee Member Date
Associate Professor of Chemical and Materials Engineering, NJIT

BIOGRAPHICAL SKETCH

Author: Qi Wang
Degree: Doctor of Philosophy
Date: May 2022

Undergraduate and Graduate Education:

- Doctor of Philosophy in Chemistry, New Jersey Institute of Technology, Newark, NJ, 2022
- Master of Science in Food Safety and Technology, Illinois Institute of Technology, Chicago, IL, 2017
- Bachelor of Science in Food Quality and Safety, Shihezi University, Xinjiang, P. R. China, 2014

Major: Chemistry

Presentations and Publications:

- Q. Wang, Q. Wang, Y. Zhang, Y. M. Mohamed, C. Pacheco, N. Zheng, R. N. Zare and H. Chen, *Chemical Science*, 2021, **12**, 969-975.
- Q. Wang, M. Bhattarai, P. Zhao, T. Alnsour, M. Held, A. Faik and H. Chen, *Journal of the American Society for Mass Spectrometry*, 2020, **31**, 2226-2235.
- P. Zhao, Q. Wang, M. Kaur, Y.-I. Kim, H. D. Dewald, O. Mozziconacci, Y. Liu and H. Chen, *Analytical Chemistry*, 2020, **92**, 7877-7883.
- C. Liu, Q. Wang, B. E. Hivick, Y. Ai, P. A. Champagne, Y. Pan and H. Chen, *Analytical Chemistry*, 2020, **92**, 15291-15296.
- K. Sambath, Z. Wan, Q. Wang, H. Chen and Y. Zhang, *Organic Letters*, 2020, **22**, 1208-1212.
- M. M. Rahman, C. Liu, E. Bisz, B. Dziuk, R. Lalancette, Q. Wang, H. Chen, R. Szostak and M. Szostak, *The Journal of Organic Chemistry*, 2020, **85**, 5475-5485.
- K. Chiu, Q. Wang, H. Gunawardena, M. Held, A. Faik, H. Chen. *International Journal of Mass Spectrometry*, 2021, **469**, 116688.

M. M. Rahman, D. J. Pyle, E. Bisz, B. Dziuk, K. Ejsmont, R. Lalancette, Q. Wang, H. Chen, R. Szostak, M. Szostak. *The Journal of Organic Chemistry*, 2021, **86**, 10455-10466.

W. Zhang, Q. Wang, and H. Chen. *Frontiers of Environmental Science and Engineering*, 2022, **16**, 11

Z. Wan, S. Yu, Q. Wang, J. Tobia, H. Chen, Z. Li, X. Liu, Y. Zhang. *ChemPhotoChem*, 2022, e202100250.

C. Wu, Q. Wang, H. Chen, M, Li. *Water Research*, submitted.

Q. Wang, Z. Liu, Y. Liu, H. Chen. *Journal of the American Society for Mass Spectrometry*, accepted.

I dedicate this work to my parents and friends, who have done so much for me throughout my life and have unequivocally supported me in all my decisions

ACKNOWLEDGEMENT

I would like to acknowledge my advisor, Dr. Hao Chen, for all his support and trust in me throughout my research and graduate career.

I would also like to acknowledge my dissertation committee members, Dr. Zeyuan Qiu, Dr. Alexei Khalizov, Dr. Yuanwei Zhang, and Dr. Sagnik Basuray for their feedback on my dissertation.

I would like to acknowledge funding support from National Science Foundation (CHE-1915878) and National Institutes of Health (1R15GM137311-01).

I would like to acknowledge our industry collaborator Dr. Yong Liu (Merck) and Dr. Harsha Gunawardena (JNJ) for their valuable comments and suggestions.

I would also like to acknowledge the technical support from Dr. Carlos Pacheco, David Fisher, and Chaudhery M Hussain.

I would like to acknowledge my group members: Dr. Pengyi Zhao, Yongling Ai, Joanne Chiu, Huifang (Bella) Yao, Joel Praneeth, and Md Tanim-Al-Hassan, for their help and support throughout my work.

I would like to acknowledge the Department of Chemistry and Environmental Science faculty and staff for always being willing and ready to help at a moment's notice. In particular, I would like to acknowledge Genti M Price, John Krane, Edgardo Farinas, and Chunmeng Lu for directly supporting this work in various ways.

I would also acknowledge my family and friends for their unequivocally support in all my decisions.

TABLE OF CONTENTS

Chapter	Page
1 INTRODUCTION.....	1
1.1 Mass Spectrometry.....	1
1.2 Mass Spectrometer.....	1
1.3 Ionization Methods.....	2
1.3.1 Electron Impact.....	2
1.3.2 Chemical Ionization.....	3
1.3.3 Atmospheric Pressure Chemical Ionization.....	3
1.3.4 Matrix-Assisted Laser Desorption Ionization.....	4
1.3.5 Electrospray Ionization.....	5
1.3.6 Paper Spray Ionization.....	8
1.4 Mass Analyzers.....	8
1.4.1 Quadrupole Mass Analyzer.....	9
1.4.2 Ion Trap Mass Analyzer.....	10
1.4.3 Time-of-Flight Mass Analyzers.....	11
1.4.4 Fourier-Transform Ion Cyclotron Resonance Mass Analyzers.....	12
1.4.5 Orbitrap Mass Analyzers.....	13
1.5 Detectors.....	14
1.6 Coupling Electrochemistry with Mass Spectrometry.....	15
1.7 Coulometric Mass Spectrometry Absolute Quantitation.....	16
2 REACTION SCREENING FOR ELECTROSYNTHESIS.....	18
2.1 Introduction.....	18

TABLE OF CONTENTS
(Continued)

Chapter	Page
2.2 Apparatus.....	21
2.2.1 Small Scale Electrosynthesis Setup.....	21
2.2.2 Large Scale Electrosynthesis Setup.....	21
2.2.3 H-type Divided Electrolysis Cell Setup.....	22
2.3 Results and Discussion.....	23
2.4 Conclusion.....	33
3 NOVAL OLIGOSACCHARIDE DETECTION METHOD.....	34
3.1 Introduction.....	34
3.2 Experimental Section.....	37
3.2.1 Desalting Paper Spray Apparatus.....	37
3.2.2 Non-radioactive Glycosyltransferase Reactions.....	38
3.2.3 Radioactive Glycosyltransferase Reactions.....	38
3.3 Results and Discussions.....	39
3.4 Conclusions.....	51
4 NITROSAMINE QUANTITATION.....	53
4.1 Introduction.....	53
4.2 Apparatus.....	56
4.3 Results and Discussions.....	58
4.4 Conclusions.....	80
5 SUMMARY AND FUTURE PLAN.....	81
APPENDIX A REACTION SCREENING.....	82

TABLE OF CONTENTS
(Continued)

Chapter	page
A.1 a) NanoESI-MS Spectrum Showing the Formation of the Product 3a by Divided Cell Electrolysis (the Anode RVC Side); b) MS/MS Spectrum of [3a +H] ⁺	82
A 2 NMR Characterization.....	83
APPENDIX B OLIGOSACCHARIDE DETECTION.....	124
B.1 DPS-MS Condition Optimization.....	124
B.2 MS Spectrum of 50 μM Maltoheptaose in 50 mM Tris Buffer (pH 7) Acquired using Cotton as SPE Stationary Phase and Subsequent nanoESI Analysis.....	125
B.3 Extracted Ion Chromatogram (EIC) for the Ion of <i>m/z</i> 1175.4.....	126
B.4 MS Spectra Acquired using 10 μL of 5 nM Glucose Tetrasaccharide in 50 mM Tris-HCl Buffer by: a) PSI, b) nanoESI and, c) DPS.....	127
B.5 Spectra of 5 nM 3α, 6α -Mannopentaose (10 μL) in 50 mM Tris buffer Acquired by a) PSI, b) nanoESI, and c) DPS.....	127
B.6 Raw Data Values of β-cyclodextrin Analysis with I.S. (5 μM Maltoheptaose) for Triplicate Measurements.....	128
B.7 X6 Calibration Curve.....	129
B.8 C6 Calibration Curve.....	130
B.9 Estimation of the Acceptor C6 and the Product (P2) Concentrations using DPS-MS and Radioactive Assay, as Function of the Amount of AtXXT1 Protein used in the Enzymatic Reactions.....	131
APPENDIX C NITROSAMINE QUANTITATION.....	132
C.1 <i>N</i> -nitro-4-phenylpiperidine (III) Quantitation.....	132

TABLE OF CONTENTS
(Continued)

Chapter	page
C.2 <i>N</i> -nitrosodibutylamine (IV) Quantitation.....	133
C.3 <i>N</i> -nitrosodipropylamine (V) Quantitation.....	135
C.4 <i>N</i> -nitrosopiperidine (VI) Quantitation.....	136
REFERENCES.....	138

LIST OF TABLES

Table		Page
2.1	Reaction Optimization.....	29
4.1	<i>N</i> -nitrosamine Chemical Reduction using Different Reductants.....	59
4.2	Electric Current and MS Data for <i>N</i> -nitrosodiethylamine (I).....	63
4.3	Electric Current and MS Data for <i>N</i> -nitro-4-phenylpiperidine (II).....	65
4.4	List of <i>N</i> -nitrosamines Quantified by CMS.....	65
4.5	Electric Current and MS Data for 3 μ L of 0.291 μ M <i>N,N</i> -diphenylhydrazine (3).....	67
4.6	Electric Current and MS Data for <i>N</i> -nitrosamine VII (0.91 mg <i>N</i> -nitrosamine VII Was Used).....	72
4.7	Electric Current and MS Data for <i>N</i> -nitrosamine VII (150 ng <i>N</i> -nitrosamine VII Was Used).....	75
4.8	Electric Current and MS Data for <i>N</i> -nitrosamine VII (in the Test Sample With Drug Matrix).....	79

LIST OF FIGURES

Figure		Page
1.1	Diagram of mass spectrometer.....	2
1.2	Diagram of electron impact ionization.....	3
1.3	Diagram of atmospheric pressure chemical ionization.....	4
1.4	Diagram of matrix-assisted laser desorption ionization.....	5
1.5	Diagram of electrospray ionization.....	6
1.6	Proposed ESI mechanism models.....	7
1.7	Analysis of a dried blood spot using paper spray ionization.....	8
1.8	Diagram of quadrupole mass analyzer.....	10
1.9	Diagram of ion trap mass analyzer.....	11
1.10	Diagram of time-of-flight mass analyzer.....	12
1.11	Diagram of Fourier-transform ion cyclotron resonance mass analyzer.....	13
1.12	Diagram of orbitrap mass analyzer.....	14
1.13	Diagram of electron multiplier ion detector.....	15
1.14	Workflow of coulometric absolute quantitation (CMS).....	17
2.1	Proposed mechanism for the [3+2] annulation reaction of <i>N</i> -cyclopropylanilines and styrene.....	20
2.2	Small scale electrosynthesis setup.....	21
2.3	Large scale electrosynthesis setup.....	22
2.4	H-type divided electrolysis cell setup.....	23
2.5	Intermolecular [3+2] annulation of <i>N</i> -cyclopropyl-3, 5-dimethylaniline (CPDA) 1a and styrene 2a by electrolysis.....	24

LIST OF FIGURES
(Continued)

Figure		Page
2.6	MS spectra showing a) the formation of radical cation $1a^+$ when the cell was turned on with 1a being introduced into the flow cell via channel 1 and MeCN being introduced via channel 2; b) the product ion $[3a+H]^+$ was observed when the cell was turned on with 2a being introduced via channel 2. c) MS/MS spectrum of m/z 266.....	25
2.7	Online MS monitoring of the oxidation of 1a by $3a^+$: a) chemical equation showing the reaction between 1a and $3a^+$; b) MS spectra showing the formation of the radical cation $3a^+$ when the oxidation potential was applied to the cell. The signal of $3a^+$ was lower when the solution injected via channel 2 changed from MeCN (black line) to 1a (red line). C) MS spectra showing the formation of radical cation $1a^+$ (red line) when the cell was turned on with 3a being introduced into the flow cell via channel 1 and 1a being introduced via channel 2. No formation of radical cation $1a^+$ was observed (black line) when the cell was turned on with 1 mM LiOTf in MeCN being introduced into the flow cell via channel 1 and 1a being introduced via channel 2.....	27
2.8	MS spectrum showing the formation of the product 3a by large scale electrolysis cell.....	28
2.9	The substrate scope of intermolecular [3 + 2] annulation by the electrochemical approach (percentages show the isolation yields). The ratios for cis/trans product isomers are also listed.....	31
3.1	Schematic presentation of the workflow and setup of DPS-MS.....	37
3.2	Equations for glycosyltransferase reactions catalyzed by a) AtGUX1 and b) AtXXT1.....	38
3.3	MS spectra of 50 μ M maltoheptaose in 50 mM Tris buffer (pH 7) acquired by a) conventional paper spray and b) desalting paper spray. c) collision-induced dissociation (CID) MS/MS analysis of $[maltoheptaose+Na]^+$ ion at m/z 1175.....	41
3.4	MS spectra of a) 500 nM maltoheptaose in 50 mM Tris-HCl buffer (analyte/buffer ratio: 1:105), b) 5 nM maltoheptaose in 50 mM Tris-HCl buffer (analyte/buffer ratio: 1:107), inset of Figure 3.3b shows the zoomed-in spectrum of m/z 1175.4.....	43

LIST OF FIGURES
(Continued)

Figure	Page
3.5 MS spectra of 50 μ M maltoheptaose dissolved in a) 50 mM PBS buffer pH=7, b) 50 mM HEPES pH=7, and c) 50 mM synthetic urine. The top panels and bottom panels show conventional paper spray and desalting paper spray results, respectively.....	45
3.6 MS Spectra of 50 μ M oligosaccharide in 50 mM Tris-HCl buffer (pH 7) acquired by desalting paper spray of a) glucose tetrasaccharide , b) 3 α ,6 α mannopentaose, and c) β -cyclodextrin. The green circle represents one monosaccharide ring (i.e., glucose or mannose).....	46
3.7 MS Spectra of 5 nM cyclodextrin in 50 mM Tris buffer acquired by: a) PSI, b) nanoESI, and c) DPS; d) shows linear relationship of β -cyclodextrin signal vs. concentration (200 nM-50 μ M β -cyclodextrin in 50 mM Tris-HCl buffer, pH 7) using 5 μ M maltoheptaose as an I.S.. Spectra in a-c were acquired using only 10 μ L solution.....	46
3.8 DPS-MS analysis of AtGUX1-GST reactions. MS spectra from a) control sample (no UDP-glucuronic acid), and reaction samples catalyzed by b) 36 ng AtGUX1 protein, c) 72 ng AtGUX1 protein, d) 144 ng AtGUX1 protein, and e) 216 ng AtGUX1 protein.....	49
3.9 Estimation of the acceptor X6 and the product (P1) concentrations using DPS-MS and radioactive assay, as function of the amount of AtGUX1 protein used in the enzymatic reactions.....	50
4.1 Workflow for absolute quantitation of N-nitrosamines by CMS.....	56
4.2 Schematic drawing of the LC/EC/MS setup used for absolute quantitation of N-nitrosamines by CMS.....	58

LIST OF FIGURES
(Continued)

Figure	page
4.3 (a) NanoESI-MS spectrum and (b) NMR spectrum of <i>N</i> -nitrosodiethylamine after chemical reduction.....	61
4.4 ESI-MS spectra of hydrazine 1 (from <i>N</i> -nitrosodiethylamine reduction) when the applied potential was (a) 0 V and (b) +0.3 V (vs Ag/AgCl). EIC of [1+H] ⁺ at <i>m/z</i> 89 when the applied potential was (c) 0 V and (d) +0.3 V (vs Ag/AgCl). Electric current responses were shown due to the oxidation of (e) a blank solvent and (f) 1	62
4.5 NanoESI-MS spectrum of <i>N</i> -nitroso-4-phenylpiperidine (II) after chemical reduction.....	64
4.6 ESI-MS spectra of hydrazine 2 (from reduction of 1-nitroso-4-phenylpiperidine) when the applied potential was (a) 0 V and (b) +0.3 V. EIC of hydrazine ion at <i>m/z</i> 178 was recorded when the applied potential was (c) 0 V and (d) +0.3 V (vs Ag/AgCl). Electric current responses were shown due to the oxidation of (e) a blank solvent and (f) 2	64
4.7 ESI-MS spectra of 3 μL of 0.291 μM <i>N,N</i> -diphenylhydrazine 3 when the applied potential was (a) 0 V and (b) +0.3 V. EIC of hydrazine ion at <i>m/z</i> 185 was recorded when the applied potential was (c) 0 V and (d) +0.3 V (vs Ag/AgCl). Electric current responses were shown due to the oxidation of (e) a blank solvent and (f) 0.291 μM 3	66
4.8 MS/MS spectrum of radical cation of <i>N,N</i> -diphenylhydrazine 3 at <i>m/z</i> 184.....	67
4.9 Synthesis route for nitrosamine VII	68

LIST OF FIGURES
(Continued)

Figure	Page
4.10 NanoESI-MS spectra of <i>N</i> -nitrosamine VII (a) before chemical reduction, (b) after chemical reduction using 20 equiv. zinc powder at room temperature with nitrogen protection and stirring for 2 h, and (c) after chemical reduction using 10 equiv. zinc powder at room temperature and vortexing for 0.5 h.....	69
4.11 Proposed mechanism for electrochemical oxidation of hydrazine 7	70
4.12 MS/MS spectra of ions of two <i>N</i> -nitrosamine VII reduction products at <i>m/z</i> 335 (a) and <i>m/z</i> 350 (b).....	70
4.13 ESI-MS spectra of hydrazine 7 (from reduction of 0.91 mg of <i>N</i> -nitrosamine VII) when the applied potential was (a) 0 V and (b) +0.3 V. EIC of hydrazine ion at <i>m/z</i> 350 was recorded when the applied potential was (c) 0 V and (d) +0.3 V (vs. Ag/AgCl). Electric current responses were shown due to the oxidation of (e) a blank solvent and (f) 7	71
4.14 EIC spectra of the protonated <i>N</i> -nitrosamine VII of <i>m/z</i> 364 before (a) and after (b) chemical reduction (zinc equiv. 10.).....	71
4.15 EIC spectra for the protonated 7 at <i>m/z</i> 350 (a) and the protonated side product ion at <i>m/z</i> 335 after zinc (>9000 equiv.) reduction of 150 ng of <i>N</i> -nitrosamine VII	73
4.16 EIC spectra for the protonated <i>N</i> -nitrosamine VII at <i>m/z</i> 364 before (a) and after (b) zinc (>9000 equiv.) reduction.....	74
4.17 Electrochemical oxidation current of hydrazine 7 (blue curve), side amine product (red curve) and blank solvent (black curve) under oxidation potential 0.3 V (vs. Ag/AgCl). The amine product has no oxidation current under the oxidation condition used.....	74

LIST OF FIGURES
(Continued)

Figure	page
4.18 ESI-MS spectra of hydrazine 7 (from reduction of 150 ng N-nitrosamine VII) when the applied potential was (a) 0 V and (b) +0.3 V. The peak of the oxidized product [7-H] ⁺ was seen at <i>m/z</i> 348 in (b). EIC of 7 was recorded when the applied potential was (c) 0 V and (d) +0.3 V (vs Ag/AgCl). Electric current responses were shown due to the oxidation of (e) a blank solvent and (f) 7	75
4.19 Workflow for extracting 150 ng VII from 10 g drug matrix using 2-propanol as extraction solvent and condensing the sample for LC isolation.....	77
4.20 EIC spectra of N-nitrosamine VII (<i>m/z</i> 364) after (a) and before (b) IPA extraction from N-nitrosamine VII sample with drug matrix and LC isolation.....	77
4.21 EIC spectra for N-nitrosamine VII before (a) and after (b) zinc reduction (in the test sample with drug matrix).....	78
4.22 EIC spectra for hydrazine 7 at <i>m/z</i> 350 (a) and amine side product at <i>m/z</i> 335 (b) after zinc reduction (in the test sample with drug matrix).....	78
4.23 ESI-MS spectra of hydrazine 7 (from reduction of N-nitrosamine VII in the test sample with drug matrix) when the applied potential was (a) 0 V and (b) +0.3 V. EIC of 7 at <i>m/z</i> 350 was recorded when the applied potential was (c) 0 V and (d) +0.3 V (vs Ag/AgCl). Electric current responses were shown due to the oxidation of (e) a blank solvent and (f) 7	79

CHAPTER 1

INTRODUCTION

1.1 Mass Spectrometry

Mass spectrometry (MS) has become a powerful technique among analytical techniques that measures the mass-to-charge ratio (m/z) of ionized analytes. It can be used for sample quantitation, unknown analyte analysis, and structure identification. Benefit from its high sensitivity and specificity, MS has been employed on variable compounds tests, from small molecules¹ to large biomolecules² and material polymer.³ Over the past decades, MS has undergone revolutionary improvement on both hardware and software, enabling its application in different fields, such as pharma/biopharma,⁴⁻⁶ environmental science,⁷⁻⁹ genomics,¹⁰ proteomics,¹¹⁻¹³ metabolomics,¹⁴⁻¹⁵ forensics,¹⁶⁻¹⁷ sports doping.¹⁸⁻²⁰

1.2 Mass Spectrometer

A mass spectrometer consists of three main components: ion source, mass analyzer, and ion detector (Figure 1.1). A neutral sample is ionized by different ionization methods at the ion source part, the charged ions are separated based on the mass-to-charge ratio (m/z), the detector converts the ion energy into electrical signals. The computer is used to collect and analyze the detector signal. In addition, gas supply and vacuum systems are typically connected with the mass spectrometer.

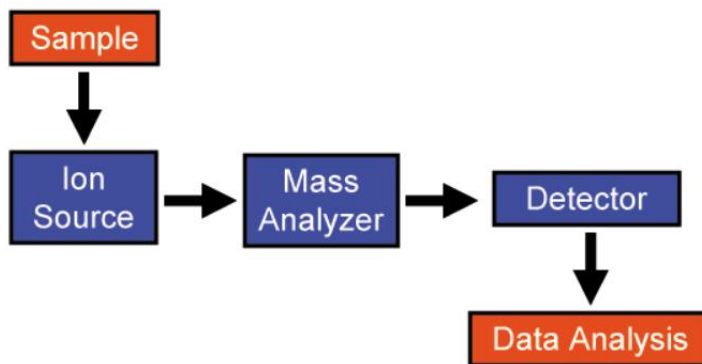


Figure 1.1 Diagram of mass spectrometer.

1.3 Ionization Methods

As a key part of the mass spectrometer, the ion source plays an indispensable role in sample ionization, in other words, samples become charged via ionization inside the ion source. Ionization methods have been revolutionized over the past few decades. Depending on the target sample polarity, size, physical makeup, volatility, thermal lability, and also the followed mass analyzer, different ionization methods can be used. The reported common modes of ionization include electron impact (EI), chemical ionization (CI), electrospray ionization (ESI), matrix-assisted laser desorption ionization (MALDI), and atmospheric pressure chemical ionization (APCI).

1.3.1 Electron Impact

Electron impact (EI) ionization is widely used for relatively low molecular weight and thermally stable gas-phase sample analysis. As shown in Figure 1.2, when a neutral analyte molecule passes through a 70 eV electron stream created by filament, one electron from the analyte is ejected to generate an analyte parent ion. Because the excess energy can cleave covalent bonds, analyte fragment ions are also detected. While the analyte fragment

can serve as a spectrometric “fingerprint” of the analyte, the intact analyte info may not be retained. Therefore, EI cannot handle ionization of the involatile and thermally unstable analyte.²¹

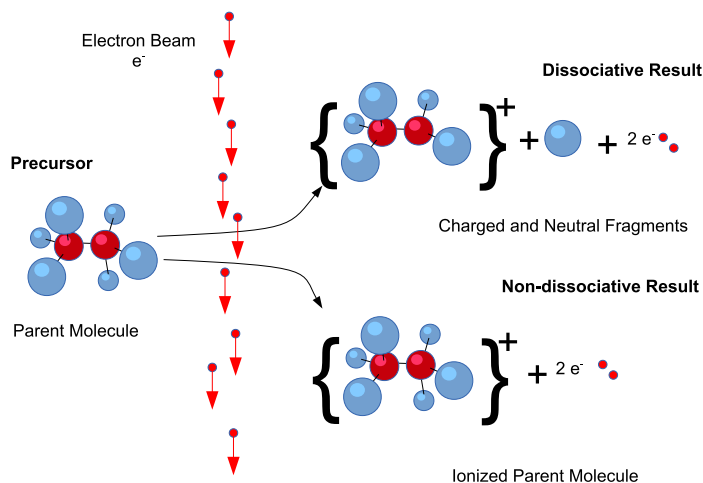


Figure 1.2 Diagram of electron impact ionization.

1.3.2 Chemical Ionization

To reduce the excessive fragment during EI and increase the abundance of the precursor ions that can be used to determine the molecular weight of the analyte, chemical ionization employs an ionized reagent gas (methane, isobutene, or ammonia) to trigger the neutral analyte molecule ionization. Different from the EI-formed analyte radical ions, EI generates analyte protonated or deprotonated ions and adducted ions when the reagent gas pressure is too high.

1.3.3 Atmospheric Pressure Chemical Ionization

Compared with EI and CI, atmospheric pressure chemical ionization is a soft ionization method that uses a corona discharge electrode to ionize the analyte particularly for small

and less-polar analytes under atmospheric pressure.²² As in Figure 1.3 analyte solution is infused into a pneumatic nebulizer, where it undergoes nebulization to form a fine droplets spray. Desolvated analyte plume generated by heated desolvation gas reacts with corona discharge electrode ionized reagent gas through gas-phase reactions. Similar to CI, proton transfer in positive mode yields protonated analyte $[A+H]^+$. In contrast, deprotonated analyte $[A-H]^-$ is formed by deprotonation in negative mode.

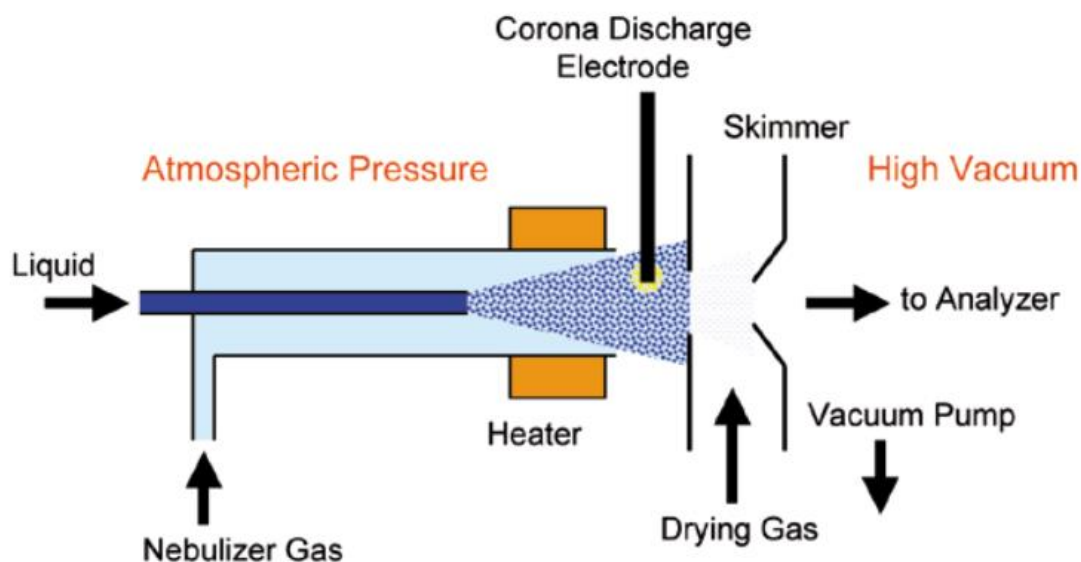


Figure 1.3 Diagram of atmospheric pressure chemical ionization.

1.3.4 Matrix-Assisted Laser Desorption Ionization

Matrix-assisted laser desorption ionization (MALDI) is one of the recent developments of soft ionization strategies in the field of mass spectrometry. It was first invented by Koichi Tanaka and developed by Franz Hillenkamp and Michael Karas. In MALDI,²³ pulsed laser radiates on the analyte-matrix mixture on the metal plate, sublimable matrix absorbs and transfers vibrational energy to analyte molecules, resulting in analyte ablation and desorption. During this process, the analytes get ionized by protonation or deprotonation²¹ (Figure 1.4). MALDI allows the high molecular weight biological analyte and labile

biomolecular detection as intact ions with singly charged species. The amount of analyte needed for MALDI is very low (< pmol). High salt tolerance (mM level) is another advantage of MALDI. Conventional, MALDI is perfectly interfaced with a time-of-flight (TOF) mass analyzer, more recently, it is coupled to an orbitrap mass analyzer for MS imaging applications.²²

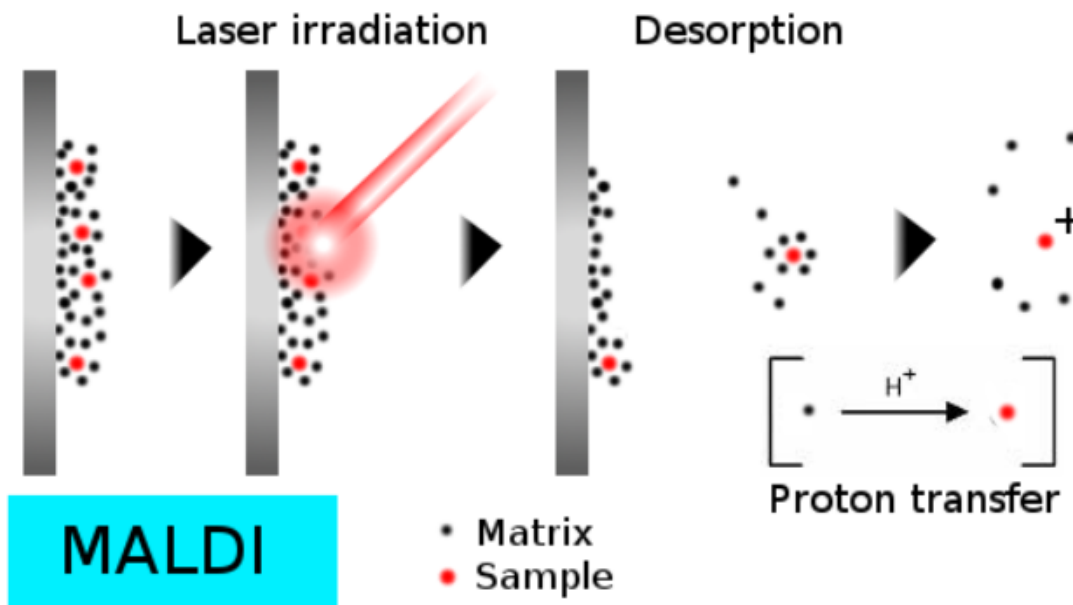


Figure 1.4 Diagram of matrix-assisted laser desorption ionization.

1.3.5 Electrospray Ionization

The idea of electrospray was carried out by Chapman in the late 1930s,²⁴ Dole realized the practical development of electrospray ionization (ESI) for mass spectrometry filed in the late 1960s.²⁵ More recently, Fenn's work on biopolymers detection including oligonucleotide and proteins (MW up to 130KDa)²³ rejuvenate the ESI application to biological macromolecules. ESI involves applying a high voltage ($\pm 2\sim 6$ kV) to the spray needle at atmospheric pressure, the infused analyte solution gets charged and evaporated by heated or dry sheath gas (Figure 1.5). As a result, the solution becomes a large droplet

and further diminishes into droplet size with charges. The charge polarity is controlled by applying positive or negative spray voltage. Multiple charges state detection enables the detection of large molecules such as peptides, proteins, and oligonucleotides with a limited m/z range. Also, multiple charges state also assists MS/MS dissociation.

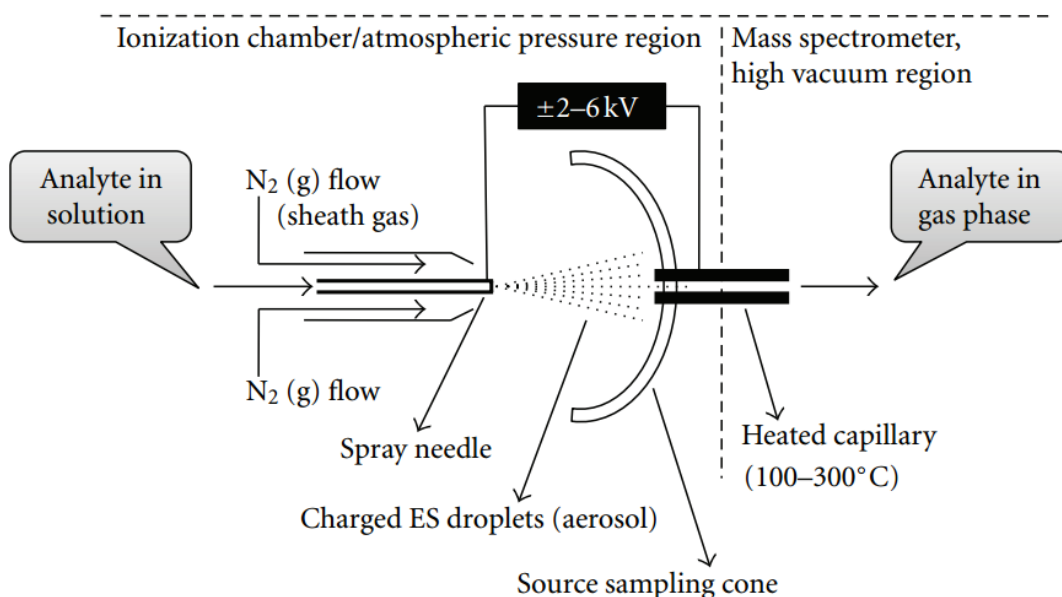


Figure 1.5 Diagram of electrospray ionization.

The mechanism of ESI has remained relatively elusive.²⁴ Three models are proposed to elucidate the ESI mechanism (Figure 1.6), including the ion evaporation model (IEM), charged residue model (CRM), and chain ejection model (CEM). Small molecule injected into gas phase is via IEM mechanism. In this case, a smaller droplet containing a solvated ion is desorbed from the highly charged larger droplet, the same process is repeated until only the desolvated ions remain. CRM mechanism is widely accepted on large globular species ESI ionization such as the folded proteins. For the CRM, the droplet shrinks after solvent evaporation until just desolvated ions are leftover. Once proteins get

unfolded under a specific condition, the protein chain migrates to the droplet surface immediately, then the unfolded protein chain is expelled and ejected. This is the third ESI mechanism called the chain ejection model (CEM).

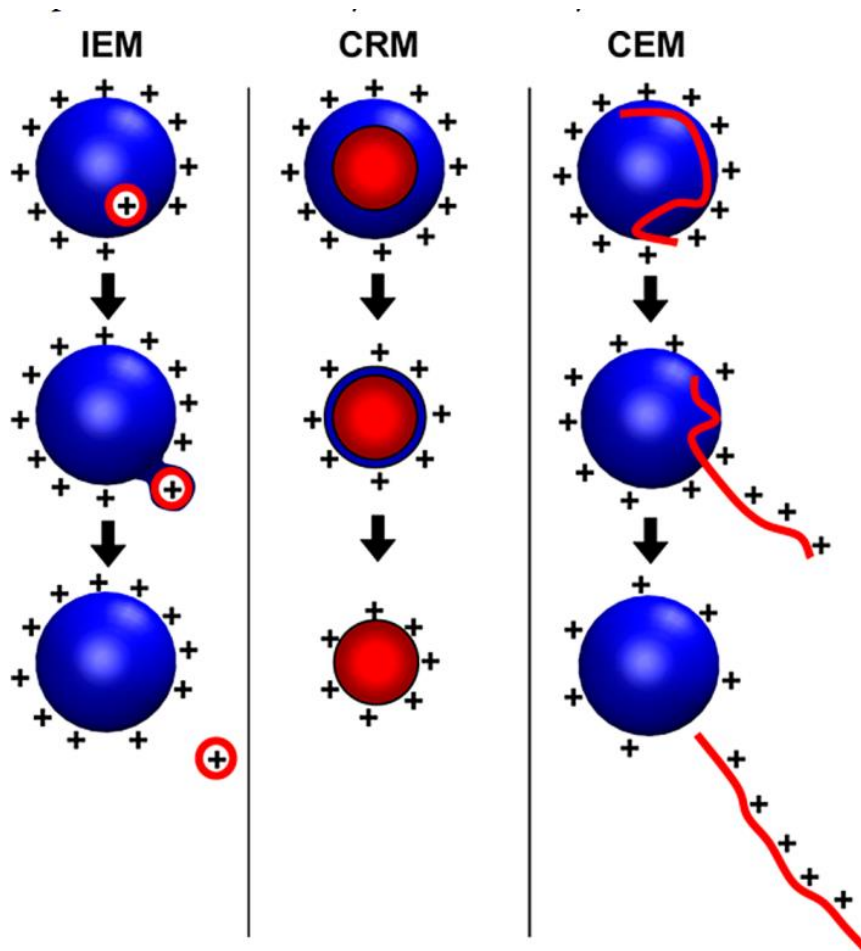


Figure 1.6 Proposed ESI mechanism models.²⁴

Nanoelectrospray ionization (nanoESI) is a special version of ESI by using a low flow rate (10~100 nL/min), pulled capillary emitter (1~2 μm I.D.) without using sheath gas.²⁵ nanoESI advanced in higher sensitivity, matrix tolerance, and less sample consumption compared to ESI.

1.3.6 Paper Spray Ionization

Paper spray (PS) ionization is first invented by Cooks and Ouyang in 2010.²⁶ As an ionization method that has characteristics on both ESI and ambient ionization method, PS demonstrates its potential on complex sample qualitative and quantitative fast analysis, especially on point-of-care application. Benefit from its minimal sample pretreatment, low cost, little biohazard, and less chemical consumption. PS becomes a popular method and has already been applied in the various clinical application including drugs, metabolites, lipids, and proteins.²⁷ As seen in Figure 1.7 The methodology of PS is straightforward, the target analyte is loaded onto the paper substrate without sample pretreatment, high spray voltage is applied after sample drying. More recently, modification of paper spray using different substrate materials has been realized an improved sensitivity and application for PS.

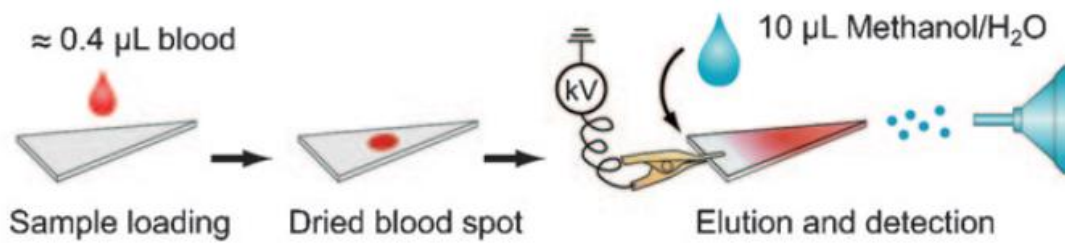


Figure 1.7 Analysis of a dried blood spot using paper spray ionization.²⁶

1.4 Mass Analyzers

As one of the indispensable components of the mass spectrometer, a mass analyzer is primarily used for analyte ion discrimination and filtration based on analyte mass-to-charge ratio (m/z),²⁸ In some scenarios, it can be also used for the ion selection, fragmentation, or other functions.² Commonly used mass analyzer including quadrupole, ion trap, time-of-

flight (TOF), Fourier-transform ion cyclotron resonance (FTICR), and Orbitrap. Numerous hybrids of these analyzers are employed to realize broad application because there is no single mass analyzer that is compatible with all sample analyses. More detail for each mass analyzer is discussed below.

1.4.1 Quadrupole Mass Analyzer

Quadrupole mass analyzer is one of the essentially used mass analyzers, originally invented by Wolfgang Paul and Helmut Steinwedel. A Quadrupole consists of four parallel circular or hyperbolic cross-section rods (Figure 1.8). Each opposing rod pair is connected electrically. As a radio frequency (RF) and direct current (DC) combination potential is applied, the ions travel along rods oscillate, only the ions with particular m/z will have stable trajectories at specific DC and RF potential. Other ions will bump into the rods and be filtered out.²⁸ Except for the quadrupole, other multipoles are depending on the amount of the rod, called hexapole or octupole. By adjusting DC potential to 0 and only applying RF potential, all ions get a chance to pass through, under such scenario, RF-only multipoles play as ion transmission guides. It can also act as collision cells for performing collision-induced dissociation (CID) when inert gas is infused. The fragmentation is controlled by varying the RF potential. Quadrupole mass analyzers are advantageous in simplicity, reliability, and robustness. Benefit from its fast duty cycles and relatively low vacuum requirements, interfacing quadrupole or multipole with gas chromatography (GC) and liquid chromatography (LC) is straightforward. But limited at mass resolution (<3000), mass accuracy (>100 ppm), and mass range (up to 3000 amu).²²

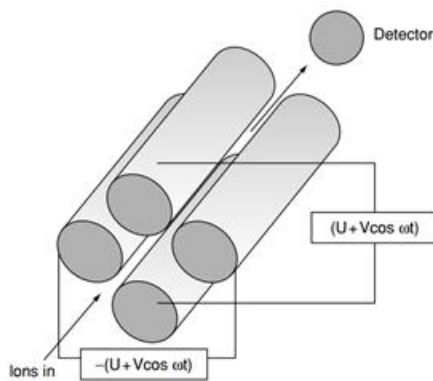


Figure 1.8 Diagram of quadrupole mass analyzer.²¹

1.4.2 Ion Trap Mass Analyzer

Ion trap mass analyzer can be described as a special version of quadrupole mass analyzer, as known as a Paul trap. It consists of two endcap electrodes and one ring electrode (Figure 1.9). The ions are trapped and accumulated by modulating the RF field once they enter the ion trap by the small hole on the endcap electrode, the resolution and sensitivity of the ion trap mass analyzer are slightly better than quadrupole mass analyzer.²² The trapped ions are ejected in the order of increasing m/z from the trap to detector by changing the RF potential. Instead of using as a primary mass analyzer, ion trap now is more often used as a precursor mass filter for MS/MS analysis. The main reason is its small volume and low price.

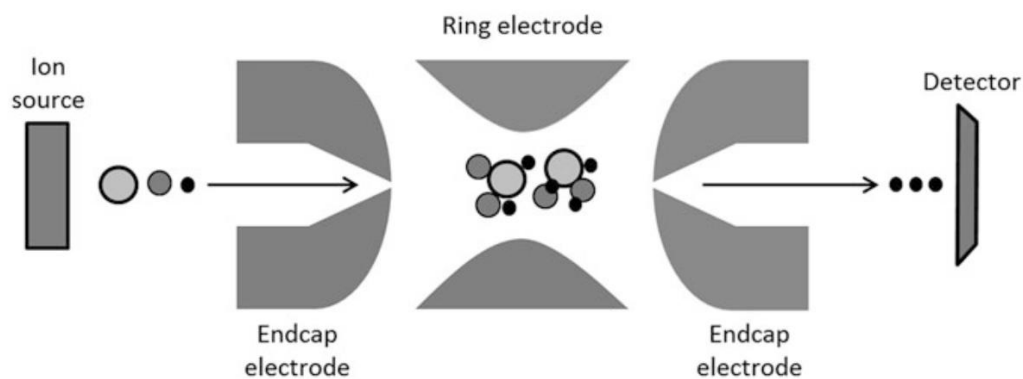


Figure 1.9 Diagram of ion trap mass analyzer.

1.4.3 Time-of-Flight Mass Analyzer

Time-of-flight (TOF) mass analyzer is another commonly used mass analyzer. As shown in Figure 1.10, acceleration grids and drift tubes are the two main components of the TOF analyzer. More recently, TOF is further advanced on its resolution increasing by adding electrostatic mirrors and using delayed extraction techniques.²⁸ The principle of the TOF analyzer is that ions with different masses reach the detector at a different time due to the different drift velocities they have after grid acceleration. Compared with other mass analyzers, TOF theoretically possesses an unlimited mass range, this makes TOF a popular analyzer for large biomolecules such as protein or antibodies. Besides, being perfectly compatible with MALDI propels TOF mass analyzer to the forefront.

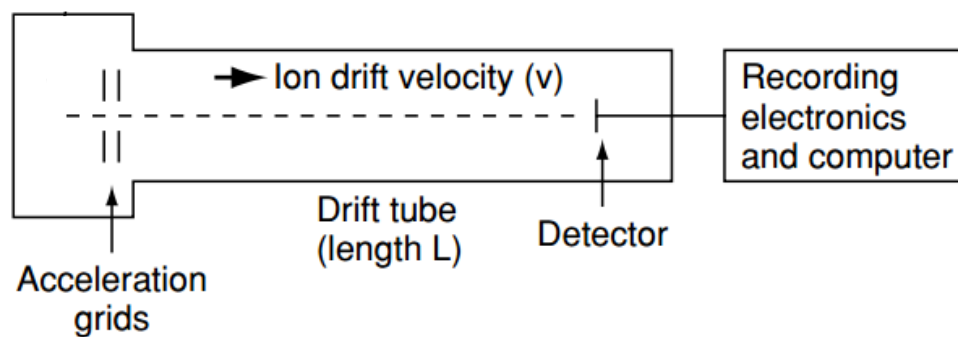


Figure 1.10 Diagram of time-of-flight mass analyzer.

1.4.4 Fourier-Transform Ion Cyclotron Resonance Mass Analyzer

Fourier-transform ion cyclotron resonance (FTICR) mass analyzer, known as its high resolution (2.5×10^6) and mass accuracy (0.6 ppm)²² compared with other mass analyzers, is a Penning trap that uses the magnetic field instead of the electric field to trap the injected ions (Figure 1.11). Under Lorentz force, ions move in circular orbits of characteristic frequency, called the cyclotron frequency, that is proportional to m/z . With the assistance of Fourier transform of the signal, target compound m/z is determined. Benefit from its high mass accuracy, FTICR is widely applied in the proteomics field. While the limitations of FTICR include large instrument size because of the large superconducting magnets, the high cost of maintaining the FTICR under good condition, and slow scan speeds.

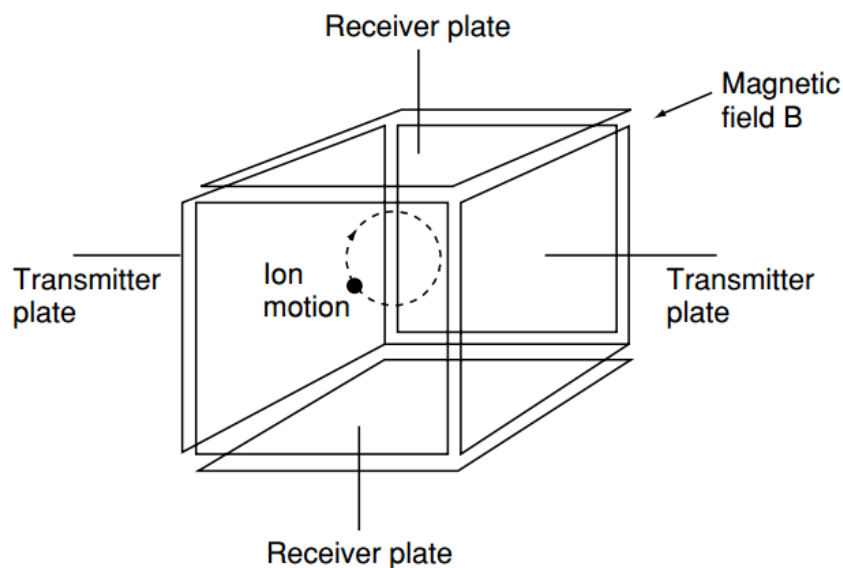


Figure 1.11 Diagram of Fourier-transform ion cyclotron resonance mass analyzer.

1.4.5 Orbitrap Mass Analyzer

Orbitrap Mass analyzer is similar to FTICR mass analyzer, both are using Fourier transform to convert the signal to m/z spectrum. Unlike FTICR mass analyzer, Orbitrap employs the electric field to induce the ions' oscillation. Orbitrap consists of three main parts: the inner central electrode and two outer electrodes separated by a dielectric ring (Figure 1.12). The tangentially injected ions, from the out electrodes hole, are bent towards the inner electrode, under specific potential, the centrifugal force caused by ions' tangential velocity balances the electric field force. As a result, the ions keep rotating around the inner electrode, due to the conical shape of electrodes, a harmonic axial oscillation occurs. The axial harmonic frequency is proportional to the ion m/z . Orbitrap realizes comparable resolution, especially for high m/z ions, in comparison to FTICR, but with much smaller size, cost, and maintenance. Orbitrap not only can interface to LC but also ambient real-

time ionization methods. But the duty cycle of Orbitrap is slower than that of TOF mass analyzer.

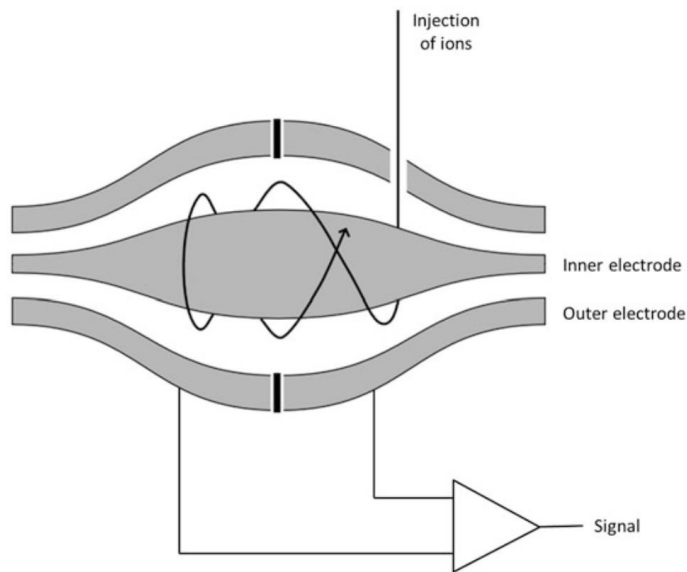


Figure 1.12 Diagram of orbitrap mass analyzer.

1.5 Detectors

Depending on the type of the mass spectrometer, a variety of detectors are used for converting ion kinetic energy into electrical signals. The most commonly used detector is the electron multiplier. the detector consists of a series of dynodes with increasing potential (Figure 1.13). When ion beam strikes the first dynode, secondary electrons are released and an electron cascade takes place as numerous dynodes are involved, as a result, the signals are amplified up to the order of 10^6 .²¹ Photomultiplier conversion dynode is similar to electron multiplier yet not as commonly used. The secondary electrons strike a phosphorus screen instead of a dynode, the released photons are detected by a photomultiplier. Photomultiplier conversion dynode realizes similar sensitivity to the electron multiplier but possesses an improved lifetime. The main reason is that the

photomultiplier tube is sealed in a high vacuum. Faraday cup is a detector with low sensitivity but high accuracy. So, it normally works for isotope ratio measurement MS detection, for example, gas isotope ratio mass spectrometry (GIRMS) and inductively coupled plasma mass spectrometry (ICPMS).²¹

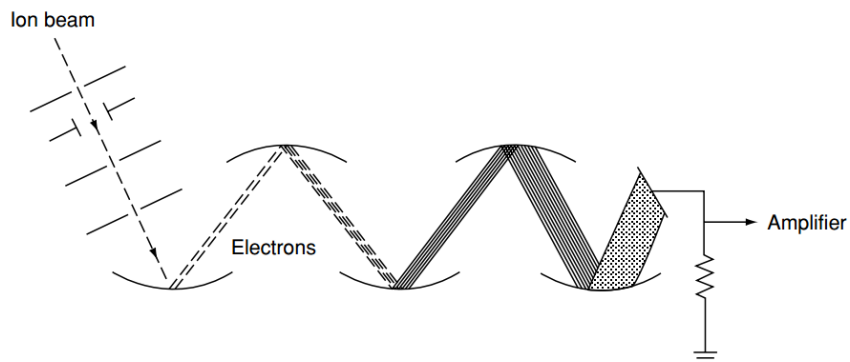


Figure 1.13 Diagram of electron multiplier ion detector.²¹

1.6 Coupling Electrochemistry with Mass Spectrometry

Hyphenation of electrochemistry (EC) and mass spectrometry (MS) in off-line and online approaches become more and more attractive strategies in the analytical chemistry field. By using highly sensitive MS, the electrochemically generated intermediates, products, and mechanism are characterized and elucidated.²⁹ The first mass spectrometric analysis offline collected electrochemically generated compound can be traced back to 1970.³⁰ Wolter and Heitbaum conducted the first online EC-MS measurement for gaseous and volatile electrochemical reactions.³¹ After improving the interfacing, the same group did the non-volatile EC oxidation product MS analysis online.³² Volk applied EC-MS for bioanalytical field for uric acid oxidation intermediate and product characteristics.³³⁻³⁴ The first attempts

to couple EC with electrospray ionization were carried out by Zhou and Van Berkel.³⁵ Variable interfacing instrument setups are demonstrated in several reviews.³⁶⁻⁴⁴ Benefit from the ability to separate products from the electrolyte, differential electrochemistry mass spectrometry (DEMS) has been applied to CO₂ reduction,⁴⁵⁻⁴⁶ lithium-ion battery,⁴⁷ methanol oxidation,⁴⁸ carbon corrosion,⁴⁹ and hydroxylamine oxidation.⁵⁰ Direct interfacing of EC and MS are also employed in lot of research due to their flexible and diverse setups. For example, energy carrier,⁵¹ electrosyntheses,⁵² protein cleavage,⁵³ disulfide bond mapping,⁵⁴ double bonds location,⁵⁵ and antibiotics degradation.⁵⁶ Liquid chromatography (LC) or capillary electrophoresis (CE) is integrated to add retention or migration time as additional information for EC-MS-based protein digestion⁵⁷ and nucleobase oxidation.⁵⁸ With the development of EC-MS, the transfer from the proof-of-concept setup to the standardized application is possible future plan.

1.7 Coulometric Mass Spectrometry Absolute Quantitation

To eliminate the need for using standards or calibration curves for absolute quantitation, a new strategy of using electrochemistry-assisted mass spectrometry, namely coulometric mass spectrometry (CMS), was developed. The CMS method application includes absolute quantitation of organic compounds, peptides, and proteins.⁵⁹⁻⁶⁴ As illustrated in Figure 1.14, CMS quantitation strategy involves LC separation and oxidation in an electrochemical flow cell and is followed by online MS detection. The oxidation results in an electrical current that can be integrated over time to obtain the total electric charge Q in the electrochemical oxidation reaction. According to Faraday's Law, Q is proportional to the quantity of the oxidized hydrazine: $Q=nzF$, where n denotes the moles of the oxidized hydrazine, z is the

number of electrons transferred per molecule during the oxidation reaction, and F is the Faraday constant ($9.65 \times 10^4 \text{ C/mol}$). Thus, $n = Q/(zF)$. On the other hand, from the acquired MS spectra before and after EC oxidation, the oxidation conversion yield Δi can be determined by measuring the relative change of the hydrazine peak area in the extracted ion chromatogram (EIC) upon oxidation. Thus, the total amount of the hydrazine can be calculated as $n/\Delta i = Q/(zF\Delta i)$.

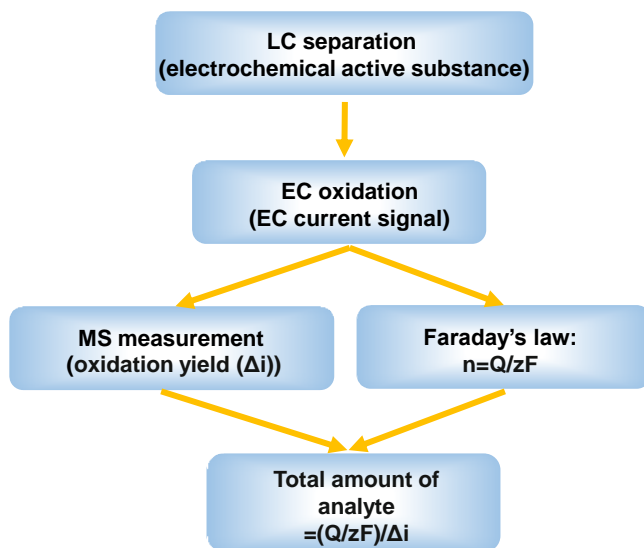


Figure 1.14 Workflow of coulometric mass spectrometry (CMS) for absolute quantitation.

CHAPTER 2

REACTION SCREENING FOR ELECTROSYNTHESIS

2.1 Introduction

Recently, synthetic organic electrochemistry has achieved a dramatic uptick in popularity.⁶⁵⁻⁸¹ Electrosynthesis uses a pair of electrodes to add or subtract electrons to or from the substrate, which triggers the formation of the target product.⁸²⁻⁹² Compared with non-electrochemical synthesis, electrosynthesis has the advantages of offering more selective, safer, and less energy consumption approaches.⁹³⁻¹⁰² One of the more challenging and thus elusive electrosynthesis that attracts much attention¹⁰³⁻¹⁰⁷ is net redox neutral reactions, in which both oxidation and reduction steps are involved to achieve overall redox neutrality. Initial anode oxidation or cathode reduction of the substrate to form a product radical cation or anion is usually paired with an opposite single-electron transfer (SET) event to furnish a neutral product.

Two possible conditions can trigger the occurrence of redox neutral electrochemical reactions. One involves the product radical cation or anion being stable enough to migrate to the cathode or anode so that a SET reduction or oxidation occurs to yield the final neutral product.¹⁰⁵⁻¹⁰⁷ The other requires the product radical cation or anion to undergo SET oxidation or reduction with the starting material in a chain mechanism. The former is more arduous to meet as a tandem oxidation/reduction has to occur on a macroscopically separated anode and cathode. Most of the reported redox-neutral electrochemical syntheses are centered on the latter condition. Notable examples include [2 + 2] cycloaddition¹⁰⁸⁻¹¹¹ and [4 + 2] Diels–Alder¹¹²⁻¹¹⁵ cycloaddition reactions mediated

by anodically produced radical cations of dienes or dienophiles. Chiba¹¹⁶ raised the importance of a redox tag on the chain event of these reactions. Radical anions of activated alkenes generated by cathodic reduction are equally capable of promoting these two classes of cycloaddition reactions. Xu¹¹⁷ developed a redoxneutral method for intramolecular hydroamidation of alkenes without relying on a chain event. The hydroamidation was achieved by an intramolecular addition of an amidyl radical generated via ferrocene as the redox catalyst to an alkene. The resulting carbon radical then abstracted a hydrogen atom from 1,4-cyclohexadiene (1,4-CHD) to complete the redox neutral process. For a handful of examples invoking a chain mechanism, catalytic current efficiency was usually used as the primary evidence,^{108, 118} and limited kinetic studies were sometimes reported to strengthen the argument.¹¹⁹ Ambiguity about the chain event often remains.

We previously developed a [3 + 2] annulation of *N*-cyclopropylanilines (CPA) with alkenes by photoredox catalysis¹²⁰ and subsequently investigated its mechanism.¹²¹ As shown in Figure 2.1 top panel, upon irradiation, Ru(II)(bpz)₃²⁺ is promoted to the excited triplet state Ru(II)*(bpz)₃²⁺, which oxidizes CPA to the radical cation. The radical cation subsequently undergoes ring-opening, and then adds to styrene to produce the [3 + 2] annulation product radical cation. Finally, the radical cation is reduced via two mechanisms: a photoredox reaction and a chain reaction. We questioned whether we could achieve the annulation reaction by direct electrolysis presumably via the chain process completely. However, converting the photoredox catalysis to electrochemistry for this annulation reaction was nontrivial, as net redox neutral reactions are known to be problematic for electrochemistry but facile by photoredox catalysis. Herein, we report our studies in developing the electrocatalytic redox neutral [3 + 2] annulation of *N*-cyclopropylanilines

and alkenes by the chain mechanism (Figure 2.1, bottom panel). We took full advantage of the capabilities of the integrated online EC/MS platform as a screening tool to expedite the discovery. As evidenced by net redox neutral reactions, photochemistry and electrochemistry complement each other. This study overcame the inherent limitation of net redox neutral reactions in electrochemistry and used it as a template to address other types of challenging electrosynthesis reactions.

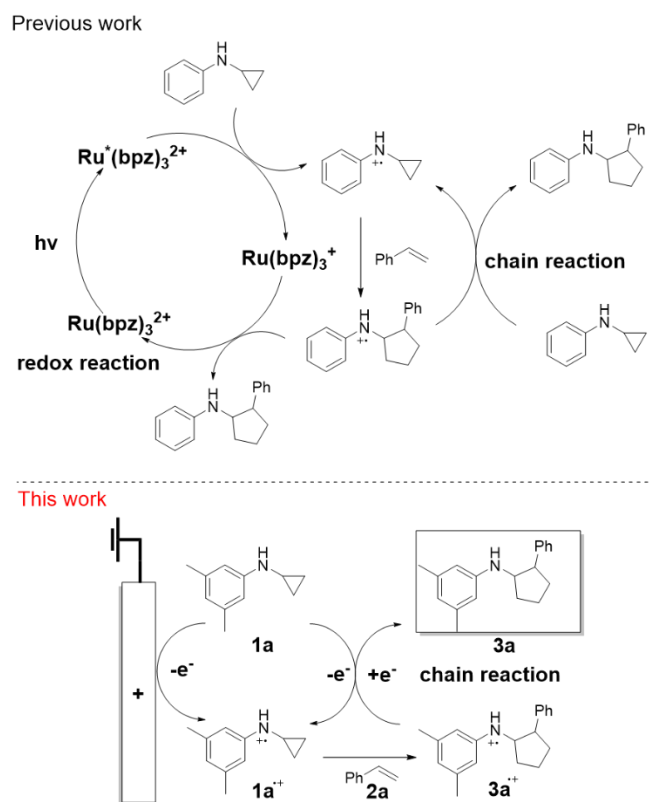


Figure 2.1 Proposed mechanism for the [3+2] annulation reaction of *N*-cyclopropylanilines and styrene (top panel illustrates the reaction catalyzed with photocatalyst; bottom panel displays the reaction triggered electrochemically without using catalyst).

2.2 Apparatus

Two home-built electrosynthesis platforms are built for reaction screening.

2.2.1 Small Scale Electrosynthesis Set-up

As shown in Figure 2.2, small scale electrosynthesis setup, it consisted of an electrochemical thin-layer flow cell, a short piece of a fused silica capillary as a microreactor and an online MS detector, with one reactant was fused into the flow cell via channel 1 and another reactant introduced for reaction via channel 2. The flow cell was equipped with a glassy carbon disc (i.d., 6 mm) as the working electrode (WE), Ag/AgCl (3 M NaCl) as the reference electrode (RE), and the cell stainless steel body serving as a counter electrode (CE). The solution flowing out of the capillary microreactor was soft ionized by sonic spray ionization (SSI). The solution flowing out of the capillary microreactor was soft ionized by sonic spray ionization (SSI).

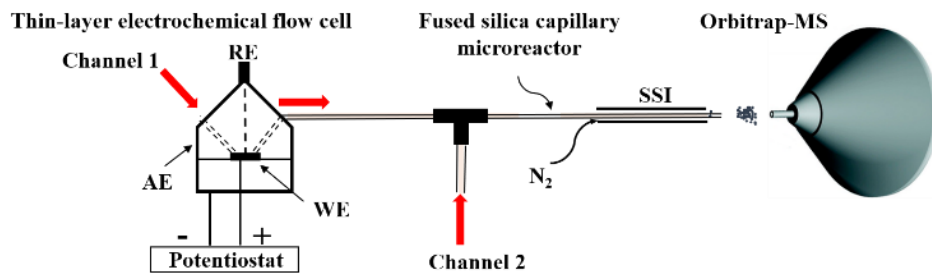


Figure 2.2 Small scale electrosynthesis setup.

2.2.2 Large Scale Electrosynthesis Set-up

Large scale electrosynthesis was conducted in a 20 mL clear screw glass vial equipped with one Pt plate (2 cm×1 cm×0.1 cm, length×width×thickness) and one piece of reticulated vitreous carbon electrode (2 cm×1.3 cm×1.3 cm, length×width×thickness) as cathode and anode respectively. The reaction mixture was degassed by freeze-pump-thaw cycles. A

TEKPOWER variable linear direct current (DC) power supply was used to control the current (1 mA) for electro-oxidation.

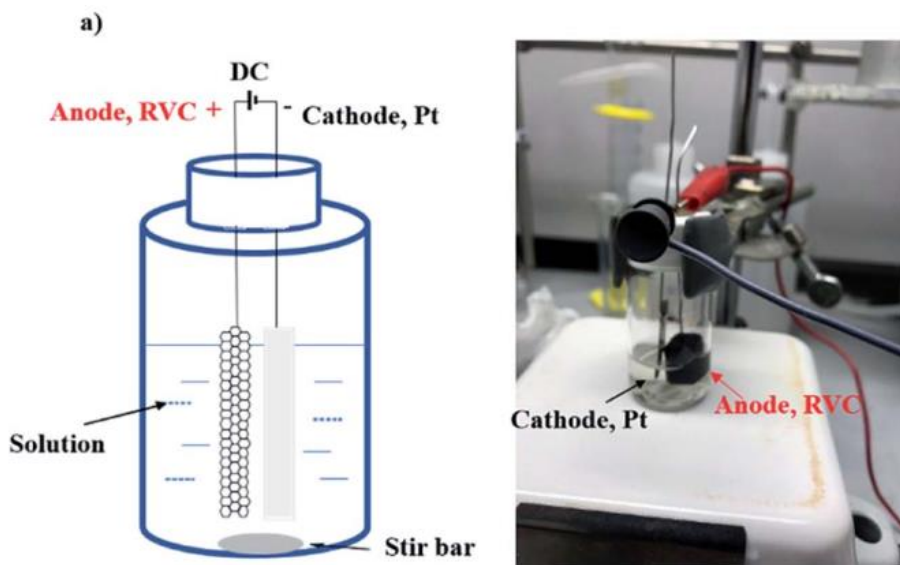


Figure 2.3 Large scale electro-synthesis setup.

2.2.3 H-type Divided Electrolysis Cell Setup

H-type divided cell with two compartments separated with a frit membrane. The two electrodes, RVC and Pt electrodes were inserted into one chamber each separately (Figure 2.4). The reaction mixture was degassed by freeze-pump-thaw cycles. A TEKPOWER variable linear direct current (DC) power supply was used for electro-oxidation.

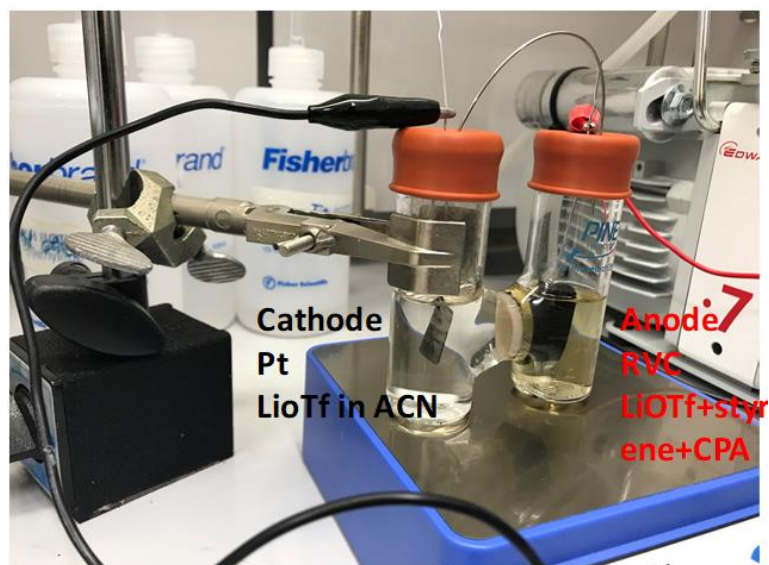


Figure 2.4 H-type divided electrolysis cell setup.

2.3 Results and Discussion

To prove that the electrochemical method can be used to generate the [3 + 2] annulation reaction product, *N*-cyclopropyl-3,5-dimethylaniline (CPDA, **1a**), and styrene (**2a**) were first chosen as reactants (Figure 2.5). A small-scale test was performed using an electrochemical thin-layer flow cell along with online MS monitoring. A solution of **1a** (1 Mm) and lithium triflate (LiOTf, 1 Mm) in MeCN was infused into the cell via channel 1 and MeCN was infused via channel 2 (flow rate: 50 μ L/min for each channel). When a potential of +3.0 V (vs.Ag/AgCl) was applied to the WE, as shown in the recorded SSI-MS spectrum (Figure 2.6a), the **1a**⁺ of m/z 161 (theoretical m/z 161.11990, measured m/z : 161.12017, mass error 1.68 ppm) was detected, indicating the occurrence of the electro-oxidation of **1a**. When **2a** was introduced to replace MeCN via channel 2, indeed, the protonated [3 + 2] annulation product [**3a** + H]⁺ (theoretical m/z 266.19033, measured m/z : 266.18972, mass error 2.29 ppm) was observed (Figure 2.6b). Upon collision-induced

dissociation (CID), the ion of m/z 266 gave rise to fragment ions of m/z 145, 122, and 91 by losses of $C_8H_{11}N$, $C_{11}H_{12}$, and $C_{12}H_{17}N$, respectively, consistent with its assigned structure (Figure 2.6c). At the same time, the intensity of the $1a^{+}$ decreased from 1.6×10^6 (Figure 2.5a) to 1.9×10^4 (Figure 2.6b), indicating that $1a^{+}$ did react with $2a$ to produce the [3 + 2] annulation product. The +1 ion of $3a$ instead of $3a^{+}$ was observed probably due to the charge transfer between $3a^{+}$ and $1a$ to form $3a$ which was ionized as the +1 ion by SSI.

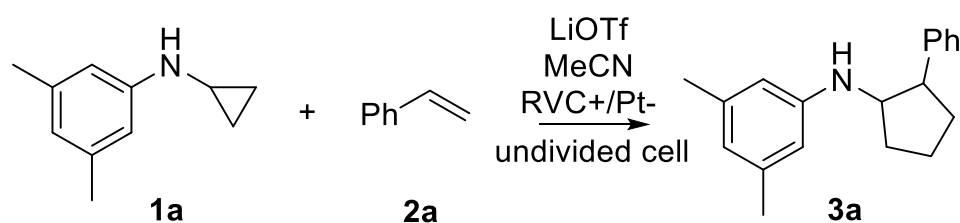


Figure 2.5 Intermolecular [3+2] annulation of *N*-cyclopropyl-3,5-dimethylaniline (CPDA) **1a** and styrene **2a** by electrolysis.

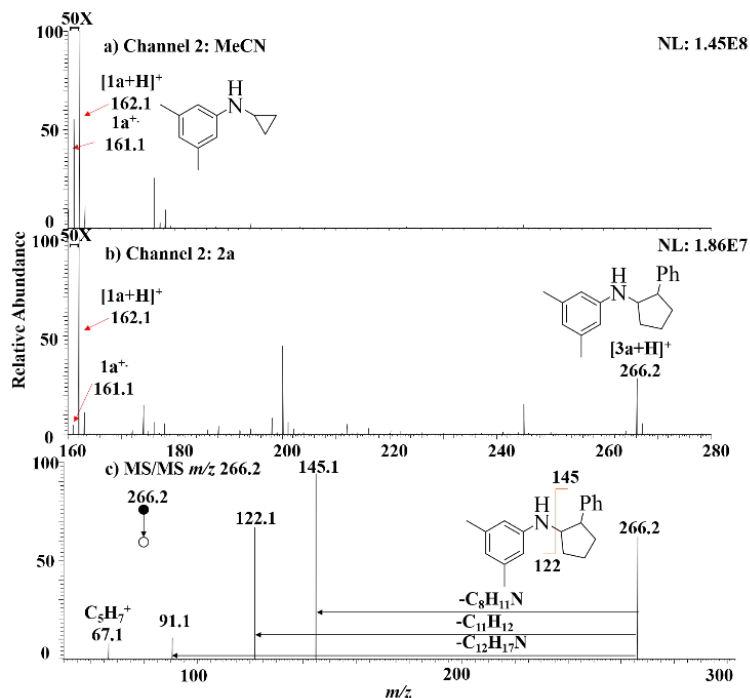


Figure 2.6 MS spectra showing a) the formation of radical cation $1a^+$ when the cell was turned on with $1a$ being introduced into the flow cell via channel 1 and MeCN being introduced via channel 2; b) the product ion $[3a+H]^+$ was observed when the cell was turned on with $2a$ being introduced via channel 2. © MS/MS spectrum of m/z 266.

Small scale electrolysis setup also allowed us to verify whether or not the charge transferred between $3a^+$ and $1a$ could take place, a key step in the chain reaction mechanism (Figure 2.7a), that would be needed to generate the neutral product $3a$. Using the EC/MS setup, a solution of the annulation product $3a$ (1 mM) and LiOTf (1 mM) in MeCN was infused into the flow cell through channel 1, and MeCN was injected via channel 2. A potentiostat was used to supply the potential for electrooxidation. The injection flow rate for both channels was 15 μ L/min. A voltage of +3.0 V (vs. Ag/AgCl) was applied to the flow cell to trigger the oxidation of $3a$. The expected radical cation $3a^+$ was detected (Figure 2.7b, black line, theoretical 265.18250, measured 265.18234, mass error 0.60 ppm). When the solvent (MeCN) was replaced by $1a$ (0.1 mM in MeCN) in

channel 2, the intensity of $\mathbf{3a}^+$ decreased (Figure 2.7b, red line), indicating the consumption of $\mathbf{3a}^+$ by $\mathbf{1a}$. At the same time, radical cation $\mathbf{1a}^+$ was detected (Figure 2.7c, red line, theoretical 161.11990, measured 161.12002, mass error 0.74 ppm). To confirm that the observed $\mathbf{1a}^+$ was not due to oxidation of $\mathbf{1a}$ by other oxidative species from the cell, a control experiment was performed in which only LiOTf (1 mM) in MeCN (without $\mathbf{3a}$) was infused into the cell for oxidation under the same conditions and then mixed with $\mathbf{1a}$. In this control experiment, no $\mathbf{1a}^+$ was generated (Figure 2.7c, black line). This set of data confirmed the oxidation of $\mathbf{1a}$ by the annulation product radical cation $\mathbf{3a}^+$ (Figure 2.7a) did occur, being the critical step responsible for completing the redox neutral reaction.

As encouraged by the success of observing individual key reaction steps that are needed for electrosynthesis of $\mathbf{3a}$ from $\mathbf{1a}$ and $\mathbf{2a}$, we attempted bulk solution electrolysis using the large-scale electrolysis setup. A solution of $\mathbf{1a}$ (100 mM, 1 mmol), styrene $\mathbf{2a}$ (1 M, 10 mmol), and LiOTf (1 M, 10 mmol) in 10 mL MeCN was added into the electrolysis cell. After 9 h at 1 mA direct current provided by a direct current (DC) power supply, the protonated [3 + 2] annulation product [$\mathbf{3a} + \text{H}$]⁺ (theoretical m/z : 266.19033, measured m/z : 266.19003, mass error -1.13 ppm) was detected by MS and appeared as the dominant peak in the MS spectrum (Figure 2.8), indicating a good yield of the reaction. Upon CID, the ion m/z 266 gave rise to fragment ions of m/z 145, 122, and 91 upon CID by losses of $\text{C}_8\text{H}_{11}\text{N}$, $\text{C}_{11}\text{H}_{12}$, and $\text{C}_{12}\text{H}_{17}\text{N}$, respectively, consistent with its assigned structure. Using dibromomethane as the internal standard, the NMR yield was measured to be 68%. This result showed that the scale-up electrolysis for intermolecular [3 + 2] annulation reaction worked.

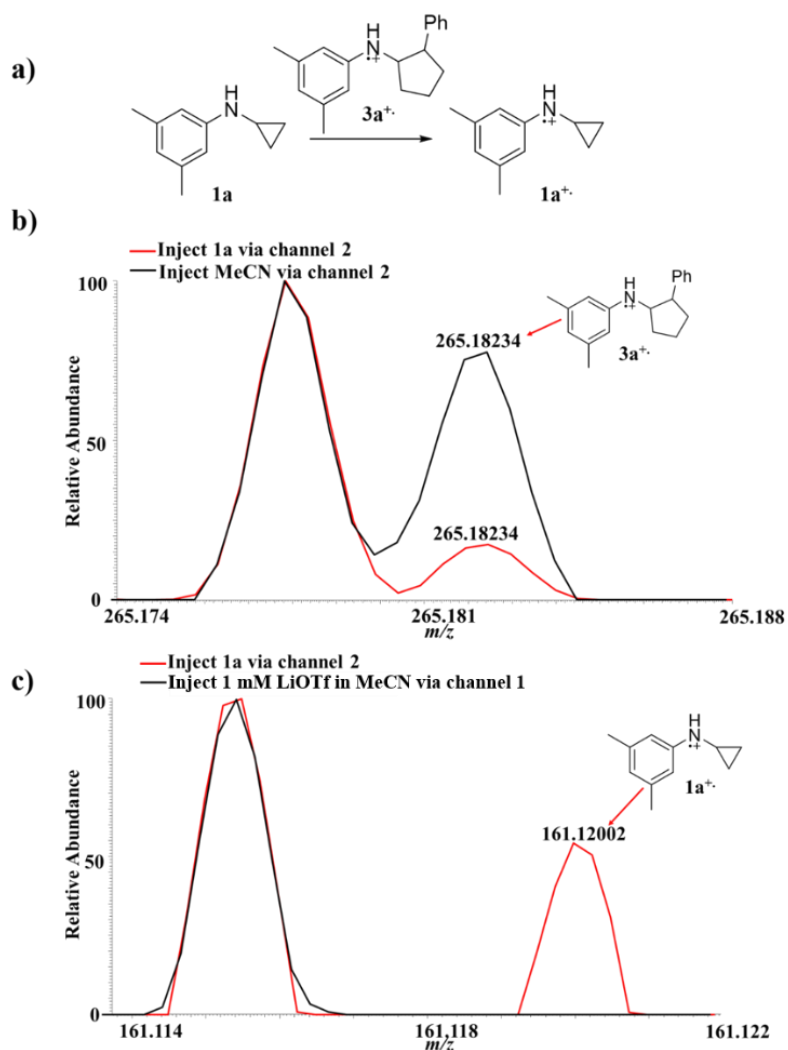


Figure 2.7 Online MS monitoring of the oxidation of **1a** by **3a⁺**: a) chemical equation showing the reaction between **1a** and **3a⁺**; b) MS spectra showing the formation of the radical cation **3a⁺** when the oxidation potential was applied to the cell. The signal of **3a⁺** was lower when the solution injected via channel 2 changed from MeCN (black line) to **1a** (red line). C) MS spectra showing the formation of radical cation **1a⁺** (red line) when the cell was turned on with **3a** being introduced into the flow cell via channel 1 and **1a** being introduced via channel 2. No formation of radical cation **1a⁺** was observed (black line) when the cell was turned on with 1 Mm LiOTf IN MeCN being introduced into the flow cell via channel 1 and **1a** being introduced via channel 2.

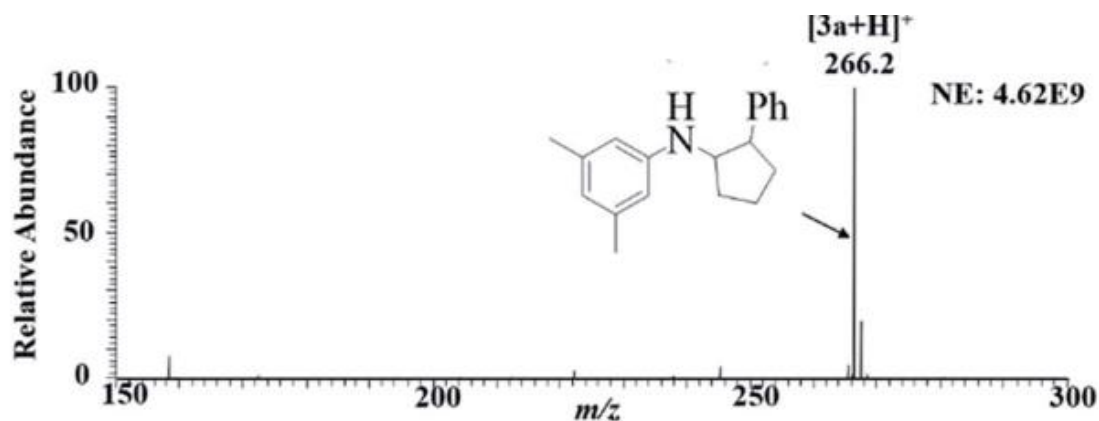


Figure 2.8 MS spectrum showing the formation of the product **3a** by large scale electrolysis cell.

We thus went ahead to optimize the electrolysis conditions, and again, **1a** and **2a** were chosen as the model substrates (Table 2.1). A constant current (entries 1 and 2) or a constant voltage (entries 3 and 4) was used for electrolysis. No product was observed using a higher current (entry 2) while a higher voltage led to a lower yield (entry 4). Compared with the constant voltage mode, the constant current was preferred because it gave the same yield (NMR yield) in a shorter reaction time (75%, 9 h for entry 1 vs. 75%, 12 h for entry 3). Switching the anode from porous RVC to planar Pt furnished the product in a lower yield (entry 5), probably because the porous RVC electrode provided a large electrode surface area to react with reactants. Doubling the amount of LiOTf (entry 6) or replacing LiOTf with other electrolytes (entries 7 and 8) all resulted in lower yields. The yield was also reduced when the amount of styrene was doubled (entries 9), probably caused by the side effect from styrene polymerization on the electrode. Likewise, halving the amount of LiOTf or styrene resulted in lower yields with more unreacted *N*-cyclopropylaniline. Finally, the addition of water completely inhibited the product formation (entry 10) and

replacing MeCN with MeOH led to a lower yield (entry 11). Thus entry 1 experimental conditions were adopted for electrolysis of different substrates.

Table 2.3 Reaction Optimization

Entry	Variation from standard condition	Reaction yield [a]	Reactant leftover (Y/N)	Reaction time
1	None	75%	N	9h
2	$I_{\text{cell}}=4 \text{ mA}$	No product	N	9h
3	$E_{\text{cell}}=3.5 \text{ V}$	75%	N	12h
4	$E_{\text{cell}}=4.5 \text{ V}$	42%	N	12h
5	Pt+/Pt-, $E_{\text{cell}}=3.5 \text{ V}$	40%	Y	12h
6	LiOTf (20 equiv.)	65%	N	9h
7	Electrolyte LiClO_4	15%	Y	9h
8	Electrolyte Me_2NOAc	42%	Y	9h
9	Styrene (20 equiv.)	20%	Y	9h
10	Solvent MeCN/ H_2O 9:1	No product	Y	9h
11	Solvent MeOH	35%	Y	9h

[a] NMR yield with dibromoethane used as the reference.

After optimizing the reaction conditions, a variety of *N*-cyclopropylamines and alkenes were investigated, and good isolation yields were obtained (Figure 2.9). An aryl group on *N*-cyclopropylamines could promote the initial oxidation to occur as it decreased the redox potential of *N*-cyclopropylamines.¹²² Substituents such as methyl and chlorine on the aromatic ring of cyclopropylamine were tolerated (3a and 4a). *N*-Cyclopropylamines substituted with other arenes such as biphenyl and naphthalene also worked (5a and 6a). Substituents on the phenyl group of styrenes such as ortho-bromine and paramethoxy groups had little effect on the yields (3c, 3d, 4c, 4e, 5b, and 5d). Substitution of the phenyl

group of styrene by a naphthyl group lowered the yield (4d). Other types of *pi* bonds were explored. Acrylonitrile gave acceptable to good yields of the annulation products (3b, 4b, 5c, and 6b). The diastereoselectivity for the annulation reaction was generally poor, as most of them gave a 1 : 1 mixture except 4a and 5c (2 : 1 and 4 : 1 were observed for the two products, respectively, with the *cis* isomer as the major product). Phenylacetylene was shown to be a viable annulation partner (4f).

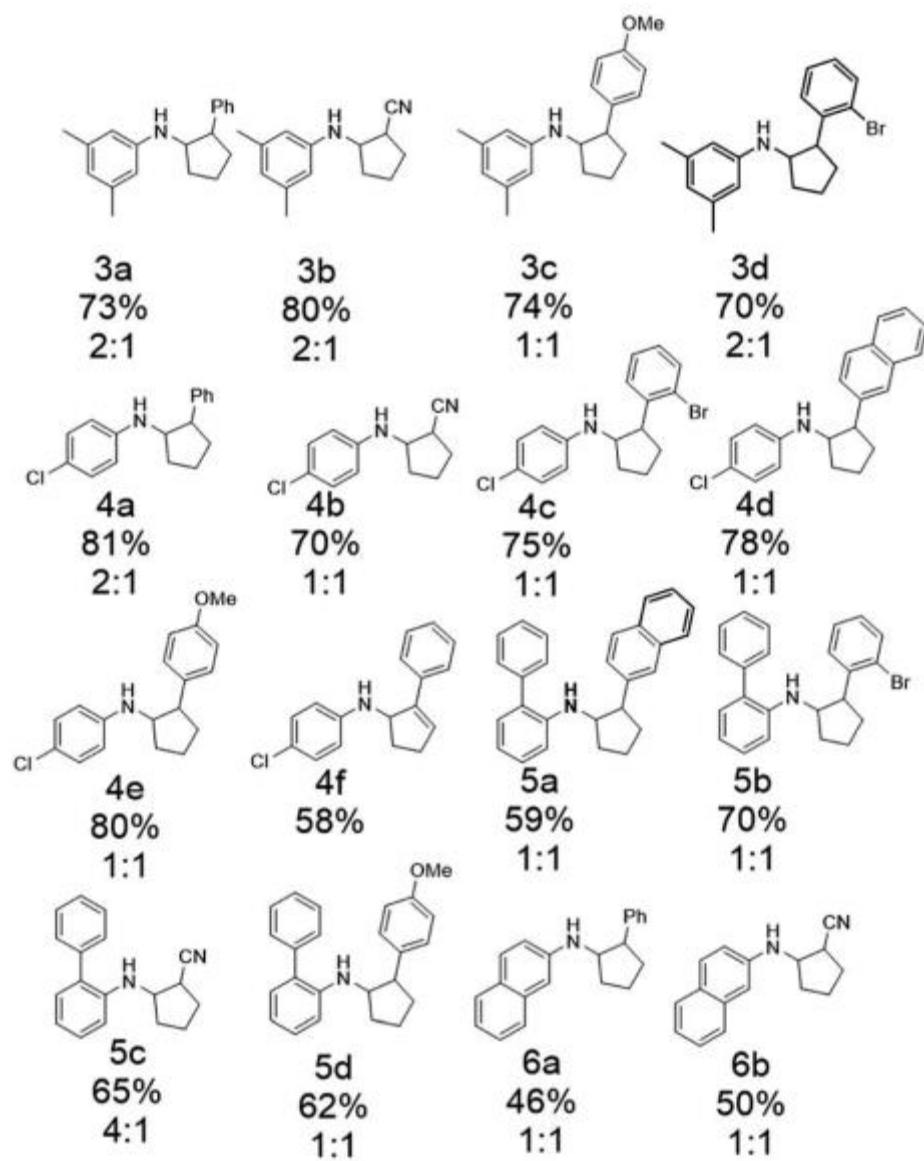


Figure 2.9 The substrate scope of intermolecular [3 + 2] annulation by the electrochemical approach (percentages show the isolation yields). The ratios for cis/trans product isomers are also listed.

Mechanistically, after establishing the chain mechanism as a viable pathway to achieve the redox neutral reaction, we questioned the feasibility of the other conditions in which the product radical cations were reduced on the cathode. We carried out the reaction

of **1a** and **2a** using an H-type divided electrolysis cell (Figure 2.4). A solution of **1a** (32 mM, 0.64 mmol), **2a** (300 mM, 6 mmol), and LiOTf (300 mM) in 20 mL MeCN was added into one chamber of the electrolysis cell (the anode RVC side) and 20 mL of MeCN containing 300 mM LiOTf was added into the other chamber (the cathode Pt side). After 9 h of electrolysis with an applied 1 mA constant current across the two electrodes, interestingly, the protonated [3 + 2] annulation product [**3a** + H]⁺ (theoretical *m/z*: 266.19033, measured *m/z*: 266.18938, mass error -3.57 ppm) was detected from the anode side chamber (Appendix A.1 the NMR yield was 23%). In contrast, no product or reactant was detected in the cathode side chamber, indicating that no product or reactant could pass through the frit membrane. The formation of **3a** in the divided cell suggested that the reduction of the **3a** radical cation was caused by the starting reactant **1a** with simultaneous formation of the **1a** radical cation via the chain mechanism rather than caused by the cathode reduction. The yield was lower than in the un-divided cell. Presumably because the membrane increased the resistance, a higher voltage was needed to apply to the cell to maintain a constant current (5.0–6.5 V for 1 mA electrolysis). As shown in Table 2.1 (entry 4), a higher voltage harmed the annulation reaction.

A comparison between the total charge required for the reaction and the electrical input could also help to clarify if the reaction involves the chain reaction mechanism.¹¹⁰ According to Faraday's law, the total electric charge (*Q*) responsible for oxidizing/reducing a reactant in a redox reaction, is directly proportional to the quantity of the oxidized/reduced substance: $Q = nzF$, where *n* is the moles of the reactant, *z* is the number of electrons transferred per molecule for the redox reaction (*z* = 1 for oxidation of **1a**), and *F* is the Faraday constant ($9.65 \times 10^4 \text{ C/mol}$). According to $Q = nzF$, $1 \times 10^{-3} \text{ mol} \times$

$1 \times 9.65 \times 10^4 \text{ C/mol} = 96.5 \text{ C}$ electricity would be needed for the complete oxidation of 1 mmol **1a** experimentally. As mentioned before, 1 mA was applied to the undivided electrolysis cell for 9 h to complete the electrolysis. The actual consumption of electricity was calculated to be $1 \times 10^{-3} \text{ A} \times 9 \times 3600 \text{ s} = 32.4 \text{ C}$ based on $Q=it$, where i was the applied current and t was the reaction time. Therefore, the reaction was driven to completion with 0.34 equiv. of the current. The catalytic current used for the reaction also supported the chain reaction mechanism.

2.4 Conclusions

A new type of challenging electrochemical redox neutral reaction was developed using our homemade online EC/MS platform. Without using any catalyst, the [3 + 2] annulation of *N*-cyclopropylamines and alkenes proceeded by direct electrolysis instead. Various mechanistic investigations including the use of a divided cell, measurements of the catalytic current, and online MS monitoring of the key electron transfer step between the product radical cation and the reactant supported that the reaction was completed via a chain reaction process. Considering that a chain reaction mechanism is often accompanied by a photoredox reaction in photocatalysis, we expect that electrolysis can be applied to many other visible-light-mediated reactions as an alternative catalyst-free approach.

CHAPTER 3

NOVAL OLIGOSACCHARIDE DETECTION METHOD

3.1 Introduction

Carbohydrates play an indispensable role in the physiology of humans and plants. For example, carbohydrates represent the storage energy in cells (starch and glycogen); they provide structural strength to plants and play a role in signaling.¹²³ The enzymes responsible for the synthesis of all carbohydrates on earth are called glycosyltransferases (GTs). Biochemical characterization of GTs is a challenge due to several factors: 1) GT proteins are present in small amounts in cells, 2) GTs are difficult to purify, and 3) their transfer reaction products are difficult to detect and characterize as these products are produced in very small quantities. In general, detection of transferase activity typically requires the use of sensitive assays that utilize radioactive nucleotide diphosphate (NDP) sugars, the activated state of monosaccharides, which serve as the sugar donor during transferase reaction catalyzed by GTs within the cell.¹²⁴ Thus, developing a strategy to produce GTs *in vitro* in combination with a rapid and sensitive detection method (as an alternative to radioactive precursors) to monitor transferase reaction products (i.e., oligosaccharides) would tremendously benefit the field of glycomics and open the possibility to design high-throughput analytical methods for GT activities.

Traditionally, electrospray ionization mass spectrometry (ESI-MS) and matrix-assisted laser desorption-ionization mass spectrometry (MALDI-MS) are often used to characterize *N*-linked glycans¹²⁵⁻¹²⁸ and plant cell wall polymers.¹²⁹ Accurate molecular mass, along with tandem mass analysis, provides unprecedented capability for glycan

structure characterization and sugar sequence assignment.¹³⁰⁻¹³⁵ However, because of signal suppression by more readily ionized compounds (e.g., salts and other solutes), it is still challenging to detect and analyze oligosaccharides in complex biological mixtures.¹³⁶ Thus, efficient ionization and detection of these carbohydrates require enrichment and desalting steps. Traditional desalting methods include reversed-phase liquid chromatography (RPLC),¹³⁷ size-exclusion chromatography (SEC),¹³⁸ anion-exchange chromatography (AEC),¹³⁹⁻¹⁴¹ lectin-affinity chromatography,¹⁴²⁻¹⁴³ hydrophilic interaction liquid chromatography (HILIC),¹⁴⁴⁻¹⁴⁷ and graphite affinity chromatography.^{144, 148-152} All these desalting methods are time-consuming and have limitations such as low enrichment efficiency and nonspecific binding of oligo-saccharides due to their high polarities. For example, although low limits of detection (LOD) of 100 pmol and 50 fmol were reported for ESI-MS and MALDI-MS methods, respectively,¹⁵³⁻¹⁵⁴ those methods took time ranging from 50 min to 2 h. Additionally, derivatization is needed prior to MALDI-MS analysis due to the low ionization efficiency of oligosaccharides, which is also time-consuming. Thus, developing a fast and sensitive MS detection method for analyzing oligosaccharide in complex matrices is still needed.

Cellulose hydrophilic interaction solid-phase extraction (SPE) microtip has been applied for *N*-glycan purification and enrichment.¹⁴² In this method, glycans are first adsorbed on the cellulose-based SPE cartridge by hydrogen bonding. Salts are washed away with an organic solvent containing only 10% water. By adjusting the water content of the solvent from 10% to 90% (v/v), adsorbed glycans can be eluted from the cellulose substrate. Herein, we present a new approach, termed as desalting paper spray mass spectrometry (DPS-MS), that takes use of the same triangular paper substrate for both

carbohydrate desalting and spray ionization, for fast and sensitive analysis of various oligosaccharide types in complex media including GT reactions. Samples are directly deposited on paper, and oligosaccharides are retained through hydrogen bonding. Unbound salts and other chemicals in the reaction mixture are washed away with ACN/H₂O (90/10 v/v) solution. The adsorbed relatively pure, oligosaccharides are eluted from the paper using high water content (90%) and low ACN content (10%). The released oligosaccharides are ionized through the application of a high voltage for spray ionization. This new analytical method is not only fast (ca. <5 min per sample) and straight-forward, but is also highly sensitive (e.g., LOD of 1.1 nM for β -cyclodextrin). This method could successfully detect various oligosaccharides from nonvolatile buffers (e.g., Tris, phosphate and HEPES buffers). To test the validity of this method for biological samples, we produced two well-characterized Arabidopsis GTs (AtXXT1 and AtGUX1) through in vitro coupled Transcription/Translation System (TNT®) and used the produced GTs in glycosyl transfer reactions. Our DPS-MS method could directly detect products generated by these GTs despite the high salt concentration and proteins (from the in vitro transcription/translation system). Furthermore, quantitative analysis by DPS-MS is feasible. For instance, the acceptor sugars in GT reaction control samples were measured with a small deviation (6.5%~11.6%) from theoretical values. The combination of in vitro transcription/translation synthesis of GTs from plasmid DNA and DPS-MS detection method provide great potential for on-site, high-throughput characterization of GT activities and for carbohydrate diagnostics in general.

3.2 Experimental Section

3.2.1 Desalting Paper Spray Apparatus

The filter paper was cut into a triangle (10 mm \times 5 mm, height \times base) after sequential sonication-assisted cleaning in acetone, methanol, and methanol/water (50:50 v/v, 15 min each). As shown in Figure 3.1, a 10 μ L sample solution was dropped onto the paper triangle that was placed on top of Kim-Wipe to facilitate the absorption by capillarity. Desalting was achieved by loading 10 μ L ACN/H₂O solution (90/10 v/v) onto the paper placed on top of another Kim-Wipe to wick the eluent containing salts and other chemicals. The paper triangle was then held in front of the MS inlet (8 mm away) using a high voltage cable alligator clip, and 10 μ L of ACN/H₂O/FA solution (10/90/1 v/v/v) was added directly onto the paper triangle to elute the target compounds for ionization upon application of a high voltage (3.5 kV) to the wetted paper. Paper spray optimization was guided by the previous works of Ouyang, Cooks, and coworkers.¹⁵⁵ Experimental conditions were optimized including: paper tip to MS inlet distance (8 mm); sample loading volume (10 μ L); spray voltage (3.5 kV); washing solvent (10 μ L H₂O/ACN, 10/90 v/v), and spray solvent (10 μ L H₂O/ACN/FA, 90/10/1 v/v/v) (see Appendix B.1).

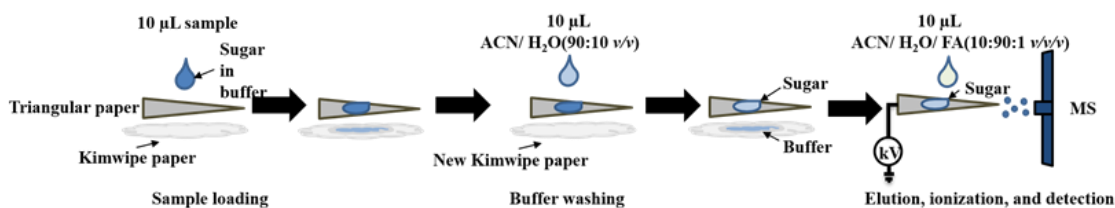


Figure 3.1 Schematic presentation of the workflow and setup of DPS-MS.

3.2.2 Non-radioactive Glycosyltransferase Reactions

Enzymatic reactions (Figure 3.2) were carried out in 50 μ L reaction solution. For AtGUX1, the reaction mixture contained 25 μ g xylohexaose (X6, acceptor) and 5 mM UDP-glucuronic acid (donor), 1 mM MnCl₂ and 1 mM MgCl₂ in 50 mM Tris-HCl buffer, pH 7.4. For AtXXT1, the reaction mixture contained 25 μ g cellobiohexaose (C6, acceptor), 5 mM UDP-xylose (donor), 1 mM MnCl₂, and 1 mM MgCl₂ in 50 mM Tris-HCl buffer, pH 7.4. Transfer reactions were carried out for 3 h at 28°C after adding different amounts of expressed GST-tagged proteins (36-216 ng, estimated via western blotting). The reactions were stopped by adding 0.3 mL of water and then freeze-dried. For DPS-MS analysis, three reactions were combined, freeze-dried, and then resuspended in 500 μ L aqueous solvent.

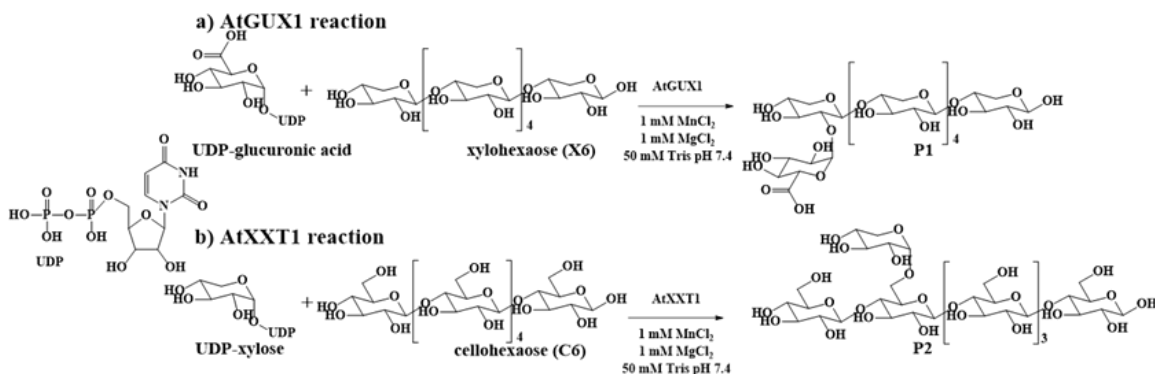


Figure 3.2 Equations for glycosyltransferase reactions catalyzed by a) AtGUX1 and b) AtXXT1.

3.2.3 Radioactive Glycosyltransferase Reactions

Each AtXXT1 catalyzed reaction mixture contained 25 μ g cellobiohexaose (C6, acceptor), UDP-[¹⁴C] xylose (60,000 cpm, 7.141 GBq/mmol) and cold UDP-xylose (3 μ M), 1 mM MnCl₂ and 1 mM MgCl₂ in 50 mM Tris-HCl buffer, pH 7.4. The reactions were carried out for 3 h at 28°C in presence of various amounts of expressed fusion proteins (0-216 ng,

estimated via western blotting analysis). The reactions were stopped by adding 0.3 mL of water, and sufficient ion-exchange resin (DOWEX 1X8-100 resin (Cl) 1:1 (v/v) was added to remove unused UDP-[¹⁴C] xylose. The incorporation of [¹⁴C]xylose onto cellohexaose was measured (as cpm) after resuspension in 5 mL of liquid scintillation solution using a LS 6500 multi-purpose scintillation counter (Beckman). Using specific radioactivity, the amount of products formed were estimated (as nM). All reactions were performed in duplicate.

Each AtGUX1 catalyzed reaction mixture contained 25 µg xylohexaose (X6, acceptor), UDP-[¹⁴C] glucuronic acid (80,000 cpm, 9.213 GBq/mmol) and cold UDP-glucuronic acid (3 µM). 1 mM MnCl₂ and 1 mM MgCl₂ in 50 mM Tris-HCl buffer, pH 7.4. Reactions were carried out for 3 h at 28°C in the presence of various amounts of expressed fusion proteins (0-216 ng, estimated via western blotting analysis). Reactions were stopped by adding 0.3 M acetic acid. [¹⁴C] glucuronic acid-containing xylohexaose was separated from free UDP-[¹⁴C] glucuronic acid by paper chromatography, as described earlier.¹⁵⁶ [¹⁴C] glucuronic acid-containing xylohexaose stay at the origin and [¹⁴C] radiolabel was measured (as cpm) after cutting the origin of paper chromatography and submersion in 5 mL of liquid scintillation solution as described for AtXXT1. All assays were performed in duplicate.

3.3 Results and Discussion

In most biological samples, oligosaccharides are present among a mixture of various other chemicals, including salts and proteins. Therefore, the removal of these contaminants is necessary for efficient MS analysis. First, we sought to test hydrophilic interaction bonding between oligosaccharides and cotton fibers as SPE stationary phase. In these tests, we used

50 μM maltoheptaose in 50 mM Tris-HCl buffer (pH 7) using Manfred method.¹⁵⁷ Our results showed that maltoheptaose could adsorb onto cotton, and the addition of ACN/H₂O mixture (83/17 v/v) allowed removal of the buffer. Maltoheptaose was then eluted with H₂O/ACN/FA (80/20/0.1 v/v/v) and collected for nanoESI-MS analysis. Although we could successfully detect the protonated maltoheptaose ion at m/z 1153 with a mass error of 0.40 ppm (Appendix B.2, measured m/z 1153.38806, theoretical m/z 1153.38760), the protocol was time-consuming as the eluted maltoheptaose needed to be loaded to a nanoESI emitter. To speed up the analysis, we replaced nanoESI with DPS. The rationale being that the substrate for paper spray ionization mainly contains the same composition of cellulose as the SPE stationary phase and could serve as both a desalting media and a spray emitter for oligosaccharide ionization. In this protocol, we first examined DPS's capability to analyze trace oligosaccharides in a complex matrix solution, using 5 μM maltoheptaose in 50 mM Tris-HCl buffer (pH 7) as a test sample. Due to significant signal suppression from salt (buffer), both conventional PSI (Figure 3.3a, following the PSI-MS procedure described in the Experimental Section) and nanoESI (data not shown) failed to detect maltoheptaose from the sample, without desalting. By contrast, using our DPS-MS method, sodium and potassium adduct ions of maltoheptaose at m/z 1175 (measured m/z 1175.37197, theoretical m/z 1175.36955, mass error: 2.06 ppm) and m/z 1191 (measured m/z 1191.34469, theoretical m/z 1191.34349; mass error: 1.01 ppm) were observed (Figure 3.3b). The identity of the maltoheptaose peak was further confirmed through collision-induced dissociation (CID) analysis of the ion at m/z 1175, which produced fragment ions of m/z 1013, 851, 689, and 527 by consecutive losses of hexose residues (C₆H₁₀O₅, 162 Da), consistent with its structure (Figure 3.3c). In this DPS-MS experiment, as the spray

solvent of H₂O/ACN/FA (90/10/1 v/v/v) containing 90% water, there was a time delay of about 0.3 min to get a stable EIC current for *m/z* 1175.4 (Appendix B.3). The delay might be caused by the electrophoretic migration of oligosaccharide sample to the paper tip for spray. The signal was then stabilized for about 0.8 min (0.3-1.1 min) before declining.

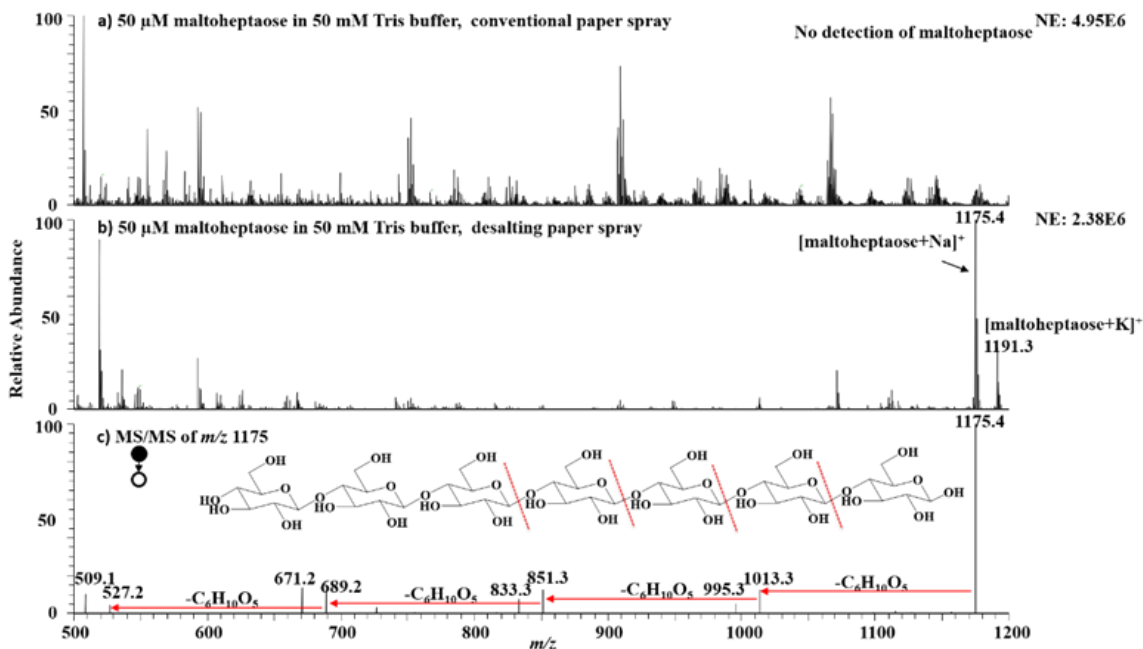


Figure 3.3 MS spectra of 50 μM maltoheptaose in 50 mM Tris buffer (pH 7) acquired by a) conventional paper spray and b) desalting paper spray. c) collision-induced dissociation (CID) MS/MS analysis of $[\text{maltoheptaose}+\text{Na}]^+$ ion at *m/z* 1175.

Next, we sought to evaluate the detection sensitivity of the DPS-MS method. For this experiment, we used samples containing a constant concentration of Tris buffer (50 mM), while the concentration of maltoheptaose was adjusted from 500 nM to 5 nM. Such that, the Tris-HCl concentration was 1×10^5 to 1×10^7 times higher than maltoheptaose. We could detect the sodium adduct ion of maltoheptaose at *m/z* 1175 in samples containing

500 nM maltoheptaose in 50 mM Tris-HCl buffer (Figure 3.4a). Importantly, when the concentration of maltoheptaose was further lowered to 5 nM (Tris-HCl/maltoheptaose ratio was 1×10^7), the analysis of 10 μ L of this 5 nM solution (total amount 50 fmol) showed clear detection of the ion at m/z 1175 (Figure 3.4b). Our data indicate that, despite the increase by 4 orders of the magnitude of the ratio of Tris-HCl to maltoheptaose and the reduced intensity of m/z 1175 by around 300 times (Figure 3.3b 2.38×10^6 vs. Figure 3.4b inset 9.04×10^3), the signal at m/z 1175 corresponding to the sodium adduct ion of maltoheptaose was still detectable. In other words, the DPS method appears to have a good desalting capability. In addition, compared to traditional MS methods, DPS-MS requires much less time (< 5 min per sample) to analyze trace amounts of oligosaccharides in matrix samples. For example, although LOD of 100 pmol and 50 fmol were reported for ESI-MS and MALDI-MS methods, respectively²⁹⁻³⁰, those methods are time-consuming (ca. 50 to 120 min).

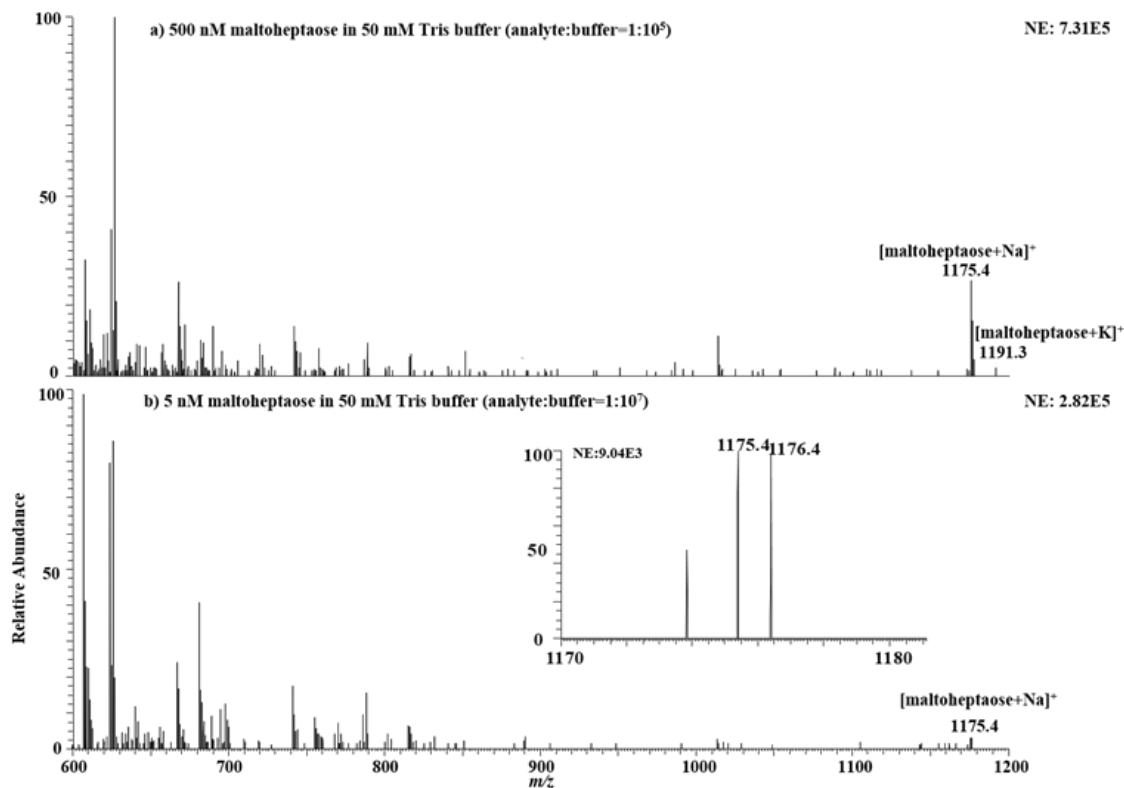


Figure 3.4 MS spectra of a) 500 nM maltoheptaose in 50 mM Tris-HCl buffer (analyte/buffer ratio: 1:10⁵), b) 5 nM maltoheptaose in 50 mM Tris-HCl buffer (analyte/buffer ratio: 1:10⁷), inset of Figure 3.3b shows the zoomed-in spectrum of m/z 1175.4.

In another set of experiments, we sought to determine if the DPS-MS method could tolerate various buffers and matrix. Thus, we dissolved maltoheptaose (50 μ M) in 50 mM PBS buffer, 50 mM HEPES, or 50 mM synthetic urine and used them to test the efficiency of DPS-MS method compared to conventional PSI-MS (Figure 3.4). When HEPES and PBS buffers were tested, desalting was achieved using 10 μ L of ACN/H₂O solution (80/20 v/v) instead of 10 μ L ACN/H₂O solution (90/10 v/v) for better signal-to-noise ratio (S/N). While conventional PSI failed to detect maltoheptaose signal (top panels in Figure 3.4a,

3.4b, and 3.4c), DPS-MS method successfully detected maltoheptaose signal at m/z 1175.4 with a mass error of <1.5 ppm (bottom panels in Figures. 3.4a, 3.4b, and 3.4c).

Glucose tetrasaccharide, 3 α -,6 α -mannopentaose, and β -cyclodextrin (all at 50 μ M in 50 mM Tris-HCl buffer, pH 7) were also tested using the DPS-MS method. Our data show that DPS-MS could detect all these oligosaccharides, as shown in Figure 3.5, namely [tetrasaccharide+Na]⁺ at m/z 689.21234 with a mass error of 1.83 ppm (theoretical m/z 689.21108), [3 α -,6 α mannopentaose +Na]⁺ at m/z 851.26567 with a mass error of 2.08 ppm (theoretical m/z 851.26390), and [β -cyclodextrin+Na]⁺ at m/z 1157.35962 with a mass error of 0.55 ppm (theoretical m/z 1157.35898).

Furthermore, DPS-MS proved to be quite sensitive, as trace amounts of oligosaccharides could be detected, as depicted in MS spectra acquired using 10 μ L of 5 nM β -cyclodextrin (50 fmol) in 50 mM Tris-HCl buffer, pH 7 (buffer/ β -cyclodextrin ratio: 1×10^7) (Figure 3.6c). Conventional PSI-MS and nanoESI-MS could not tolerate signal suppression issues from the buffer and failed to detect β -cyclodextrin at this concentration (5 nM) (Figure 3.6a and 3.6b). Similarly, 10 μ L of 5 nM glucose tetrasaccharide (Appendix B.4c) and 3 α -,6 α -mannopentaose (50 fmol each) (Appendix B.5c) in 50 mM Tris-HCl buffer, pH 7, (Tris-HCl/analyte ratio: 1×10^7) were also successfully detected using DPS-MS. Again, no oligosaccharide signal was detected by conventional PSI-MS and nanoESI-MS (Appendix B.4a,b and Appendix B.5a, b).

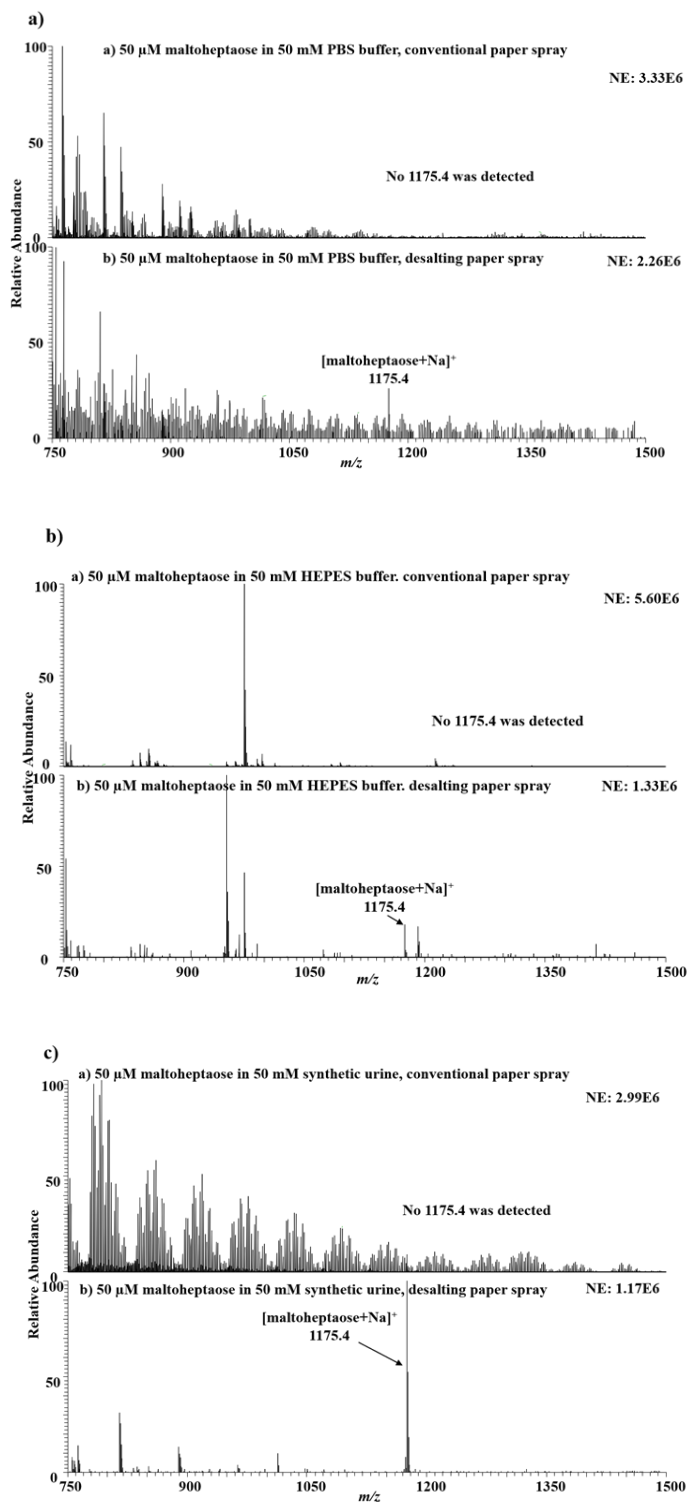


Figure 3.5 MS spectra of 50 μM maltoheptaose dissolved in a) 50 mM PBS buffer pH=7, b) 50 mM HEPES pH=7, and c) 50 mM synthetic urine. The top panels and bottom panels show conventional paper spray and desalting paper spray results, respectively.

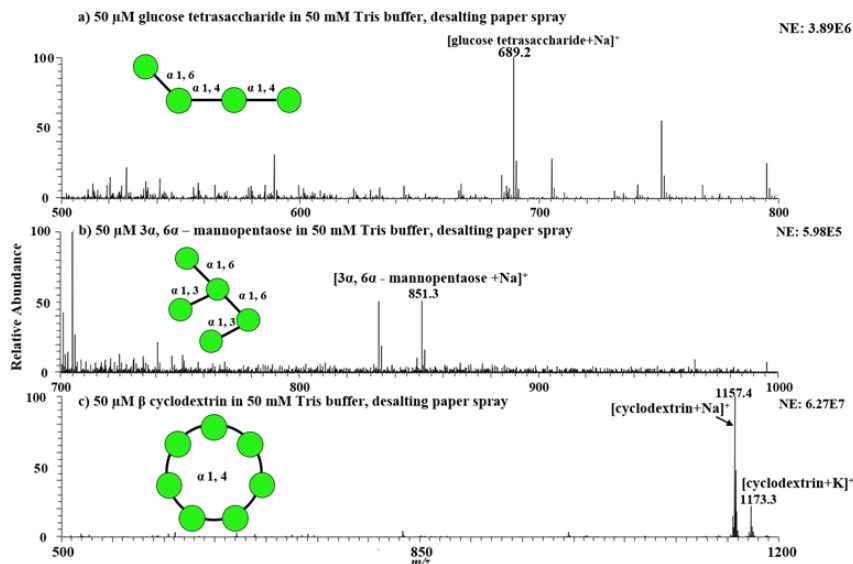


Figure 3.6 MS Spectra of 50 μM oligosaccharide in 50 mM Tris-HCl buffer (pH 7) acquired by desalting paper spray of a) glucose tetrasaccharide, b) 3 α ,6 α mannopentaose, and c) β -cyclodextrin. The green circle represents one monosaccharide ring (i.e., glucose or mannose).

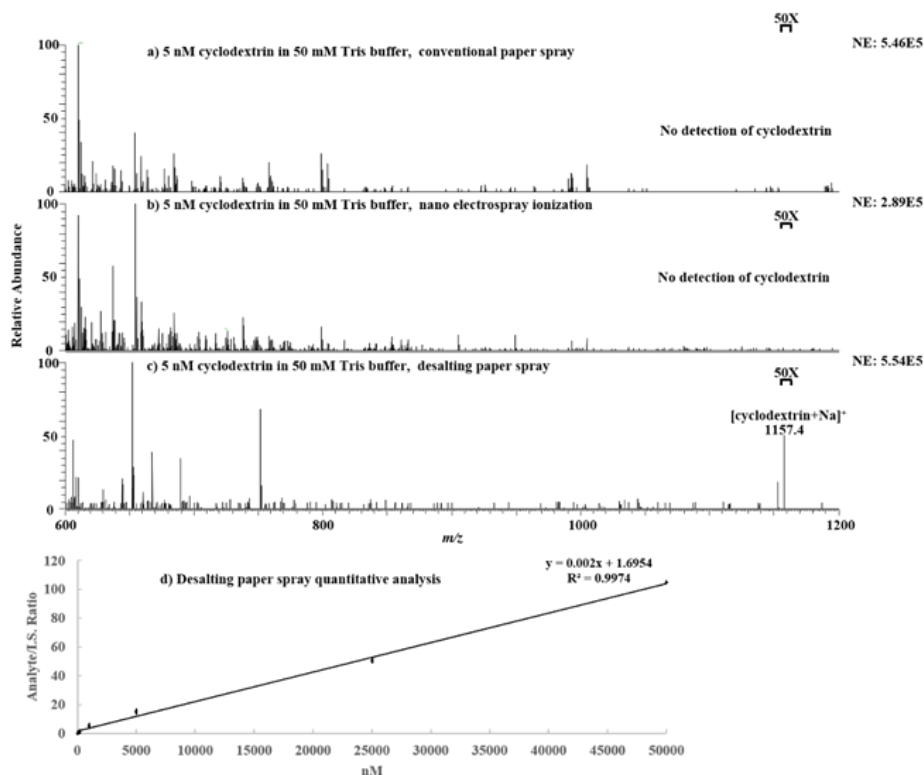


Figure 3.7 MS Spectra of 5 nM cyclodextrin in 50 mM Tris buffer acquired by: a) PSI, b) nanoESI, and c) DPS; d) shows linear relationship of β -cyclodextrin signal vs. concentration (200 nM-50 μM β -cyclodextrin in 50 mM Tris-HCl buffer, pH 7) using 5 μM maltoheptaose as an I.S.. Spectra in a-c were acquired using only 10 μL solution.

To determine whether DPS-MS could be quantitative, we doped an internal standard (I.S.) with various concentrations of β -cyclodextrin solution, and the signal intensity ratio of β -cyclodextrin to the internal standard was plotted against β -cyclodextrin concentration. As indicated in Figure 3.6d, the plot was linear over β -cyclodextrin concentrations ranging from (0.2 to 50 μ M) with a correlation coefficient higher than 0.99 (unweighted linear curve fitting was used for plotting). The excellent linearity of the plot indicated the DPS-MS method can be used for quantitative analysis. Limit of detection (LOD) for β -cyclodextrin was calculated and found to be 1.1 nM (i.e., 1.3 ng/mL; see Appendix B.6); in other words, our DPS-MS detection method could handle analysis of oligosaccharide as low as 1.1 fmol in nonvolatile buffers in few minutes. In this experiment, to achieve reproducible quantitative analysis result, we adopted paper substrates with the same size and loaded the same volume (10 μ L) of sample onto the same location of the paper substrate each time. In addition, we fixed the paper substrate position (relative to MS inlet) using a high voltage cable alligator clip.

Our data showed that DPS-MS method was successful in detecting and quantifying relatively pure standard oligosaccharides under different buffer conditions. However, these buffers do not represent the complex mixture of biological and enzyme reactions that usually include buffers and other ions as well as some organelles. To further test the validity of DPS-MS method in analyzing more complex mixtures from biological samples, we used the method to detect products generated by in vitro glycosyltransferase (GT) reactions. In GT reactions, sugars are transferred from UDP-activated sugars onto the acceptor (mostly oligosaccharides), producing new oligosaccharides (products). In this study, two well characterized GTs were used, namely AtGUX1¹⁵⁸ (Figure 3.2a) and AtXXT1¹⁵⁹ (Figure

3.2b). Currently, GTs are heterologously produced in organisms (expression systems) such as bacteria, yeast, or eukaryotic cells (from plants or animals)¹⁶⁰⁻¹⁶⁴ and then partially purified for testing their activity using radioactive assays. However, these expression systems are time consuming and cannot be adapted for fast analysis. To overcome these limitations, we opted for an in vitro Coupled Transcription/Translation Systems to produce GT proteins for enzyme activity testing. To demonstrate the validity of this approach, we used two well characterized *Arabidopsis* GTs, namely, AtGUX1 or AtXXT1. These two GTs are membrane proteins. To improve their solubility, GTs were synthesized as fusion proteins with a GST tag at their C-terminal ends. Transferase activity of these GTs was monitored via both radioactive assays and DPS-MS detection method. In addition, to determine the lower limit of detection (for both radioactive assay and DPS-MS method, five different amounts (36 to 216 ng) of AtGUX1-GST or AtXXT1-GST were added to UDP-activated monosaccharides (UDP-glucuronic acid for AtGUX1 and UDP-xylose for AtXXT1) and acceptor oligosaccharide (X6 for AtGUX1 and C6 for AtXXT1) mixture (50 μ L) containing 50 mM Tris-HCl (pH 7.4), 1 mM MgCl₂, and 1 mM MnCl₂ to promote the enzymatic reactions. After reaction, each reaction mixture was subsequently analyzed by DPS-MS. One control sample without adding UDP-xylose was also tested. For the AtGUX1 reaction control sample, no donor UDP-glucuronic acid was added. For AtXXT1 reaction control sample, no donors (UDP-xylose for AtXXT1) was included.

As shown in Figure 3.7a, acceptor X6, m/z 833.3 (mass error < 2.5 ppm), was observed, with no glycosyl transfer reaction product P1 (Figure 3.2a) detected in the control reaction. However, with both donor (UDP-glucuronic acid) and acceptor (X6) substrates present in the reaction mixture, a new oligosaccharide product, m/z 1009.3 (mass

error < 3.0 ppm), was detected, and its intensity increased with increased AtGUX1-GST-fusion protein added to the reaction (Figure 3.7b-e). Furthermore, DPS-MS was used to quantify the amount of remaining X6 acceptor, using X6 alone as a standard. Increasing the concentration of the standard X6 relative to the internal standard, β -cyclodextrin (m/z 1157.4), gave excellent linearity between the X6 signal and concentration (Appendix B.7 RSD < 6%). The concentration of the remaining X6 in the enzymatic reaction thereby could be quantified (Figure 3.8, square dots). The concentration of the glycosyl transfer reaction product was estimated based on X6 consumption (Figure 3.8, green

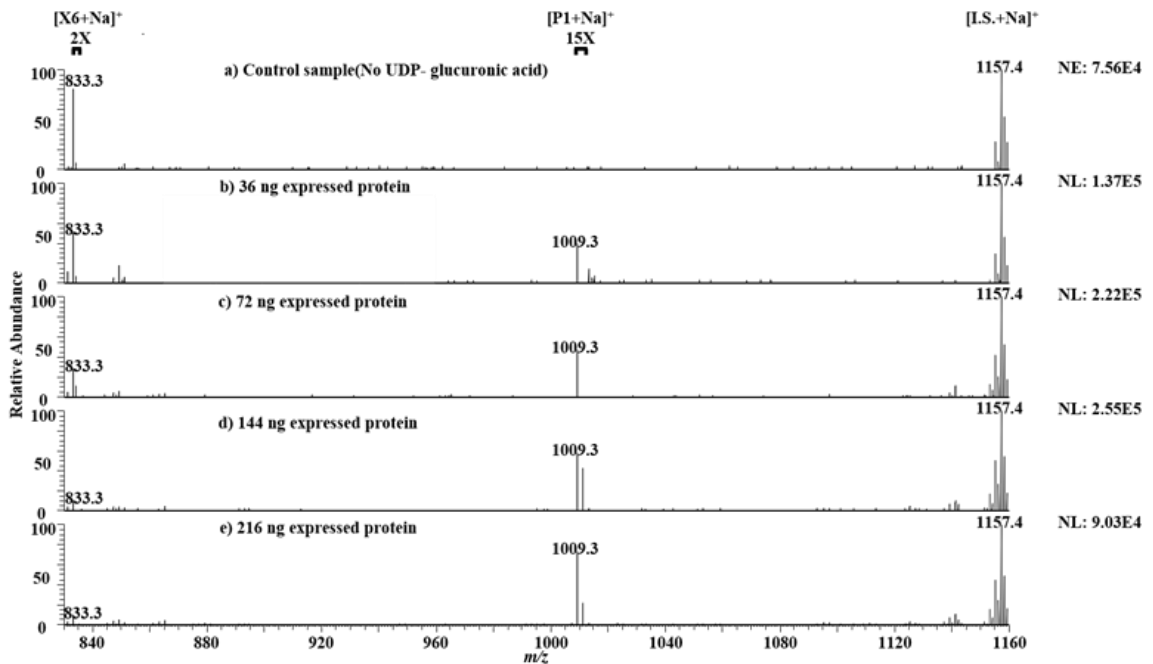


Figure 3.8 DPS-MS analysis of AtGUX1-GST reactions. MS spectra from a) control sample (no UDP-glucuronic acid), and reaction samples catalyzed by b) 36 ng AtGUX1 protein, c) 72 ng AtGUX1 protein, d) 144 ng AtGUX1 protein, and e) 216 ng AtGUX1 protein.

triangular dots) assuming a 1:1 stoichiometric reaction ratio between X6 and product. The measured concentration of X6 in the control sample was 197.1 μM , compared to a theoretical concentration of 185 μM , giving a measurement error of only 6.5%. The small measurement error validated the quantitative ability of the DPS-MS method. Traditionally, product analysis of GT-catalyzed reactions requires the use of radioactive assays using [^{14}C]-labeled sugar donors, which are expensive and present a safety hazard. For comparison, a radioactive assay was also performed under similar experimental conditions except that less UDP-sugar donor was used. As indicated in Figure 3.8 (red triangular dots), radioactive assays showed a similar trend, namely an increase in the amount of the product (P1) with the increased amounts of AtGUX1-GST enzyme, which agrees with DPS-MS result (green triangular dots).

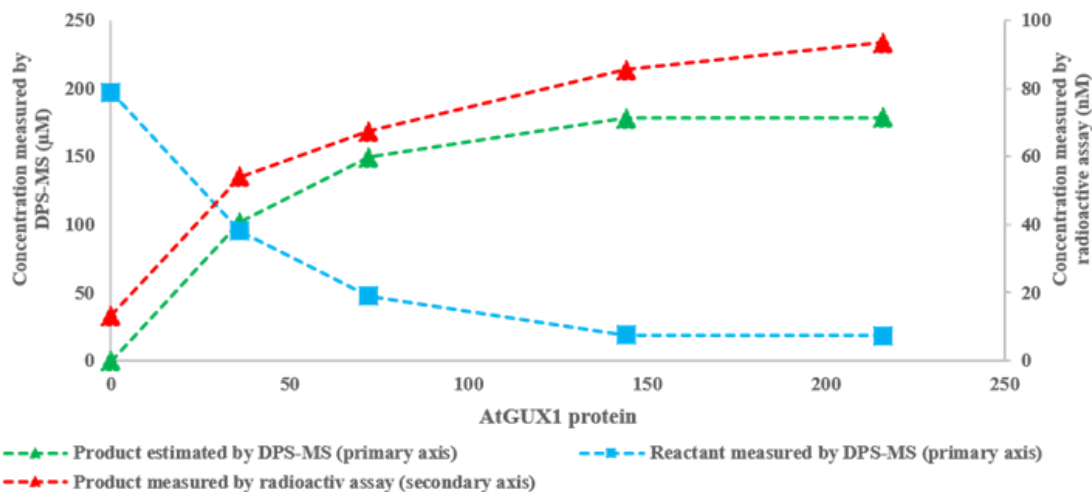


Figure 3.9 Estimation of the acceptor X6 and the product (P1) concentrations using DPS-MS and radioactive assay, as function of the amount of AtGUX1 protein used in the enzymatic reactions.

Similar analysis was conducted for glycosyl transfer reaction catalyzed by AtXXT1-GST fusion protein produced by in vitro coupled Transcription/Translation system. AtXXT1 uses C6 oligosaccharide as the acceptor and UDP-xylose as the donor (Figure 3.2b). The remaining C6 acceptor sugar was quantified based on the acquired standard calibration curve (Appendix B.8, RSD < 3%). The measurement C6 concentration in the control sample was 131.9 μ M, close to the expected theoretical concentration of 151 μ M (12.6% error). For the reaction samples, it was found that the intensity of acceptor (C6) decreased with the increased amount of fusion protein added to the enzymatic reaction; while the formed oligosaccharide product (P2, m/z 1145.4, mass error < 3 ppm) increased (Appendix B.9). Again, DPS-MS and radioactivity assay gave a similar trend of product formation (Appendix B.9, i.e., an increase in the amount of the resulting product (P2) with using increased amounts of AtXXT1-GST enzyme), which confirms the robustness and reproducibility of the DPS-MS method.

3.4 Conclusions

As reported herein, DPS-MS integrates purification and ionization together for the detection of oligosaccharides. This approach is not only a fast (<5 min) as demonstrated by detection of 50 fmol of oligosaccharides in different nonvolatile buffers and LOD of 1.1 nM for β -cyclodextrin in 50 mM Tris buffer (pH 7). By using our approach, we successfully quantified standard oligosaccharides (β -cyclodextrin, X6, and C6) as well as oligosaccharide product from GT reactions. We showed that DPS-MS detection is also accurate, as it measured the amount of acceptor in GT reaction control sample with acceptable error (6.5%~11.6%). In addition, DPS-MS detection of GT reaction product

was in good agreement with radioactive assay results. Although LOD of DPS-MS is ~100 times higher compared to radioactive assay (11 femtomole for DPS-MS vs. 0.1 femtomole for radioactive assay), DPS-MS method is fast, reliable, and can be adapted to future rapid analysis of GT activity. This work demonstrated that a high-throughput pipeline combining *in vitro* synthesis of GTs and DPS-MS detection is possible and opens new doors for GT functional genomics

CHAPTER 4

NITROSAMINE QUANTITATION

4.1 Introduction

N-nitrosamines ($R_2N-N=O$), containing a nitroso group bonded to an amine, are formed when amines react with nitrosating agents such as nitrous acid.¹⁶⁵⁻¹⁶⁶ Under cytochrome P450 enzymatic catalysis, *N*-nitrosamine can be converted into diazonium, a DNA alkylating agent.¹⁶⁷ Due to the DNA damage potential, most *N*-nitrosamines are classified as Group 2A or Group 2B possible carcinogens to humans by International Agency for Research on Cancer (IARC). *N*-nitrosamines are considered to be part of “cohort of concern” by both European Medicine Agency (EMA) and U.S. Food and Drug Administration (FDA).¹⁶⁸⁻¹⁶⁹ *N*-nitrosamines are frequently detected during food processing and water treatment.¹⁷⁰ Recently unexpected finding of *N*-nitrosamine impurities in drugs such as angiotensin II receptor blockers, ranitidine, nizatidine, and metformin¹⁷¹ at unacceptable levels led to costly drug recalls.¹⁷² Health authorities responded to these findings by putting guidance for tight control of *N*-nitrosamines. FDA recommends manufacturers to take appropriate measures to control *N*-nitrosamine impurities to acceptable levels; for example, the acceptable intake (AI) limits of *N*-nitrosodimethylamine (NDMA) and *N*-nitroso-*N*-methyl-4-aminobutanoic acid (NMBA) are 96 ng/day, and the AI limits for *N*-nitrosodiethylamine (NDEA), *N*-nitrosomethylphenylamine (NMPA), *N*-nitrosoisopropylethylamine (NIPEA), and *N*-nitrosodiisopropylamine (NDIPA) should not be more than 26.5 ng/day. Therefore, identification and quantitation of *N*-nitrosamine impurities have become an urgent task in the pharmaceutical industry.

Currently, most regulations and analytical methods focus on the common and simple *N*-nitrosamines and rely on the use of standard nitrosamines for quantitation. For instance, gas chromatography-mass spectrometry (GC-MS) and liquid chromatography-mass spectrometry (LC-MS)¹⁷³⁻¹⁷⁶ are two main approaches for quantifying *N*-nitrosamine typically generated during the manufacturing process. Hyphenation of GC with other detectors was also performed for the *N*-nitrosamine determination in water, such as using GC-FID (flame ionization detector) and GC-NPD (nitrogen-phosphorous detector).¹⁷⁷⁻¹⁸¹ Determination of *N*-nitrosamines in food products was reported using LC-DAD (diode array detector)¹⁸² and fluorometric detector.¹⁸³ Starting materials, recovered solvents, catalysts, and reagents were recognized as the root sources of *N*-nitrosamines. Those traditional methods can satisfy the need for quantitation, as they target *N*-nitrosamine whose standards are commercially available or affordable. However, analysis becomes a considerable challenge due to the lack of standards for novel *N*-nitrosamines, which can potentially be generated from active pharmaceutical ingredients (API) or API impurities possessing secondary or tertiary amine functional groups. Synthesis of API-derived *N*-nitrosamine reference standards or stable isotope-labeled internal standards could be costly and time-consuming, for which additional safety measurement needs to be in place during synthesis/purification given the potential mutagenicity nature of *N*-nitrosamines. For instance, the synthesis of 1 g of drug-simulant *N*-nitrosamine **VII** used in this paper costed over \$15,000 and 1-month of lead time. Without standards, conventional methods are inapplicable for absolute *N*-nitrosamine quantitation. Although some non-chromatographic methods were developed, including electrochemistry-based sensor¹⁸⁴⁻¹⁸⁶ and UV-photolysis coupling chemiluminescence detection to address this issue,¹⁸⁷ those methods

are generally less selective and used to measure the total amount of *N*-nitrosamines in a sample. Therefore, a selective and sensitive method capable of absolute quantitation of *N*-nitrosamine without using standards would be ideal for tackling such a challenge.

In this study, to eliminate the need for using standards or calibration curves for quantitation, we present a new strategy of using electrochemistry-assisted mass spectrometry, namely coulometric mass spectrometry (CMS). We recently have applied our CMS method^{59-62, 64, 188} for direct absolute quantitation of organic compounds, peptides, and proteins. As illustrated in Figure 4.1, our quantitation strategy involves the chemical reduction of *N*-nitrosamine to hydrazine. Then the electrochemically active hydrazine is subject to LC separation and oxidation in an electrochemical flow cell and followed with online MS detection. The oxidation results in an electrical current that can be integrated over time to obtain the total electric charge Q in the electrochemical oxidation reaction. According to Faraday's Law, Q is proportional to the quantity of the oxidized hydrazine: $Q=nzF$, where n denotes the moles of the oxidized hydrazine, z is the number of electrons transferred per molecule during the oxidation reaction, and F is the Faraday constant (9.65×10^4 C/mol). Thus, $n=Q/(zF)$. On the other hand, from the acquired MS spectra before and after EC oxidation, the oxidation conversion yield Δi can be determined by measuring the relative change of the hydrazine peak area in the extracted ion chromatogram (EIC) upon oxidation. Thus, the total amount of the hydrazine can be calculated as $n/\Delta i=Q/(zF\Delta i)$. In this case, hydrazine undergoes electrochemical oxidation reaction at a low oxidation potential (0.3 V vs. Ag/AgCl), presumably by losing one electron ($z=1$) to form hydrazine radical cation, which subsequently loses one hydrogen to form iminium cation (Figure 4.1).¹⁸⁹ Since the reduction yield can also be determined by comparison the MS

ion signal of *N*-nitrosamine before and after zinc reduction; therefore nitrosamine quantity can also be figured out based on the moles of hydrazine. Herein, to validate this CMS approach for *N*-nitrosamine absolute quantitation, several simple *N*-nitrosamines were successfully quantified with very good measurement accuracy ($\leq 1.1\%$). This new quantitation method is also highly sensitive. For instance, we have obtained accurate quantitation for *N,N*-diphenylhydrazine at the level of ca. 0.9 pmol (0.16 ng) using our CMS method. Furthermore, quantitation of drug-simulant *N*-nitrosamine **VII** in the presence of drug matrix at low level (150 ng **VII** in 10 g drug matrix, i.e., 15 ppb) using our CMS method was also successfully demonstrated.

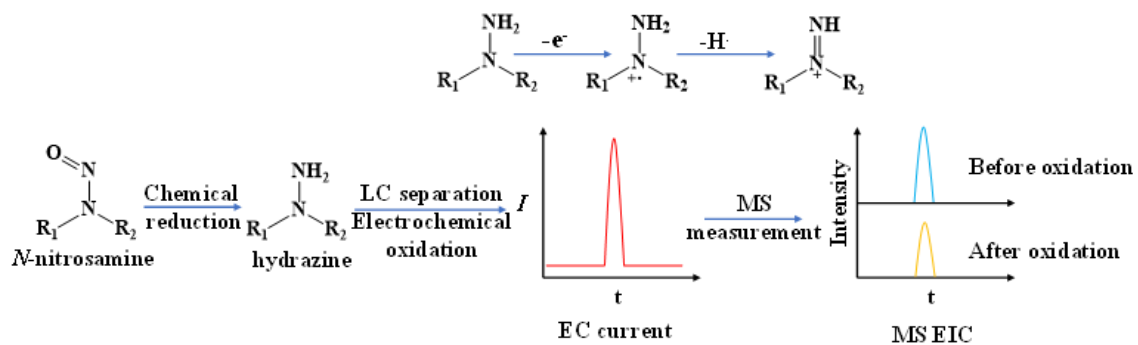


Figure 4.1 Workflow for absolute quantitation of *N*-nitrosamines by CMS.

4.2 Apparatus

LC/EC/MS setup was used for CMS quantitation (Figure 4.2). In our experiment, an UPLC (Waters, Milford, MA) was used to inject the reduced *N*-nitrosamines (i.e., hydrazines) into a thin-layer electrochemical flow cell consisting of a dual gold disc working electrode (WE, 3 mm I.D. each), an Ag/AgCl (3 M NaCl) reference electrode, and a stainless steel block as the counter electrode (BASi, West Lafayette, IN, USA; cell dead volume: ca. 1 μ L) for

oxidation, followed with online MS detection using a high-resolution Orbitrap Q Exactive mass spectrometer equipped with heated electrospray ionization (HESI) source (Thermo Scientific, San Jose, CA, USA). Either a C18 column (Waters BEH C18, 2.1 mm × 100 mm, 1.7 μm) or a HILIC column (Waters BEH HILIC, 2.1 mm × 50 mm, 1.7 μm) was used for the separation, depending on polarities of hydrazines. WE was polished with alumina slurry before and after use. A potential of +0.30 V (vs. Ag/AgCl) was applied to the WE to induce the oxidation of hydrazines. During electrochemical oxidation, an electric current was generated and recorded by a potentiostat. Origin 2017 was used to calculate the total electric charge of Q by integrating the electric current peak with time. Before and after oxidation, ion intensities of the hydrazines were recorded with MS. The flow rate of sheath gas and the applied ionization voltage were 10 L/h and + 4 kV, respectively. The ion transfer inlet capillary temperature was kept at 250°C. Mass spectra were acquired and processed by Xcalibur (Thermo Fisher 3.0.63).

For UPLC separation using a C18 column, mobile phase A (deionized water with 0.1% formic acid) and mobile phase B (acetonitrile with 0.1% formic acid) were used with a flow rate of 200 μL/min. In a gradient elution mode, the mobile phase B was increased from 5% to 32% in 6 min and to 95% in 2 min, kept at 95% for 2 min before returning to 5%. The injection volume was 3 μL or 5 μL per injection. The isocratic mode was used for HILIC column separation, in which 5% mobile phase A (100 mM ammonium acetate in deionized water, pH 5.0), and 95% mobile phase B (acetonitrile) were pumped at a flow rate of 200 μL/min for 15 min with a sample injection volume of 3 μL.

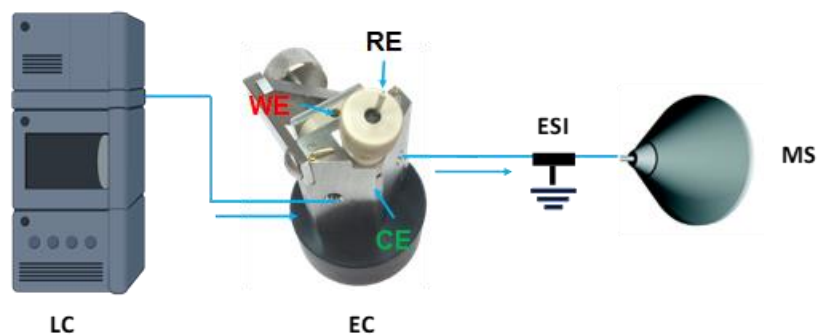


Figure 4.2 Schematic drawing of the LC/EC/MS setup used for absolute quantitation of *N*-nitrosamines by CMS.

4.3 Results and Discussion

The requirement of our CMS method is that the analyte needs to be electrochemically active. Our preliminary CV scan (Appendix C) showed an oxidation peak for *N*-nitrosamine at 2.2 V (vs. Ag/AgCl), while no *N*-nitrosamine reduction peak was observed 1 mM NDEA in anhydrous MeCN containing 0.1 M LiOTf using the boron-doped magic diamond (BDD) electrode. Such a high oxidation potential would only be possible in anhydrous MeCN solvent, not compatible with our LC/EC/MS runs where aqueous solvent was used. This is in line with the literature report that direct electrochemical oxidation of *N*-nitrosamines requires a relatively high oxidation potentials¹⁹⁰⁻¹⁹¹ or a modified electrode.¹⁹² Thus, we employed a chemical reduction strategy to convert *N*-nitrosamine into hydrazine first, a common practice in the organic chemistry field, then applied CMS to quantify the resulting hydrazine, as hydrazine can be easily oxidized electrochemically in aqueous solvent. The hydrazine measured by CMS would reflect the amount of its precursor *N*-nitrosamine.

In our experiment, some reductants were screened, such as sodium dithionite ($\text{Na}_2\text{S}_2\text{O}_4$), dithiothreitol (DTT), tris(2-carboxyethyl)phosphine (TCEP), hydroxylamine, ascorbic acid, and zinc powder. Reduction product, hydrazine, was afforded only under acid condition using zinc dust as a reductant (Table 4.1) with nearly quantitative yield. Based on previous hydrazine electrochemical characterization,¹⁸⁹ hydrazine was shown to have a high electrochemical activity (losing one electron to form hydrazine radical cation at oxidation potential 0.3 V vs. Ag/AgCl). So, using CMS to quantify the hydrazine product from *N*-nitrosamine reduction can be a rational strategy to determine the *N*-nitrosamine amount.

Table 4.1 *N*-nitrosamine Chemical Reduction using Different Reductants

Reduction conditions	Reduce nitrosamine to hydrazine?
Sodium dithionite ($\text{Na}_2\text{S}_2\text{O}_4$, 100 mM) vortex 1h at room temperature ¹	No
Dithiothreitol (DTT, 10-20 mM) vortex 1h at 37°C. ²⁻³	No
Tris(2-carboxyethyl)phosphine (TCEP) ⁴	No
Hydroxylamine (200 -700 mM) vortex 1h at room temperature ⁵⁻⁶	No
Ascorbic acid (5 mM) and CuCl (5 μM) vortex 1h at room temperature ⁷	No
Zinc (30 equiv.) in MeOH/AcOH=8:1 (v/v) for 2h at room temperature ⁸	Yes

In our CMS experiment, *N*-nitrosodiethylamine **I**, was first examined. 3 μL of **I** (0.0279 mmol, 2.84 mg) and 36.6 mg zinc dust (0.560 mmol) were mixed in 450 μL

methanol/acetic acid mixture (*v/v* 8:1), stirred for 2 h at room temperature under nitrogen protection. After reaction, the solution was filtered through 0.2 μm filter, vacuum dried, and reconstituted in 1 mL MeCN, followed by a 1000X dilution for CMS analysis (final concentration: 27.9 μM). Nanoelectrospray ionization mass spectrometry (nanoESI-MS) was used to evaluate the reduction yield by measuring *N*-nitrosodiethylamine ion signal change after reduction (Figure 4.3a). The chemical reduction yield was 99.9% by MS measurement, based on comparing the hydrazine product ion $[1+\text{H}]^+$ intensity (1.33E^9 , measured value m/z 89.10752, theoretical value m/z 89.10732, mass error 2.24 ppm) to the total ion intensities of $[1+\text{H}]^+$ and unreduced *N*-nitrosamine ion $[\text{I}+\text{H}]^+$ (1.99E^6 , negligible compared to $[1+\text{H}]^+$ intensity; measured value m/z 103.08688, theoretical value m/z 103.08659, mass error 2.81 ppm). The reduction yield was further confirmed by NMR analysis which showed a yield of 99.8% (Figure 4.3b) using dibromomethane as the internal standard. MS yield was thus adopted due to its simplicity in ion intensity measurements.

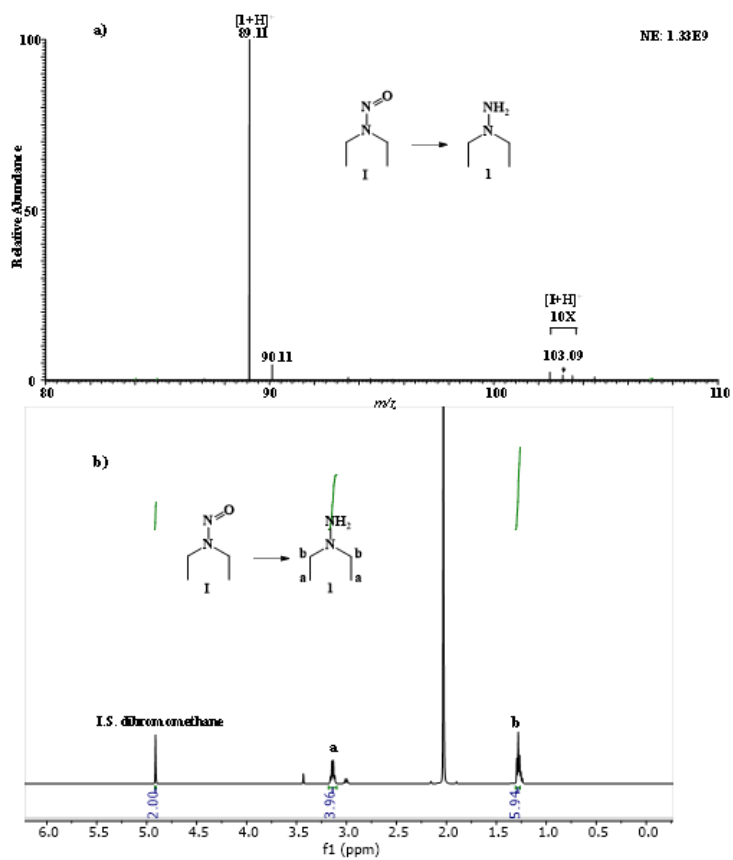


Figure 4.3 (a) NanoESI-MS spectrum and (b) NMR spectrum of N-nitrosodiethylamine after chemical reduction.

The resulting hydrazine **1** from reduction of N-nitrosodiethylamine (3 μ L, 27.9 μ M, theoretical amount: 83.7 pmol) was subjected for CMS analysis, which involved LC separation, electrochemical oxidation, and online MS detection sequentially. Before electrolysis, the protonated **1** was detected at m/z 89 (Fig 4.4a), and a small oxidation peak at m/z 87 was observed, probably due to the in-source oxidation of **1**.¹⁹³⁻¹⁹⁴ Previous literature reported that hydrazine loses one electron to form radical cation at a low oxidation potential (+0.3 V vs. Ag/AgCl) and can further loses one more electron at higher oxidation potential to form a dication (+0.75 V vs. Ag/AgCl) using gold electrode. Our CMS experiment adopted a low oxidation potential of +0.3 V vs. Ag/AgCl since it would avoid

the side oxidation reactions such as water hydrolysis, which would contribute to a better current baseline. As shown in Figure 4.4b, the peak intensity at m/z 87 increased and the ion intensity of m/z 89 decreased after electro-oxidation. Figure 4.4c and 4.4d show the EIC of m/z 89 with the applied potential of 0 V and +0.3 V (vs. Ag/AgCl), respectively. The integrated area for the peak shown in Figure 4.4d was smaller by 45.8% compared to that of the peak shown in Figure 4.4c, indicating that the oxidation yield for **1** was 45.8% (Table 4.2). On the other hand, the **1** oxidation current peak was detected, as shown in Figure 4.4f (Figure 4.4e shows the background current diagram for the blank solvent sample under the same + 0.3 V potential as a contrast). Based on the integration of the current peak area, the amount of the oxidized **1** was calculated to be 38.1 pmol. Therefore, our measured amount of **1** was 38.1 pmol/45.8%=83.0 pmol. Considering 99.9% reduction yield, the *N*-nitrosamine amount was determined as 83.0 pmol. In a triplicate measurement, the averaged amount of the *N*-nitrosamine was 82.9 pmol (see detailed data in Table 4.2), which has a small quantity discrepancy of -0.9% compared with theoretical value of 83.7 pmol (the injection amount as mentioned above).

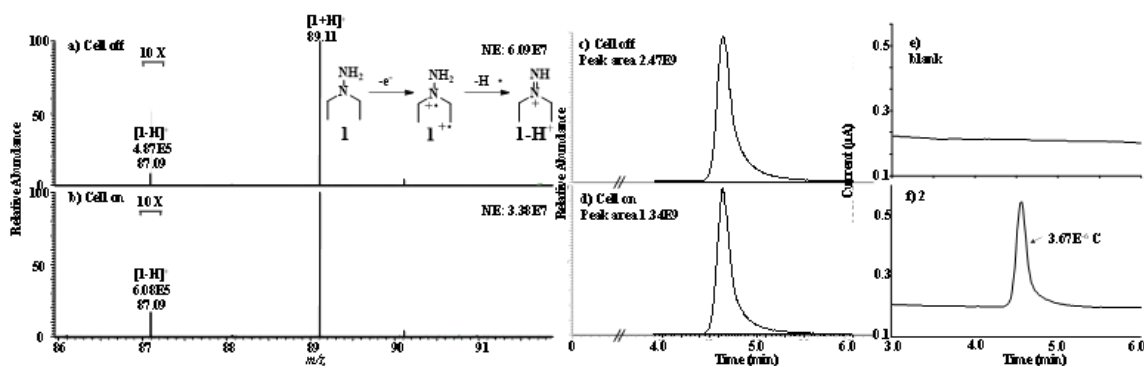


Figure 4.4 ESI-MS spectra of hydrazine **1** (from *N*-nitrosodiethylamine reduction) when the applied potential was (a) 0 V and (b) +0.3 V (vs Ag/AgCl). EIC of [I+H]⁺ at m/z 89 when the applied potential was (c) 0 V and (d) +0.3 V (vs Ag/AgCl). Electric current responses were shown due to the oxidation of (e) a blank solvent and (f) **1**.

Table 4.2 Electric Current and MS Data for N-nitrosodiethylamine (**I**)

Sample	Q(μ A. min)	Q(C)	Amount of the oxidized hydrazine (pmol)	EC oxidation yield	Measured hydrazine amount (pmol)	Averaged hydrazine amount (pmol)	Chemical reduction yield	Measured nitrosamine amount (pmol)	Theoretical nitrosamine amount (pmol)	Measurement error
N-nitrosodiethylamine I	6.49E-02	3.89E-06	4.04E+01	47.28%	8.54E+01					
	6.12E-02	3.67E-06	3.81E+01	45.84%	8.30E+01	8.28E+01	99.85%	8.29E+01	8.37E+01	-0.93%
	6.16E-02	3.70E-06	3.83E+01	47.90%	8.00E+01					

sample	EIC peak area of m/z 89 before oxidation	EIC peak area of m/z 89 after oxidation	oxidation yield
N-nitrosodiethylamine I	2467290802	1300799223	47.28%
	2467290802	1336356863	45.84%
	2467290802	1285497957	47.90%

Another simple model compound *N*-nitrosamine **II** (*N*-nitroso-4-phenylpiperidine) was also examined. After zinc reduction, hydrazine **2** was produced. As shown in Figure 4.4, the intensity of the hydrazine product ion [**2**+H]⁺ was 1.31E8 and the unreduced [**II**+H]⁺ was 3.04E5. This nanoESI-MS measurement showed that the yield of chemical reduction was about 99.8%, again, nearly quantitative. After reduction, the solution was filtered, dried, and reconstituted in 1 mL MeCN, followed by 1000X dilution for CMS analysis (final concentration: 28.0 μ M, injection volume of 3 μ L, theoretical injection amount: 84.0 pmol). Before electrolysis, the protonated hydrazine **2** was detected at m/z 178 (Figure 4.6a). A small oxidation peak at m/z 176 was observed, probably due to the in-source oxidation of **2**. After electrolysis in the electrochemical cell (Figure 4.6b), the peak intensity at m/z 176 increased significantly. Figure 4.6c and 4.6d showed the EIC of m/z 178 with the applied potential of 0 V and + 0.3 V, respectively. The integrated area for the peak shown in Figure 4.6d was smaller by 32.2% compared to that of the peak shown in Figure 4.6c, indicating that the oxidation yield was 32.2% (Table 4.3). On the other hand, the oxidation current peak was detected, as shown in Figure 4.6f (Figure 4.6e shows the

background current diagram for the blank solvent sample under the same + 0.3 V potential as a contrast). Based on the integration of the current peak area, the amount of the oxidized hydrazine **2** on average was calculated to be 27.0 pmol. Therefore, our measured amount of hydrazine was 27.0 pmol/32.2%=83.9 pmol. Considering the 99.8% reduction yield, the measured *N*-nitroso-4-phenylpiperidine (*N*-nitrosamine **II**) was 83.9 pmol. Average result from a triplicate measurement was 83.8 pmol, which is close to the theoretical injection amount of 84.0 pmol (measurement error: -0.3%, Table 4.3).

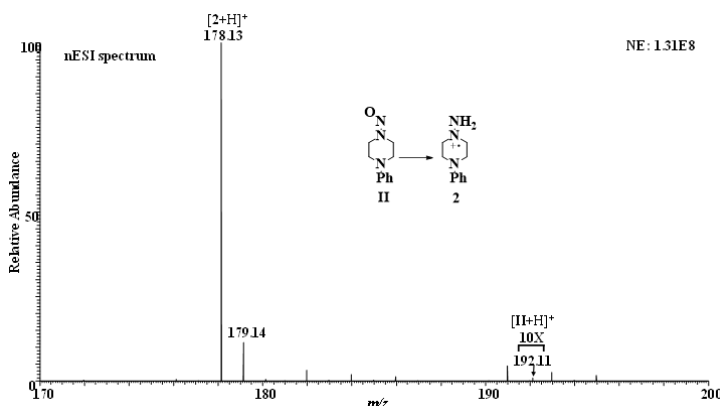


Figure 4.5 NanoESI-MS spectrum of *N*-nitroso-4-phenylpiperidine (**II**) after chemical reduction.

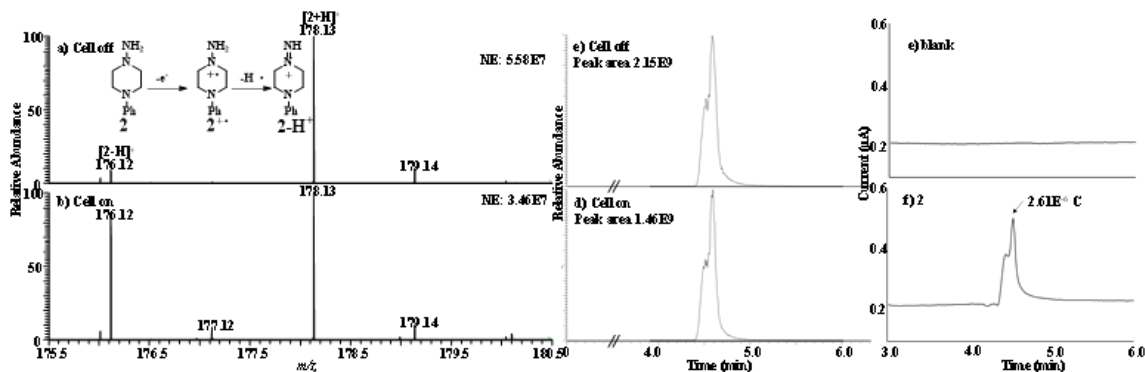


Figure 4.6 ESI-MS spectra of hydrazine **2** (from reduction of 1-nitroso-4-phenylpiperidine) when the applied potential was (a) 0 V and (b) +0.3 V. EIC of hydrazine ion at m/z 178 was recorded when the applied potential was (c) 0 V and (d) +0.3 V (vs Ag/AgCl). Electric current responses were shown due to the oxidation of (e) a blank solvent and (f) **2**.

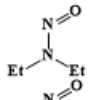
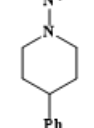
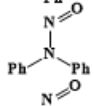
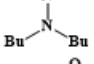
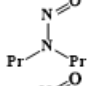
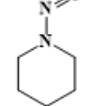
Table 4.3 Electric current and MS data for *N*-nitro-4-phenylpiperidine (II)

Sample	Q(μ A, min)	Q(C)	Amount of the oxidized hydrazine (pmol)	EC oxidation yield	Measured hydrazine amount (pmol)	Averaged hydrazine amount (pmol)	Chemical reduction yield	Measured nitrosamine amount (pmol)	Theoretical nitrosamine amount (pmol)	Measurement error
<i>N</i> -nitro-4-phenylpiperidine II	4.35E-02	2.61E-06	2.70E+01	32.25%	8.39E+01					
	5.02E-02	3.01E-06	3.12E+01	37.65%	8.29E+01	8.36E+01	99.77%	8.38E+01	8.40E+01	-0.28%
	5.20E-02	3.12E-06	3.24E+01	38.53%	8.40E+01					

sample	EIC peak area of m/z 178 before oxidation	EIC peak area of m/z 178 after oxidation	oxidation yield
<i>N</i> -nitro-4-phenylpiperidine II	1455784984	2148625954	32.25%
	1339576322	2148625954	37.65%
	1320765646	2148625954	38.53%

The validity of the CMS *N*-nitrosamines absolute quantitation approach was further conducted with 4 more *N*-nitrosamines. As summarized in Table 4.4, various *N*-nitrosamines at pmol range were successfully quantified using this new CMS quantitation method, with quantitation error no more than 1.1% (Appendix 4.1-7).

Table 4.4 List of *N*-nitrosamines quantified by CMS

#	Name	Structure	Chemical formula	molecular weight	Theoretical amount (pmol)	Measured amount (pmol)	quantitation measurement error
I	<i>N</i> -nitrosodiethylamine (NDEA)		C ₄ H ₁₀ N ₂ O	102.1	83.7	82.9	-0.9%
II	<i>N</i> -nitroso-4-phenylpiperidine (NPhPIP)		C ₁₁ H ₁₄ N ₂ O	190.2	84.0	83.8	-0.3%
III	<i>N</i> -nitrosodiphenylamine (NDPhA)		C ₁₃ H ₁₀ N ₂ O	198.2	90.0	90.7	0.8%
IV	<i>N</i> -nitrosodibutylamine (NDBA)		C ₉ H ₁₈ N ₂ O	158.2	75.0	74.2	-1.1%
V	<i>N</i> -nitrosodipropylamine (NDPA)		C ₈ H ₁₄ N ₂ O	130.2	45.0	44.8	-0.6%
VI	<i>N</i> -nitrosopiperidine (NPIP)		C ₇ H ₁₀ N ₂ O	114.1	89.4	88.4	-1.1%

In addition, we examined the quantitation sensitivity of our CMS method and 3 μL of 0.291 μM *N,N*-diphenylhydrazine **3** (0.873 pmol) was injected for CMS analysis. As shown in Figure 4.7a and 4.7b, hydrazine electrochemical oxidation product at m/z 183 peak intensity increased after turning on the electrochemical cell. In contrast, EIC peak area of m/z 185 was decreased by 17.8% upon electrooxidation (Figure 4.7c and 4.7d). After integrating the EC current area, we were able to quantify hydrazine as low as 0.873 pmol (\sim 0.16 ng, quantitation error: 1.3%, Table 4.5). Interesting, in Figure 4.7a, hydrazine radical cation at m/z 184 (theoretical m/z 184.09950, measured m/z 184.09966, mass error: 0.87 ppm) was also detected, as a result of inherent electrochemical oxidation during electrospray ionization, which is in agreement with the previously reported one electron transfer mechanism for hydrazine oxidation. CID MS/MS analysis showed that fragment ion of m/z 168 was formed by loss of amine radical $\text{NH}_2\cdot$ from m/z 184, consistent with the structure assignment of m/z 184 (Figure 4.8).

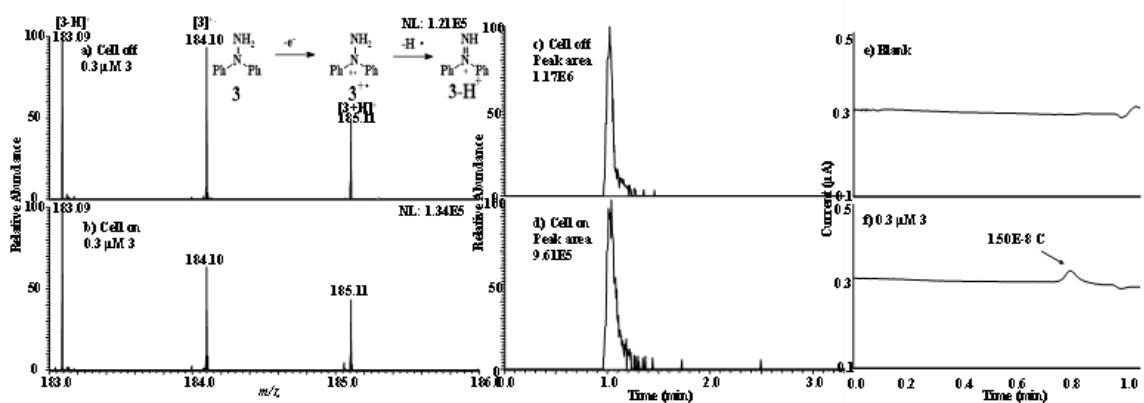
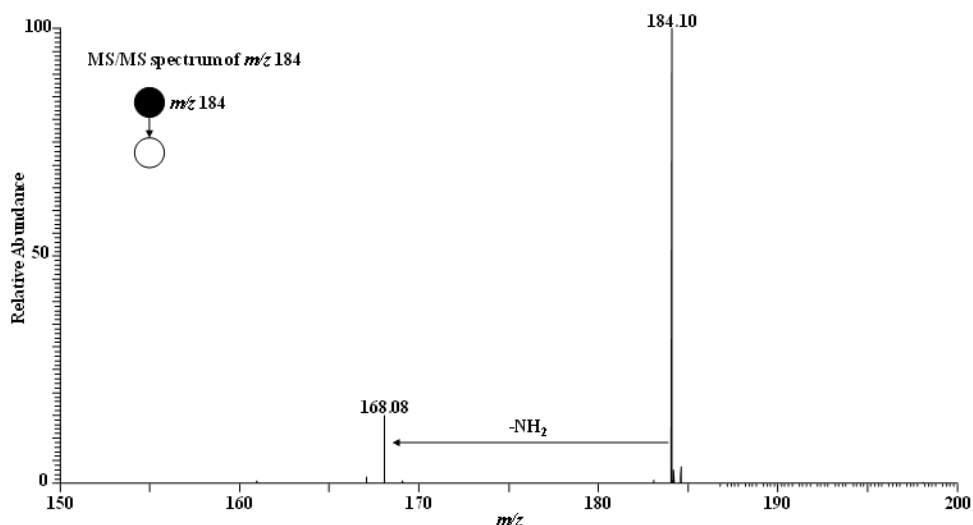


Figure 4.7 ESI-MS spectra of 3 μL of 0.291 μM *N,N*-diphenylhydrazine **3** when the applied potential was (a) 0 V and (b) +0.3 V. EIC of hydrazine ion at m/z 185 was recorded when the applied potential was (c) 0 V and (d) +0.3 V (vs Ag/AgCl). Electric current responses were shown due to the oxidation of (e) a blank solvent and (f) 0.291 μM **3**.

Table 4.5 Electric current and MS data for 3 μL of 0.291 μM *N,N*-diphenylhydrazine (**3**)

Sample	Q($\mu\text{A} \cdot \text{min}$)	Q(C)	Amount of the oxidized hydrazine (pmol)	EC oxidation yield	Measured hydrazine amount (pmol)	Averaged hydrazine amount (pmol)	Theoretical hydrazine amount (pmol)	Measurement error
<i>N,N</i> -diphenylhydrazine hydrochloride	1.50E-04	9.00E-09	9.33E-02	10.52%	8.86E-01			
	2.50E-04	1.50E-08	1.55E-01	17.80%	8.73E-01	8.85E-01	8.73E-01	1.33%
	1.30E-04	7.80E-09	8.08E-02	9.04%	8.94E-01			

Sample	EIC peak area of m/z 185 before oxidation	EIC peak area of m/z 185 after oxidation	oxidation yield
<i>N,N</i> -diphenylhydrazine hydrochloride	1169195	1046180	10.52%
	1169195	961079	17.80%
	1169195	1063493	9.04%

**Figure 4.8** MS/MS spectrum of radical cation of *N,N*-diphenylhydrazine **3** at m/z 184.

After the success of quantifying simple *N*-nitrosamines based on Zn reduction strategy followed with CMS quantitation of the resulting hydrazines, we explored the possibility of quantifying a *N*-nitrosamine stemming from drug-simulant substrate (*N*-nitrosamine **VII**, Figure 4.9) that has a more complex structure than those of simple nitrosamines examined above. Till now, quantitative analysis of complex *N*-nitrosamine remains unexplored, mainly because of the unavailable *N*-nitrosamine standards. However,

it has become an urgent issue in the pharmaceutical field. This issue emphasizes the advantage of our approach, where no standard is needed for quantitation.

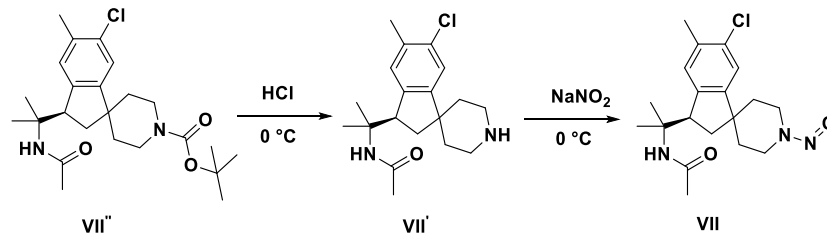


Figure 4.9 Synthesis route for nitrosamine **VII**

As of proof-of-concept test, *N*-nitrosamine **VII** was synthesized as shown in Figure 4.9, following a reported protocol for deprotection and nitrosation of a precursor compound **VII''**.¹⁹⁵ We estimated a cost of about \$15,000 and 1-month time for custom-synthesis, purification and full characterization of 1 g of **VII**. The experimental condition for reducing *N*-nitrosamine **VII** was first optimized to prevent the formation of over-reduction amine side product. In a trial, **VII** (0.91 mg, 0.0025 mmol) was added with 20 equiv. Zn (1.64 mg, 0.025 mmol) in MeOH/AcOH (8:1 v/v) and stirred at room temperature. As shown in Figure 4.10a, no corresponding hydrazine product **7** (Figure 4.11) was observed in the MS spectrum before chemical reduction. Although nearly all of **VII** (0.91 mg, 0.0025 mmol) was consumed, a reduction side product, the denitrosylated amine, was also detected at *m/z* 335 ([C₁₉H₂₇ClN₂O+H]⁺, Figure 4.10b). The two reduction product structures were confirmed using MS/MS (Figure 4.12). After adjusting the reduction condition by reducing Zn amount from 20 equiv. to 10 equiv. and reaction time from 2h to 0.5h, no reduction side product was detected (Figure 4.10c) and **VII** was exclusively converted into hydrazine **7**. Based on LC/MS analysis of the *N*-nitrosamine **VII** sample before and after reduction, the reduction yield was determined to be 47.2%. CMS was then conducted and 3 μL of reduced

N-nitrosamine solution containing hydrazine **7** (original amount of *N*-nitrosamine **VII**: 75 pmol) was injected for LC separation; the result was shown in Figure 4.13. The ion intensity of **7** oxidation product (the proposed oxidation mechanism shown in Figure 4.11 shows the proposed oxidation mechanism for hydrazine **7** involving one electron transfer and one hydrogen loss to produce iminium ion at m/z 348. The oxidation yield for **7** was measured to be 6.5% based on signal change of the protonated hydrazine **7** upon oxidation (Figure 4.13c and 13d). Furthermore, according to the measured oxidation current (Figure 4.13f), the amount of the oxidized **7** was calculated to be 34.4 pmol (averaged value from a duplicate measurement). Considering the reduction yield (47.2%, Figure 4.14), the mole of the *N*-nitrosamine was determined to be 72.9 pmol. The quantitation error was -2.9% , compared with the theoretical injection amount (75.0 pmol, Table 4.6).

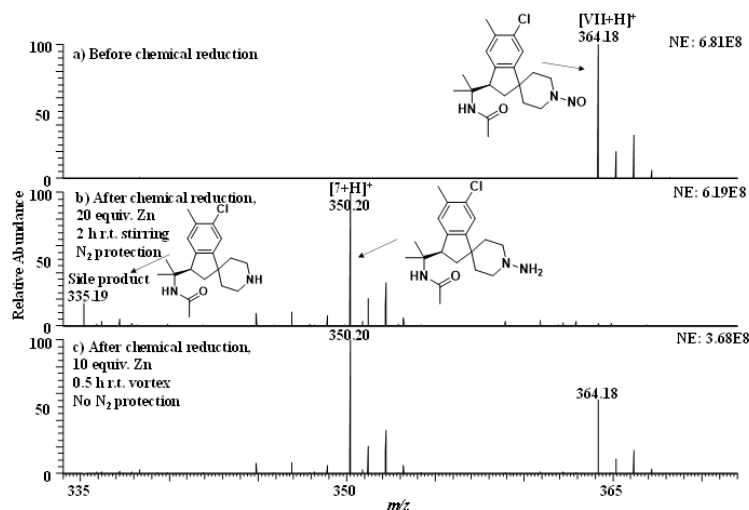


Figure 4.10 NanoESI-MS spectra of *N*-nitrosamine **VII** (a) before chemical reduction, (b) after chemical reduction using 20 equiv. zinc powder at room temperature with nitrogen protection and stirring for 2 h, and (c) after chemical reduction using 10 equiv. zinc powder at room temperature and vortexing for 0.5 h.

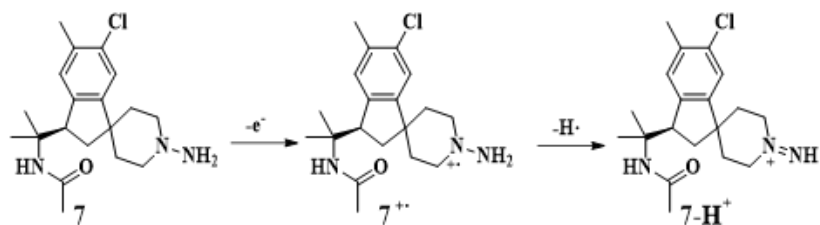


Figure 4.11 Proposed mechanism for electrochemical oxidation of hydrazine 7.

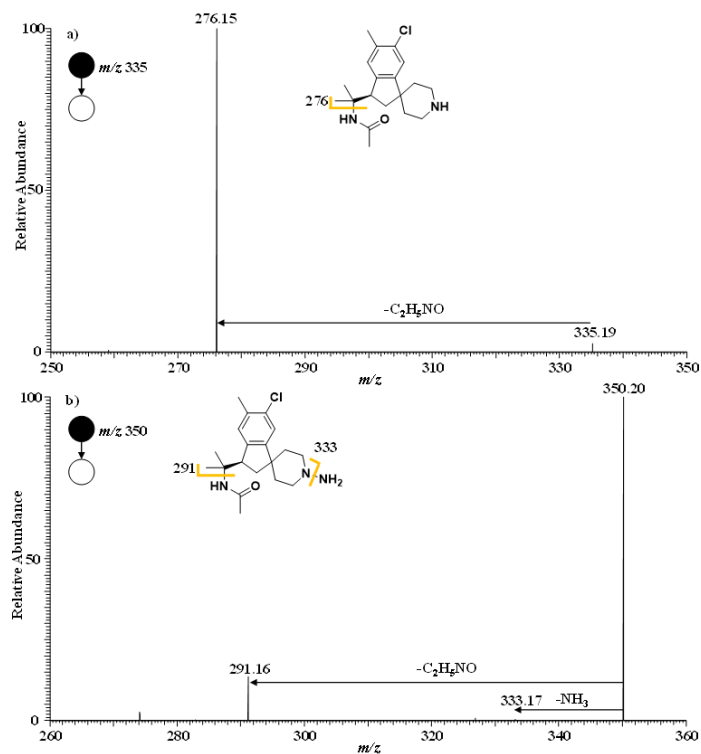


Figure 4.12 MS/MS spectra of ions of two *N*-nitrosamine VII reduction products at m/z 335 (a) and m/z 350 (b).

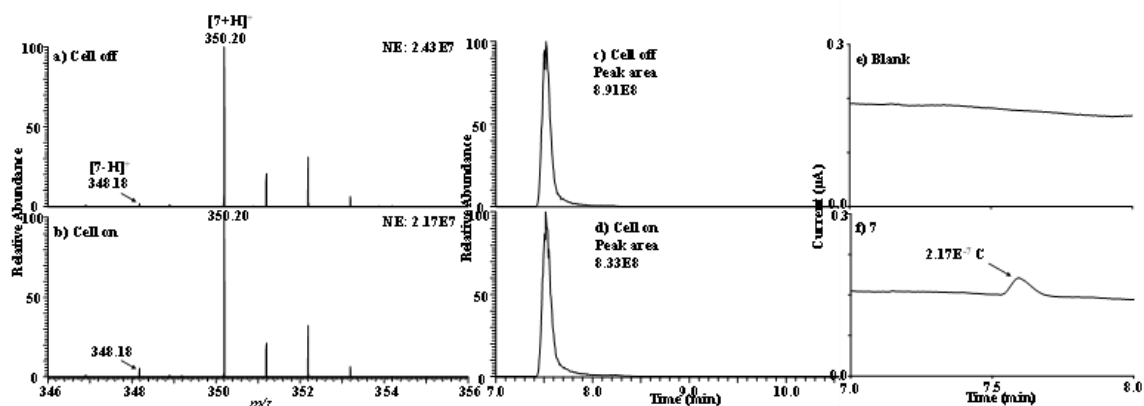


Figure 4.13 ESI-MS spectra of hydrazine **7** (from reduction of 0.91 mg of *N*-nitrosamine **VII**) when the applied potential was (a) 0 V and (b) +0.3 V. EIC of hydrazine ion at m/z 350 was recorded when the applied potential was (c) 0 V and (d) +0.3 V (vs. Ag/AgCl). Electric current responses were shown due to the oxidation of (e) a blank solvent and (f) **7**.

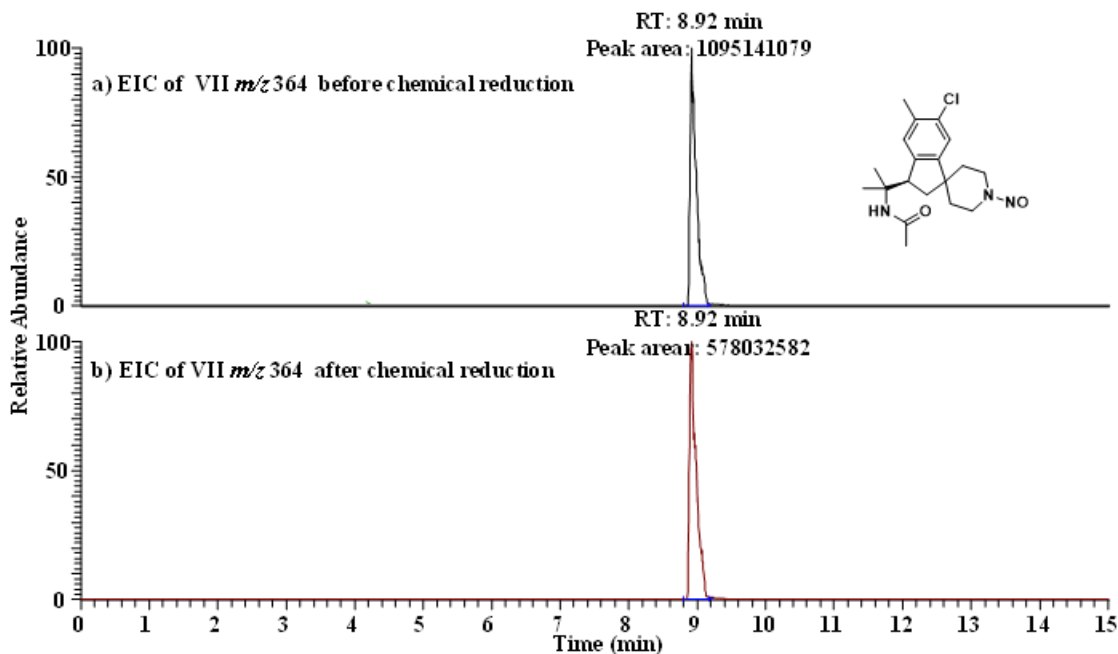


Figure 4.14 EIC spectra of the protonated *N*-nitrosamine **VII** of m/z 364 before (a) and after (b) chemical reduction (zinc equiv. 10.).

Table 4.6 Electric current and MS data for *N*-nitrosamine **VII** (0.91 mg *N*-nitrosamine **VII** was used).

Sample	Q(μ A, min)	Q(C)	Amount of the oxidized hydrazine (pmol)	EC oxidation yield	Measured hydrazine amount (pmol)	Averaged hydrazine amount (pmol)	Chemical reduction yield	Measured nitrosamine amount (pmol)	Theoretical nitrosamine amount (pmol)	Measurement error
nitrosamine VII	3.61E-03	2.17E-07	2.24E+00	6.45%	3.48E+01	3.44E+01	47.22%	7.29E+01	7.50E+01	-2.85%
	2.18E-03	1.31E-07	1.36E+00	3.98%	3.40E+01					

Sample	EIC peak area of m/z 350 before oxidation	EIC peak area of m/z 350 after oxidation	oxidation yield
nitrosamine VII	890572554	833104101	6.45%
	833761677	800548847	3.98%

Our effort was then focused on quantifying trace amounts of **VII**. In our experiment, 150 ng of **VII** was used and first reduced using 0.25 mg zinc under acid condition (MeOH/AcOH=8:1 v/v) at room temperature for 0.5 h. In this case, zinc was in much excess (zinc: *N*-nitrosamine > 9000:1), as it was difficult to accurately weigh less amount of zinc powder due to limitation of our balance. As a result, a small amount of side reduction product, the denitrosylated amine, was formed and detected (4.1% peak area compared with the ion of the hydrazine product **7**, Figure 4.15). The majority (95.6%) of the reduction product was hydrazine **7**. The reduction yield was 41.6%, as measured by EIC signal change of *N*-nitrosamine **VII** (*m/z* 364) upon reduction (Figure 4.16). Although the retention time of side product and hydrazine **7** were similar, no EC oxidation current was arising from the amine side product under 0.3 V oxidation potential (vs. Ag/AgCl), as shown in a separate electrochemical oxidation experiment (Figure 4.17). It showed that hydrazine **7** can be selectively oxidized in the electrochemical cell in the presence of the amine side product. The reduced solution was filtered, vacuumed dried, and reconstituted in 160 μ L solvent and 5 μ L of the resulting solution was injected into the CMS system. As shown in Figure 4.18 and Table 4.7, the hydrazine product **7** was quantified by CMS to be 5.1 pmol. For the amine side product, considering the similarity of proton affinities

between hydrazine and the corresponding amine (e.g., dimethylhydrazine and dimethylamine have proton affinities (PA) of 927.1 kJ/mol and 929.5 kJ/mol, respectively¹⁹⁶) and the minor amount of hydrazine product, it would be reasonable to estimate the amount of the amine side product based on its ion intensity relative to the **7** ion intensity. Such an estimation would not lead to a significant quantitation error because of their similar PA values and the minor amount of amine product (4.1% peak area compared with the reduction product **7**, Figure 4.15). In consideration of the amine side product ratio of 4.1% and reduction yield of 41.6%, therefore, the measured amount of *N*-nitrosamine **VII** would be $5.1 \text{ pmol}/(1-4.1\%)/41.6\%=12.8 \text{ pmol}$. Further, considering the dilution factor of 32, the measured *N*-nitrosamine would be 409 pmol which is close to the theoretical amount of 412 pmol (150 ng *N*-nitrosamine **VII**), with a measurement error of -0.7% (Table 4.7). Note that, in this case, CMS only used 5.1 pmol (about 1.8 ng) of hydrazine for quantitation in each run.

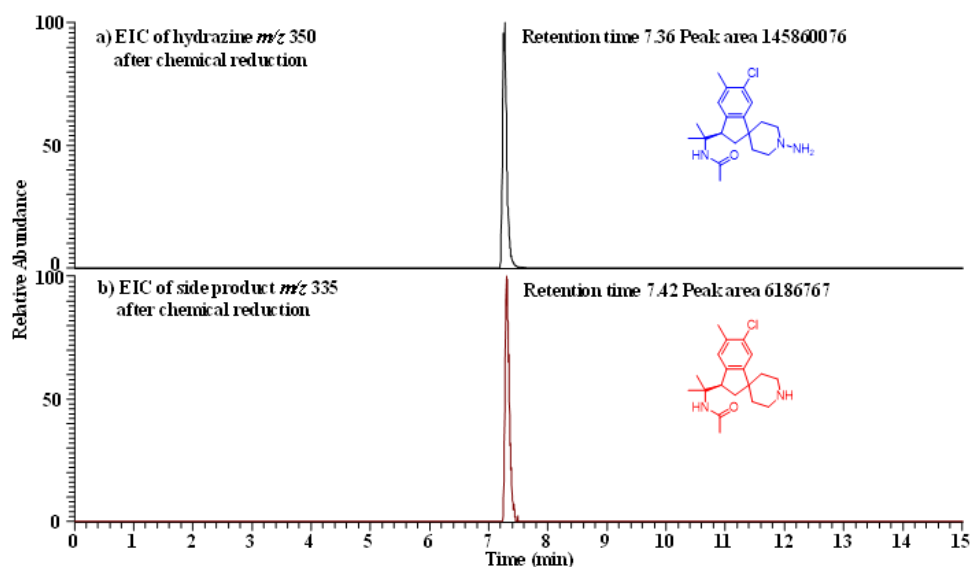


Figure 4.15 EIC spectra for the protonated **7** at m/z 350 (a) and the protonated side product ion at m/z 335 after zinc (>9000 equiv.) reduction of 150 ng of *N*-nitrosamine **VII**.

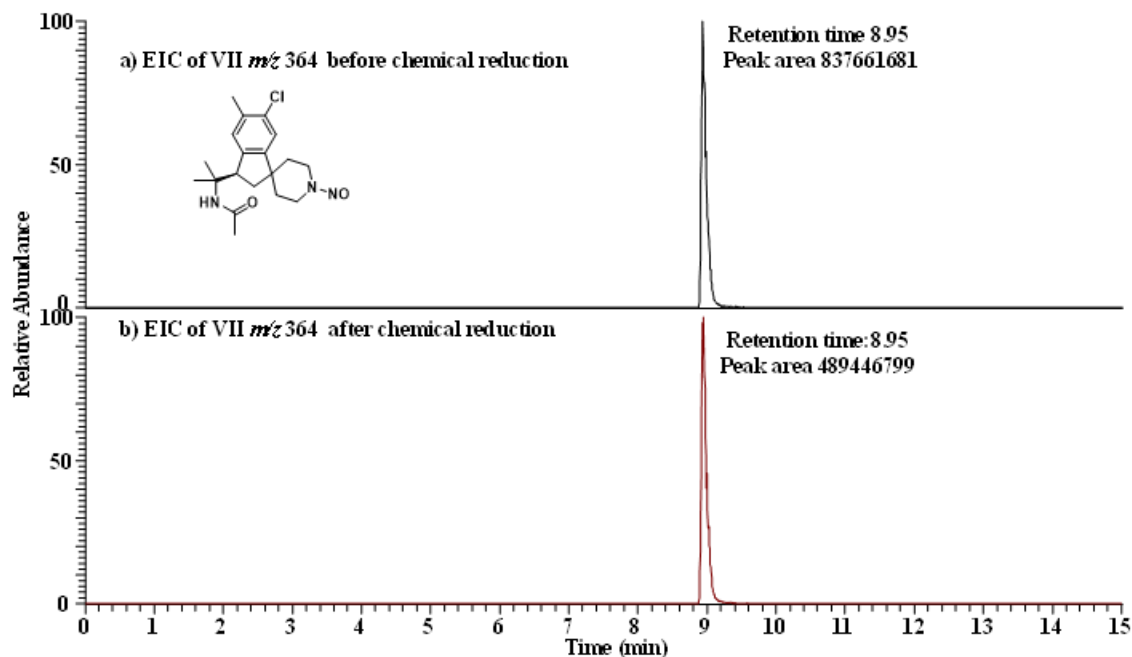


Figure 4.16 EIC spectra for the protonated *N*-nitrosamine **VII** at m/z 364 before (a) and after (b) zinc (>9000 equiv.) reduction.

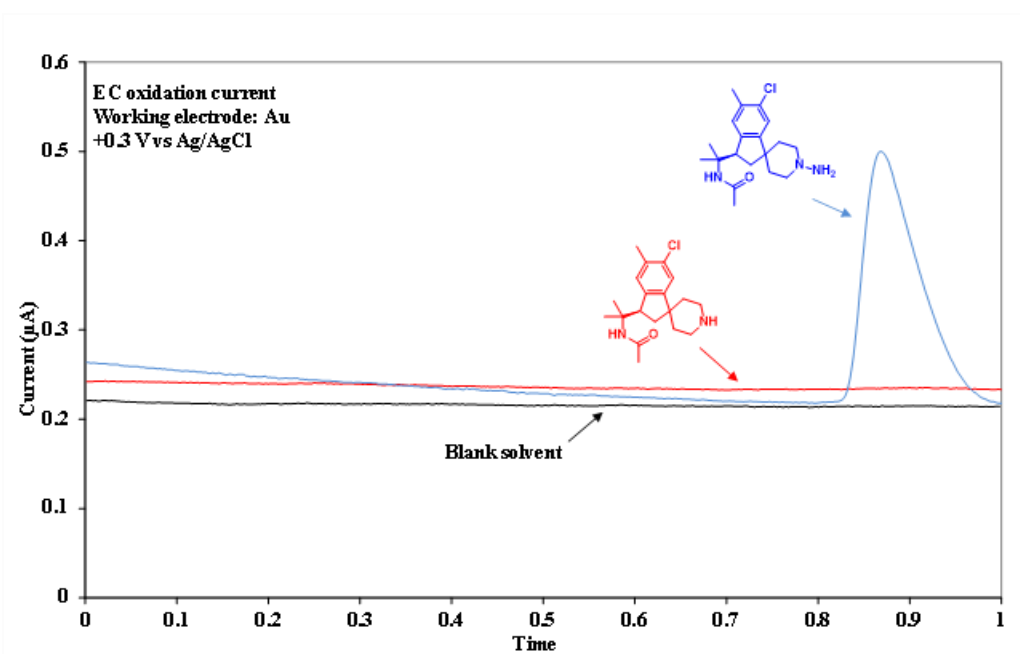


Figure 4.17 Electrochemical oxidation current of hydrazine **7** (blue curve), side amine product (red curve) and blank solvent (black curve) under oxidation potential 0.3 V (vs. Ag/AgCl). The amine product has no oxidation current under the oxidation condition used.

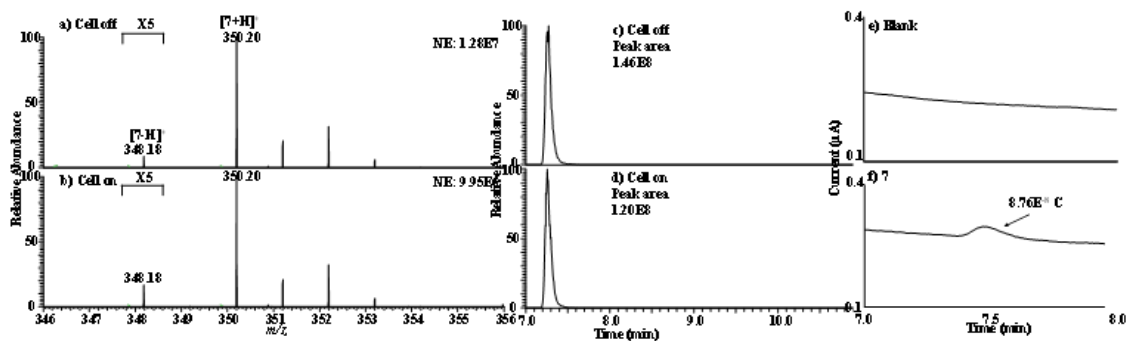


Figure 4.18 ESI-MS spectra of hydrazine **7** (from reduction of 150 ng *N*-nitrosamine **VII**) when the applied potential was (a) 0 V and (b) +0.3 V. The peak of the oxidized product [7-H]⁺ was seen at *m/z* 348 in (b). EIC of **7** was recorded when the applied potential was (c) 0 V and (d) +0.3 V (vs Ag/AgCl). Electric current responses were shown due to the oxidation of (e) a blank solvent and (f) **7**.

Table 4.7 Electric current and MS data for *N*-nitrosamine **VII** (150 ng *N*-nitrosamine **VII** was used)

Sample	Q(μA. min)	Q(C)	Amount of the oxidized hydrazine (pmol)	EC oxidation yield	Measured hydrazine amount (pmol)	Averaged hydrazine amount (pmol)	side product to hydrazine ratio	Chemical reduction yield	dilution factor	Measured nitrosamine amount (pmol)	Theoretical nitrosamine amount (pmol)	Measurement error
nitrosamine VII	1.46E-03	8.76E-08	9.1E-01	17.91%	5.07E+00	5.10E+00	4.07%	41.57%	32	4.09E+02	4.12E+02	-0.68%
	1.56E-03	9.36E-08	9.7E-01	17.86%	5.43E+00							
	1.80E-03	1.08E-07	1.1E+00	23.28%	4.81E+00							

Sample	EIC peak area of <i>m/z</i> 350 before oxidation	EIC peak area of <i>m/z</i> 350 after oxidation	oxidation yield
nitrosamine VII	145771241	119659119	17.91%
	153082814	125748066	17.86%
	155142876	119024398	23.28%

Finally, CMS was applied for quantitative analysis of *N*-nitrosamine **VII** in presence of drug matrix containing various excipients. In our experiment, to mimic *N*-nitrosamine in drug product, 150 ng of *N*-nitrosamine **VII** was doped with 10 g drug matrix (15 ppb) containing corn starch, D&C red #27 aluminum lake, dicalcium phosphate, magnesium stearate microcrystalline cellulose, polyethylene glycol, polyvinyl alcohol, silicon dioxide, stearic acid, talc, and titanium dioxide. Preliminary test showed that much lower quantitation result was obtained by direct reduction of the *N*-nitrosamine in the presence of excipients matrix, probably because of occurrence of condensation reactions

between the reduced *N*-nitrosamine (i.e., hydrazine) and excipient ingredients (e.g., carbonyl groups of sugars in matrix). To overcome this challenge, *N*-nitrosamine **VII** was first extracted from the drug matrix via solvent extraction (using 2-propanol) and isolated by LC using the reverse-phase chromatography (workflow is shown in Figure 4.19), followed by zinc reduction to afford hydrazine **7**. The extraction yield, reduction yield and amine side product percentage were determined using LC/MS analysis based on EIC peak areas (Figure 4.20, 4.21, and 4.22). Finally, as mentioned before, CMS was employed for the hydrazine product quantitation. As shown in Figure 4.23a and 4.23b, the oxidation product ion at m/z 348 had increased intensity when +0.3 V potential (vs. Ag/AgCl) was applied to WE. The protonated hydrazine **7** ion of m/z 350 shown in Figure 4.23d was smaller by 16.9% than that of the peak shown in Figure 4.23c, suggesting the oxidation yield to be 16.9% (Table 4.8). On the other hand, the **7** oxidation current peak was detected, as shown in Figure 4.23f (Figure 4.23e shows the background current diagram for the blank solvent sample under the same + 0.3 V potential as a contrast). Based on the integration of the current peak area, the amount of the oxidized **7** was calculated to be 10.0 pmol (ca. 3.5 ng). Considering the extraction and isolation yield (43.9%), the side product ratio (4.4%), the reduction yield (58.1%), and the dilution factor 10, the CMS measured amount of **VII** was $10 \text{ pmol}/43.9\%/(1-4.4\%)/58.1\%*10= 410 \text{ pmol}$ on the average from a triplicate measurement. The measurement error was -1.1% compared with the theoretical amount of 412 pmol (i.e., 150 ng *N*-nitrosamine **VII**, Table 4.8).

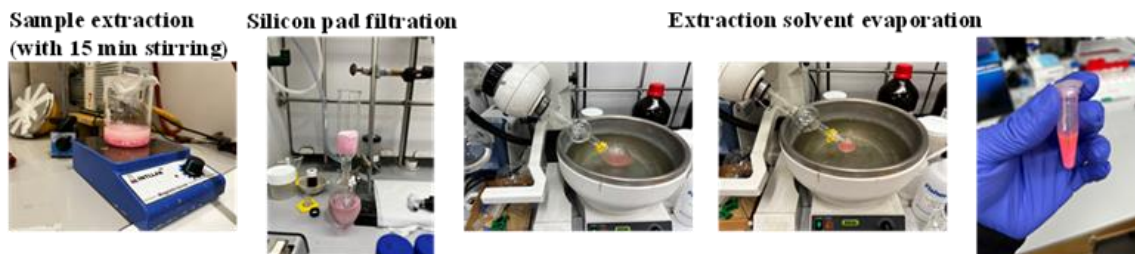


Figure 4.19 Workflow for extracting 150 ng **VII** from 10 g drug matrix using 2-propanol as extraction solvent and condensing the sample for LC isolation.

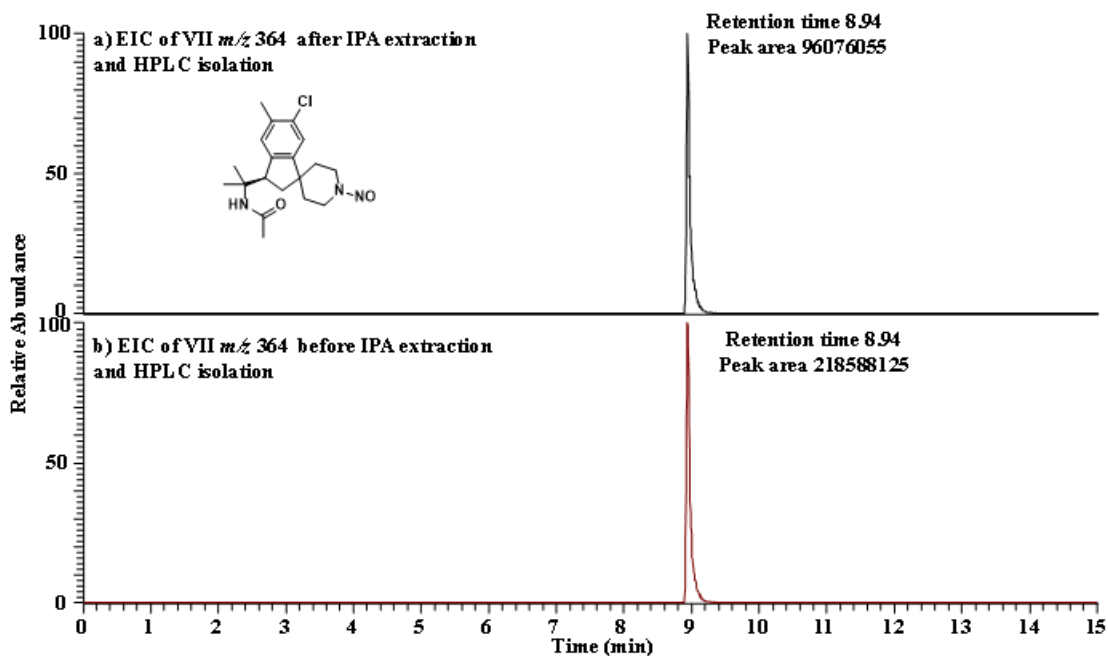


Figure 4.20 EIC spectra of *N*-nitrosamine **VII** (m/z 364) after (a) and before (b) IPA extraction from *N*-nitrosamine **VII** sample with drug matrix and LC isolation.

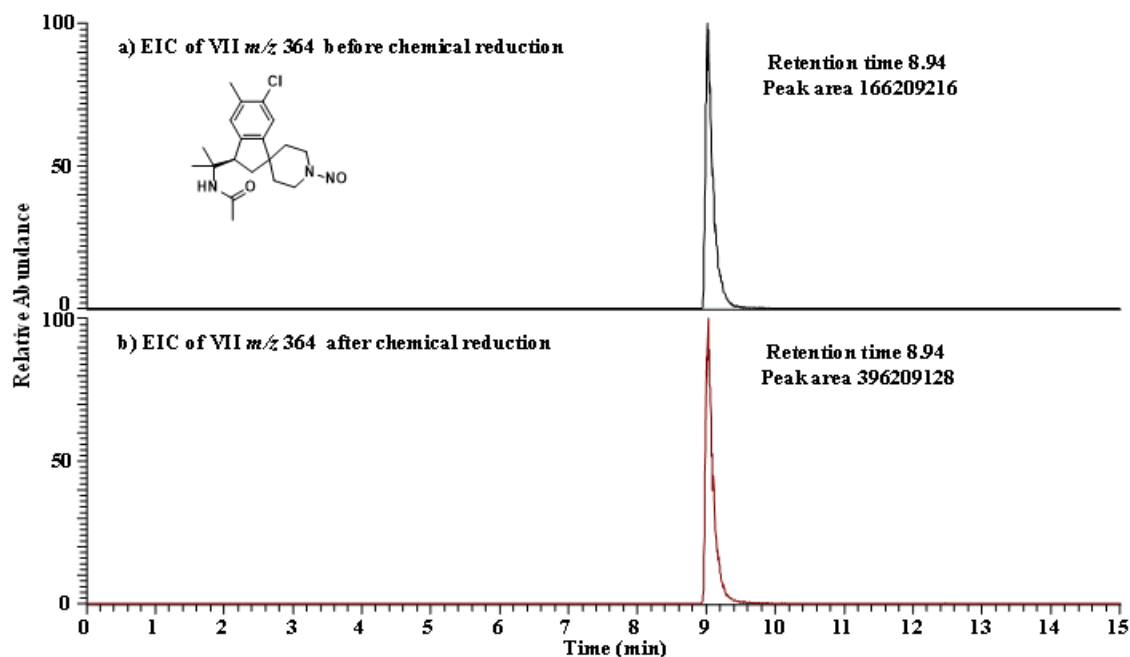


Figure 4.21 EIC spectra for *N*-nitrosamine VII before (a) and after (b) zinc reduction (in the test sample with drug matrix).

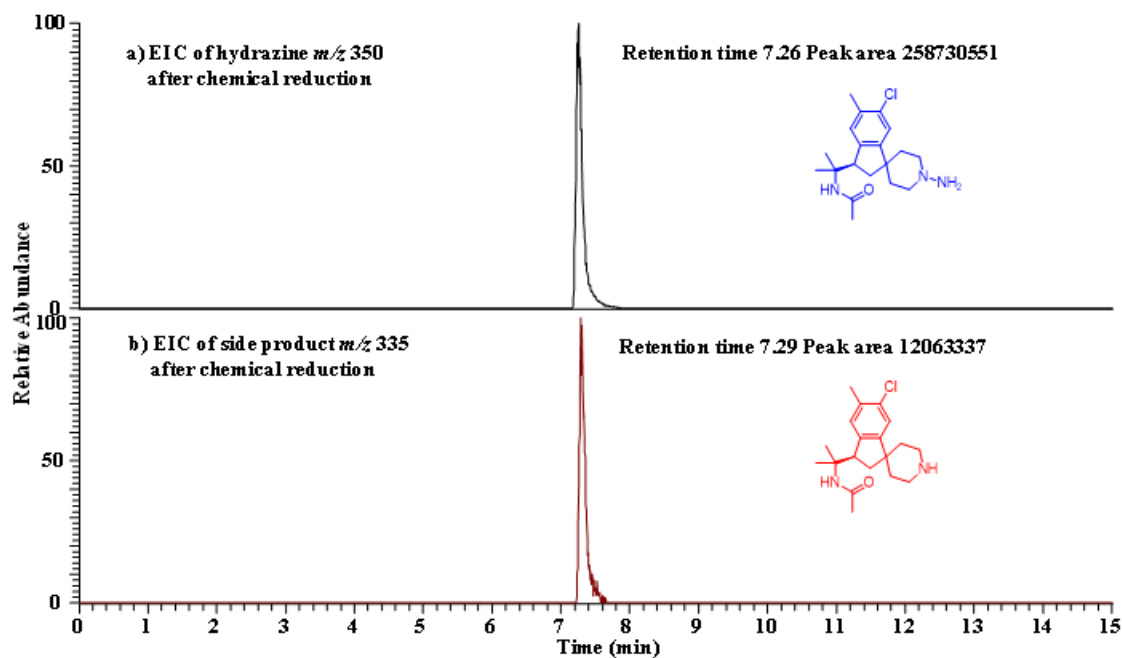


Figure 4.22 EIC spectra for hydrazine 7 at m/z 350 (a) and amine side product at m/z 335 (b) after zinc reduction (in the test sample with drug matrix).

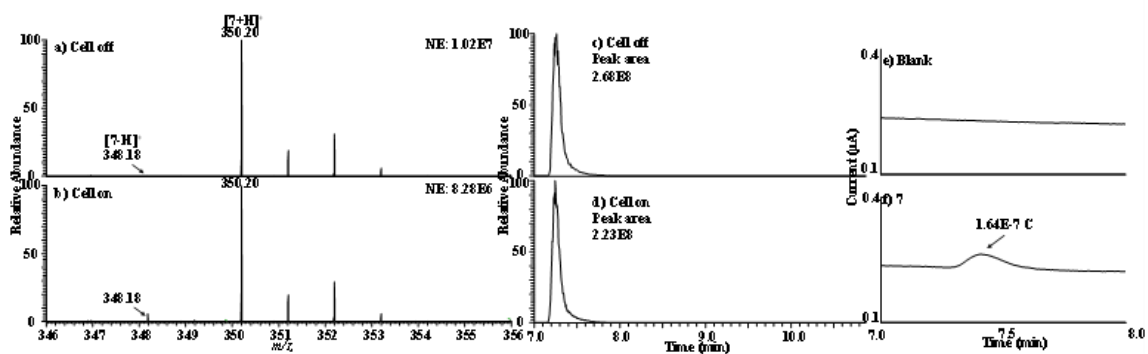


Figure 4.23 ESI-MS spectra of hydrazine **7** (from reduction of *N*-nitrosamine **VII** in the test sample with drug matrix) when the applied potential was (a) 0 V and (b) +0.3 V. EIC of **7** at m/z 350 was recorded when the applied potential was (c) 0 V and (d) +0.3 V (vs Ag/AgCl). Electric current responses were shown due to the oxidation of (e) a blank solvent and (f) **7**.

Table 4.8 Electric current and MS data for *N*-nitrosamine **VII** (in the test sample with drug matrix)

Sample	Q (pA, min)	Q (C)	Amount of the oxidized hydrazine (pmol)	EC oxidation yield	Measured hydrazine amount (pmol)	Averaged hydrazine amount (pmol)	side product to hydrazine ratio	Chemical reduction yield	extraction and isolation yield	dilution factor	Measured nitrosamine amount (pmol)	Theoretical nitrosamine amount (pmol)	Measurement error
nitrosamine VII	2.74E-03	1.64E-07	1.7E+00	17.27%	9.86E+00	9.94E+00	4.45%	58.05%	43.95%	10	4.08E+02	4.12E+02	-1.05%
	3.01E-03	1.81E-07	1.9E+00	18.85%	9.93E+00	9.94E+00							
	2.73E-03	1.64E-07	1.7E+00	16.91%	1.00E+01	1.00E+01							

Sample	EC peak area of m/z 350 before oxidation	EC peak area of m/z 350 after oxidation	EC peak oxidation yield
nitrosamine VII	268451902	222084735	17.27%
	268451902	217861278	18.85%
	268451902	223054658	18.91%

The current zinc-based chemical reduction strategy facilitates subsequent CMS analysis. The weakness is that the zinc to *N*-nitrosamine ratio is hard to control. When the *N*-nitrosamine is at trace level, it is challenging to weigh the trace amount of zinc solid. As a result, side reduction amine products can be produced due to the over-excess of Zn. However, the side product can be controlled to an insignificant amount (< 5%). Benefiting from the similar proton affinity between side product and hydrazine, the chemical reduction conversion ratio from *N*-nitrosamine to hydrazine can be estimated. In other words, *N*-nitrosamine quantitation based on zinc reduction for a trace amount of *N*-nitrosamine is feasible.

4.4 Conclusions

In summary, our results show the feasibility of using CMS to quantify *N*-nitrosamines. The major strength of this approach is that no standards or calibration curves are needed. Therefore, it overcomes a grand challenge for synthesizing standards. This method could significantly impact pharmaceutical quality control, food safety analysis, and water treatment applications in the future. Although zinc-based chemical reduction shows some limitations, especially for controlling the *N*-nitrosamine and zinc reaction ratio, other reductants with better selectivity could overcome this issue. Besides, modified electrodes could be used for directly reducing or oxidizing *N*-nitrosamines, potentially simplifying the quantitation process. These future studies are underway.

CHAPTER 5

SUMMARY AND FUTURE PLANS

In summary, this dissertation presents the capacity of mass spectrometry on interfacing with electrochemistry for capturing the short-lived reaction intermediate, elucidating reaction mechanism, and screening the novel redox neutral electrochemical reactions. Future work will focus on the use of the EC/MS platform as a quick screening tool to extend the application scope of electrochemistry-based synthesis. The developed desalting paper spray method integrates the sample pretreatment (desalting) and sample ionization in one step, significantly increasing the carbohydrate sample detection in complex matrix samples with good sensitivity and quantitation characterization. Future work will focus on the method automation to make it compatible with the high-throughput test, especially on the point-of-care clinical field application. CMS shows its merit on drug impurity *N*-nitrosamines absolute quantitation without using standards. The good measurement accuracy and drug matrix tolerance makes it can be a complementary approach for current *N*-nitrosamine quantitation. Future work with this project will be focusing on modifying the electrode to oxidize or reduce the *N*-nitrosamine directly and as well as improving the method detection limit.

APPENDIX A
REACTION SCREENING

This appendix A contains the figures and tables for reaction screening.

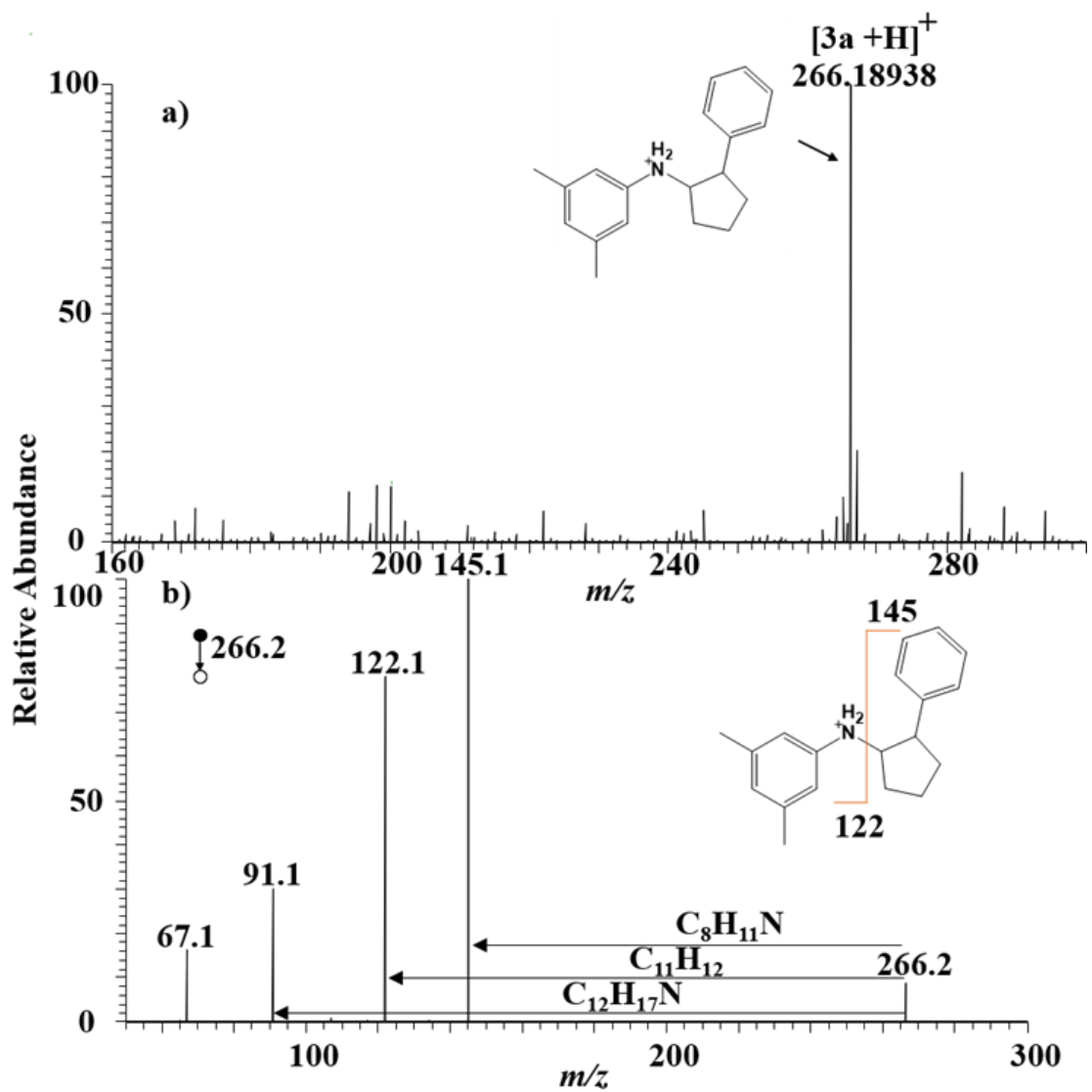
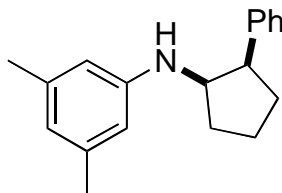


Figure A.1 NanoESI-MS spectrum showing the formation of the product **3a** by divided cell electrolysis (the anode RVC side); b) MS/MS spectrum of [3a+H]⁺.

A.2 Compound NMR characterization

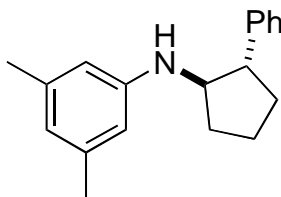
Data for **3a-cis**: colorless oil (78 mg, 47%). ^1H NMR (500 MHz, Chloroform-*d*) δ 7.32 –



7.28 (m, 2H), 7.22 (dt, $J = 7.2, 3.0$ Hz, 3H), 6.31 (s, 1H), 6.12 (s, 2H), 3.99 (q, $J = 5.8$ Hz, 1H), 3.42 (q, $J = 7.6$ Hz, 1H), 2.20 (s, 6H), 2.16 – 2.05 (m, 3H), 1.96 (tq, $J = 7.1, 3.4$ Hz, 1H), 1.81 (dddd,

$J = 13.3, 8.9, 4.9, 2.0$ Hz, 2H). ^{13}C NMR (126 MHz, CDCl_3) δ 147.87, 140.75, 138.69, 128.65, 128.31, 126.44, 118.92, 111.11, 57.40, 48.20, 31.98, 28.65, 22.04, 21.48. HRMS (ESI) m/z $[\text{M}+\text{H}]^+$, calc'd for $\text{C}_{19}\text{H}_{23}\text{N}$ 266.190; found 266.191. The diastereo was established by NOSEY experiment, the integration of correlation peak is 1735.

Data for **3a-trans**: colorless oil (43 mg, 26%). ^1H NMR (500 MHz, Chloroform-*d*) δ 7.19 (q,

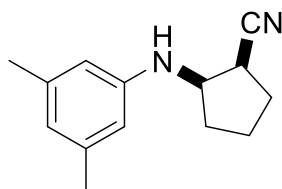


$J = 5.8, 3.8$ Hz, 4H), 7.15 – 7.09 (m, 1H), 6.24 (s, 1H), 6.08 (s, 2H), 3.67 (t, $J = 7.5$ Hz, 1H), 2.81 (q, $J = 8.6$ Hz, 1H), 2.28 (dq, $J = 14.6, 7.5$ Hz, 1H), 2.10 (s, 6H), 1.87 – 1.63 (m, 4H), 1.57 –

1.46 (m, 1H). ^{13}C NMR (126 MHz, CDCl_3) δ 148.10, 143.89, 138.78, 128.53, 127.40, 126.36, 119.07, 111.32, 61.55, 53.22, 33.63, 29.72, 23.38, 21.46. HRMS (ESI) m/z $[\text{M}+\text{H}]^+$, calc'd for $\text{C}_{19}\text{H}_{23}\text{N}$ 266.190; found 266.191. The diastereo was established by NOSEY experiment, the integration of correlation peak is 157.

Following GP2 with cyclopropylaniline (89 mg, 0.55 mmol), cycloadduct **3b** was obtained after silica gel column chromatography (15% EtOAc/hexane) as a separable mixture of two diastereoisomers.

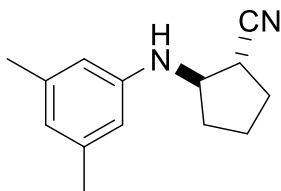
Data for **3b-cis**: colorless oil (61 mg, 52%). ^1H NMR (500 MHz, Chloroform-*d*) δ 6.44 (tt,



$J = 1.6, 0.8$ Hz, 1H), 6.32 – 6.29 (m, 2H), 3.97 (dt, $J = 9.3, 6.7$ Hz, 1H), 3.29 – 3.24 (m, 1H), 2.26 (s, $J = 0.8$ Hz, 6H), 2.20 – 2.10 (m,

2H), 2.10 – 2.02 (m, 1H), 2.02 – 1.93 (m, 1H), 1.78 – 1.67 (m, 2H). ¹³C NMR (126 MHz, CDCl₃) δ 146.60, 139.14, 120.53, 120.34, 111.68, 56.92, 34.34, 31.17, 28.77, 21.56, 21.20. HRMS (ESI) *m/z* [M+H]⁺, calc'd for C₁₄H₁₈N₂ 215.154; found 215.154.

Data for **3b-trans**): colorless oil (33 mg, 28%). ¹H NMR (500 MHz, Chloroform-*d*) δ 6.48

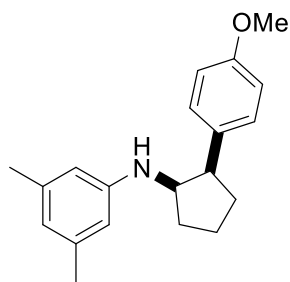


– 6.45 (m, 1H), 6.31 (d, *J* = 1.4 Hz, 2H), 4.13 (ddd, *J* = 7.0, 4.8, 3.7 Hz, 1H), 2.79 (ddd, *J* = 8.5, 4.9, 3.7 Hz, 1H), 2.26 (s, 6H), 2.13 – 1.98 (m, 3H), 1.93 – 1.86 (m, 2H), 1.58 (dtd, *J* = 12.4, 7.4,

4.8 Hz, 1H). ¹³C NMR (126 MHz, CDCl₃) δ 145.80, 139.41, 122.28, 120.86, 111.74, 59.65, 35.30, 33.27, 29.56, 23.61, 21.55. HRMS (ESI) *m/z* [M+H]⁺, calc'd for C₁₄H₁₈N₂ 215.154; found 215.154.

Following GP2 with cyclopropylaniline (93 mg, 0.58 mmol), cycloadduct **3c** was obtained after silica gel column chromatography (3% EtOAc/hexane) as a separable mixture of two diastereoisomers.

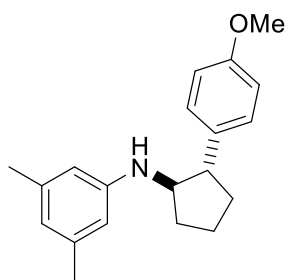
Data for **3c-cis**: colorless oil (62 mg, 36%) ¹H NMR (500 MHz, Chloroform-*d*) δ 7.16 –



7.14 (m, 2H), 6.87 – 6.84 (m, 2H), 6.33 (s, 1H), 6.14 (s, 2H), 3.93 (q, *J* = 5.8 Hz, 1H), 3.81 (s, 3H), 3.40 – 3.35 (m, 1H), 2.22 – 2.19 (s, 6H), 2.18 – 2.02 (m, 4H), 1.82 – 1.76 (m, 2H). ¹³C

NMR (126 MHz, CDCl₃) δ 158.21, 138.77, 132.61, 129.63, 127.64, 113.78, 113.73, 111.33, 55.31, 47.42, 31.89, 28.88, 26.06, 22.09, 21.55. HRMS (ESI) *m/z* [M+H]⁺, calc'd for C₂₀H₂₅NO 296.201; found 296.200.

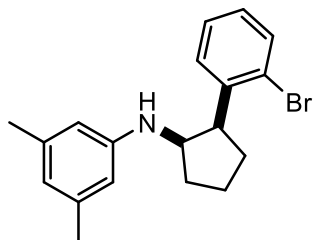
Data for **3c-trans**: colorless oil (65 mg, 38%) ¹H NMR (500 MHz, Chloroform-*d*) δ 7.22 – 7.17 (m, 2H), 6.87 – 6.83 (m, 2H), 6.34 (t, *J* = 1.5 Hz, 1H), 6.19 (s, 2H), 3.79 (s, 3H), 3.70



(td, $J = 7.8, 6.7$ Hz, 1H), 2.86 (dt, $J = 9.9, 8.0$ Hz, 1H), 2.40 – 2.32 (m, 1H), 2.20 (s, 6H), 2.17 (td, $J = 7.9, 4.2$ Hz, 1H), 1.93 – 1.82 (m, 2H), 1.78 – 1.70 (m, 1H), 1.63 – 1.55 (m, 1H). ^{13}C NMR (126 MHz, CDCl_3) δ 158.21, 148.02, 138.84, 135.79, 128.35, 119.26, 113.99, 111.50, 61.74, 55.34, 52.33, 33.50, 23.22, 21.53, 14.21. HRMS (ESI) m/z $[\text{M}+\text{H}]^+$, calc'd for $\text{C}_{20}\text{H}_{25}\text{NO}$ calc'd 296.201; found 296.200.

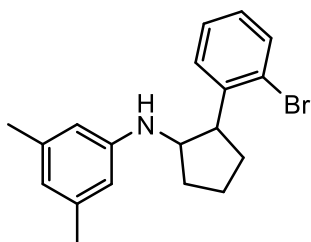
Following GP2 with cyclopropylaniline (135 mg, 0.84 mmol), cycloadduct **3d** was obtained after silica gel column chromatography (3% EtOAc/hexane) as a inseparable mixture of two diastereoisomers (only isolated *cis* isomer).

Data for **3d-cis**: colorless oil. ^1H NMR (500 MHz, Chloroform- d) δ 7.55 – 7.49 (m, 1H),



7.39 – 7.33 (m, 1H), 7.27 (d, $J = 7.0$ Hz, 1H), 7.06 (td, $J = 7.7, 1.7$ Hz, 1H), 6.25 (s, 1H), 6.04 (s, 2H), 4.16 (td, $J = 6.2, 3.1$ Hz, 1H), 3.67 (dt, $J = 12.8, 6.7$ Hz, 1H), 2.28 – 2.16 (m, 2H), 2.14 (s, 6H), 2.04 – 1.90 (m, 2H), 1.87 – 1.69 (m, 2H). ^{13}C NMR (126 MHz, CDCl_3) δ 147.58, 139.52, 138.59, 133.04, 129.08, 128.18, 127.25, 126.27, 119.04, 111.25, 55.17, 49.13, 33.49, 29.28, 22.66, 21.48. HRMS (ESI) m/z $[\text{M}+\text{H}]^+$, calc'd for $\text{C}_{19}\text{H}_{22}\text{NBr}$ calc'd 344.101; found 344.101.

Data for **3d** mixture: colorless oil (202 mg, 70%). ^1H NMR (500 MHz, Chloroform- d) δ

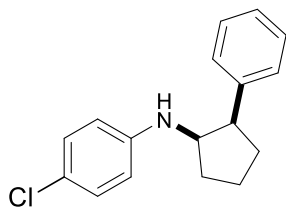


7.52 (dd, $J = 7.9, 1.3$ Hz, 3H), 7.36 (dd, $J = 7.8, 1.7$ Hz, 2H), 7.33 – 7.22 (m, 5H), 7.05 (qd, $J = 7.9, 1.8$ Hz, 3H), 6.34 – 6.31 (m, 1H), 6.26 (tt, $J = 1.5, 0.8$ Hz, 2H), 6.18 (s, 1H), 6.07 – 6.03 (m, 4H), 4.17 (td, $J = 6.1, 3.1$ Hz, 2H), 3.83 (dt, $J = 8.9, 7.3$ Hz, 1H), 3.68 (dt, $J = 11.4, 6.7$

Hz, 2H), 3.45 (dt, $J = 10.0, 8.4$ Hz, 1H), 2.47 – 2.37 (m, 1H), 2.22 – 2.13 (m, 20H), 2.01 – 1.72 (m, 12H), 1.67 – 1.56 (m, 3H). ^{13}C NMR (126 MHz, CDCl_3) δ 147.67, 142.74, 139.57, 139.06, 138.89, 138.59, 133.06, 132.91, 129.10, 128.20, 127.98, 127.90, 127.70, 127.27, 126.30, 125.54, 119.17, 119.01, 111.23, 111.19, 61.44, 55.17, 51.43, 49.17, 33.55, 33.42, 32.55, 29.33, 23.10, 22.70, 21.59, 21.53. HRMS (ESI) m/z $[\text{M}+\text{H}]^+$, calc'd for $\text{C}_{19}\text{H}_{22}\text{NBr}$ calc'd 344.101; found 344.101.

Following GP2 with cyclopropylaniline (97 mg, 0.58 mmol), cycloadduct **4a** was obtained after silica gel column chromatography (5% EtOAc/hexane) as a separable mixture of two diastereoisomers.

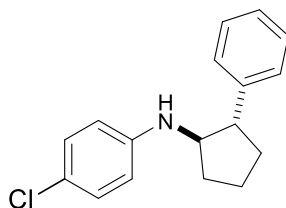
Data for **4a-cis**: colorless oil (85 mg, 54%) ^1H NMR (500 MHz, Chloroform-*d*) δ 7.28 (q,



$J = 8.9, 8.2$ Hz, 2H), 7.23 (d, $J = 7.1$ Hz, 1H), 7.18 (d, $J = 7.5$ Hz, 2H), 7.07 – 7.00 (m, 2H), 6.38 (d, $J = 8.5$ Hz, 2H), 3.95 (q, $J = 6.0$ Hz, 1H), 3.44 (q, $J = 7.4$ Hz, 1H), 2.22 – 2.04 (m, 3H), 1.97 (ddt,

$J = 13.2, 8.9, 4.6$ Hz, 1H), 1.86 – 1.70 (m, 2H). ^{13}C NMR (126 MHz, CDCl_3) δ 146.24, 140.56, 128.82, 128.59, 128.32, 126.54, 121.67, 114.38, 57.84, 48.03, 31.94, 29.03, 22.09. HRMS (ESI) m/z $[\text{M}+\text{H}]^+$, calc'd for $\text{C}_{17}\text{H}_{18}\text{NCl}$ calc'd 272.120; found 272.120.

Data for **4a-trans**: colorless oil (43 mg, 27%) ^1H NMR (500 MHz, Chloroform-*d*) δ 7.27



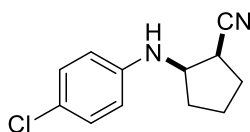
(t, $J = 7.5$ Hz, 2H), 7.23 – 7.15 (m, 3H), 7.02 (d, $J = 8.3$ Hz, 2H), 6.41 (d, $J = 8.4$ Hz, 2H), 3.71 (q, $J = 7.3$ Hz, 1H), 2.87 (q, $J = 8.5$ Hz, 1H), 2.31 (dq, $J = 14.5, 7.5$ Hz, 1H), 2.18 (dtd, $J = 12.3, 7.9,$

7.5, 3.9 Hz, 1H), 1.84 (dp, $J = 13.4, 6.9, 6.2$ Hz, 2H), 1.74 (dq, $J = 12.8, 9.2$ Hz, 1H), 1.56 (ddd, $J = 15.4, 12.9, 6.7$ Hz, 1H). ^{13}C NMR (126 MHz, CDCl_3) δ 146.41, 143.56, 128.96,

127.43, 126.58, 121.83, 114.76, 114.41, 61.97, 53.27, 33.41, 23.35, 14.25. HRMS (ESI) m/z $[M+H]^+$, $C_{17}H_{18}NCl$ calc'd 272.120; found 272.120.

Following GP2 with cyclopropylaniline (67 mg, 0.40 mmol), cycloadduct **4b** was obtained after silica gel column chromatography (15% EtOAc/hexane) as a separable mixture of two diastereoisomers.

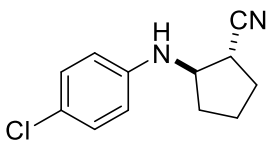
Data for **4b-cis**: colorless oil (35 mg, 40%). 1H NMR (500 MHz, Chloroform- d) δ 7.18 –



7.07 (m, 2H), 6.60 – 6.52 (m, 2H), 4.05 – 3.88 (m, 2H), 3.23 (td, J = 8.75, 4.2 Hz, 1H), 2.23 – 2.04 (m, 3H), 2.02 – 1.92 (m, 1H), 1.80

– 1.62 (m, 2H). ^{13}C NMR (126 MHz, $CDCl_3$) δ 145.22, 129.27, 122.99, 120.06, 114.67, 56.79, 34.12, 31.30, 28.85, 21.37. HRMS (ESI) m/z $[M+H]^+$, calc'd for $C_{12}H_{13}ClN_2$ 221.084; found 221.084.

Data for **4b-trans**: colorless oil (26 mg, 30%). 1H NMR (500 MHz, Chloroform- d) δ 7.25 –

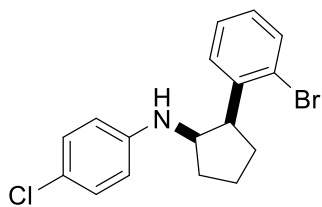


7.19 (m, 2H), 6.66 – 6.60 (m, 2H), 4.20 – 4.11 (m, 1H), 2.78 (ddd, J = 8.1, 5.4, 4.1 Hz, 1H), 2.40 (dq, J = 14.1, 7.2 Hz, 1H), 2.21 –

2.07 (m, 2H), 1.62 (dtd, J = 12.9, 7.5, 5.1 Hz, 3H). ^{13}C NMR (126 MHz, $CDCl_3$) δ 144.72, 129.44, 123.22, 122.10, 114.52, 59.54, 35.42, 33.41, 29.63, 23.60. HRMS (ESI) m/z $[M+H]^+$, calc'd for $C_{12}H_{13}ClN_2$ 221.084; found 221.084.

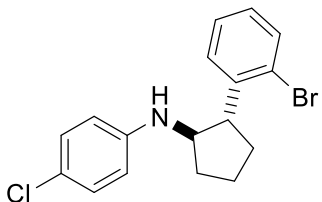
Following GP2 with cyclopropylaniline (86 mg, 0.52 mmol), cycloadduct **4c** was obtained after silica gel column chromatography (10% EtOAc/hexane) as a separable mixture of two diastereoisomers.

Data for **4c-cis**: colorless oil (69 mg, 38%). ^1H NMR (500 MHz, Chloroform-*d*) δ 7.60 –



7.56 (m, 1H), 7.41 – 7.38 (m, 1H), 7.34 – 7.29 (m, 1H), 7.14 – 7.10 (m, 1H), 7.05 – 7.00 (m, 2H), 6.39 – 6.34 (m, 2H), 4.22 (td, $J = 6.4, 3.3$ Hz, 1H), 3.75 (dt, $J = 11.2, 6.7$ Hz, 1H), 2.38 – 2.27 (m, 1H), 2.22 – 2.14 (m, 1H), 2.12 – 2.05 (m, 1H), 2.04 – 1.93 (m, 1H), 1.87 – 1.78 (m, 2H). ^{13}C NMR (126 MHz, CDCl_3) δ 146.09, 142.40, 139.30, 133.07, 129.10, 128.69, 127.27, 126.17, 121.46, 114.24, 55.34, 49.00, 33.45, 29.43, 22.71. HRMS (ESI) m/z $[\text{M}+\text{H}]^+$, calc'd for $\text{C}_{17}\text{H}_{17}\text{NClBr}$; 350.031; found 350.030.

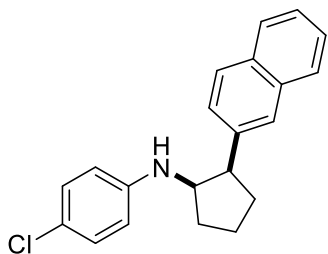
Data for **4c-trans**: colorless oil (67 mg, 37%). ^1H NMR (500 MHz, Chloroform-*d*) δ 7.60



(dt, $J = 7.8, 0.9$ Hz, 1H), 7.36 – 7.31 (m, 2H), 7.16 – 7.07 (m, 3H), 6.55 – 6.44 (m, 2H), 3.87 (dt, $J = 8.6, 7.2$ Hz, 1H), 3.52 (dt, $J = 9.9, 8.3$ Hz, 1H), 2.51 – 2.40 (m, 1H), 2.36 (dtd, $J = 13.1, 7.4, 5.2$ Hz, 1H), 2.01 – 1.91 (m, 2H), 1.76 – 1.61 (m, 2H). ^{13}C NMR (126 MHz, CDCl_3) δ 146.43, 142.41, 139.53, 132.99, 128.97, 128.02, 127.50, 125.44, 121.71, 114.31, 61.67, 51.41, 33.13, 32.48, 23.01. HRMS (ESI) m/z $[\text{M}+\text{H}]^+$, calc'd for $\text{C}_{17}\text{H}_{17}\text{NClBr}$ 350.031; found 350.030.

Following GP2 with cyclopropylaniline (72 mg, 0.43 mmol), cycloadduct **4d** was obtained after silica gel column chromatography (5% EtOAc/hexane) as a separable mixture of two diastereoisomers.

Data for **4d-cis**: colorless oil (50 mg, 36%). ¹H NMR (500 MHz, Chloroform-*d*) δ 7.89 –

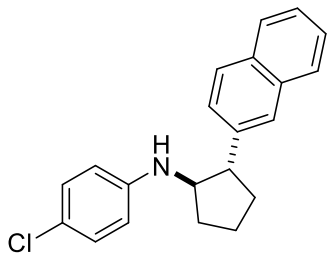


7.72 (m, 3H), 7.66 (d, *J* = 2.3 Hz, 1H), 7.57 – 7.41 (m, 2H),
7.32 (dd, *J* = 10.5, 2.3 Hz, 1H), 7.10 – 7.00 (m, 2H), 6.45 –
6.32 (m, 2H), 4.07 (q, *J* = 7.4 Hz, 1H), 3.62 (q, *J* = 9.4 Hz, 1H),
2.27 (dt, *J* = 11.8, 8.3 Hz, 2H), 2.19 – 1.99 (m, 2H), 1.95 – 1.78

(m, 2H). ¹³C NMR (126 MHz, CDCl₃) δ 146.30, 138.14, 133.37, 132.31, 128.86, 127.91,
127.70, 127.39, 126.74, 126.11, 125.63, 121.49, 114.27, 57.64, 48.08, 31.86, 28.83, 22.12.

HRMS (ESI) *m/z* [M+H]⁺, calc'd for C₂₁H₂₀ClN 322.136; found 322.135.

Data for **4d-trans**: colorless oil (58 mg, 42%). ¹H NMR (500 MHz, Chloroform-*d*) δ 7.91 –

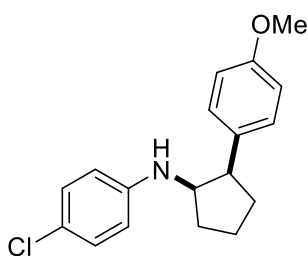


7.77 (m, 3H), 7.72 (s, 1H), 7.55 – 7.37 (m, 3H), 7.15 – 7.02 (m,
2H), 6.54 – 6.37 (m, 2H), 3.90 (q, *J* = 9.1 Hz, 1H), 3.09 (q, *J* =
10.4 Hz, 1H), 2.49 – 2.38 (m, 1H), 2.37 – 2.25 (m, 1H), 2.05 –
1.85 (m, 3H), 1.73 – 1.60 (m, 1H). ¹³C NMR (126 MHz, CDCl₃)

δ 146.60, 141.04, 133.59, 132.44, 129.43, 128.96, 128.43, 127.67, 126.15, 125.52, 121.71,
119.17, 114.50, 61.62, 53.41, 33.55, 33.50, 23.45. HRMS (ESI) *m/z* [M+H]⁺, calc'd for
C₂₁H₂₀ClN 322.136; found 322.135.

Following GP2 with cyclopropylaniline (70 mg, 0.42 mmol), cycloadduct **4e** was obtained
after silica gel column chromatography (3% EtOAc/hexane) as a separable mixture of two
diastereoisomers.

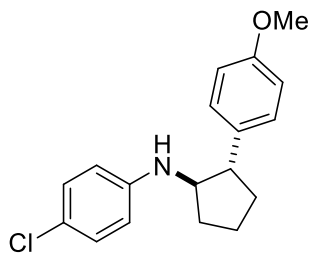
Data for **4e-cis**: colorless oil (57 mg, 45%). ¹H NMR (500 MHz, Chloroform-*d*) δ 7.14 –



7.06 (m, 2H), 7.07 – 6.99 (m, 2H), 6.88 – 6.77 (m, 2H), 6.42 –
6.33 (m, 2H), 3.89 (p, *J* = 6.9 Hz, 1H), 3.79 (s, 3H), 3.38 (q, *J* =
9.4 Hz, 1H), 2.19 – 2.01 (m, 3H), 1.94 (dtd, *J* = 16.3, 8.8, 4.1 Hz,

1H), 1.86 – 1.65 (m, 2H). ¹³C NMR (126 MHz, CDCl₃) δ 158.25, 146.43, 132.46, 129.53, 128.85, 121.39, 114.26, 113.77, 57.60, 55.26, 47.12, 31.75, 29.08, 22.05. HRMS (ESI) *m/z* [M+H]⁺, calc'd for C₁₈H₂₀ClNO 302.131; found 302.130.

Data for **4e-trans**: colorless oil (44 mg, 35%). ¹H NMR (500 MHz, Chloroform-*d*) δ 7.21 –

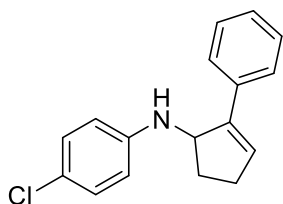


7.15 (m, 2H), 7.10 – 7.02 (m, 2H), 6.89 – 6.82 (m, 2H), 6.48 – 6.40 (m, 2H), 3.79 (s, 3H), 3.68 (q, *J* = 9.3 Hz, 1H), 2.84 (dt, *J* = 12.1, 10.0 Hz, 1H), 2.39 – 2.28 (m, 1H), 2.18 (dp, *J* = 15.1, 4.6 Hz, 1H), 1.93 – 1.80 (m, 2H), 1.78 – 1.67 (m, 1H), 1.56 (ddt,

J = 16.3, 11.1, 8.1 Hz, 1H). ¹³C NMR (126 MHz, CDCl₃) δ 158.27, 146.68, 135.46, 128.91, 128.22, 121.58, 114.41, 114.05, 61.72, 55.30, 52.41, 33.48, 33.23, 23.13. HRMS (ESI) *m/z* [M+H]⁺, calc'd for C₁₈H₂₀ClNO 302.131; found 302.130.

Following GP2 with cyclopropylaniline (79 mg, 0.47 mmol), cycloadduct **4f** was obtained after silica gel column chromatography (3% EtOAc/hexane).

Data for **4f**: colorless oil (74 mg, 58%). ¹H NMR (500 MHz, Chloroform-*d*) δ 7.55 – 7.45

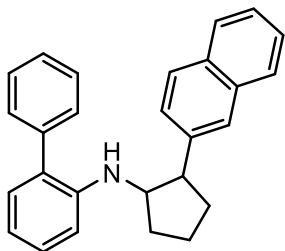


(m, 2H), 7.34 (dd, *J* = 10.4, 8.3 Hz, 2H), 7.31 – 7.24 (m, 1H), 7.21 – 7.12 (m, 2H), 6.62 – 6.54 (m, 2H), 6.44 (d, *J* = 2.9 Hz, 1H), 4.87 (d, *J* = 9.1 Hz, 1H), 3.80 (s, 1H), 2.75 – 2.62 (m, 1H),

2.55 (ddt, *J* = 22.0, 11.3, 3.9 Hz, 1H), 2.38 (ddt, *J* = 17.4, 11.3, 8.9 Hz, 1H), 2.02 (ddt, *J* = 17.0, 10.4, 3.6 Hz, 1H). ¹³C NMR (126 MHz, CDCl₃) δ 146.20, 142.55, 134.48, 130.27, 129.14, 128.63, 127.50, 126.16, 121.64, 114.09, 59.25, 31.47, 31.01. HRMS (ESI) *m/z* [M+H]⁺, calc'd for C₁₇H₁₆ClN 270.104; found 270.104.

Following GP2 with cyclopropylaniline (125 mg, 0.60 mmol), cycloadduct **5a** was obtained after silica gel column chromatography (3% EtOAc/hexane) as a inseparable mixture of two diastereoisomers (*cis/trans*=1:1).

Data for **5a**: yellowish oil (129 mg, 59%). ¹H NMR (500 MHz, Chloroform-*d*) δ 7.94 –

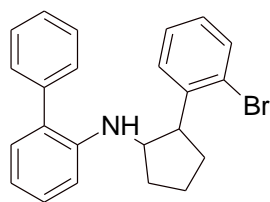


7.85 (m, 4H), 7.80 – 7.74 (m, 2H), 7.66 (d, *J* = 1.8 Hz, 1H), 7.61 – 7.52 (m, 5H), 7.46 (dd, *J* = 8.5, 1.8 Hz, 1H), 7.40 (dd, *J* = 4.9, 2.0 Hz, 3H), 7.36 – 7.24 (m, 5H), 7.12 (dd, *J* = 7.4, 1.6 Hz, 1H), 7.06 – 6.97 (m, 2H), 6.88 – 6.72 (m, 8H), 4.20 (d, *J* = 5.9 Hz, 1H),

3.91 (q, *J* = 7.5 Hz, 1H), 3.66 (dt, *J* = 9.5, 7.2 Hz, 1H), 3.03 (q, *J* = 8.5 Hz, 1H), 2.59 – 2.45 (m, 1H), 2.32 – 2.15 (m, 4H), 2.11 – 1.82 (m, 6H), 1.77 – 1.59 (m, 1H). ¹³C NMR (126 MHz, CDCl₃) δ 145.05, 144.52, 140.89, 139.46, 138.98, 138.09, 133.60, 133.56, 132.52, 132.41, 130.23, 130.17, 129.39, 128.89, 128.71, 128.51, 128.38, 128.31, 128.03, 127.79, 127.71, 127.69, 127.61, 127.41, 127.17, 126.62, 126.51, 126.21, 126.10, 125.95, 125.60, 125.51, 116.86, 116.31, 111.50, 110.45, 62.54, 57.61, 53.37, 48.78, 33.64, 32.60, 31.72, 28.76, 23.34, 22.71. HRMS (ESI) *m/z* [M+H]⁺, calc'd for C₂₇H₂₅N 364.206; found 364.206.

Following GP2 with cyclopropylaniline (104 mg, 0.50 mmol), cycloadduct **5b** was obtained after silica gel column chromatography (2% EtOAc/hexane) as a inseparable mixture of two diastereoisomers (*cis/trans*=1:1).

Data for **5b**: yellowish oil (137 mg, 70%). ¹H NMR (500 MHz, Chloroform-*d*) δ 7.48 (td,

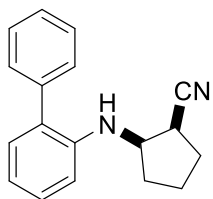


$J = 8.0, 1.6$ Hz, 2H), 7.42 – 7.36 (m, 2H), 7.35 – 7.27 (m, 8H),
7.20 – 7.14 (m, 2H), 7.10 – 6.91 (m, 8H), 6.76 – 6.58 (m, 4H),
4.20 (d, $J = 2.7$ Hz, 1H), 3.80 (dt, $J = 8.8, 7.3$ Hz, 1H), 3.65 (dt,

$J = 11.3, 6.9$ Hz, 1H), 3.37 (q, $J = 8.9$ Hz, 1H), 2.17 (d, $J = 8.2$ Hz, 2H), 2.01 – 1.80 (m,
6H), 1.79 – 1.59 (m, 3H). ¹³C NMR (126 MHz, CDCl₃) δ 144.11, 142.60, 139.35, 139.27,
139.05, 133.00, 132.78, 130.28, 130.02, 129.38, 129.26, 128.99, 128.89, 128.74, 128.67,
128.61, 128.49, 128.00, 127.87, 127.77, 127.31, 127.17, 126.84, 125.94, 125.41, 116.44,
110.68, 62.72, 54.94, 51.10, 48.96, 34.74, 33.35, 33.10, 32.49, 31.67, 29.08, 25.35, 23.19,
22.75. HRMS (ESI) m/z [M+H]⁺, calc'd for C₂₃H₂₂BrN 392.101; found 392.101.

Following GP2 with cyclopropylaniline (92 mg, 0.44 mmol), cycloadduct **5c** was obtained after silica gel column chromatography (1% EtOAc/hexane) as a separable mixture of two diastereoisomers (*cis/trans*=4:1).

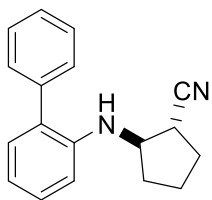
Data for **5c-cis**: colorless oil (15 mg, 13%). ¹H NMR (500 MHz, Chloroform-*d*) δ 7.53 (t, J



= 7.5 Hz, 1H), 7.49 – 7.42 (m, 2H), 7.39 – 7.34 (m, 3H), 7.30 (ddd, $J =$
8.1, 7.4, 1.6 Hz, 1H), 7.11 (dd, $J = 7.5, 1.7$ Hz, 1H), 6.88 – 6.78 (m, 1H),
4.15 (dt, $J = 7.1, 4.5$ Hz, 1H), 2.72 (td, $J = 6.6, 3.8$ Hz, 1H), 2.32 – 2.21

(m, 1H), 2.00 (q, $J = 7.2$ Hz, 2H), 1.89 – 1.70 (m, 2H), 1.46 – 1.38 (m, 1H). ¹³C NMR (126
MHz, CDCl₃) δ 143.03, 139.07, 130.60, 129.28, 129.09, 128.41, 128.19, 127.51, 122.27,
118.17, 111.46, 59.47, 35.38, 33.27, 29.45, 23.52. HRMS (ESI) m/z [M+H]⁺, calc'd for
C₁₈H₁₈N₂ 263.154; found 263.153.

Data for **5c-cis**: colorless oil (60 mg, 52%). ¹H NMR (500 MHz, Chloroform-d) δ 7.59 –

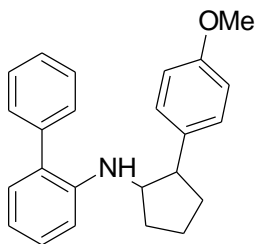


7.51 (m, 4H), 7.47 – 7.41 (m, 1H), 7.35 – 7.28 (m, 1H), 7.20 (dd, J = 7.5, 1.6 Hz, 1H), 6.90 (td, J = 7.4, 1.1 Hz, 1H), 6.75 (dd, J = 8.3, 1.1 Hz, 1H), 4.04 (dt, J = 9.4, 6.7 Hz, 1H), 3.38 (td, J = 6.9, 4.2 Hz, 1H), 2.20 –

2.07 (m, 3H), 2.01 – 1.92 (m, 1H), 1.76 (dq, J = 13.3, 8.4, 6.0 Hz, 1H), 1.64 (dtd, J = 12.9, 9.5, 8.2 Hz, 1H). ¹³C NMR (126 MHz, CDCl₃) δ 143.40, 138.99, 130.72, 129.43, 129.11, 128.73, 128.39, 127.52, 120.24, 117.93, 110.80, 56.69, 34.12, 31.34, 28.95, 21.28. HRMS (ESI) *m/z* [M+H]⁺, calc'd for C₁₈H₁₈N₂ 263.154; found 263.153.

Following GP2 with cyclopropylaniline (121 mg, 0.58 mmol), cycloadduct **5d** was obtained after silica gel column chromatography (3% EtOAc/hexane) as a inseparable mixture of two diastereoisomers (*cis/trans*=1:1).

Data for **5d**: colorless oil (123 mg, 62%). ¹H NMR (500 MHz, Chloroform-d) δ 7.47 (td, J



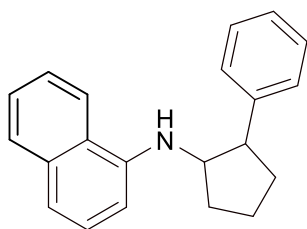
= 7.3, 2.5 Hz, 2H), 7.44 – 7.38 (m, 1H), 7.36 – 7.22 (m, 7H), 7.16 (dd, J = 8.7, 3.1 Hz, 2H), 7.11 (dt, J = 7.4, 2.1 Hz, 1H), 7.09 – 7.04 (m, 3H), 7.01 (dd, J = 8.7, 2.4 Hz, 2H), 6.90 (dd, J = 8.7, 2.9 Hz,

2H), 6.83 – 6.63 (m, 6H), 3.99 (dd, J = 10.2, 4.8 Hz, 1H), 3.87 (t, J = 2.4 Hz, 6H), 3.82 (d, J = 12.1 Hz, 1H), 3.71 (dp, J = 10.7, 6.6, 4.5 Hz, 1H), 3.46 – 3.38 (m, 1H), 2.79 (q, J = 8.5 Hz, 1H), 2.42 (d, J = 12.3 Hz, 1H), 2.15 (tdd, J = 13.6, 10.9, 7.9 Hz, 3H), 2.03 – 1.89 (m, 3H), 1.89 – 1.75 (m, 4H). ¹³C NMR (126 MHz, CDCl₃) δ 158.31, 158.14, 145.18, 144.66, 139.57, 139.38, 135.48, 132.51, 130.23, 130.19, 129.45, 129.36, 129.17, 128.94, 128.72, 128.68, 128.58, 128.39, 127.78, 127.69, 127.18, 126.75, 116.73, 116.30, 114.00, 113.86,

111.42, 110.55, 62.57, 57.65, 55.40, 55.33, 52.35, 47.69, 33.42, 32.68, 32.27, 29.13, 23.11, 22.52. HRMS (ESI) m/z $[M+H]^+$, calc'd for $C_{24}H_{25}NO$ 344.201; found 344.200.

Following GP2 with cyclopropylaniline (95 mg, 0.52 mmol), cycloadduct **6a** was obtained after silica gel column chromatography (10% EtOAc/hexane) as a inseparable mixture of two diastereoisomers (*cis/trans*=1:1).

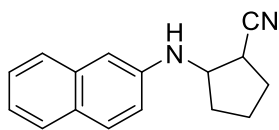
Data for **6a**: colorless oil (69 mg, 46%). 1H NMR (500 MHz, Chloroform-*d*) δ 7.70 (ddt, J



= 23.7, 16.2, 8.2 Hz, 4H), 7.40 – 7.30 (m, 5H), 7.22 (ddd, J = 10.5, 6.7, 3.5 Hz, 7H), 7.17 – 7.07 (m, 6H), 6.53 (dd, J = 24.2, 7.5 Hz, 2H), 4.05 (q, J = 5.9 Hz, 1H), 3.88 (q, J = 7.2 Hz, 1H), 3.50 (p, J = 7.4 Hz, 1H), 3.04 (q, J = 8.4 Hz, 1H), 2.57 (d, J = 6.7 Hz, 1H), 2.42 (dq, J = 14.8, 7.6 Hz, 1H), 2.29 – 2.09 (m, 4H), 1.92 – 1.73 (m, 6H). ^{13}C NMR (126 MHz, $CDCl_3$) δ 143.76, 142.91, 140.53, 134.38, 128.74, 128.68, 128.59, 128.52, 128.36, 127.43, 126.87, 126.69, 126.63, 126.60, 125.73, 125.61, 124.73, 124.55, 123.82, 123.63, 120.00, 119.85, 119.78, 117.85, 117.34, 116.97, 105.90, 104.93, 61.69, 57.40, 53.33, 48.79, 33.60, 33.40, 32.05, 28.96, 23.70, 22.79. HRMS (ESI) m/z $[M+H]^+$, calc'd for $C_{21}H_{21}N$ 288.175; found 288.174.

Following GP2 with cyclopropylaniline (62 mg, 0.34 mmol), cycloadduct **6c** was obtained after silica gel column chromatography (3% EtOAc/hexane) as a inseparable mixture of two diastereoisomers (*cis/trans*=1:1).

Data for **6b**: colorless oil(40 mg, 50%). ^1H NMR (500 MHz, Chloroform- d) δ 7.84



(dddd, $J = 40.0, 28.1, 8.3, 2.9$ Hz, 3H), 7.55 – 7.27 (m, 6H), 6.64

(dd, $J = 9.0, 1.6$ Hz, 1H), 4.70 (d, $J = 9.9$ Hz, 1H), 4.34 (d, $J = 6.4$

Hz, 1H), 4.17 (p, $J = 9.1$ Hz, 1H), 3.41 (td, $J = 8.9, 5.1$ Hz, 1H), 2.47 (dq, $J = 17.5, 8.8$ Hz,

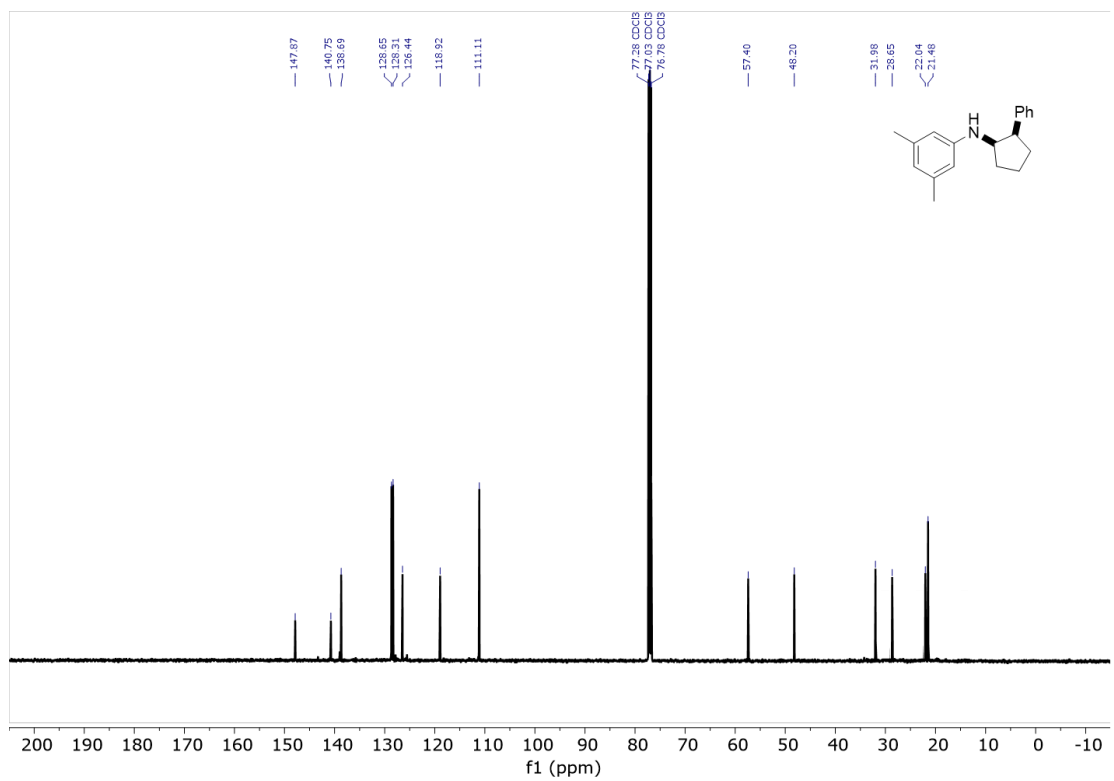
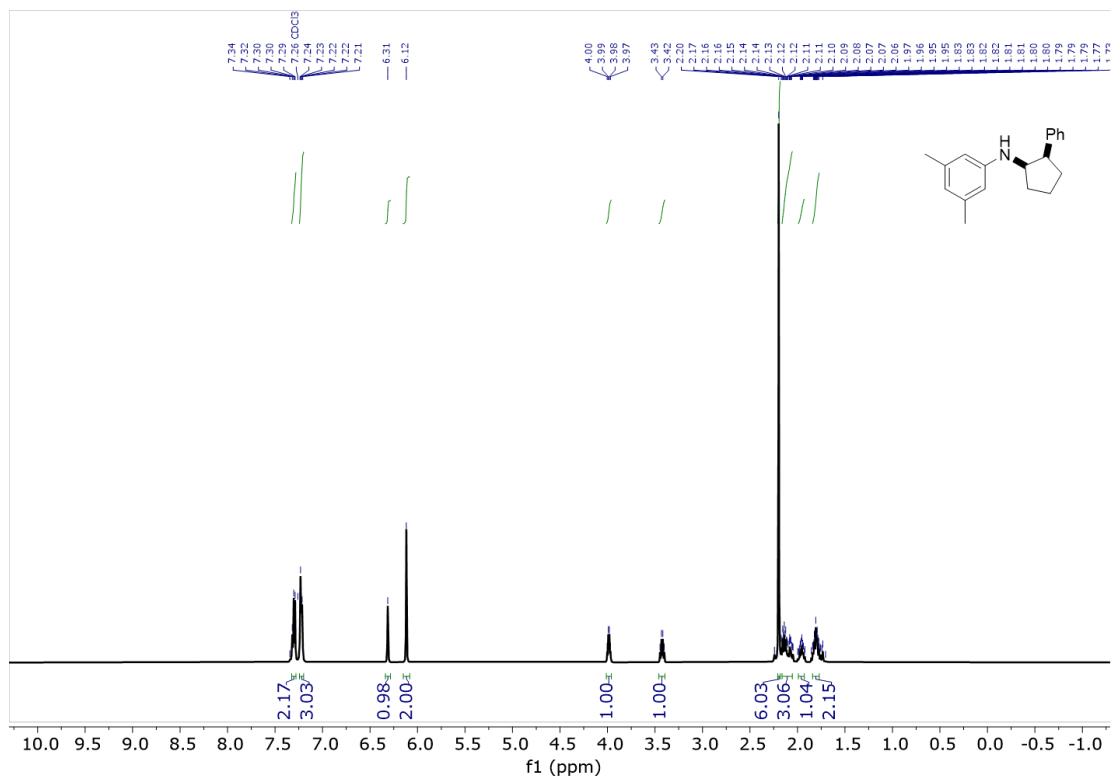
1H), 2.33 (ddt, $J = 14.1, 10.4, 5.4$ Hz, 1H), 2.28 – 1.95 (m, 5H), 1.95 – 1.71 (m, 3H). ^{13}C

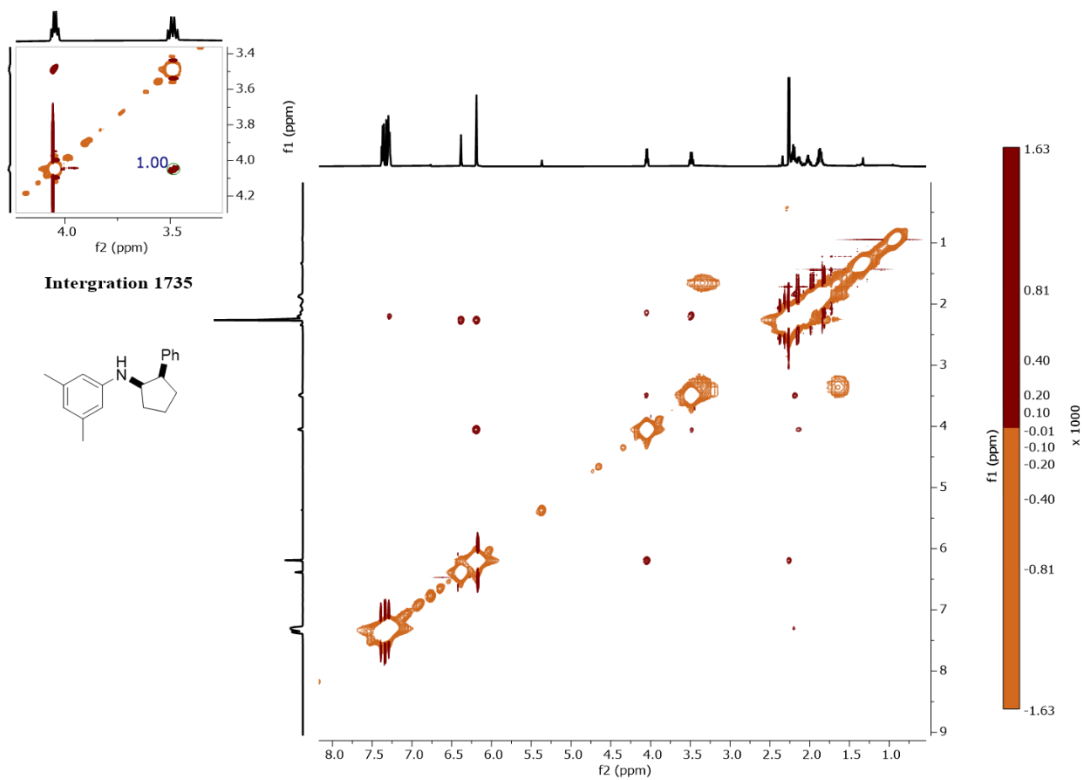
NMR (126 MHz, CDCl_3) δ 141.88, 141.27, 134.44, 128.87, 128.67, 128.56, 126.57,

126.22, 126.02, 126.00, 125.18, 125.09, 123.71, 123.55, 122.31, 120.26, 120.02, 119.62,

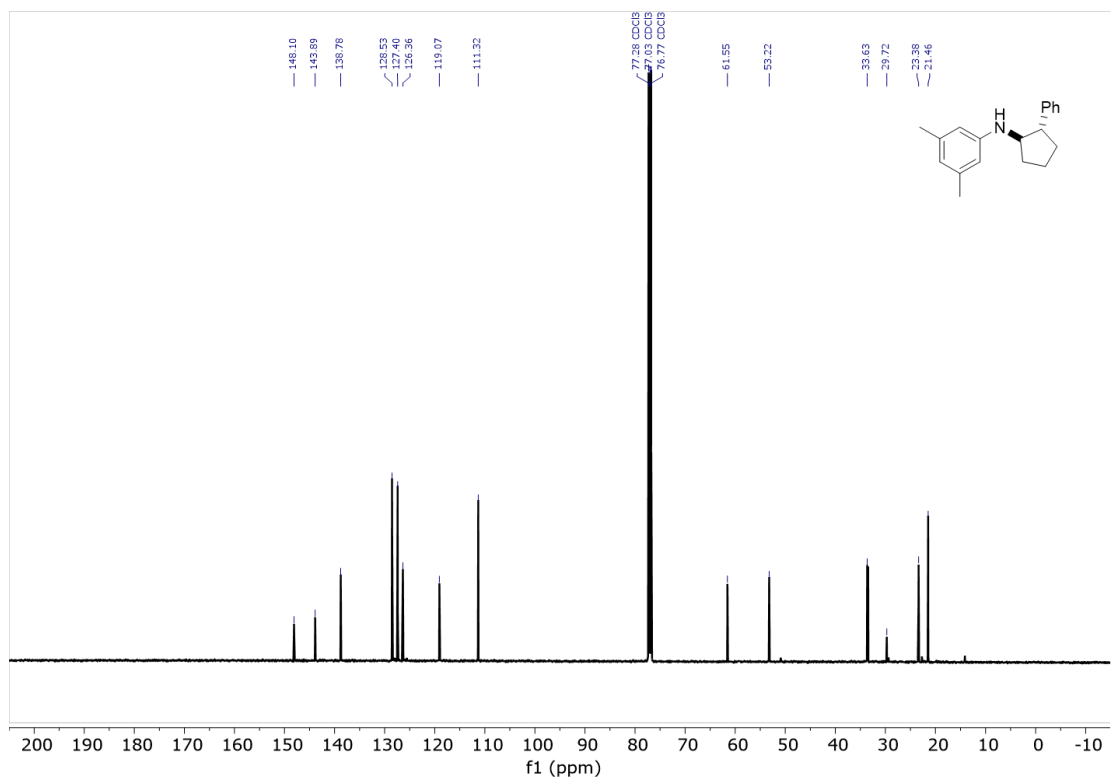
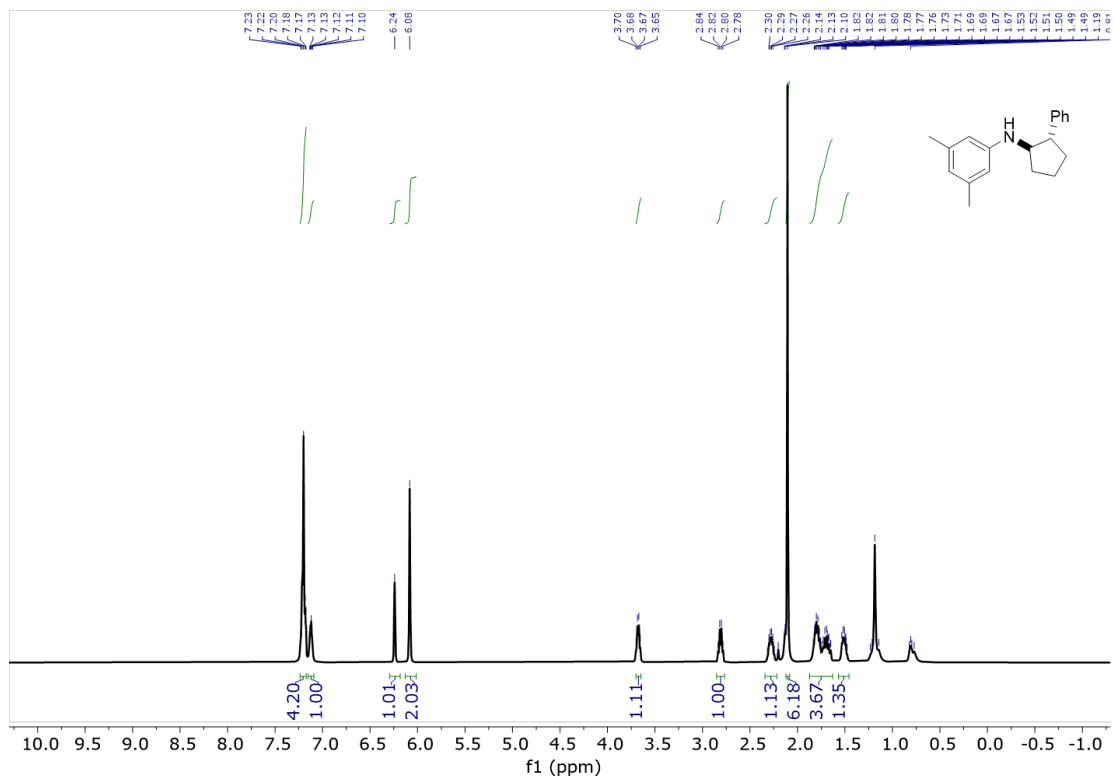
118.70, 118.58, 106.00, 105.59, 59.35, 56.62, 35.32, 34.33, 33.63, 31.46, 29.84, 29.04,

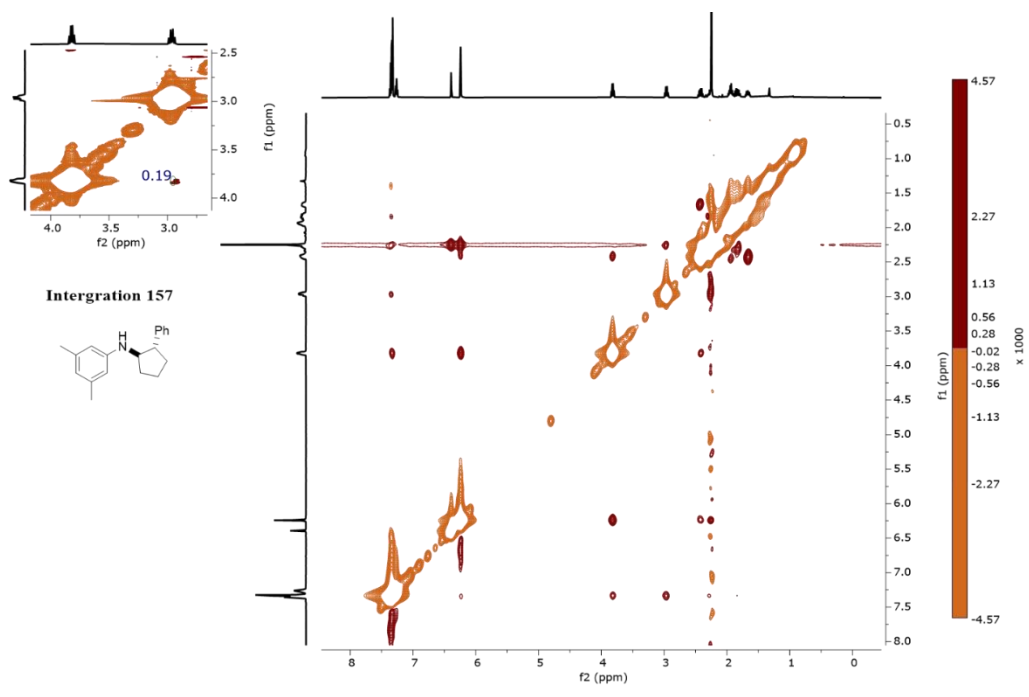
23.94, 21.59. HRMS (ESI) m/z $[\text{M}+\text{H}]^+$, calc'd for $\text{C}_{16}\text{H}_{16}\text{N}_2$ 237.139; found 237.138.



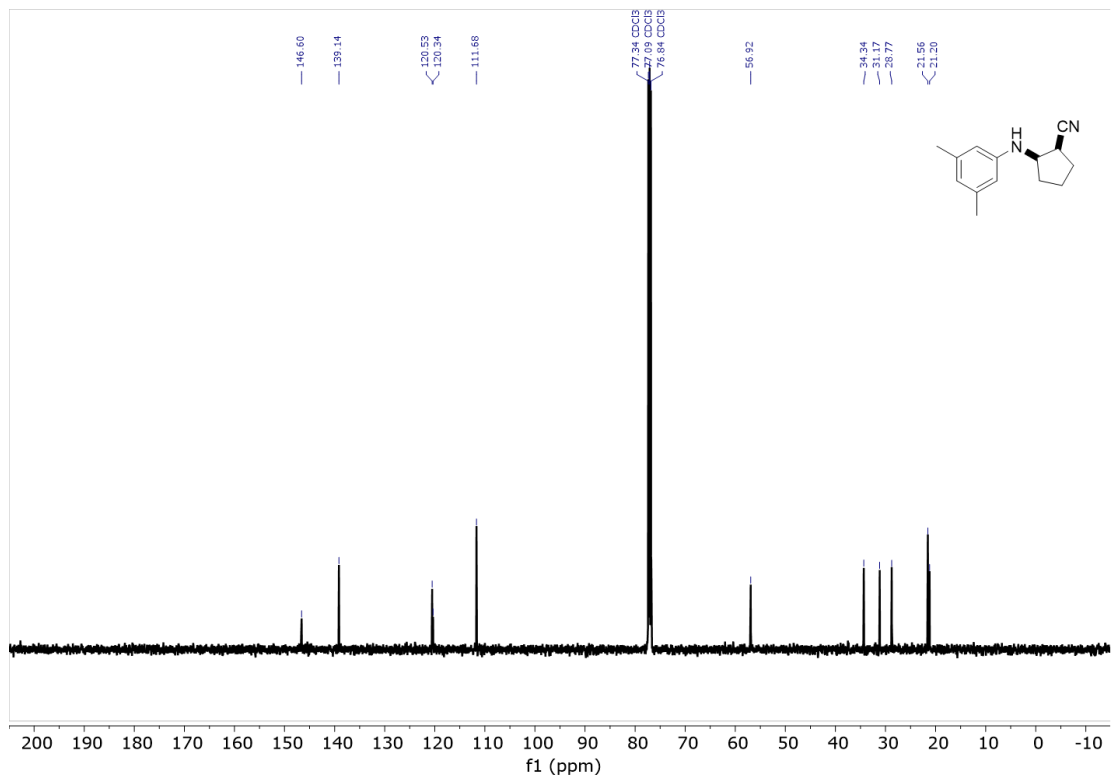
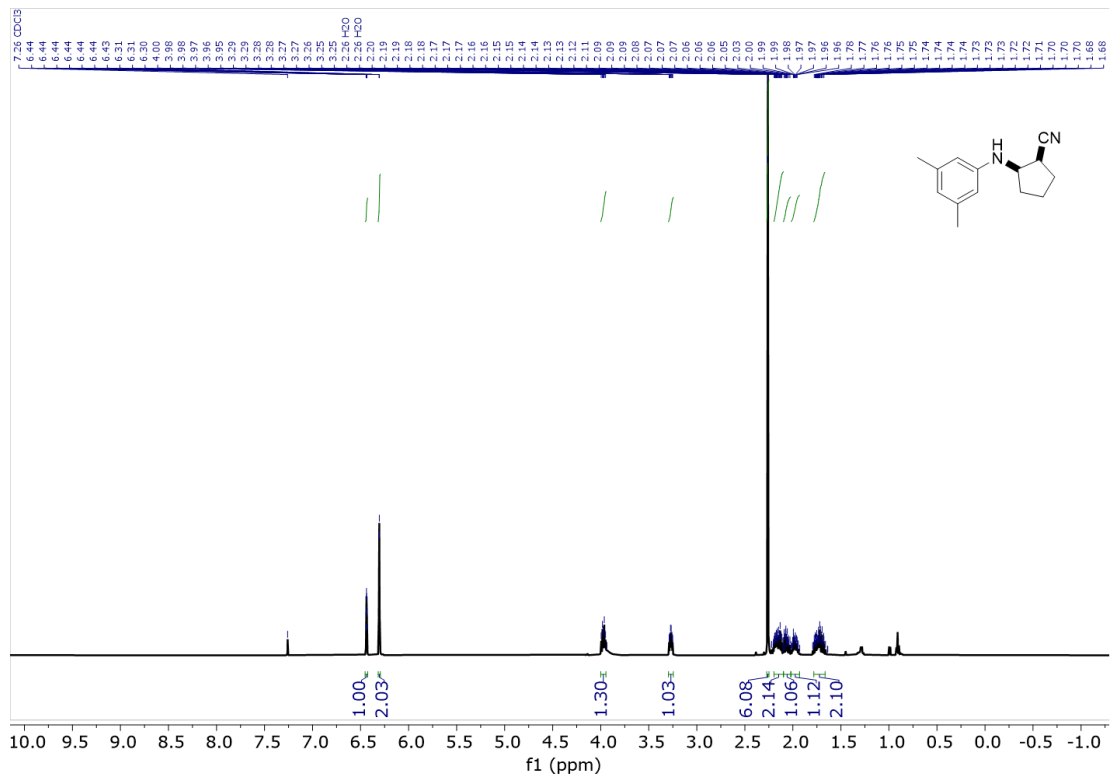


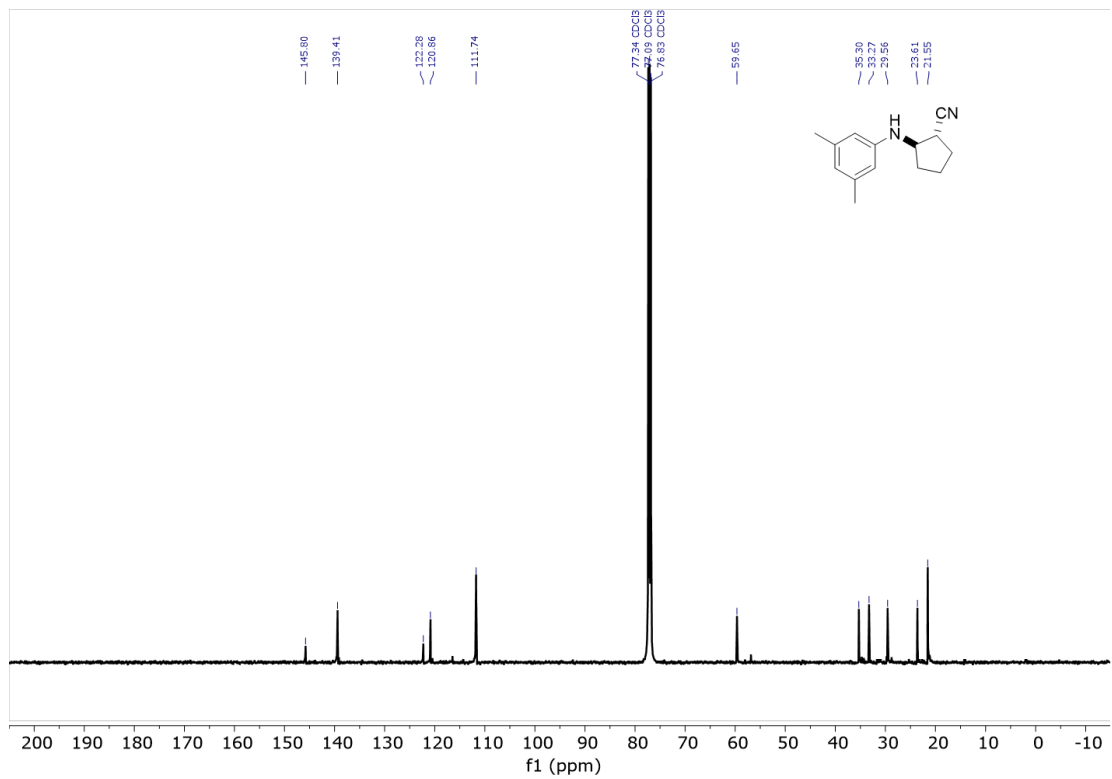
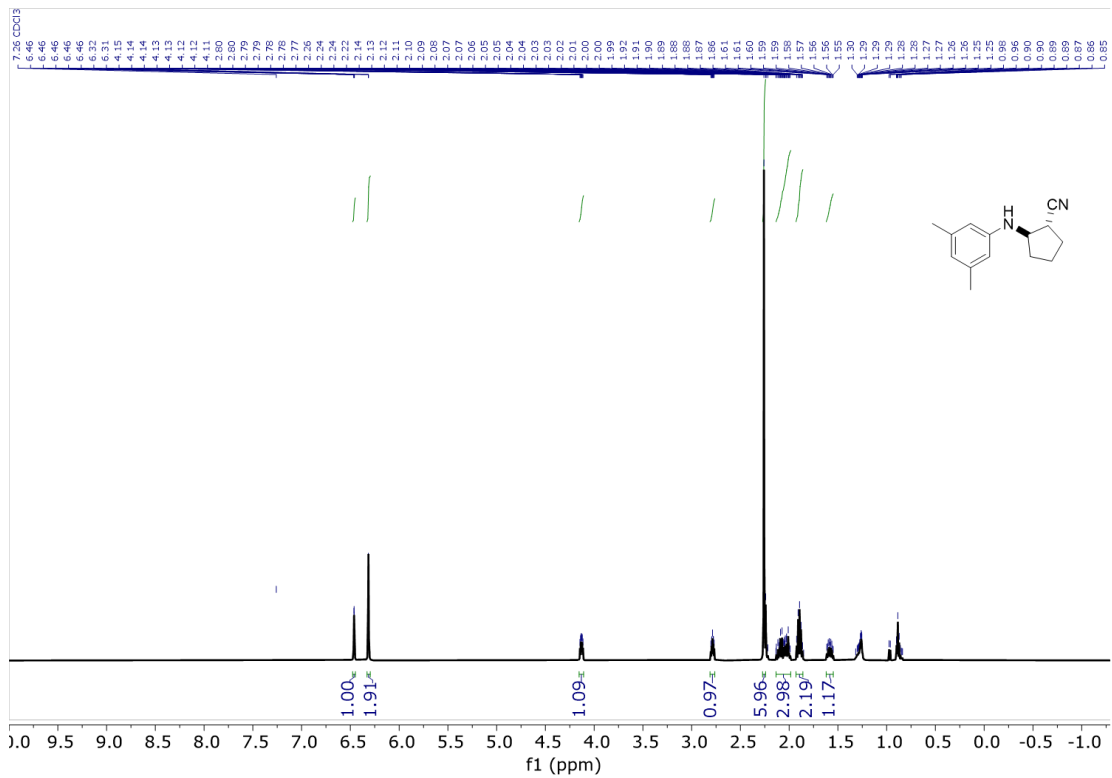
Correlation peak integration is 1735

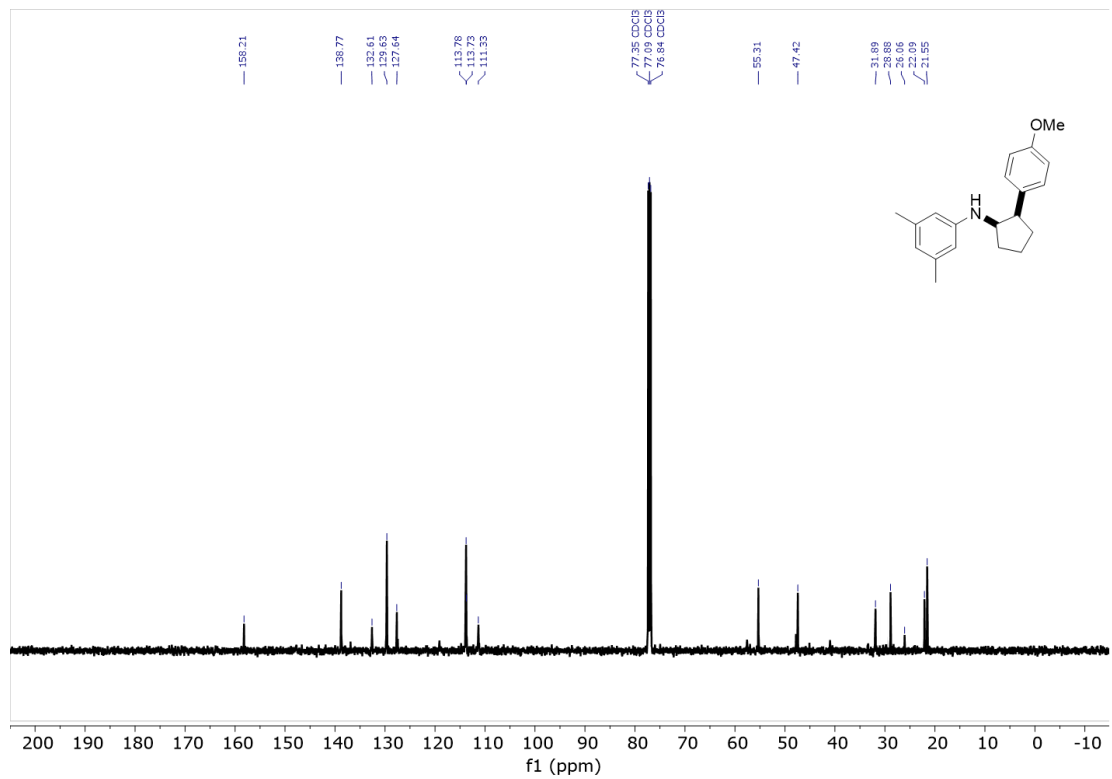
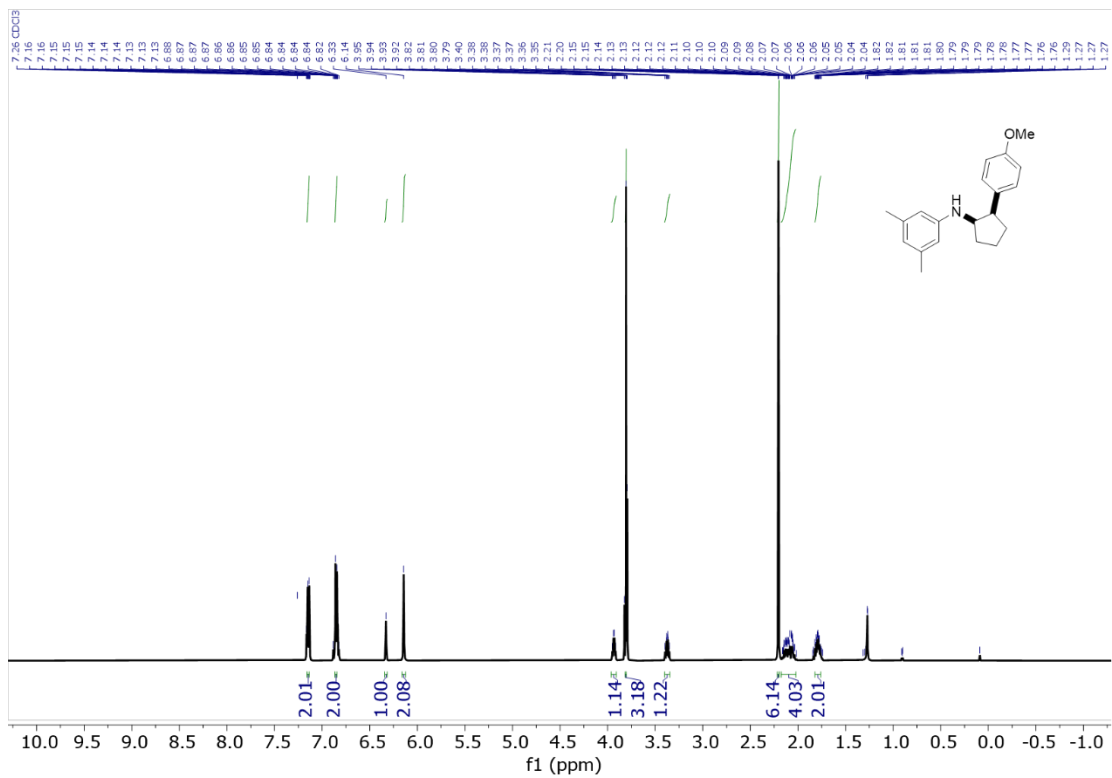


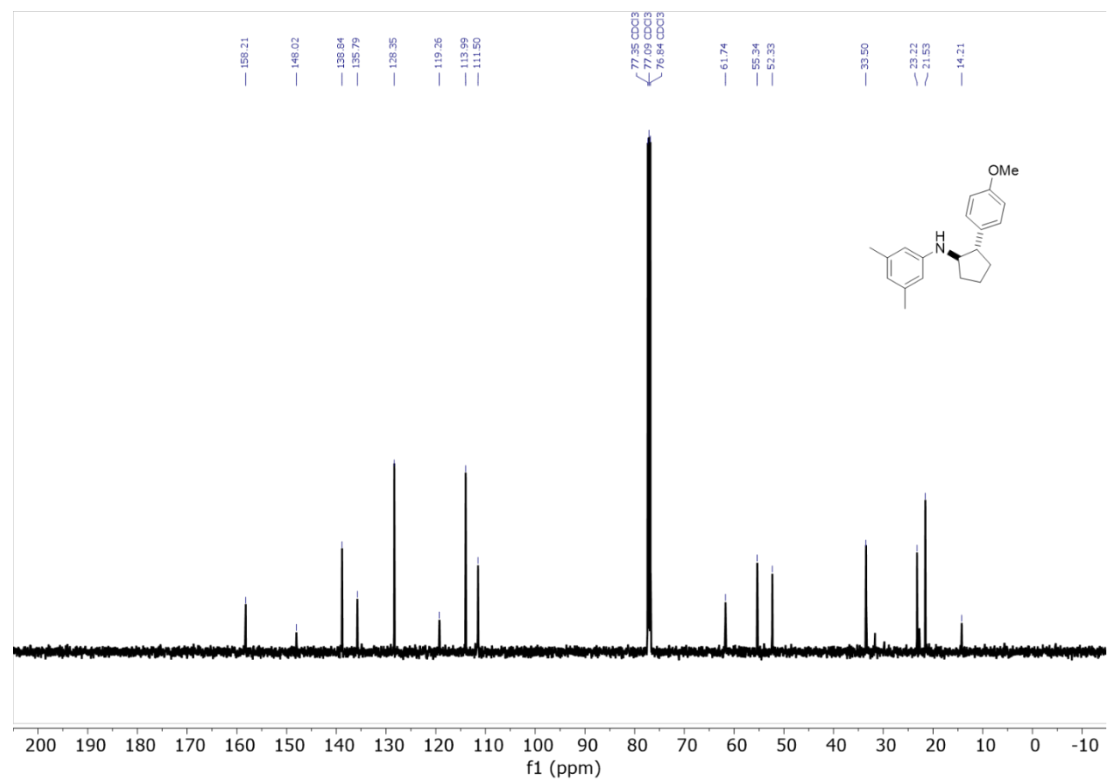
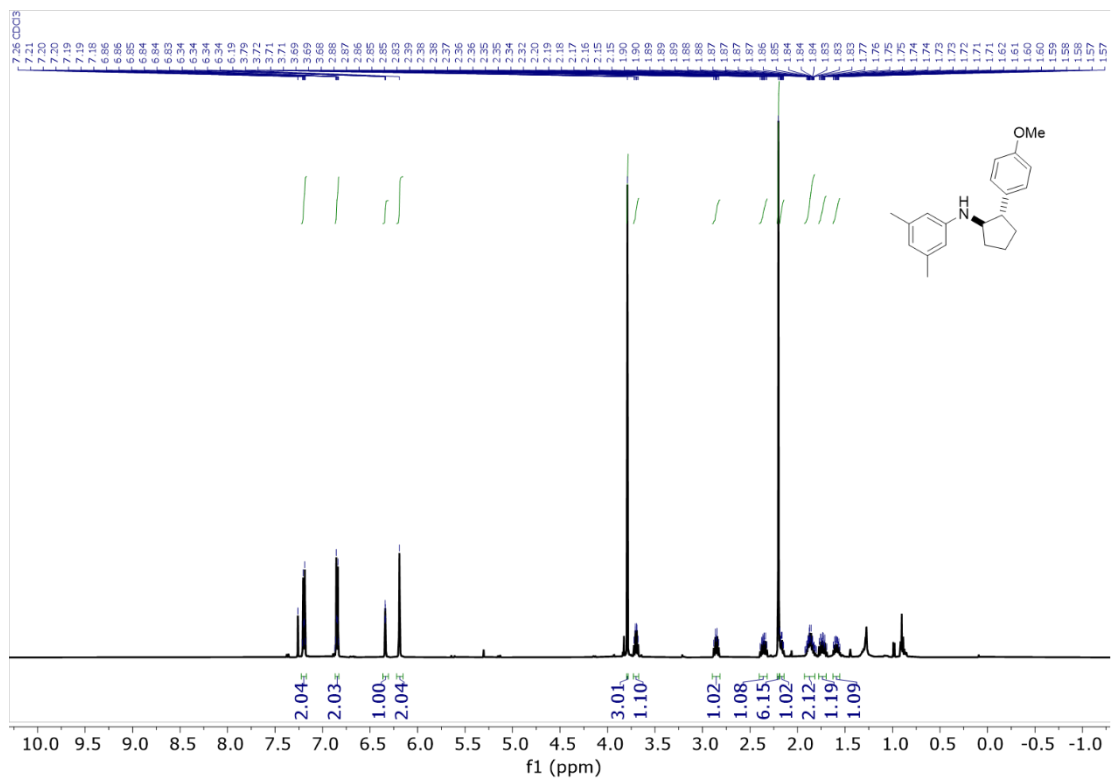


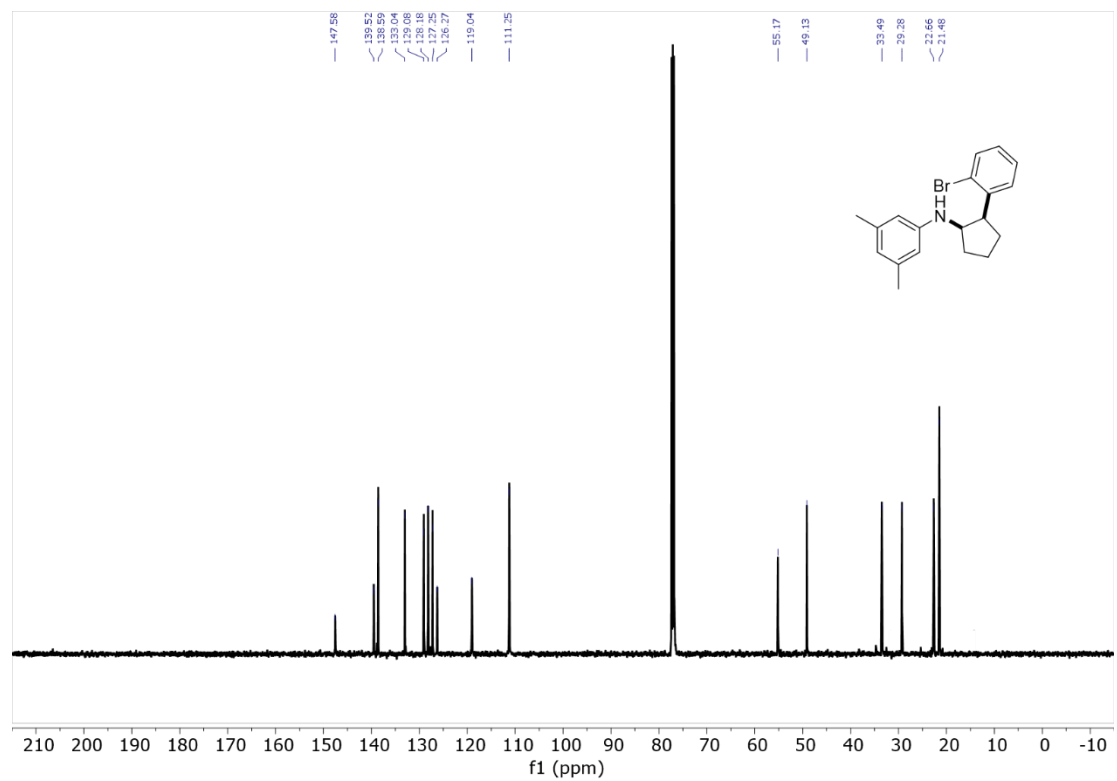
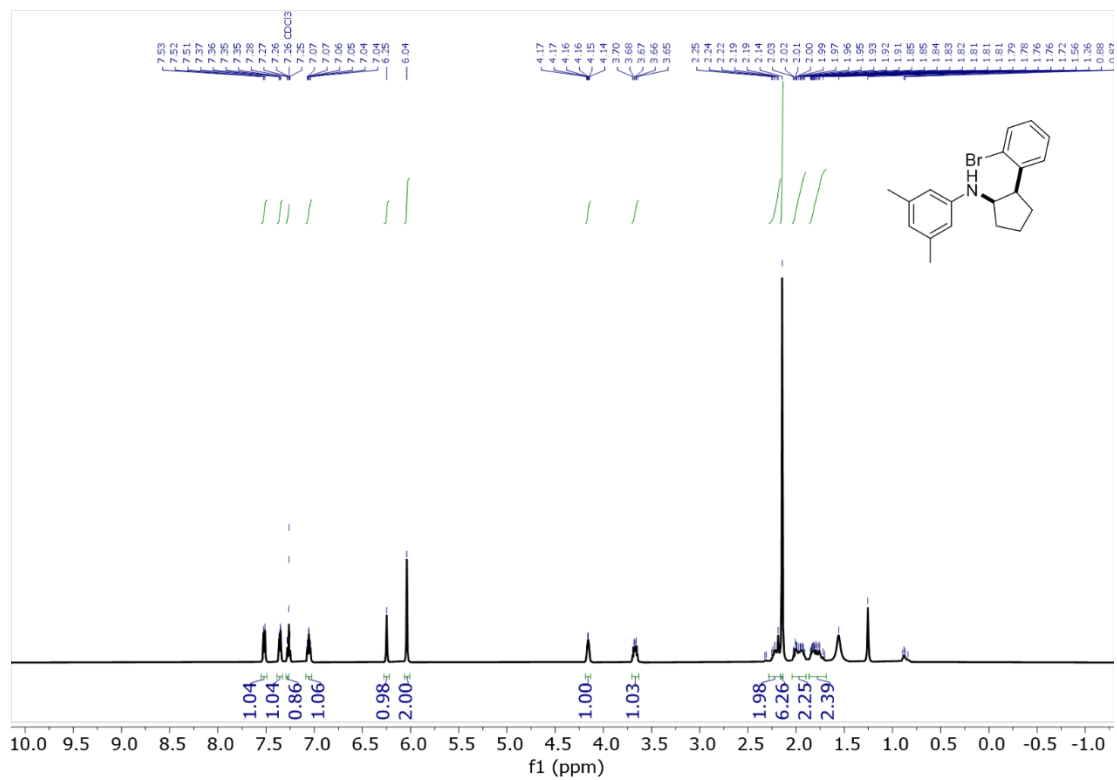
Correlation peak integration is 157

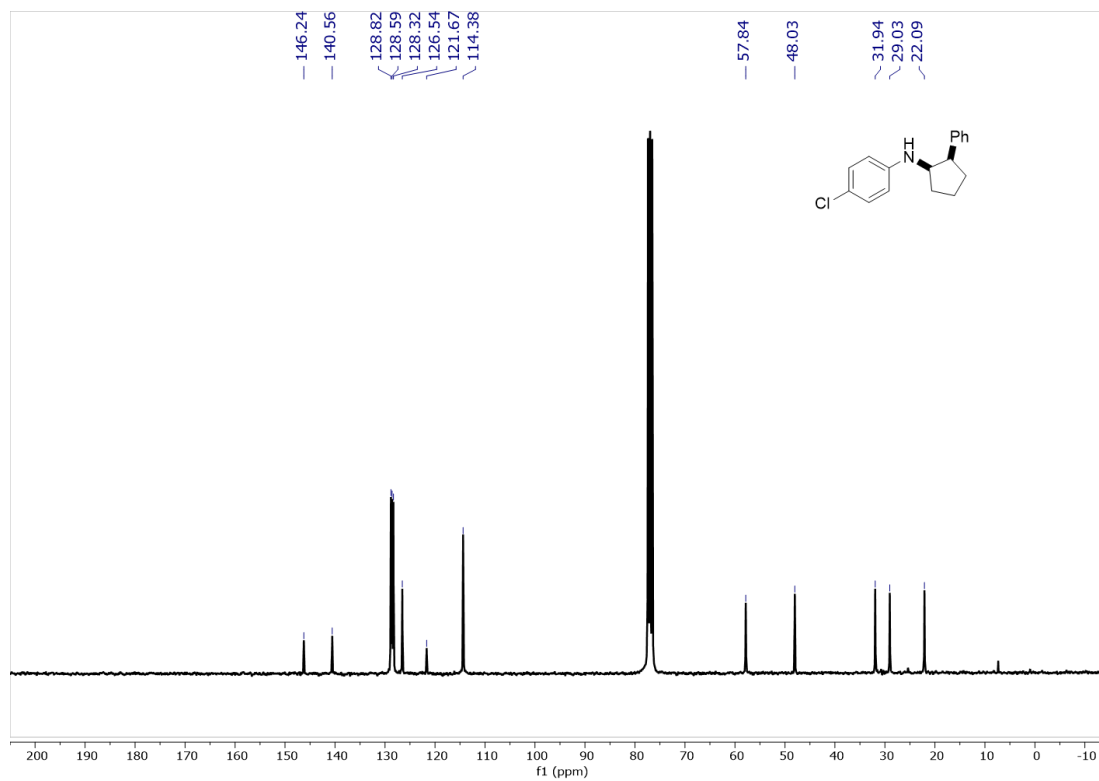
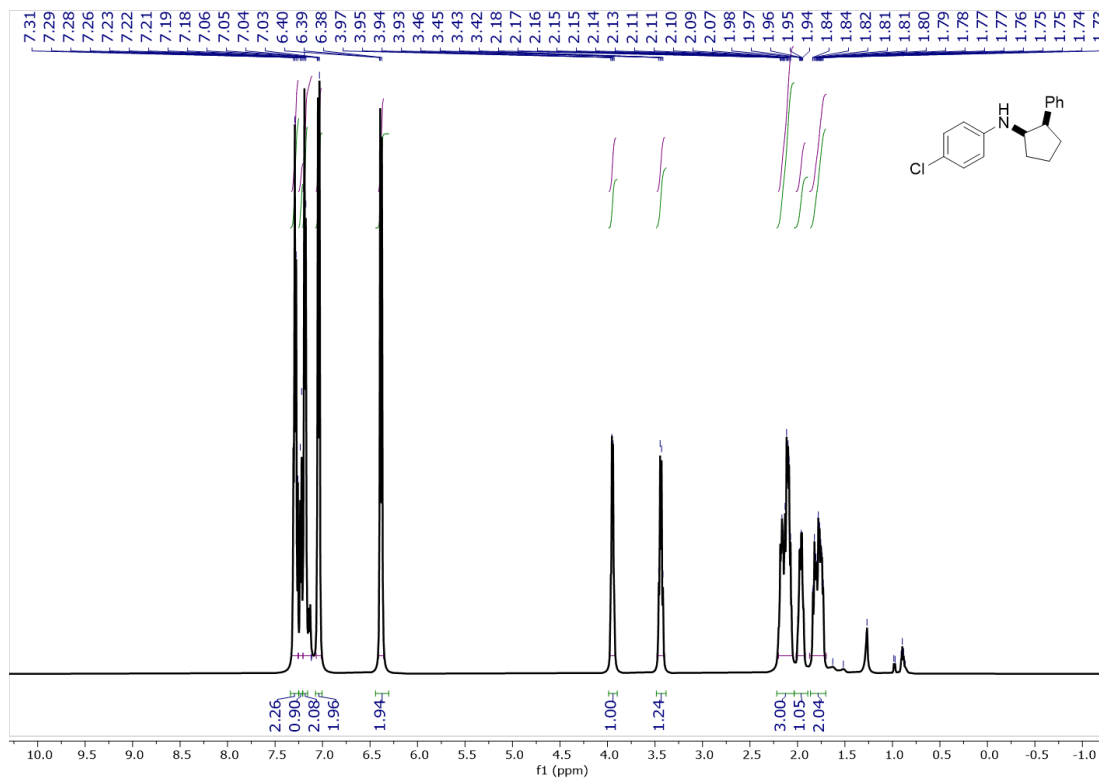


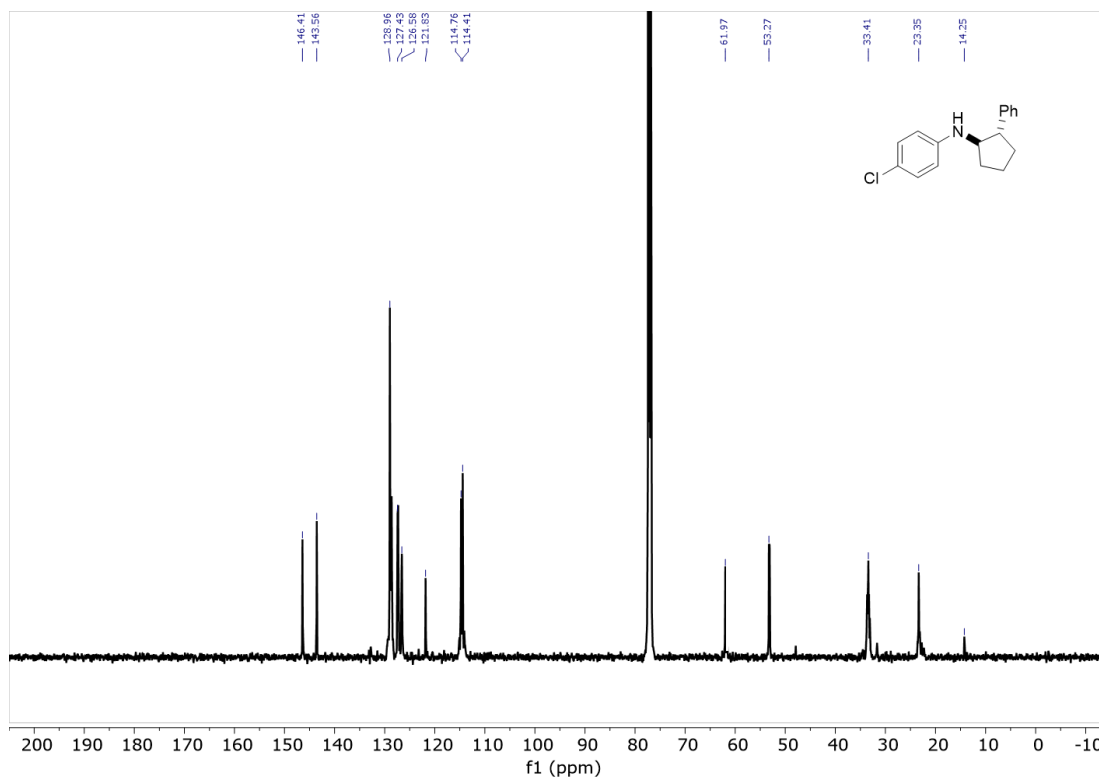
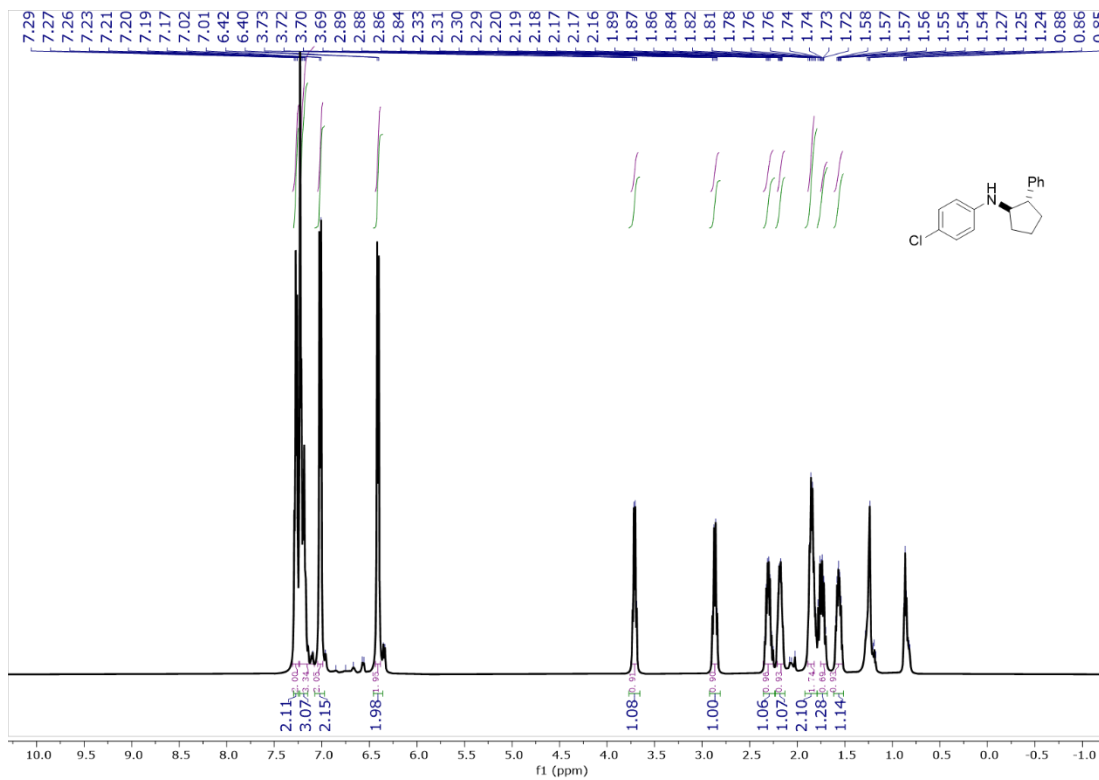


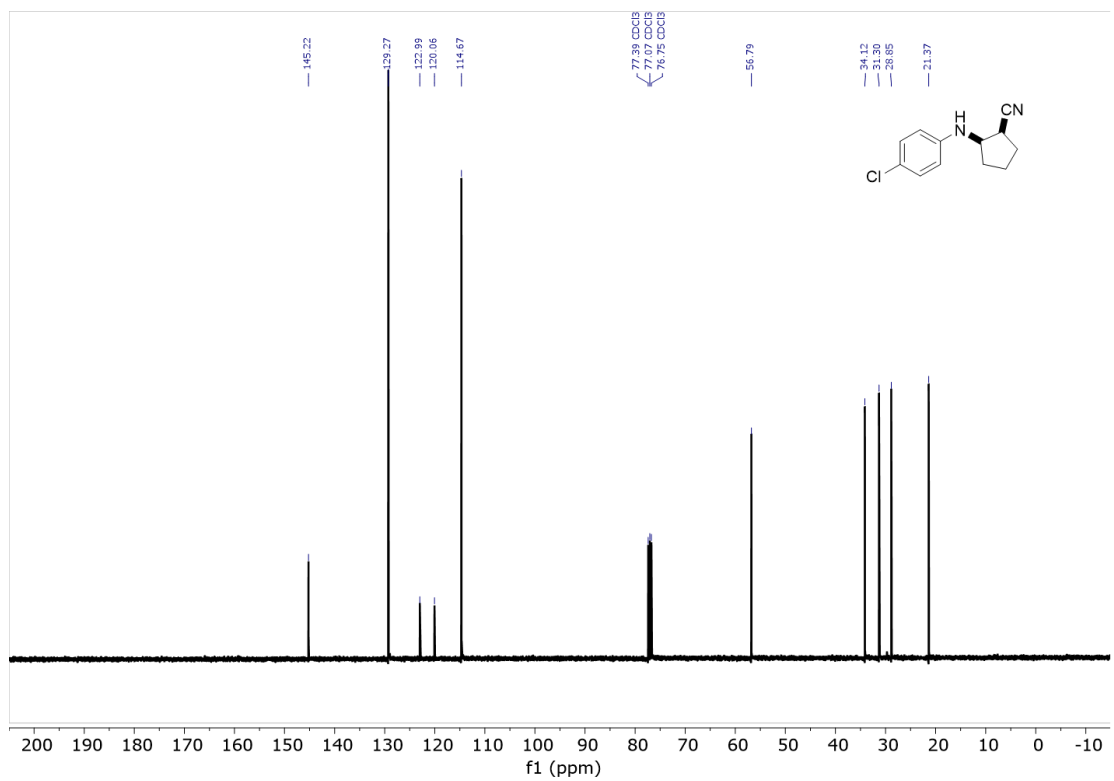
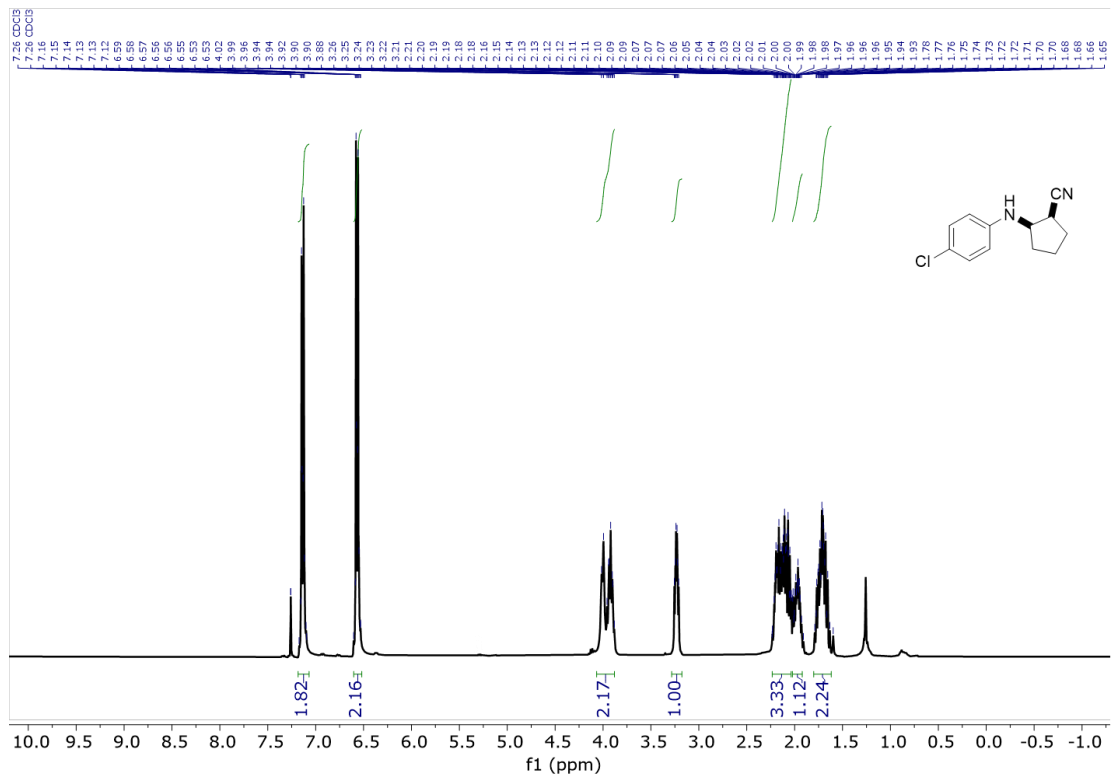


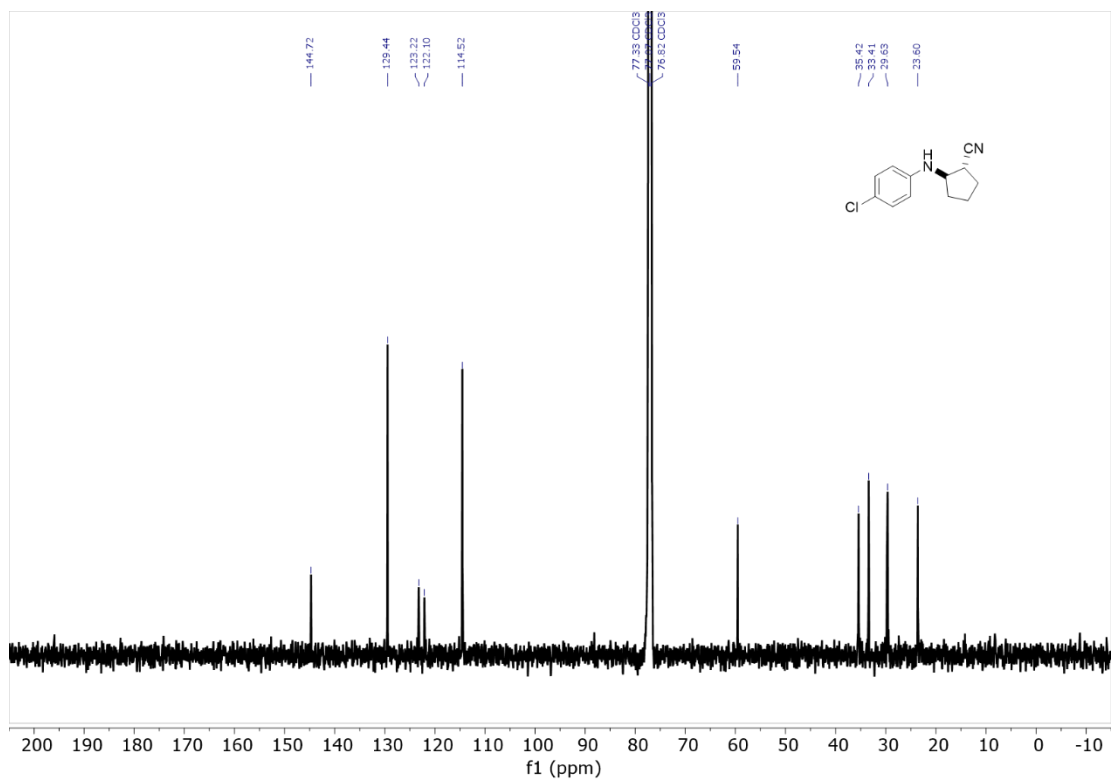
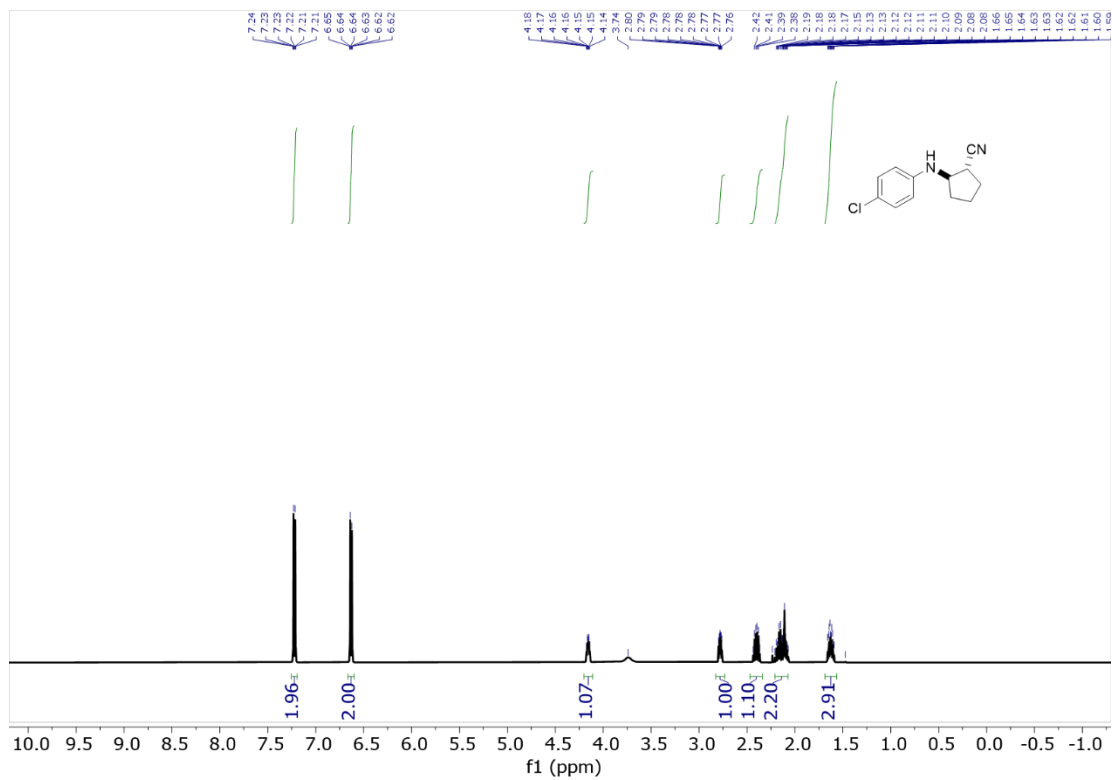


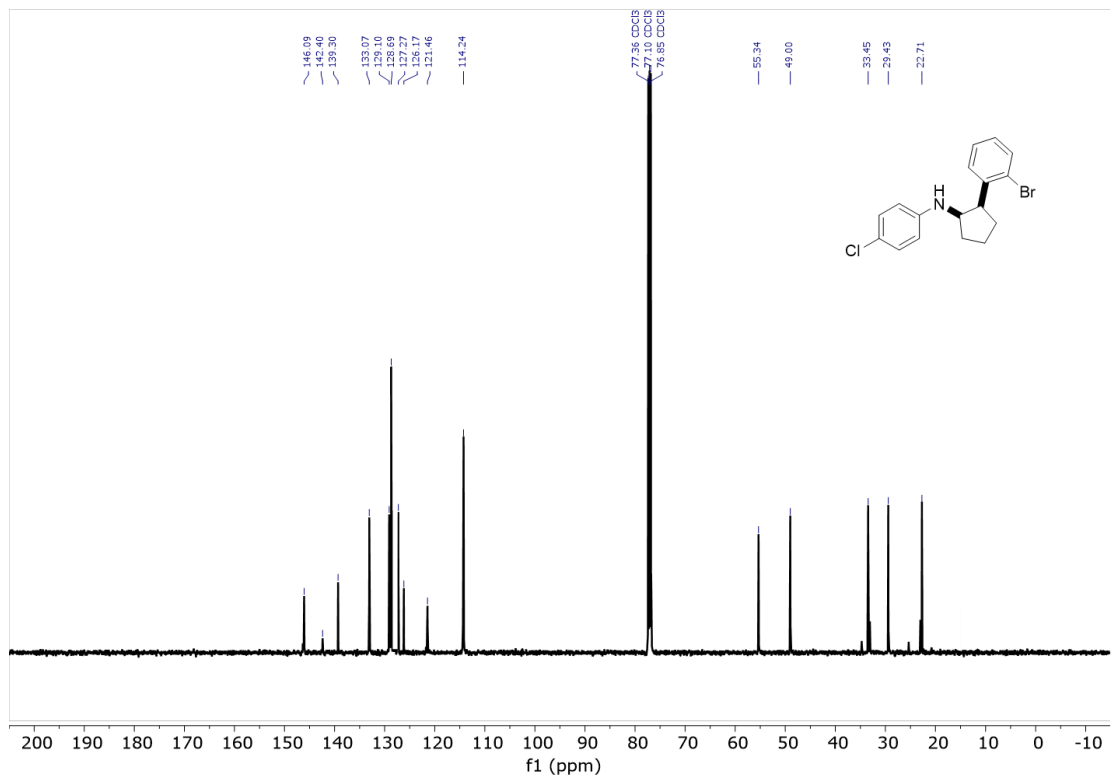
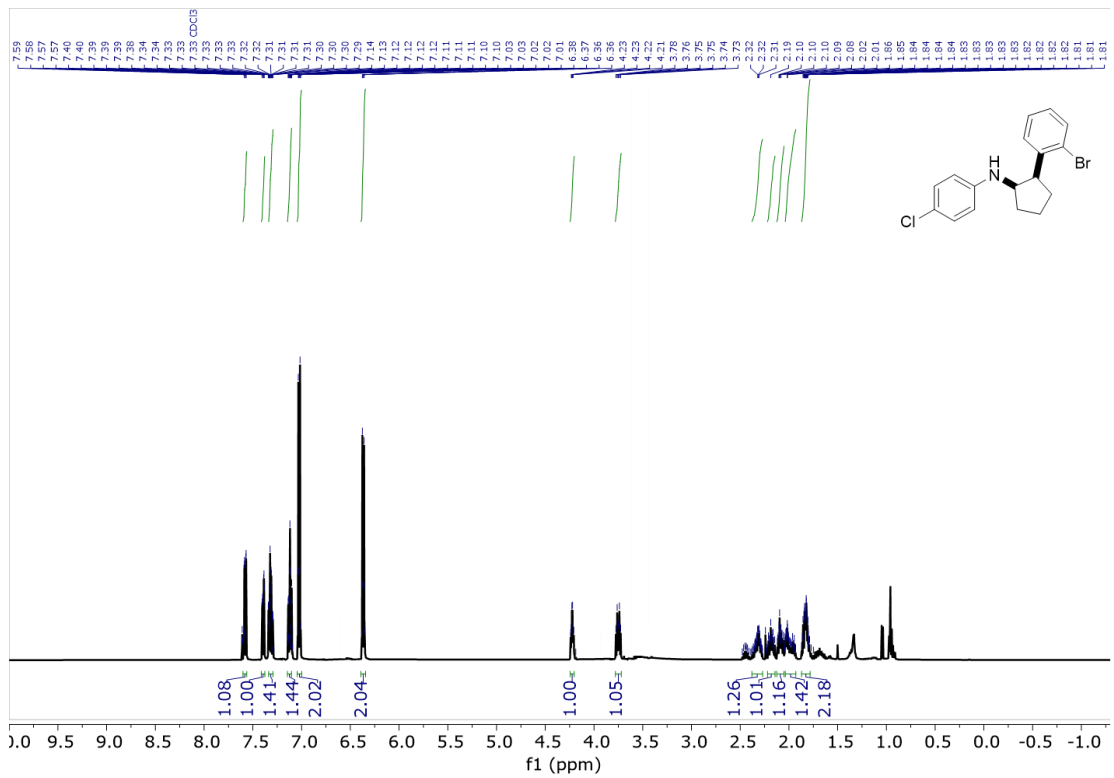


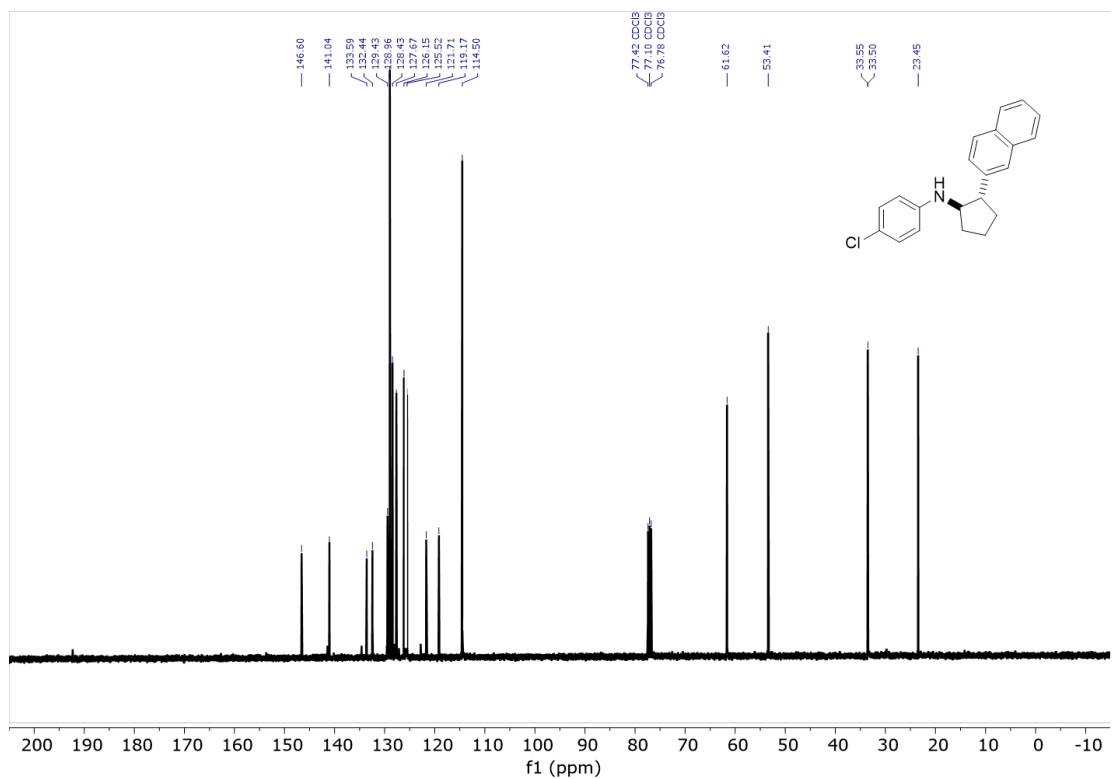
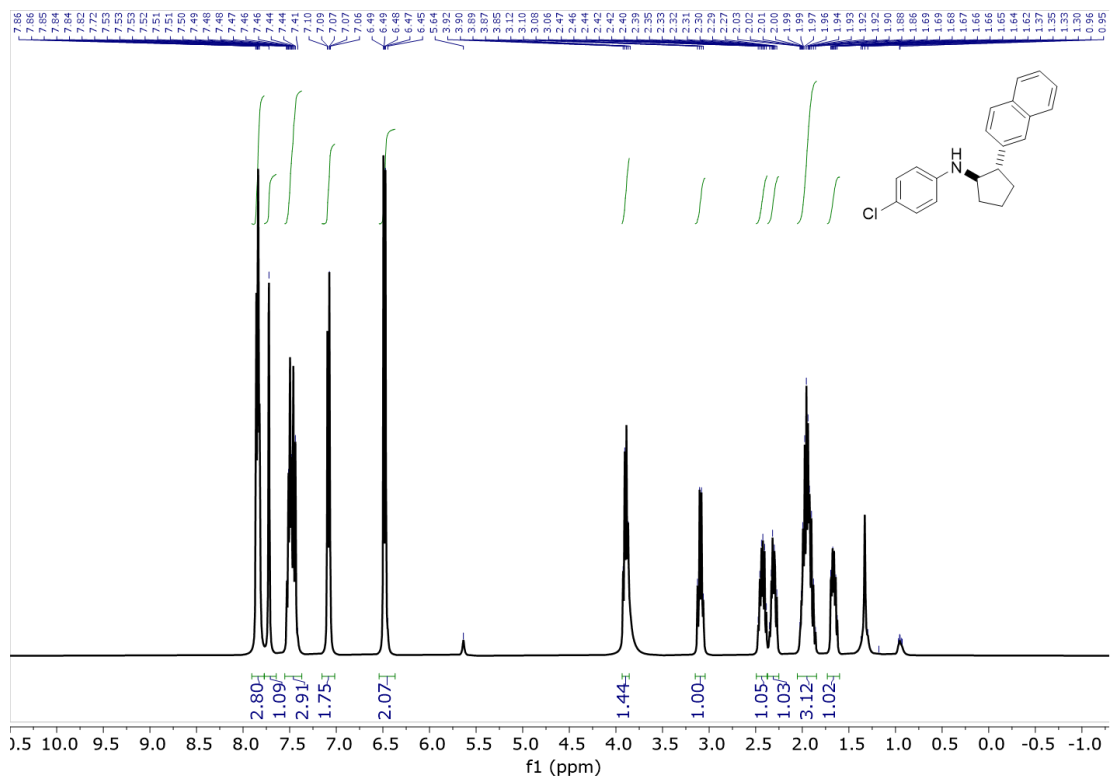


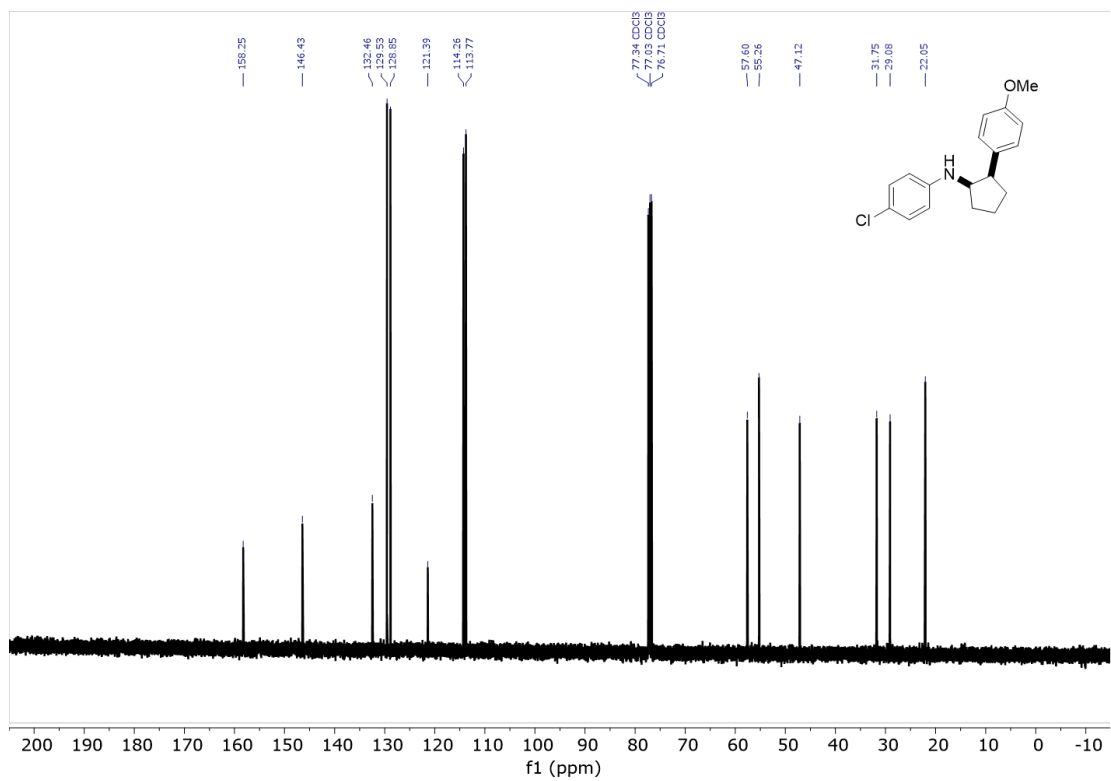
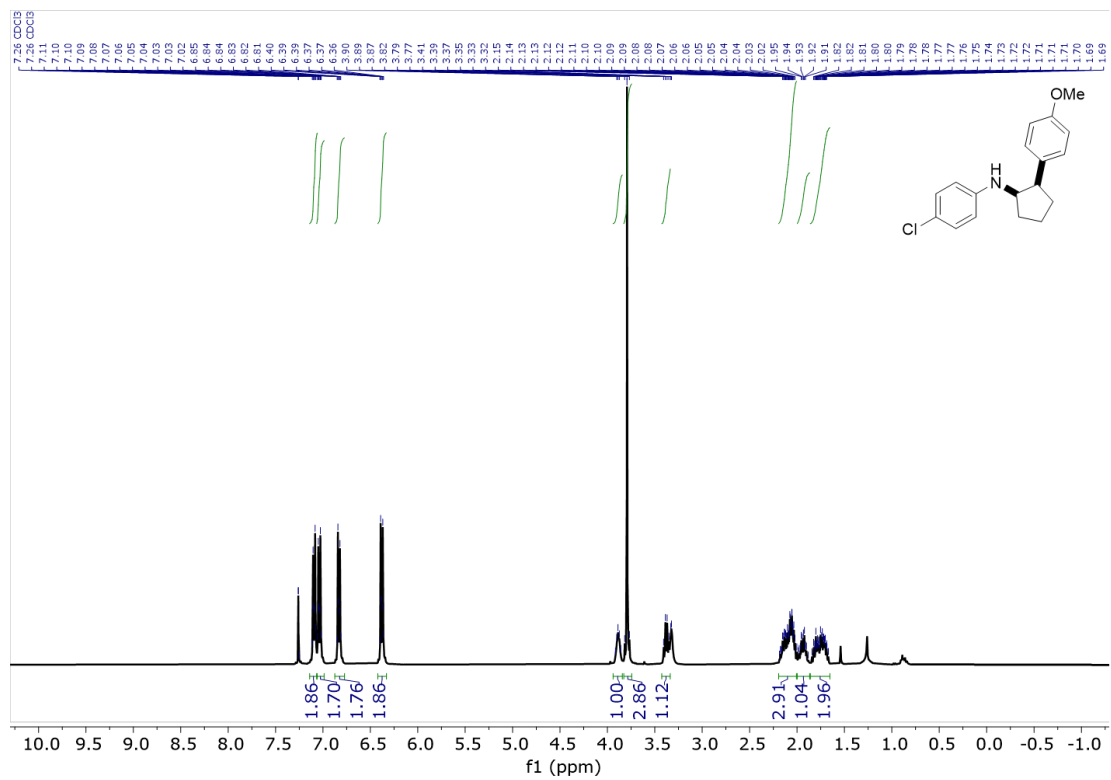


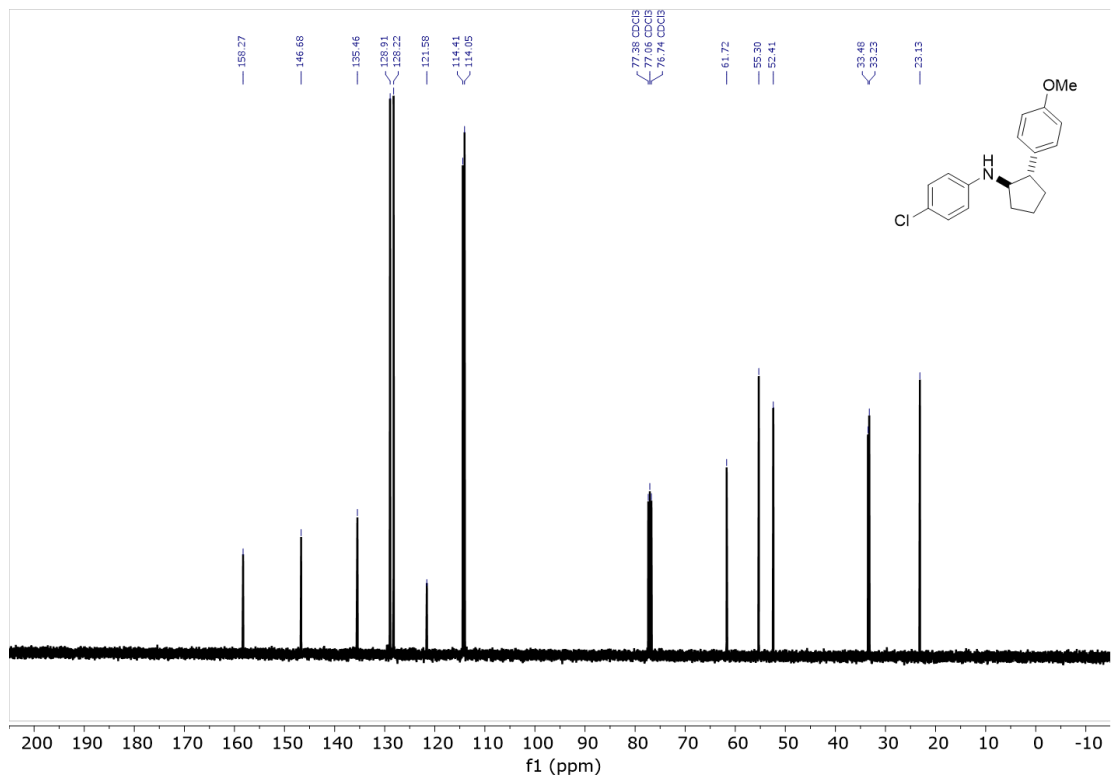
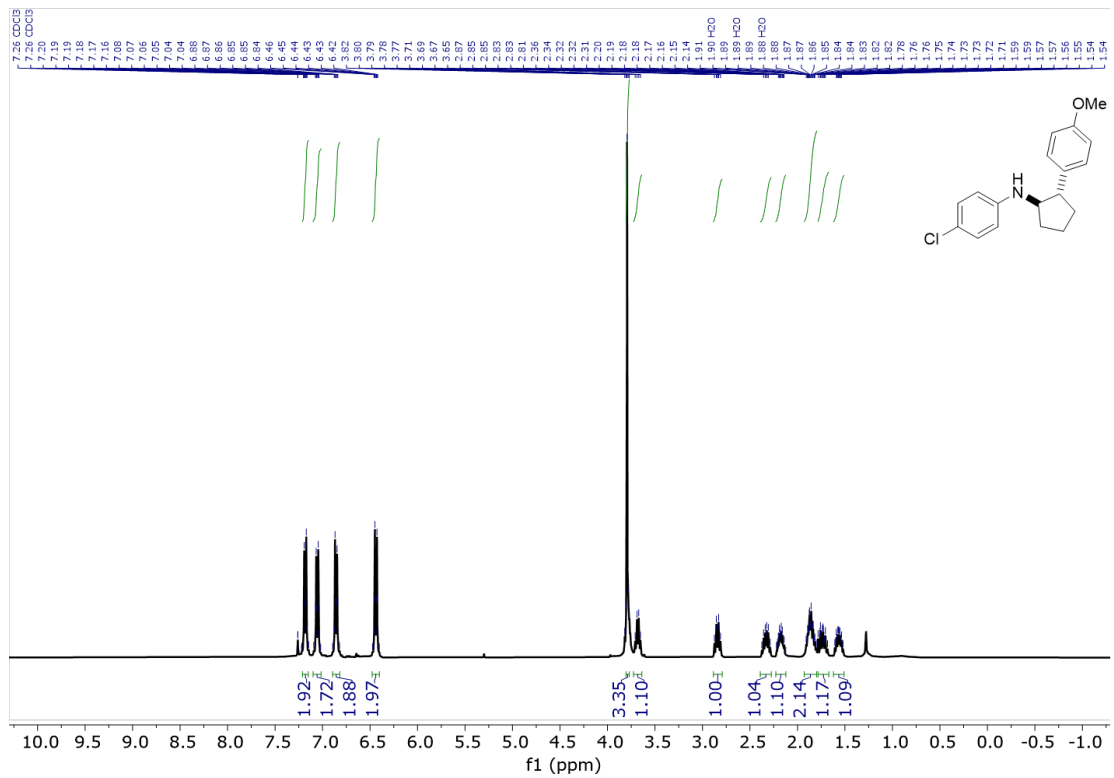


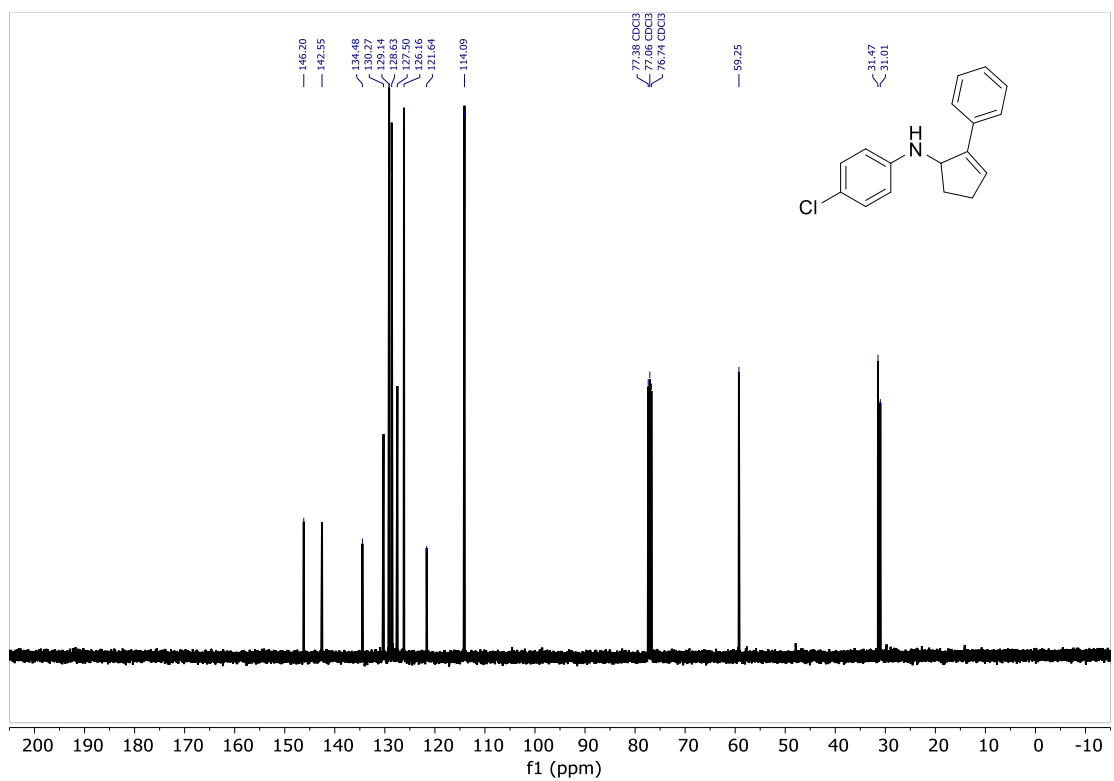
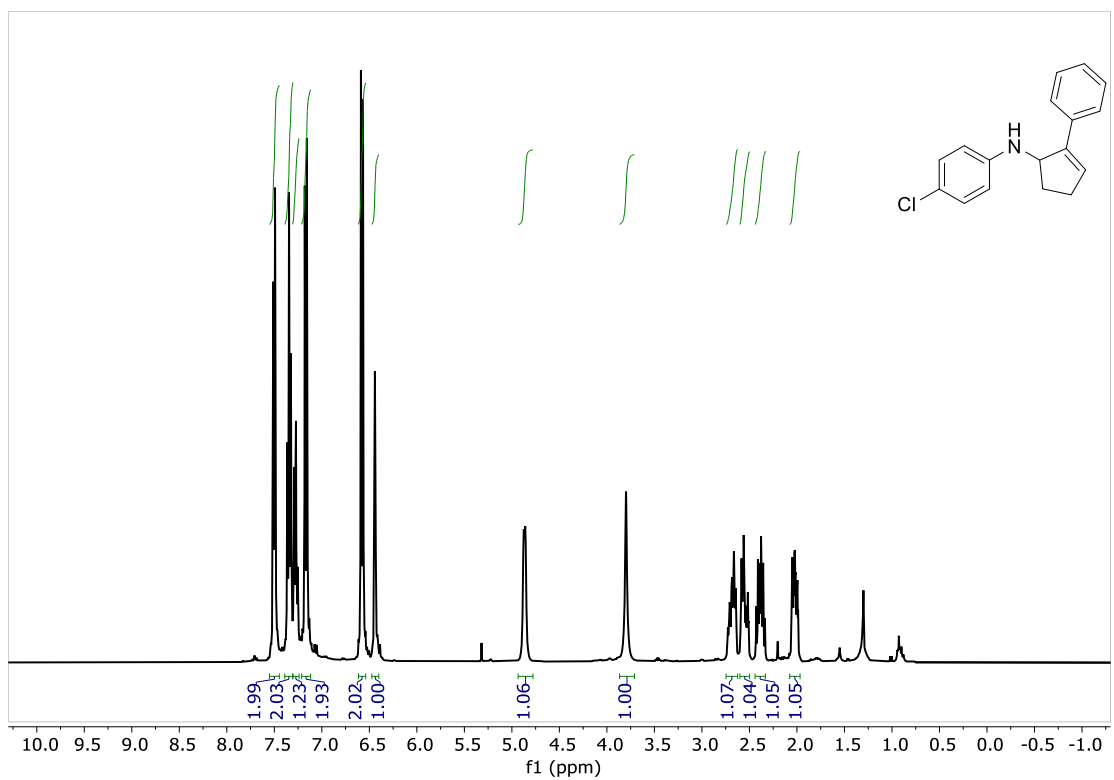


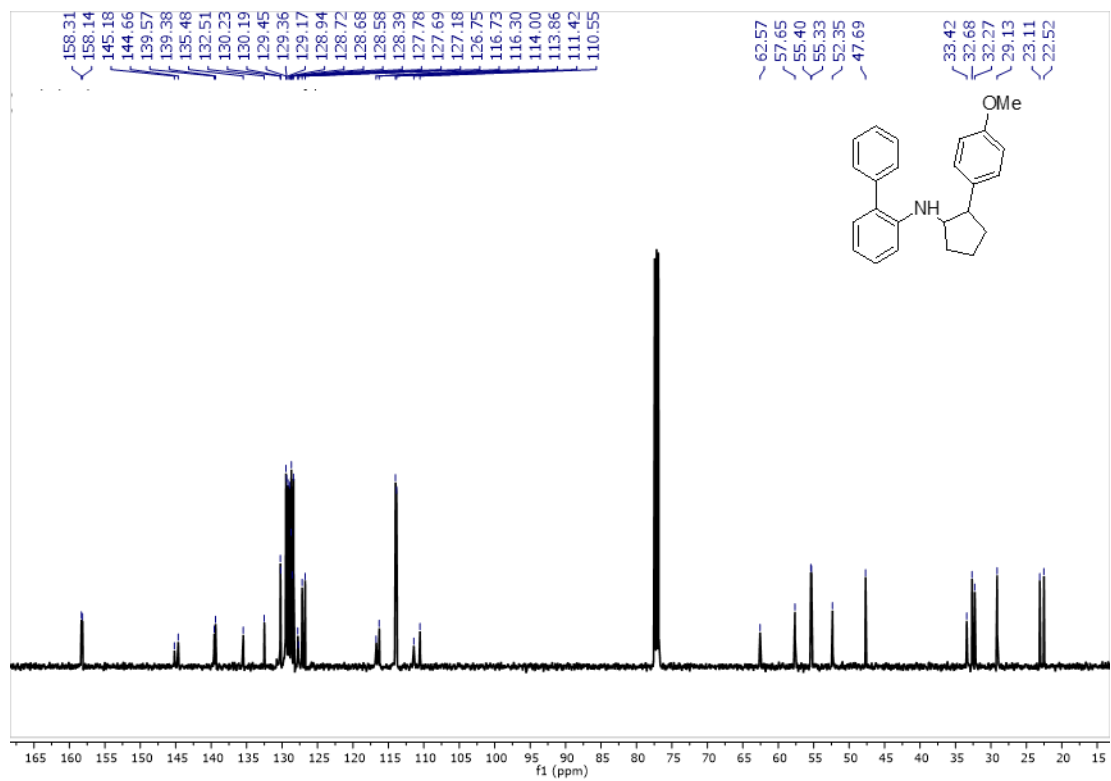
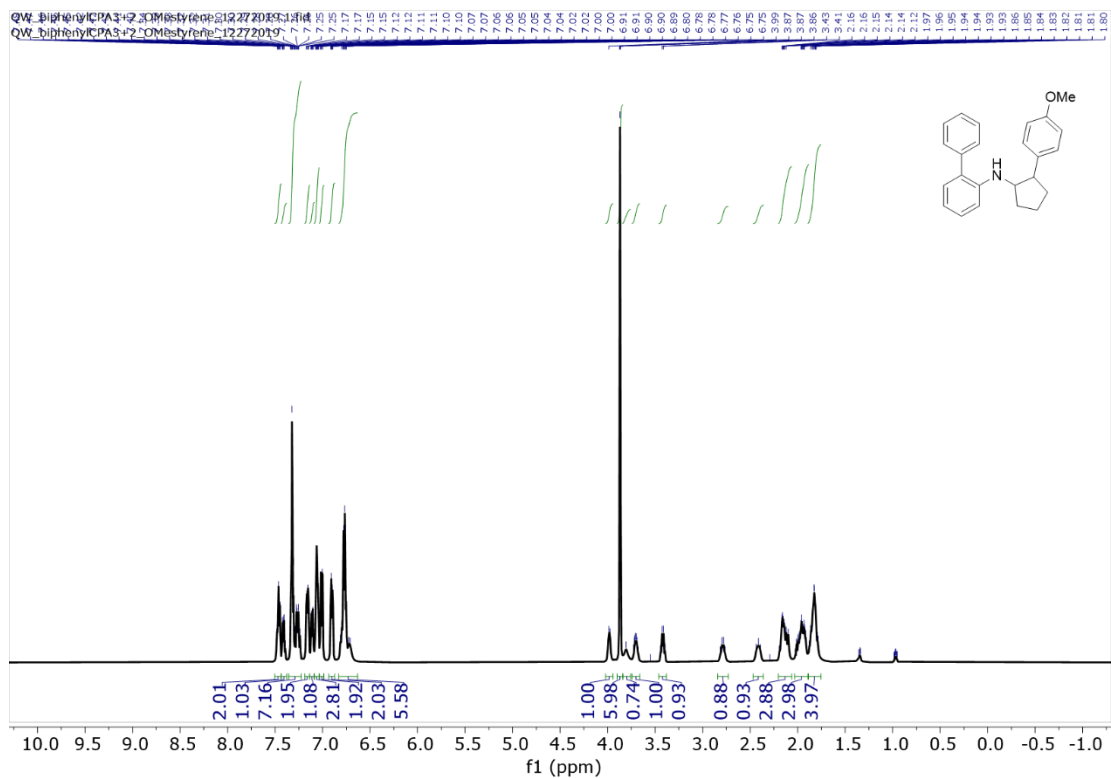


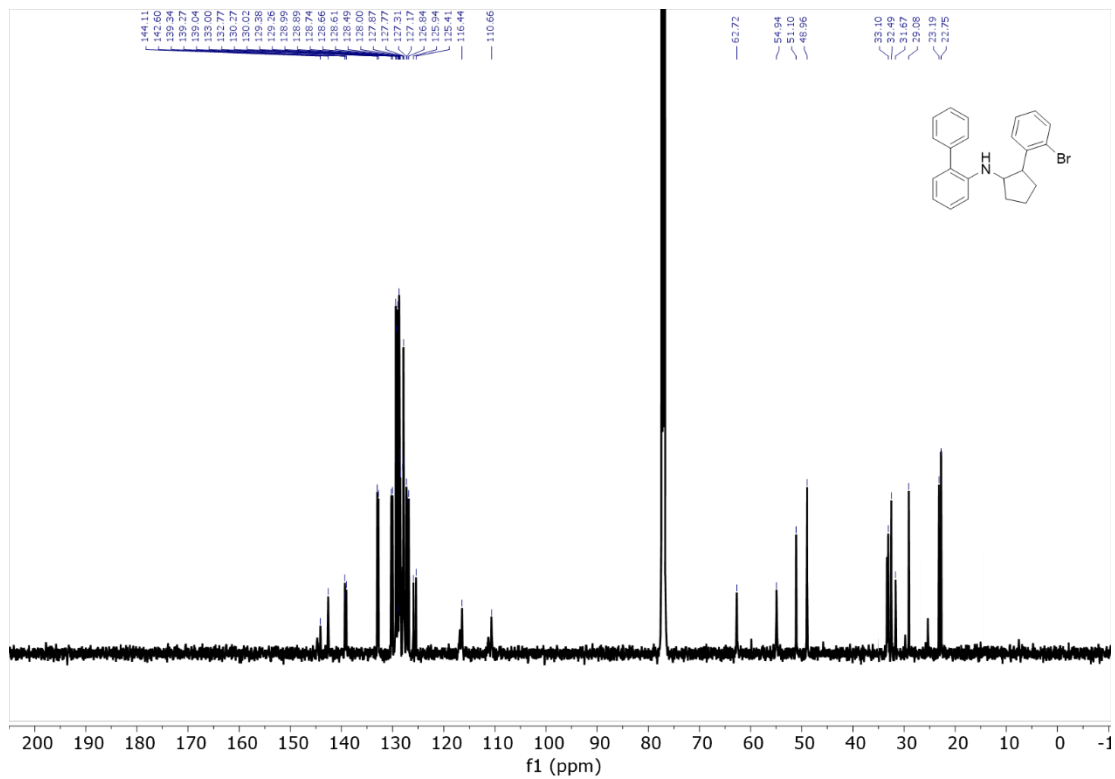
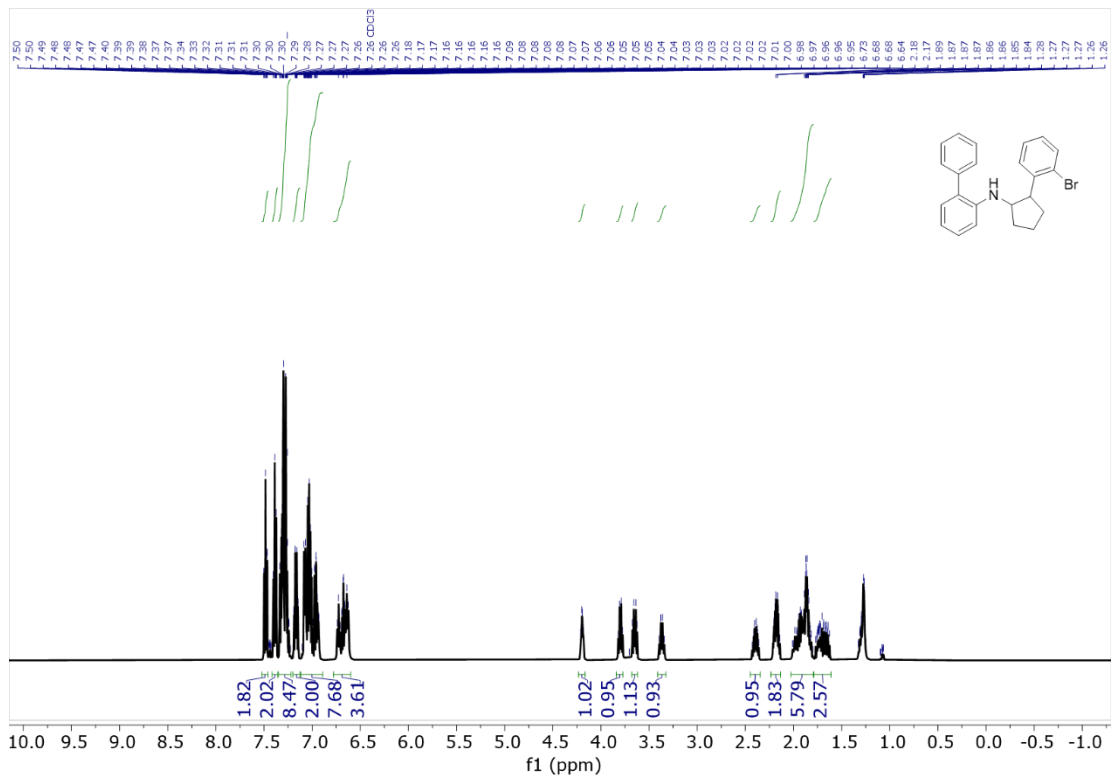


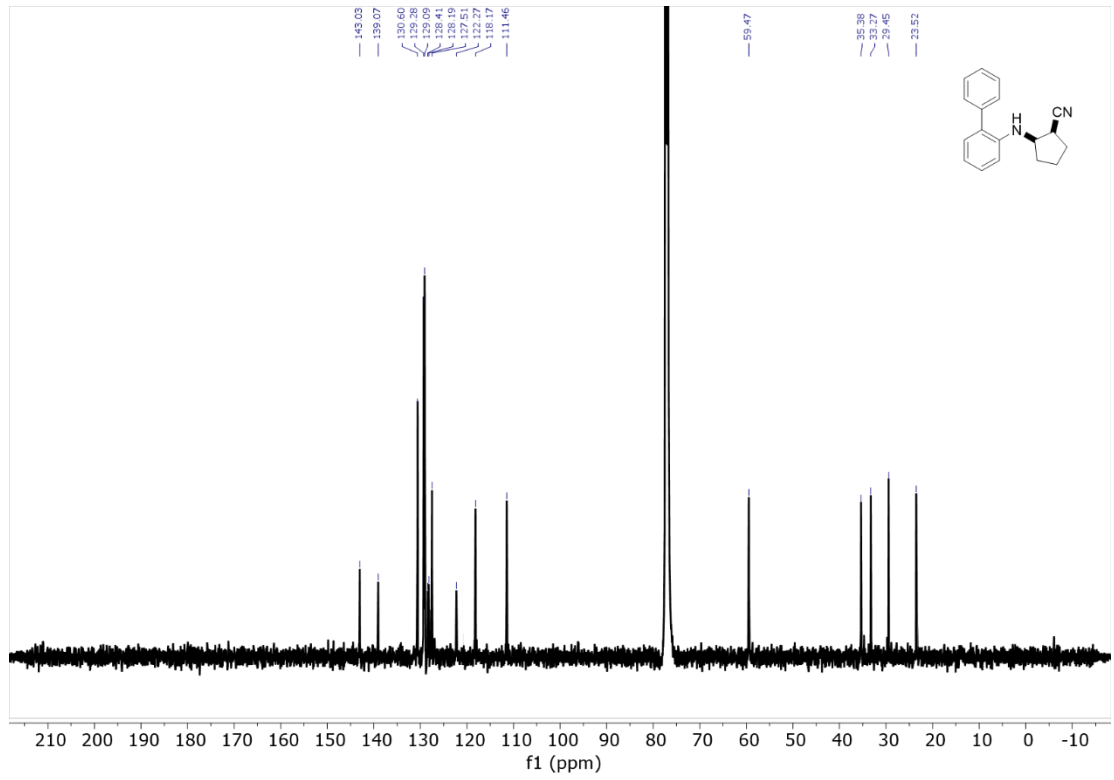
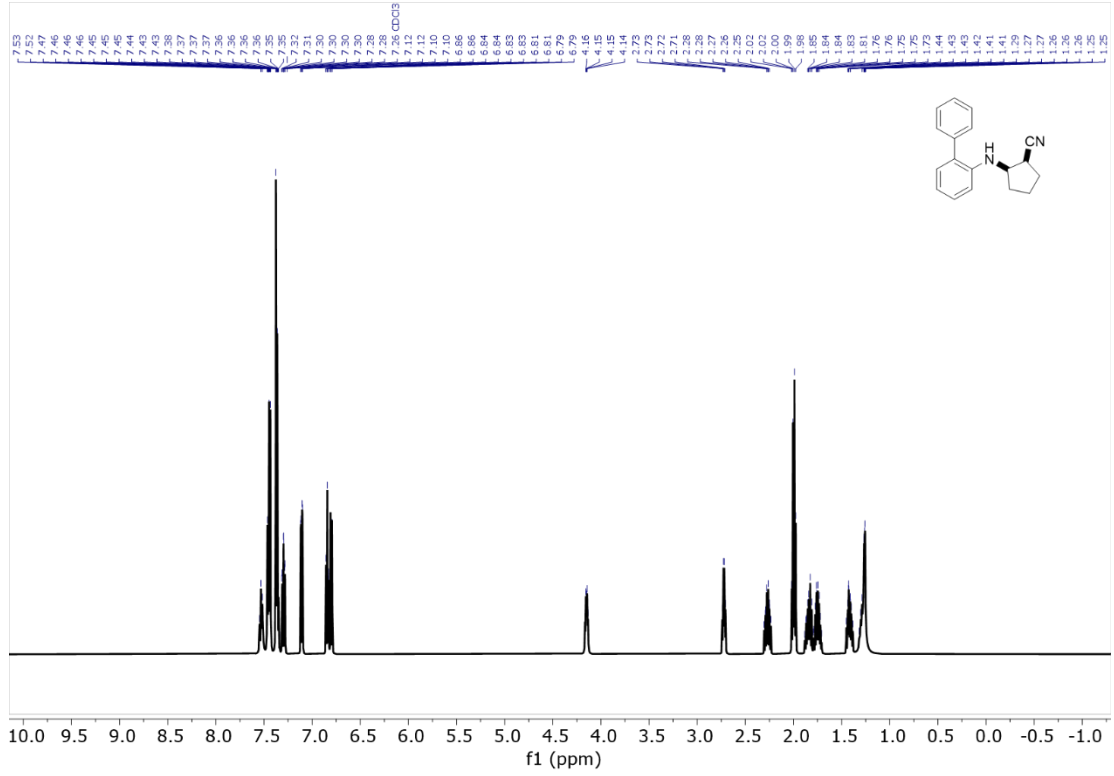


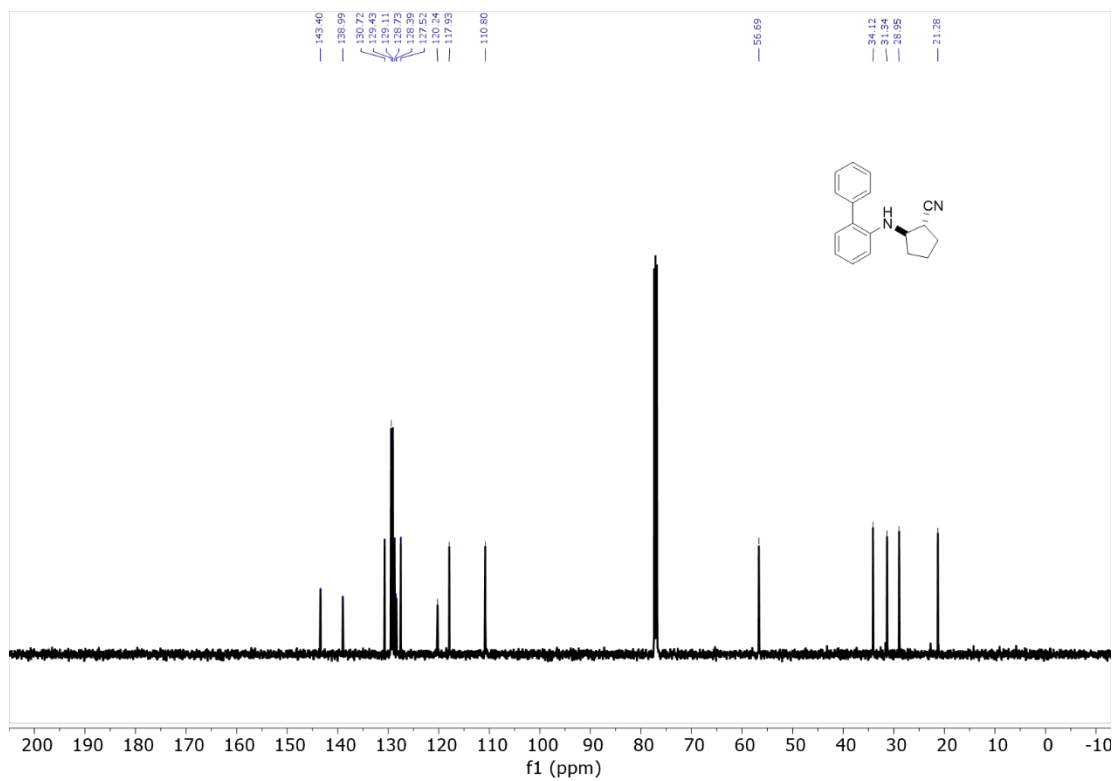
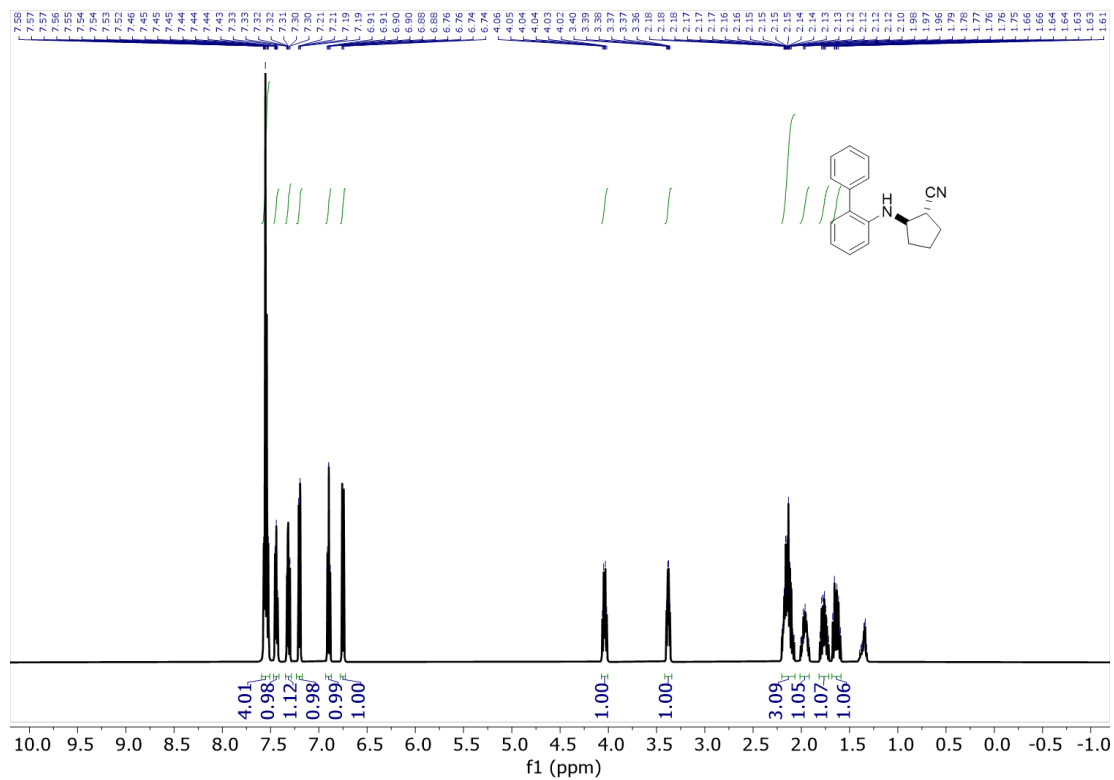


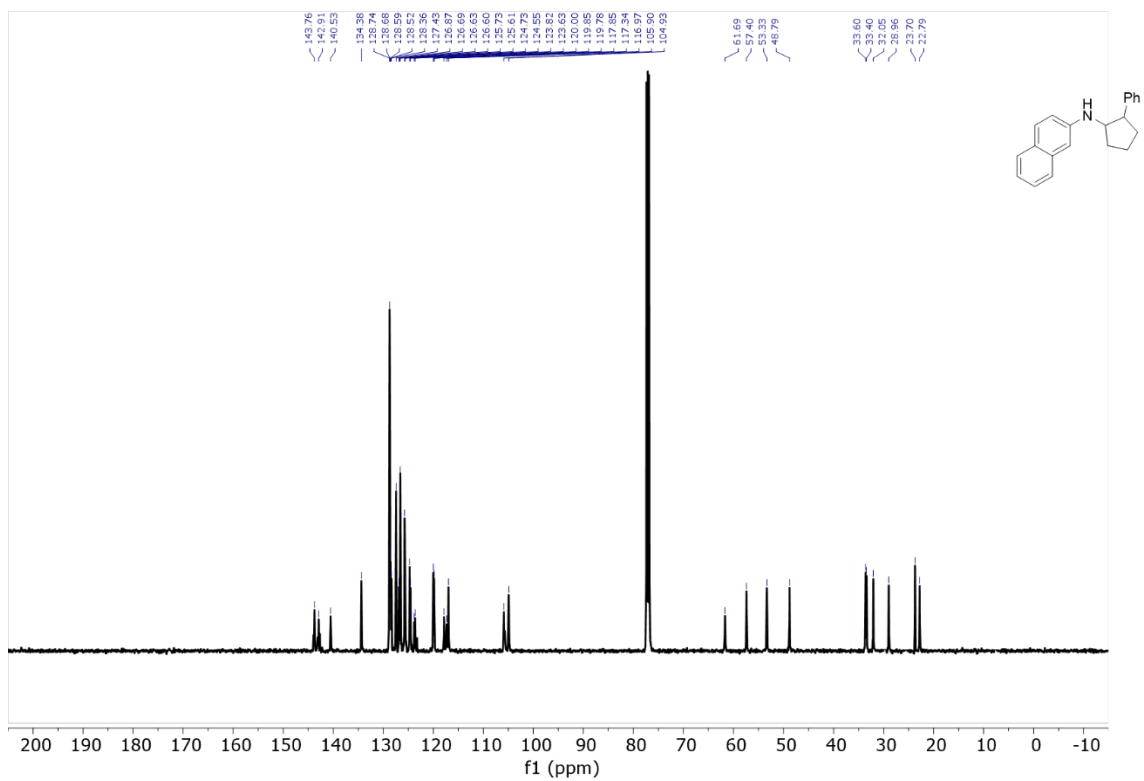
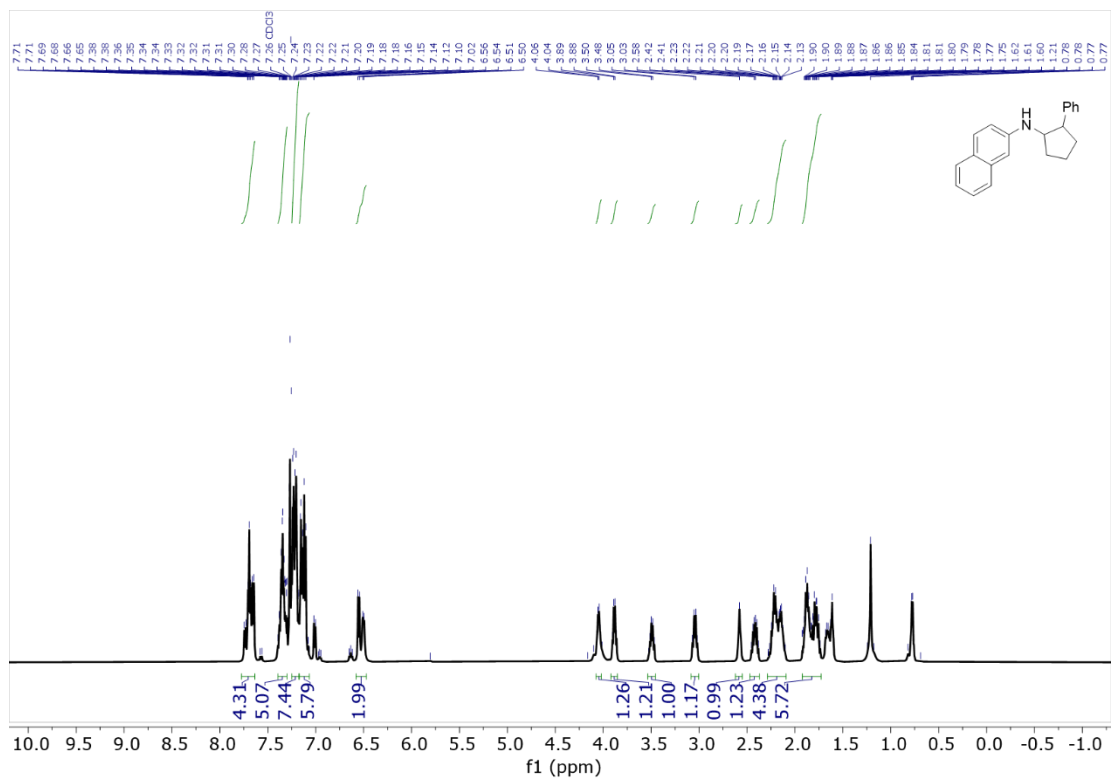


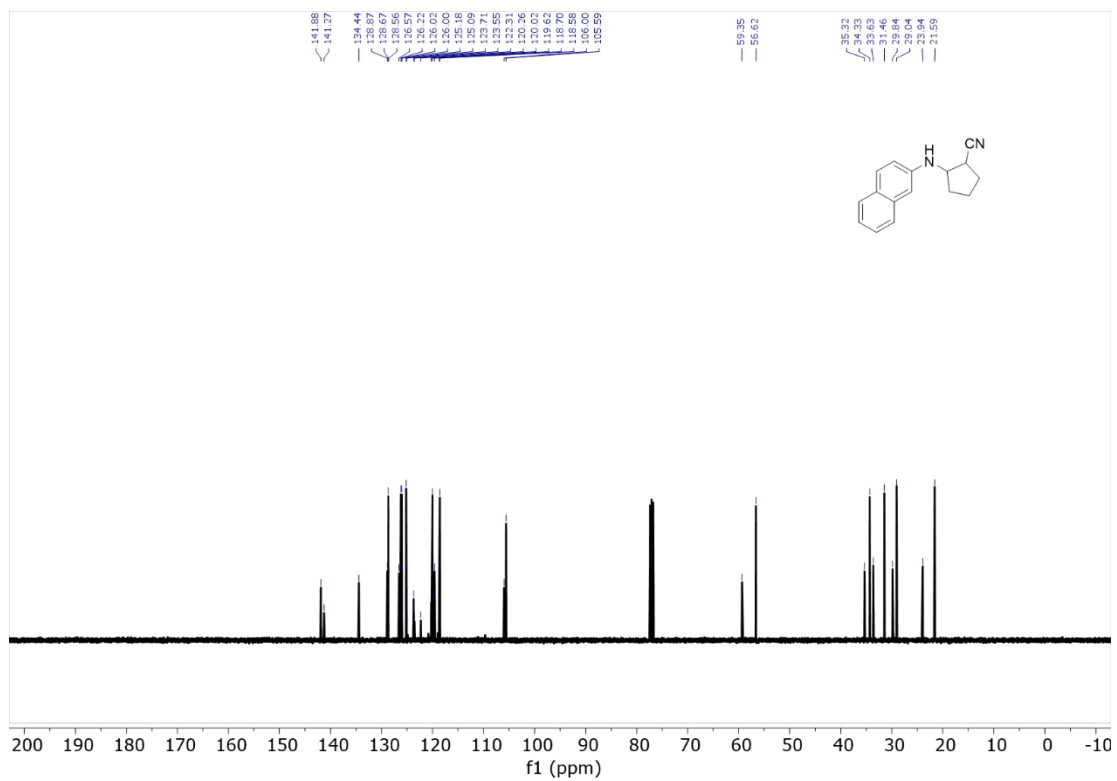
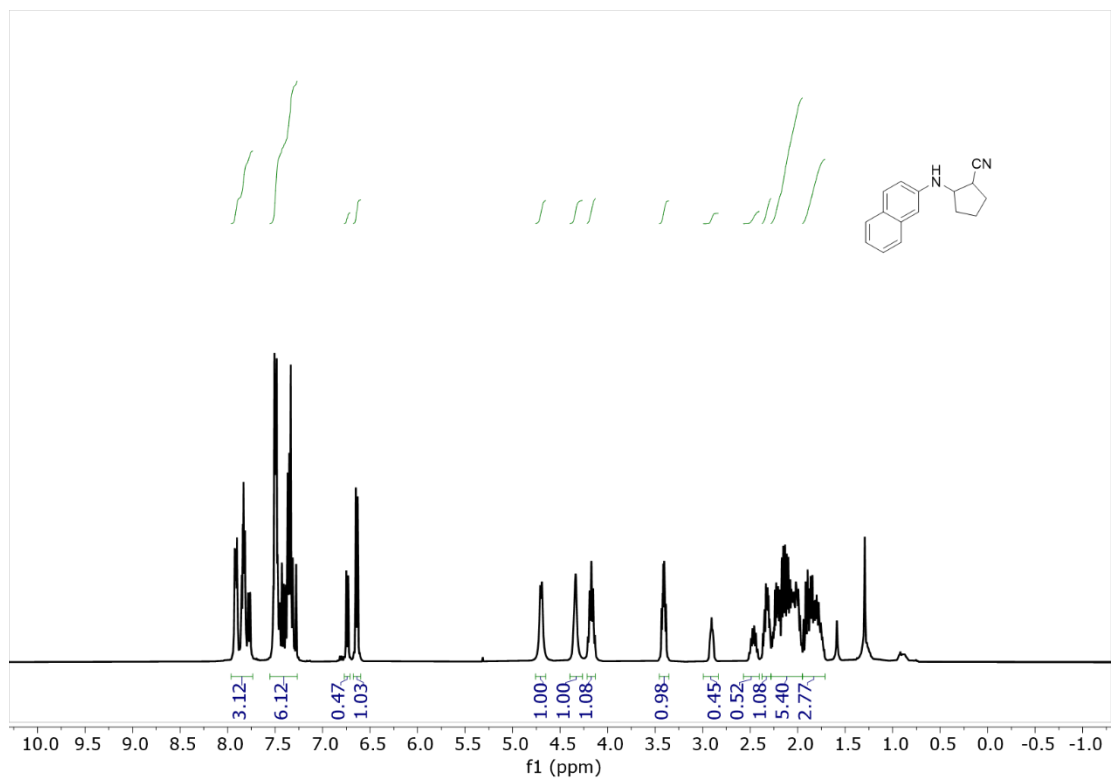












APPENDIX B

OLIGOSACCHARIDE DETECTION

This appendix B contains the figures and tables for oligosaccharide detection.

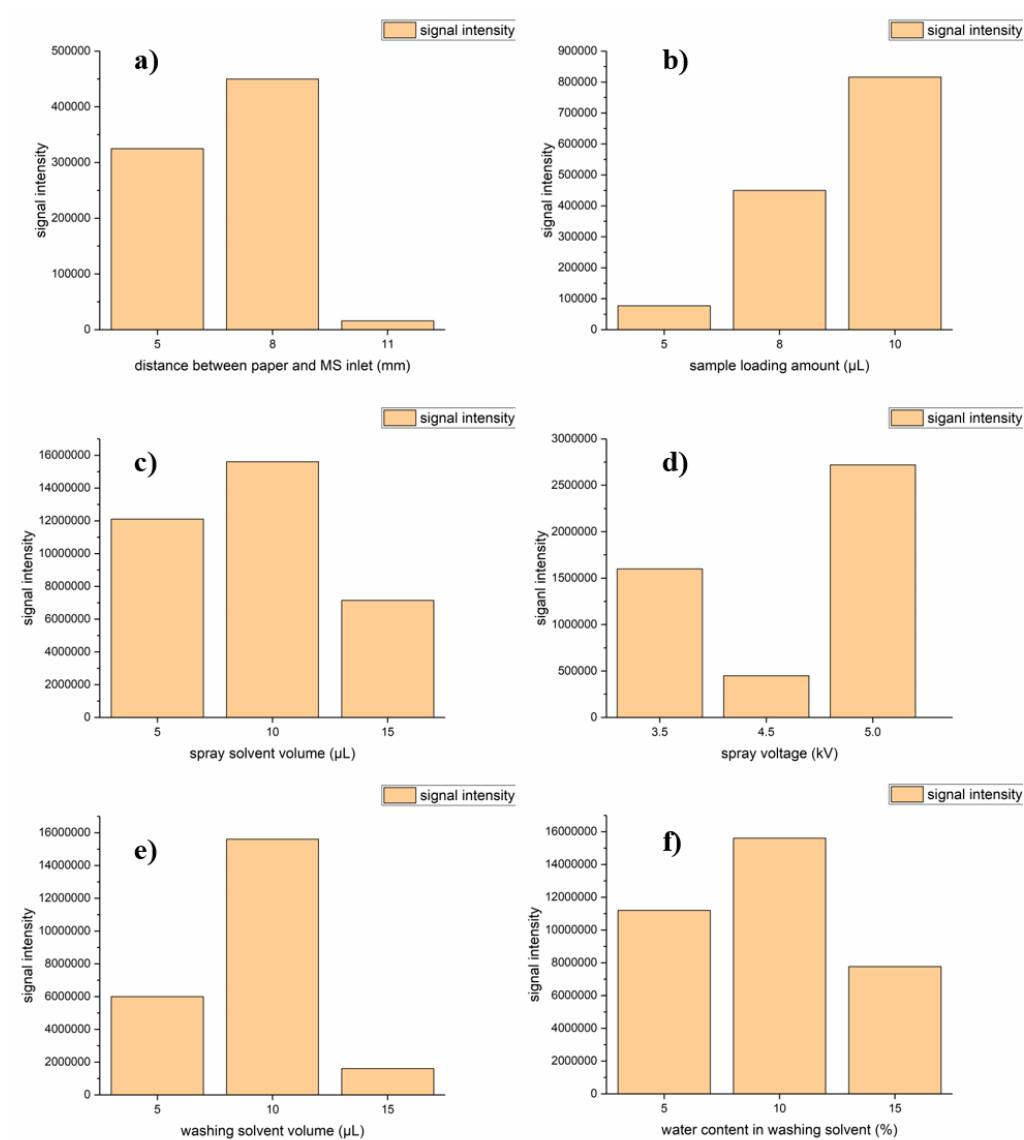


Figure B.1 DPS-MS condition optimization: a) distance between paper and MS inlet, b) sample loading amount, c) spray solvent volume, d) spray voltage, e) washing solvent volume and, and f) water content in washing solvent.

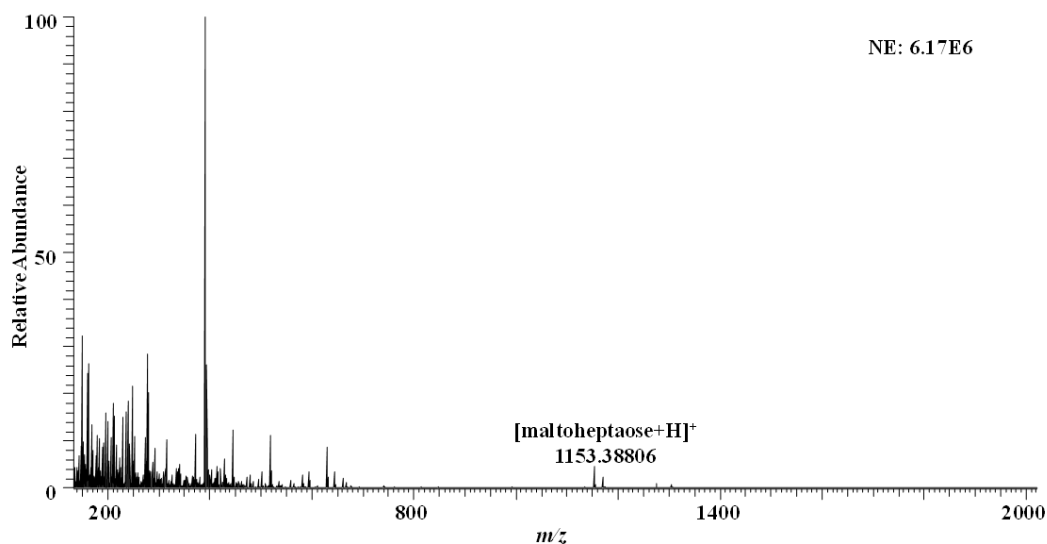


Figure B.2 MS Spectrum of 50 μM maltoheptaose in 50 mM Tris buffer (pH 7) acquired using cotton as SPE stationary phase and subsequent nanoESI analysis

50 μM maltoheptaose aqueous solution was used as a test sample to optimize the DPS condition, and the intensity of sodium adducted maltoheptaose was taken as the criteria for optimization of different parameters (Figure S1). The distance between triangular paper and MS inlet distance was set to 8 mm (Figure S1a). Signal intensity showed a positive response to sample loading volume from 5 μL to 10 μL (Figure S1b). When 10 μL washing solvent and spray solvent were used in experiment, the target peak presented the highest signal intensity (Figure S1c and S1e). Although spray voltage 5 kV provided the highest target signal intensity compared with 3.5 kV and 4.5 kV, we finally selected 3.5 kV as the spray voltage because some noise peaks were also seen in 5 kV spectrum due to high ionization potential. Water content in washing solvent was also investigated (Figure S1f). Finally, the optimized experimental conditions included: paper tip to MS inlet distance (8 mm); sample loading volume (10 μL); spray voltage (3.5 kV);

washing solvent (10 μL $\text{H}_2\text{O}/\text{ACN}$ 10/90 v/v), and spray solvent (10 μL $\text{H}_2\text{O}/\text{ACN}/\text{FA}$ 90/10/1 v/v/v).

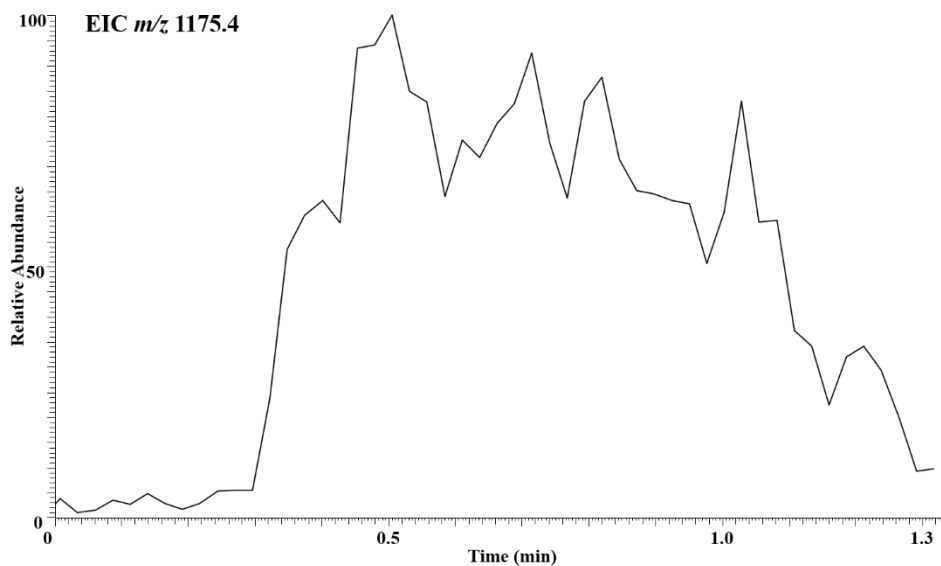


Figure B.3 Extracted ion chromatogram (EIC) for the ion of m/z 1175.4 from 50 μM maltoheptaose in 50 mM Tris buffer (pH 7) acquired using DPS-MS. When the potential was applied at $t=0$ min, there is a time delay of about 0.3 min to get a stable EIC current for m/z 1175.4. The delay might be caused by the electrophoretic migration of oligosaccharide sample to the paper spray tip. The signal was stabilized for about 0.8 min (0.3-1.1 min) before declining.

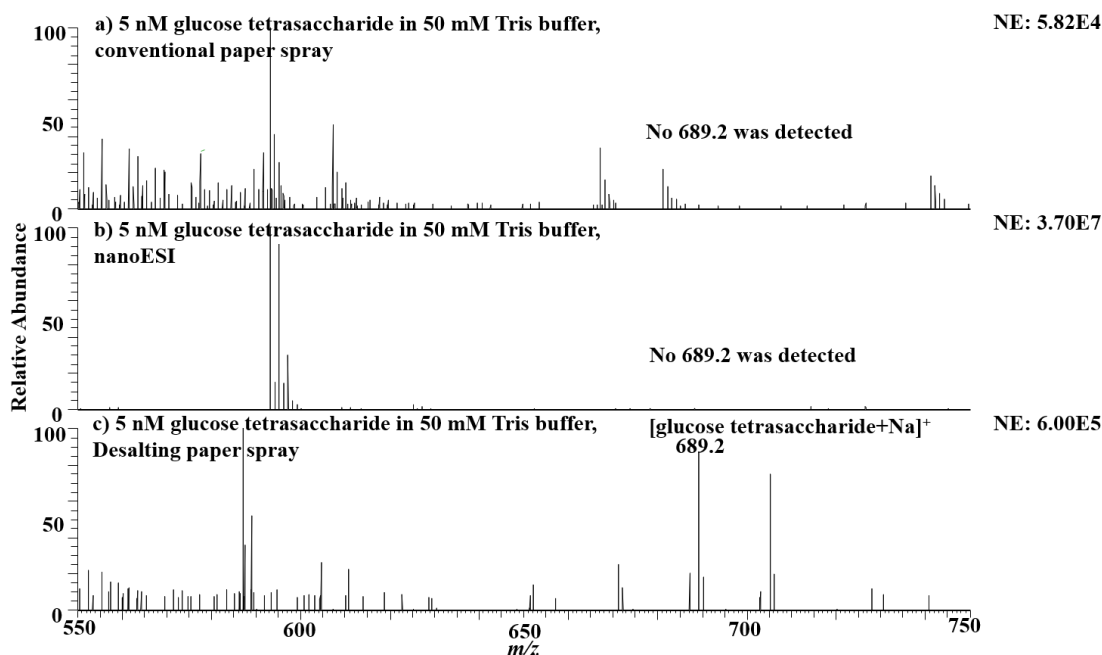


Figure B.4 MS spectra acquired using 10 μ L of 5 nM glucose tetrasaccharide in 50 mM Tris-HCl buffer by: a) PSI, b) nanoESI and, c) DPS.

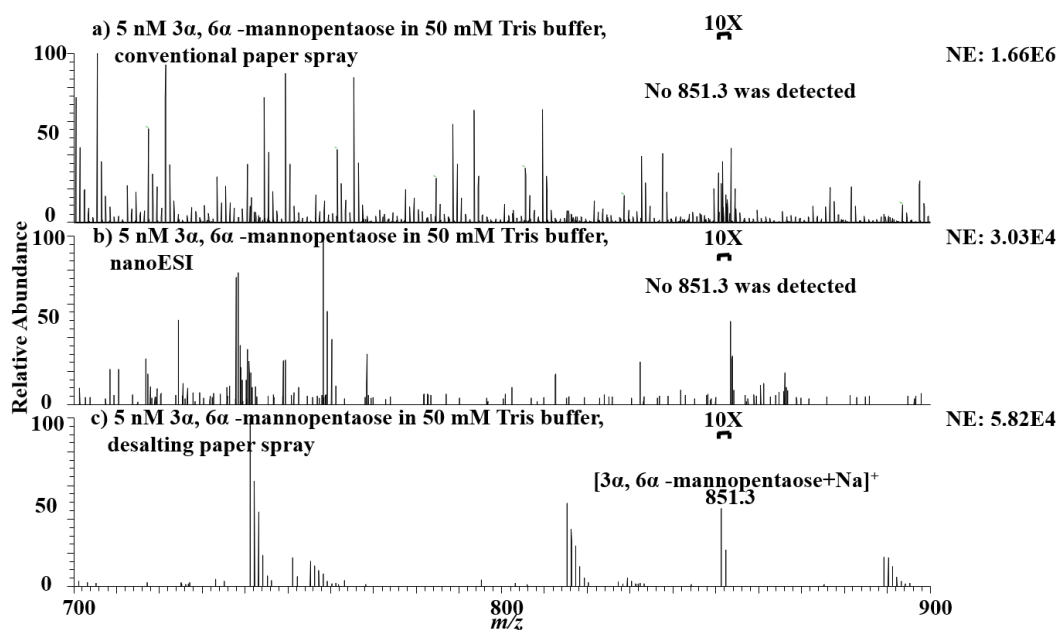


Figure B.5 Spectra of 5 nM 3 α , 6 α -mannopentaose (10 μ L) in 50 mM Tris buffer acquired by a) PSI, b) nanoESI, and c) DPS.

Table B.6 Raw data values of β -cyclodextrin analysis with I.S. (5 μ M maltoheptaose) for triplicate measurements

No	Concentration (nM)	Analyte <i>m/z</i>	Mass error (ppm)	Analyte intensity	Internal standard <i>m/z</i>	Mass error (ppm)	Analyte intensity	Intensity ratio(analyte /internal standard %)	Averaged intensity ratio	Standard deviation (noise)
1	200	1157.36253	3.07	1.48E3	1175.37167	1.80	1.80E5	0.82	0.93	7.70E-4
		1157.35950	0.45	2.43E3	1175.37305	2.98	2.53E5	0.96		
		1157.36108	1.81	3.95E3	1175.37158	1.73	3.94E5	1.00		
2	1000	1157.35986	0.76	3.72E4	1175.36938	0.14	7.56E5	4.92	5.02	1.19E-3
		1157.36035	1.18	1.68E4	1175.37134	1.52	3.40E5	4.94		
		1157.36011	0.98	6.22E4	1175.37073	1.00	1.20E6	5.18		
3	5000	1157.36035	1.18	1.22E3	1175.36829	1.07	8.56E3	14.25	15.1	7.04E-3
		1157.35815	0.72	1.27E5	1175.37305	2.98	8.42E5	15.08		
		1157.36084	1.61	2.62E3	1175.3717	1.83	1.64E4	15.98		
4	25000	1157.35121	1.93	1.27E4	1175.37158	1.73	2.55E4	49.80	50.5	5.79E-3
		1157.35986	0.76	2.07E4	1175.37012	0.48	4.10E4	50.49		
		1157.35999	0.87	3.77E4	1175.37073	1.00	7.36E4	51.22		
5	50000	1157.36096	1.71	1.61E4	1175.37073	1.00	1.54E4	104.55	105.08	3.81E-3
		1157.35667	2.00	4.39E3	1175.36938	0.14	4.17E3	105.28		
		1157.35999	0.87	3.31E3	1175.37085	1.11	3.14E3	105.41		

LOD calculation:

$$\text{LOD concentration} = 3 * \text{Noise} / \text{sensitivity}$$

Here,

Sensitivity = 0.002 (from the slope of the calibration curve in Figure 3d)

Noise = 0.00077 (use the standard deviation of the triplicate measurement for the low concentration sample of 200 nM β -cyclodextrin)

$$\text{LOD} = 3 * 0.00077 / 0.002$$

$$= 1.16 \text{ nM}$$

$$= 1.32 \text{ ng/mL}$$

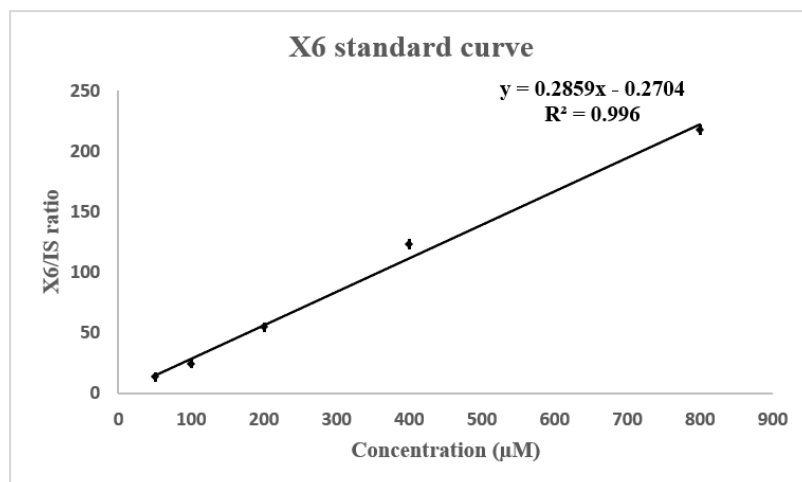


Figure B.7a Plot of X6 intensity (relative to I.S. 30 µM β-cyclodextrin) vs. concentration.

Table B.7b Raw data values of X6 analysis with an I.S. (30 µM β-cyclodextrin) for triplicate measurements.

Xylohexaose (X6) Concentration (µM)	X6 m/z	Intensity	Mass Error (ppm)	Internal standard m/z	Intensity	Mass error (ppm)	X6/I.S. ratio	RSD
50	833.25267	3.25E+04	-0.80	1157.35854	2.37E+05	-0.38	13.71%	0.30%
	833.25315	4.23E+04	-0.23	1157.35904	3.09E+05	0.05	13.69%	
	833.25129	1.17E+04	-2.46	1157.35866	8.96E+04	-0.28	13.06%	
100	833.25348	1.88E+05	0.17	1157.35828	7.74E+05	-0.60	24.29%	0.97%
	833.25352	2.66E+04	0.22	1157.35821	1.10E+05	-0.67	24.18%	
	833.25354	4.56E+04	0.24	1157.36084	1.76E+05	1.61	25.91%	
200	833.25450	1.12E+05	1.39	1157.3622	2.01E+05	2.78	55.72%	1.37%
	833.25483	7.03E+04	1.79	1157.35841	1.32E+05	-0.49	53.26%	
	833.25739	6.11E+04	4.86	1157.36095	1.10E+05	1.70	55.55%	
400	833.25305	2.42E+05	-0.35	1157.35779	1.96E+05	-1.03	123.47%	1.07%
	833.25330	1.32E+06	-0.05	1157.35962	1.08E+06	0.55	122.22%	
	833.25430	9.65E+05	1.15	1157.35807	7.76E+05	-0.79	124.36%	
800	833.25324	2.05E+05	-0.12	1157.35954	9.13E+04	0.48	224.53%	5.84%
	833.25293	3.40E+05	-0.49	1157.35742	1.59E+05	-1.35	213.84%	
	833.25360	4.41E+05	0.31	1157.36145	2.05E+05	2.13	215.12%	

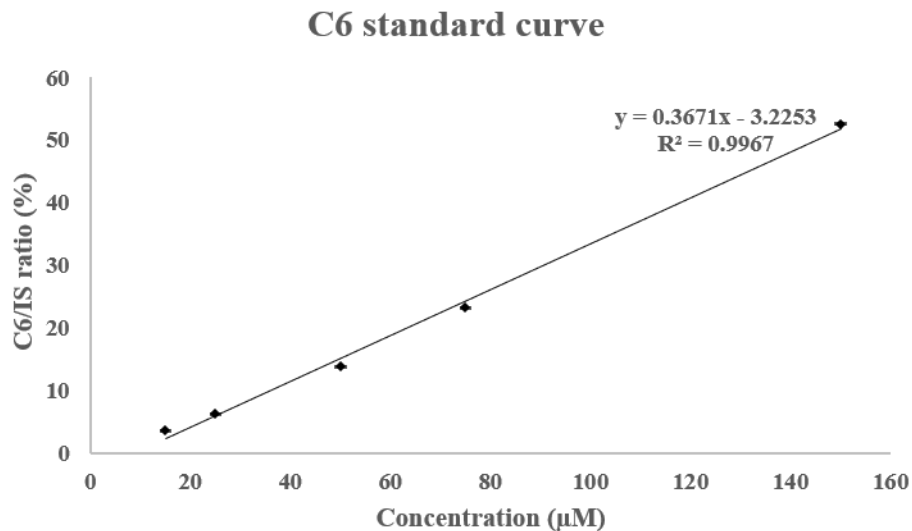


Figure B.8a Plot of C6 ion intensity (relative to I.S. 30 μM β -cyclodextrin) vs. concentration.

Table B.8b Raw data values of C6 analysis with an I.S. (30 μM β -cyclodextrin) for triplicate measurements.

Cellohexaose (C6) Concentration (μM)	C6 m/z	Intensity	Mass Error (ppm)	I.S. m/z	Intensity	Mass error (ppm)	C6/I.S. ratio	RSD
15	1013.31891	1.24E+04	2.15	1157.36152	3.44E+05	2.19	3.60%	0.12%
	1013.31744	7.07E+03	0.70	1157.36052	2.08E+05	1.33	3.40%	
	1013.31601	9.50E+03	-0.71	1157.35892	2.58E+05	-0.05	3.68%	
25	1013.31610	2.71E+04	-0.62	1157.35925	4.37E+05	0.23	6.20%	0.18%
	1013.31854	2.23E+04	1.79	1157.36267	3.39E+05	3.19	6.58%	
	1013.31482	1.28E+04	-1.88	1157.36011	2.07E+05	0.98	6.18%	
50	1013.31750	9.58E+04	0.76	1157.36108	6.93E+05	1.81	13.82%	1.19%
	1013.31726	1.35E+04	0.52	1157.36023	1.15E+05	1.08	11.74%	
	1013.31679	1.01E+05	0.06	1157.36218	6.94E+05	2.76	14.55%	
75	1013.31970	5.56E+04	3.38	1157.36218	2.39E+05	2.93	23.26%	1.50%
	1013.32037	2.29E+04	3.59	1157.36292	9.76E+04	3.40	23.46%	
	1013.31818	4.35E+04	1.43	1157.36121	1.64E+05	1.93	26.53%	
150	1013.31360	2.61E+05	-3.09	1157.35876	4.96E+05	-0.19	52.62%	2.71%
	1013.31689	1.22E+05	0.16	1157.35974	1.85E+05	0.66	55.02%	
	1013.31799	1.72E+04	1.24	1157.35986	2.97E+05	0.76	58.03%	

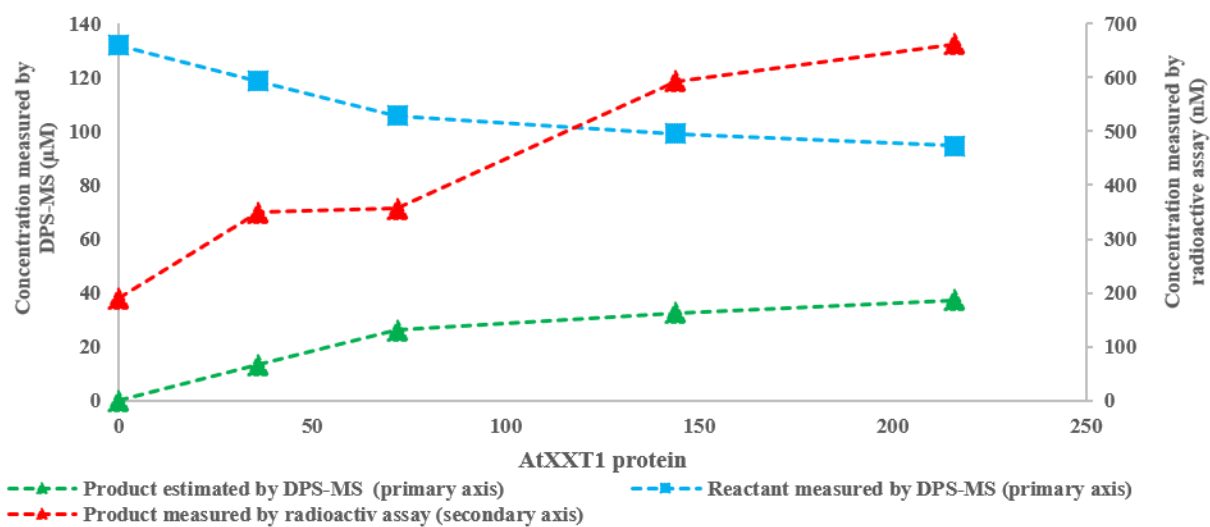


Figure B.9 Estimation of the acceptor C6 and the product (P2) concentrations using DPS-MS and radioactive assay, as function of the amount of AtXXT1 protein used in the enzymatic reactions.

APPENDIX C

NITROSAMINE QUANTITATION

This appendix C contains the figures and tables for nitrosamine quantitation.

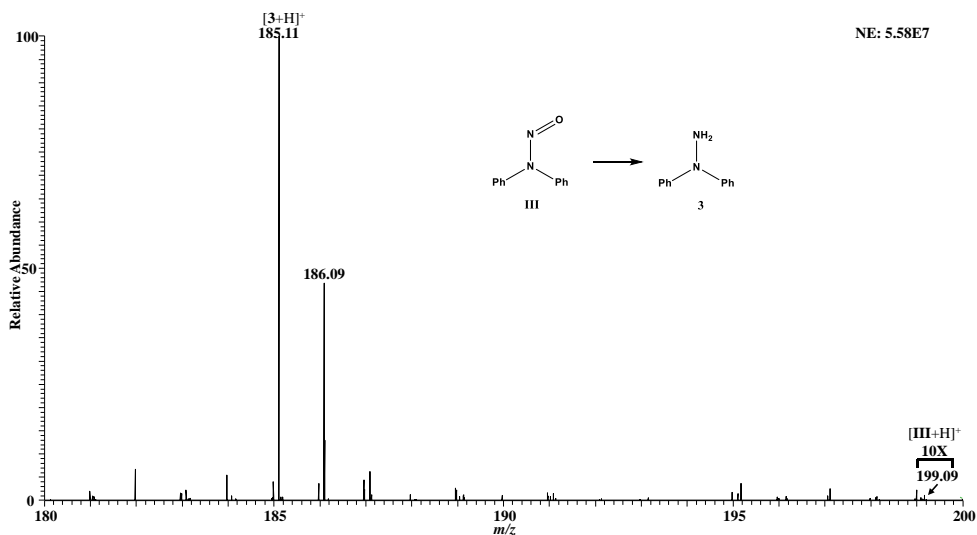


Figure C.1a NanoESI-MS spectrum of *N*-nitro-4-phenylpiperidine (**III**) after chemical reduction.

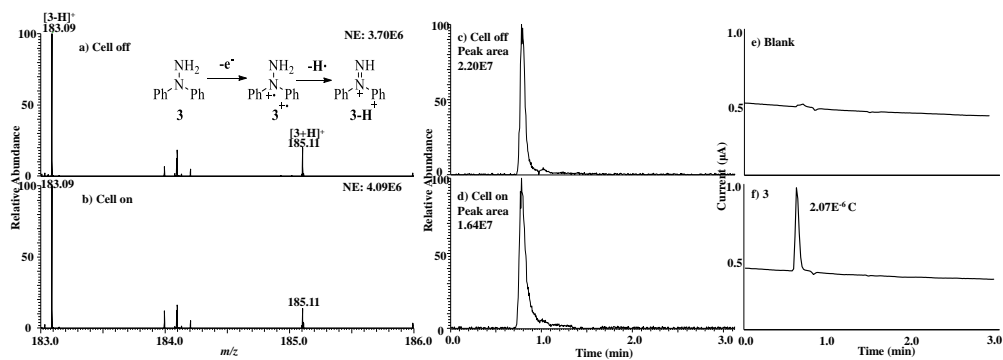
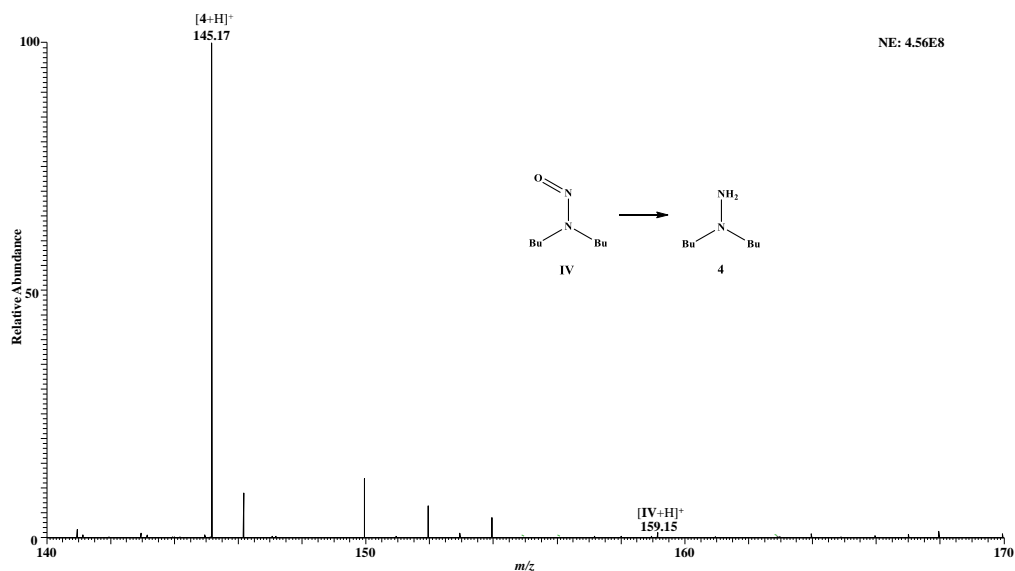


Figure C.1b. ESI-MS spectra of hydrazine **3** (from *N*-nitro-4-phenylpiperidine **III** reduction) when the applied potential was (a) 0 V and (b) +0.3 V. EIC of **3** was recorded when the applied potential was (c) 0 V and (d) +0.3 V (vs. Ag/AgCl). Electric current responses were shown due to the oxidation of (e) a blank solvent and (f) **3**.

Table C.1c. Electric current and MS data for *N*-nitro-4-phenylpiperidine (**III**)

Sample	Q(μ A. min)	Q(C)	Amount of the oxidized hydrazine (pmol)	EC oxidation yield	Measured hydrazine amount (pmol)	Averaged hydrazine amount (pmol)	Chemical reduction yield	Measured nitrosamine amount (pmol)	Theoretical nitrosamine amount (pmol)	Measurement error
<i>N</i> -nitro-4-phenylpiperidine III	7.94E-03	4.76E-07	4.94E+00	5.22%	9.46E+01					
	3.33E-02	2.00E-06	2.07E+01	27.33%	7.57E+01	8.48E+01	93.50%	9.07E+01	9.00E+01	0.75%
	3.45E-02	2.07E-06	2.14E+01	25.52%	8.40E+01					

Sample	EIC peak area of m/z 185 before oxidation	EIC peak area of m/z 185 after oxidation	oxidation yield
<i>N</i> -nitro-4-phenylpiperidine III	22010512	20861950	5.22%
	22010512	15994214	27.33%
	22010512	16394099	25.52%

**Figure C.2a.** NanoESI-MS spectrum of *N*-nitrosodibutylamine (**IV**) after chemical reduction.

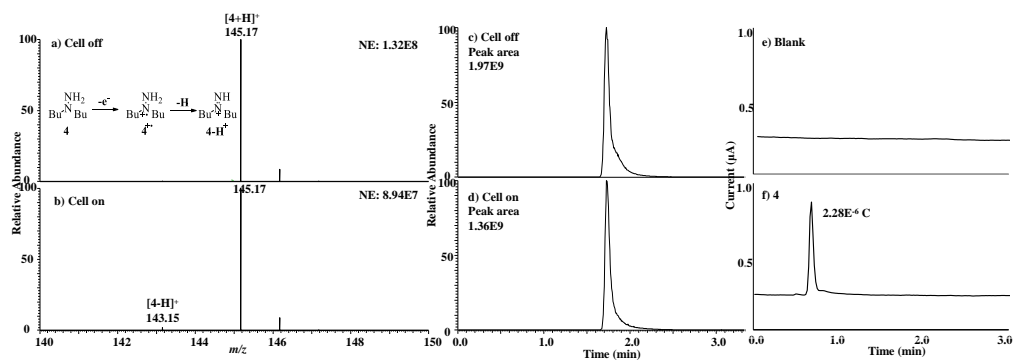


Figure C.2b. ESI-MS spectra of **4** (from *N*-nitrosodibutylamine **IV** reduction) when the applied potential was (a) 0 V and (b) +0.3 V. EIC of **4** was recorded when the applied potential was (c) 0 V and (d) +0.3 V (vs Ag/AgCl). Electric current responses were shown due to the oxidation of (e) a blank solvent and (f) **4**.

Table C.2c. Electric current and MS data for *N*-nitrosodibutylamine (**IV**).

Sample	Q(μ A, min)	Q(C)	Amount of the oxidized hydrazine (pmol)	EC oxidation yield	Measured hydrazine amount (pmol)	Averaged hydrazine amount (pmol)	Chemical reduction yield	Measured nitrosamine amount (pmol)	Theoretical nitrosamine amount (pmol)	Measurement error
<i>N</i> -nitrosodibutylamine IV	3.73E-02	2.24E-06	2.32E+01	31.87%	7.28E+01					
	3.80E-02	2.28E-06	2.36E+01	31.17%	7.57E+01	7.34E+01	99.00%	7.42E+01	7.50E+01	-1.12%
	3.75E-02	2.25E-06	2.33E+01	32.51%	7.17E+01					

Sample	EIC peak area of m/z 145 before oxidation	EIC peak area of m/z 145 after oxidation	oxidation yield
<i>N</i> -nitrosodibutylamine IV	1.972E+09	1.343E+09	31.87%
	1.972E+09	1.357E+09	31.17%
	1.972E+09	1.331E+09	32.51%

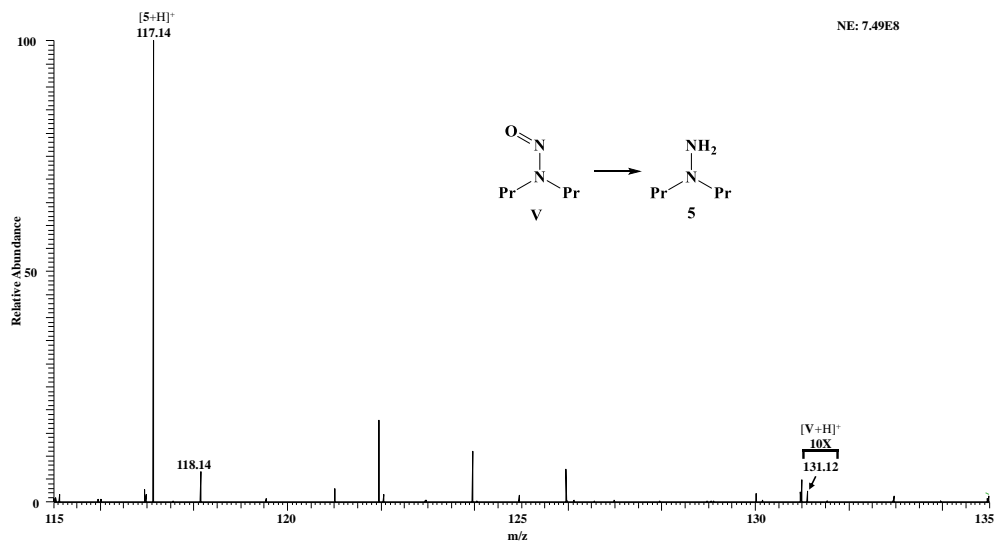


Figure C.3a NanoESI-MS spectrum of *N*-nitrosodipropylamine (**V**) after chemical reduction.

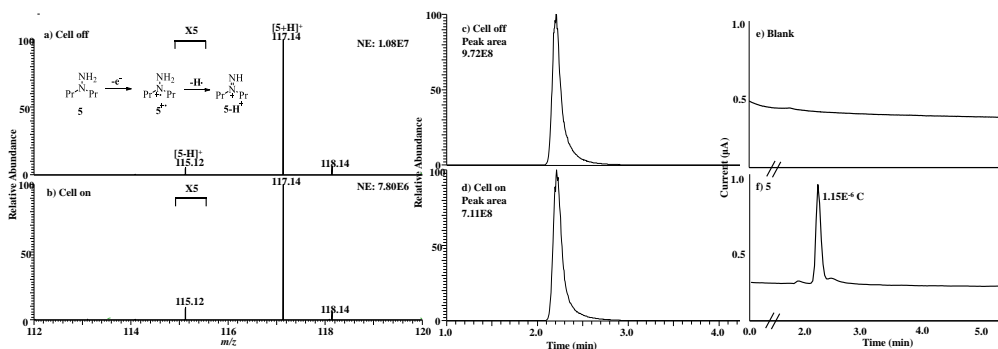
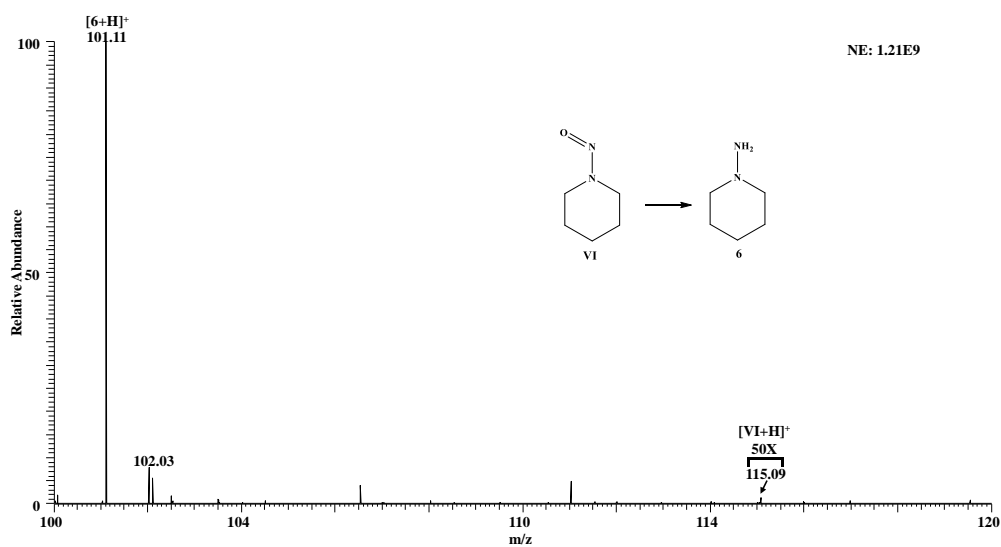


Figure C.3b ESI-MS spectra of **5** (from *N*-nitrosodipropylamine **V** reduction) when the applied potential was (a) 0 V and (b) +0.3 V. EIC of **5** was recorded when the applied potential was (c) 0 V and (d) +0.3 V (vs. Ag/AgCl). Electric current responses were shown due to the oxidation of (e) a blank solvent and (f) **5**.

Table C.3c Electric current and MS data for *N*-nitrosodipropylamine (**V**).

Sample	Q(μ A. min)	Q(C)	Amount of the oxidized hydrazine (pmol)	EC oxidation yield	Measured hydrazine amount (pmol)	Averaged hydrazine amount (pmol)	Chemical reduction yield	Measured nitrosamine amount (pmol)	Theoretical nitrosamine amount (pmol)	Measurement error
<i>N</i> -nitrosodipropylamine V	2.66E-02	1.60E-06	1.66E+01	37.16%	4.46E+01					
	1.92E-02	1.15E-06	1.20E+01	26.89%	4.45E+01	4.46E+01	99.76%	4.48E+01	4.50E+01	-0.55%
	1.96E-02	1.18E-06	1.22E+01	27.22%	4.49E+01					

Sample	EIC peak area of m/z 117 before oxidation	EIC peak area of m/z 117 after oxidation	oxidation yield
<i>N</i> -nitrosodipropylamine V	972348947	611037884	37.16%
	972348947	710923663	26.89%
	972348947	707696190	27.22%

**Figure C.4a** NanoESI-MS spectrum of *N*-nitrosopiperidine (**VI**) after chemical reduction.

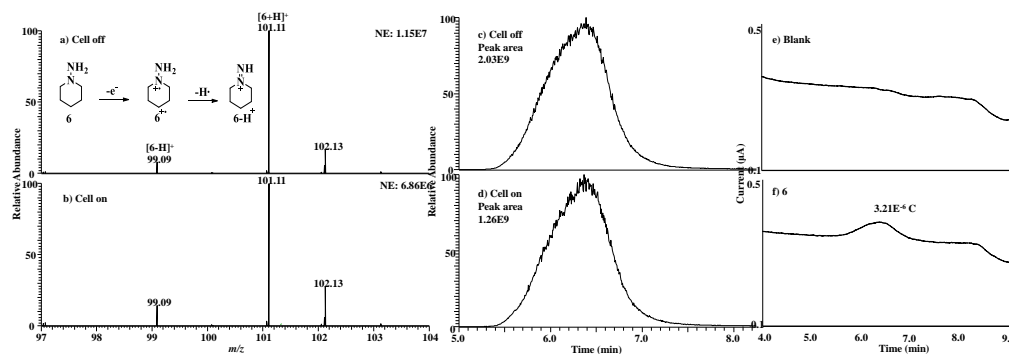


Figure C.4b ESI-MS spectra of **6** (from *N*-nitrosopiperidine **VI** reduction) when the applied potential was (a) 0 V and (b) +0.3 V. EIC of **6** was recorded when the applied potential was (c) 0 V and (d) +0.3 V (vs Ag/AgCl). Electric current responses were shown due to the oxidation of (e) a blank solvent and (f) **6**.

Table C.4c Electric current and MS data for *N*-nitrosopiperidine (**VI**).

Sample	Q(µA. min)	Q(C)	Amount of the oxidized hydrazine (pmol)	EC oxidation yield	Measured hydrazine amount (pmol)	Averaged hydrazine amount (pmol)	Chemical reduction yield	Measured nitrosamine amount (pmol)	Theoretical nitrosamine amount (pmol)	Measurement error
<i>N</i> -nitrosopiperidine VI	5.35E-02	3.21E-06	3.33E+01	37.95%	8.76E+01					
	3.69E-02	2.21E-06	2.29E+01	25.73%	8.92E+01	8.84E+01	99.90%	8.84E+01	8.94E+01	-1.08%
	3.55E-02	2.13E-06	2.21E+01	24.98%	8.83E+01					

Sample	EIC peak area of <i>m/z</i> 101 before oxidation	EIC peak area of <i>m/z</i> 101 after oxidation	oxidation yield
<i>N</i> -nitrosopiperidine VI	2033404155	1261666735	37.95%
	2033404155	1510178003	25.73%
	2033404155	1525440073	24.98%

REFERENCES

1. Kandiah, M.; Urban, P. L., Advances in ultrasensitive mass spectrometry of organic molecules. *Chemical Society Reviews* 2013, 42, 5299-5322.
2. Tamara, S.; den Boer, M. A.; Heck, A. J. R., High-resolution native mass spectrometry. *Chemical Reviews* 2021.
3. Wesdemiotis, C., Multidimensional mass spectrometry of synthetic polymers and advanced materials. *Angewandte Chemie International Edition* 2017, 56, 1452-1464.
4. Géhin, C.; Holman, S. W., Advances in high-resolution mass spectrometry applied to pharmaceuticals in 2020: A whole new age of information. *Analytical Science Advances* 2021, 2, 142-156.
5. Beccaria, M.; Cabooter, D., Current developments in LC-MS for pharmaceutical analysis. *Analyst* 2020, 145, 1129-1157.
6. Hansen, F.; Øiestad, E. L.; Pedersen-Bjergaard, S., Bioanalysis of pharmaceuticals using liquid-phase microextraction combined with liquid chromatography–mass spectrometry. *Journal of Pharmaceutical and Biomedical Analysis* 2020, 189, 113446.
7. Picó, Y.; Barceló, D., Pyrolysis gas chromatography-mass spectrometry in environmental analysis: Focus on organic matter and microplastics. *TrAC Trends in Analytical Chemistry* 2020, 130, 115964.
8. Richardson, S. D., Mass spectrometry in environmental sciences. *Chemical Reviews* 2001, 101, 211-254.
9. Jia, S.; Marques Dos Santos, M.; Li, C.; Snyder, S. A., Recent advances in mass spectrometry analytical techniques for per- and polyfluoroalkyl substances (PFAS). *Analytical and Bioanalytical Chemistry* 2022.
10. Zhang, B.; Whiteaker, J. R.; Hoofnagle, A. N.; Baird, G. S.; Rodland, K. D.; Paulovich, A. G., Clinical potential of mass spectrometry-based proteogenomics. *Nature Reviews Clinical Oncology* 2019, 16, 256-268.
11. Timp, W.; Timp, G., Beyond mass spectrometry, the next step in proteomics. *Science Advances* 2021, 6, 762-776.
12. Zhang, F.; Ge, W.; Ruan, G.; Cai, X.; Guo, T., Data-independent acquisition mass spectrometry-based proteomics and software tools: a glimpse in 2020. *Proteomics* 2020, 20, 1900276.
13. Macklin, A.; Khan, S.; Kislinger, T., Recent advances in mass spectrometry based clinical proteomics: applications to cancer research. *Clinical Proteomics* 2020, 17, 17.

14. Lanekoff, I.; Sharma, V. V.; Marques, C., Single-cell metabolomics: where are we and where are we going? *Current Opinion in Biotechnology* 2022, 75, 102693.
15. Bauermeister, A.; Mannocho-Russo, H.; Costa-Lotufo, L. V.; Jarmusch, A. K.; Dorrestein, P. C., Mass spectrometry-based metabolomics in microbiome investigations. *Nature Reviews Microbiology* 2022, 20, 143-160.
16. Brown, H. M.; McDaniel, T. J.; Fedick, P. W.; Mulligan, C. C., The current role of mass spectrometry in forensics and future prospects. *Analytical Methods* 2020, 12, 3974-3997.
17. Evans-Nguyen, K.; Stelmack, A. R.; Clowser, P. C.; Holtz, J. M.; Mulligan, C. C., Fieldable mass spectrometry for forensic science, homeland security, and different application *Mass Spectrometry Reviews* 2021, 40, 628-646.
18. Parr, M. K.; Botrè, F., Supercritical fluid chromatography mass spectrometry as an emerging technique in doping control analysis. *TrAC Trends in Analytical Chemistry* 2022, 147, 116517.
19. Thevis, M.; Piper, T.; Thomas, A., Recent advances in identifying and utilizing metabolites of selected doping agents in human sports drug testing. *Journal of Pharmaceutical and Biomedical Analysis* 2021, 205, 114312.
20. Keen, B.; Cawley, A.; Reedy, B.; Fu, S., Metabolomics in clinical and forensic toxicology, sports anti-doping and veterinary residues. *Drug Testing and Analysis* 2022, n/a.
21. Mellon, F. A., Mass spectrometry | Principles and instrumentation. In *Encyclopedia of food sciences and nutrition*, New York City, New York, Elsevier, Caballero, B., Ed. Academic Press: Oxford, 2003; pp 3739-3749.
22. Kaklamanos, G.; Aprea, E.; Theodoridis, G., Mass spectrometry: principles and instrumentation. In *Encyclopedia of food and health*, Caballero, B.; Finglas, P. M.; Toldrá, F., Eds. New York City, New York, Elsevier, Academic Press: Oxford, 2016; pp 661-668.
23. Fenn John, B.; Mann, M.; Meng Chin, K.; Wong Shek, F.; Whitehouse Craig, M., Electrospray ionization for mass spectrometry of large biomolecules. *Science (New York, N.Y.)* 1989, 246, 64-71.
24. Konermann, L.; Ahadi, E.; Rodriguez, A. D.; Vahidi, S., Unraveling the mechanism of electrospray ionization. *Analytical Chemistry* 2013, 85, 2-9.
25. Wilm, M.; Mann, M., Analytical properties of the nanoelectrospray ion source. *Analytical Chemistry* 1996, 68, 1-8.

26. Wang, H.; Liu, J.; Cooks, R. G.; Ouyang, Z., Paper spray for direct analysis of complex mixtures using mass spectrometry. *Angewandte Chemie International Edition* 2010, 49, 877-880.
27. Chiang, S.; Zhang, W.; Ouyang, Z., Paper spray ionization mass spectrometry: recent advances and clinical applications. *Expert Review of Proteomics* 2018, 15, 781-789.
28. Haag, A. M., Mass analyzers and mass spectrometers. In *Modern proteomics – sample preparation, analysis and practical applications*, Mirzaei, H.; Carrasco, M., Eds. New York City, New York, Springer International Publishing: Cham, 2016; pp 157-169.
29. Herl, T.; Matysik, F. M., Recent developments in electrochemistry–mass spectrometry. *ChemElectroChem* 2020, 7, 2498-2512.
30. Bruckenstein, S.; Gadde, R. R., Use of a porous electrode for in situ mass spectrometric determination of volatile electrode reaction products. *Journal of the American Chemical Society* 1971, 93, 793-794.
31. Wolter, O.; Heitbaum, J., Differential electrochemical mass spectroscopy (DEMS) — a new method for the study of electrode processes. *Berichte der Bunsengesellschaft für physikalische Chemie* 1984, 88, 2-6.
32. Hambitzer, G.; Heitbaum, J., Electrochemical thermospray mass spectrometry. *Analytical Chemistry* 1986, 58, 1067-1070.
33. Volk, K. J.; Lee, M. S.; Yost, R. A.; Brajter-Toth, A., Electrochemistry/thermospray/tandem mass spectrometry in the study of biooxidation of purines. *Analytical Chemistry* 1988, 60, 720-722.
34. Volk, K. J.; Yost, R. A.; Brajter-Toth, A., On-line electrochemistry/thermospray/tandem mass spectrometry as a new approach to the study of redox reactions: the oxidation of uric acid. *Analytical chemistry* 1989, 61, 1709-1717.
35. Zhou, F.; Van Berkel, G. J., Electrochemistry combined online with electrospray mass spectrometry. *Analytical Chemistry* 1995, 67, 3643-3649.
36. Faber, H.; Vogel, M.; Karst, U., Electrochemistry/mass spectrometry as a tool in metabolism studies—A review. *Analytica Chimica Acta* 2014, 834, 9-21.
37. Oberacher, H.; Erb, R.; Plattner, S.; Chervet, J.-P., Mechanistic aspects of nucleic-acid oxidation studied with electrochemistry-mass spectrometry. *TrAC Trends in Analytical Chemistry* 2015, 70, 100-111.
38. Portychová, L.; Schug, K. A., Instrumentation and applications of electrochemistry coupled to mass spectrometry for studying xenobiotic metabolism: A review. *Analytica Chimica Acta* 2017, 993, 1-21.

39. Liu, P.; Lu, M.; Zheng, Q.; Zhang, Y.; Dewald, H. D.; Chen, H., Recent advances of electrochemical mass spectrometry. *Analyst* 2013, 138, 5519-5539.
40. Oberacher, H.; Pitterl, F.; Erb, R.; Plattner, S., Mass spectrometric methods for monitoring redox processes in electrochemical cells. *Mass Spectrometry Reviews* 2015, 34, 64-92.
41. Cindric, M.; Matysik, F.-M., Coupling electrochemistry to capillary electrophoresis-mass spectrometry. *TrAC Trends in Analytical Chemistry* 2015, 70, 122-127.
42. van den Brink, F. T. G.; Olthuis, W.; van den Berg, A.; Odijk, M., Miniaturization of electrochemical cells for mass spectrometry. *TrAC Trends in Analytical Chemistry* 2015, 70, 40-49.
43. Bruins, A. P., An overview of electrochemistry combined with mass spectrometry. *TrAC Trends in Analytical Chemistry* 2015, 70, 14-19.
44. Gun, J.; Bharathi, S.; Gutkin, V.; Rizkov, D.; Voloshenko, A.; Shelkov, R.; Sladkevich, S.; Kyi, N.; Rona, M.; Wolanov, Y.; Rizkov, D.; Koch, M.; Mizrahi, S.; Pridkhochenko, P. V.; Modestov, A.; Lev, O., Highlights in coupled electrochemical flow cell-mass spectrometry, EC/MS. *Israel Journal of Chemistry* 2010, 50, 360-373.
45. Clark, E. L.; Singh, M. R.; Kwon, Y.; Bell, A. T., Differential electrochemical mass spectrometer cell design for online quantification of products produced during electrochemical reduction of CO₂. *Analytical Chemistry* 2015, 87, 8013-8020.
46. Clark, E. L.; Bell, A. T., Direct observation of the local reaction environment during the electrochemical reduction of CO₂. *Journal of the American Chemical Society* 2018, 140, 7012-7020.
47. Shen, S.; Hong, Y.; Zhu, F.; Cao, Z.; Li, Y.; Ke, F.; Fan, J.; Zhou, L.; Wu, L.; Dai, P., Tuning electrochemical properties of Li-rich layered oxide cathodes by adjusting Co/Ni ratios and mechanism investigation using in situ X-ray diffraction and online continuous flow differential electrochemical mass spectrometry. *ACS Applied Materials and Interfaces* 2018, 10, 12666-12677.
48. Mateos-Santiago, J.; Hernández-Pichardo, M. L.; Lartundo-Rojas, L.; Manzo-Robledo, A., Methanol electro-oxidation on Pt–Carbon vulcan catalyst modified with WO_x nanostructures: an approach to the reaction sequence using DEMS. *Industrial and Engineering Chemistry Research* 2017, 56, 161-167.
49. Möller, S.; Barwe, S.; Masa, J.; Wintrich, D.; Seisel, S.; Baltruschat, H.; Schuhmann, W., Online monitoring of electrochemical carbon corrosion in alkaline electrolytes by differential electrochemical mass spectrometry. *Angewandte Chemie International Edition* 2020, 59, 1585-1589.

50. Pozniak, B.; Treufeld, I.; Scherson, D., Hydroxylamine oxidation on polycrystalline gold electrodes in aqueous electrolytes: quantitative on-line mass spectrometry under forced convection. *ChemPhysChem* 2019, 20, 3128-3133.
51. Khanipour, P.; Löffler, M.; Reichert, A. M.; Haase, F. T.; Mayrhofer, K. J.; Katsounaros, I., Electrochemical real-time mass spectrometry (EC-RTMS): monitoring electrochemical reaction products in real time. *Angewandte Chemie* 2019, 131, 7351-7355.
52. Folgueiras-Amador, A. A.; Philipps, K.; Guilbaud, S.; Poelakker, J.; Wirth, T., An easy-to-machine electrochemical flow microreactor: efficient synthesis of isoindolinone and flow functionalization. *Angewandte Chemie International Edition* 2017, 56, 15446-15450.
53. van den Brink, F. T.; Zhang, T.; Ma, L.; Bomer, J.; Odijk, M.; Olthuis, W.; Permentier, H. P.; Bischoff, R.; van den Berg, A., Electrochemical protein cleavage in a microfluidic cell with integrated boron doped diamond electrodes. *Analytical Chemistry* 2016, 88, 9190-9198.
54. Cramer, C. N.; Kelstrup, C. D.; Olsen, J. V.; Haselmann, K. F.; Nielsen, P. K., Generic workflow for mapping of complex disulfide bonds using in-source reduction and extracted ion chromatograms from data-dependent mass spectrometry. *Analytical Chemistry* 2018, 90, 8202-8210.
55. Tang, S.; Cheng, H.; Yan, X., On-demand electrochemical epoxidation in nano-electrospray ionization mass spectrometry to locate carbon-carbon double bonds. *Angewandte Chemie International Edition* 2020, 59, 209-214.
56. He, J.; Li, N.; Zhang, D.; Zheng, G.; Zhang, H.; Yu, K.; Jiang, J., Real-time monitoring of ciprofloxacin degradation in an electro-Fenton-like system using electrochemical-mass spectrometry. *Environmental Science: Water Research and Technology* 2020, 6, 181-188.
57. Zhang, T.; de Vries, M. P.; Permentier, H. P.; Bischoff, R., Specific affinity enrichment of electrochemically cleaved peptides based on Cu (II)-mediated spirolactone tagging. *Analytical Chemistry* 2017, 89, 7123-7129.
58. Herl, T.; Matysik, F.-M., Investigation of the electrooxidation of thymine on screen-printed carbon electrodes by hyphenation of electrochemistry and mass spectrometry. *Analytical Chemistry* 2020, 92, 6374-6381.
59. Xu, C.; Zheng, Q.; Zhao, P.; Paterson, J.; Chen, H., A new quantification method using electrochemical mass spectrometry. *Journal of the American Society for Mass Spectrometry* 2019, 30, 685-693.
60. Zhao, P.; Guo, Y.; Dewald, H. D.; Chen, H., Improvements for absolute quantitation using electrochemical mass spectrometry. *International Journal of Mass Spectrometry* 2019, 443, 41-45.

61. Zhao, P.; Zare, R. N.; Chen, H., Absolute quantitation of oxidizable peptides by coulometric mass spectrometry. *Journal of the American Society for Mass Spectrometry* 2019, 30, 2398-2407.
62. Ai, Y.; Zhao, P.; Fnu, P. I. J.; Chen, H., Absolute quantitation of tryptophan-containing peptides and amyloid β -peptide fragments by coulometric mass spectrometry. *Journal of the American Society for Mass Spectrometry* 2021, 32, 1771-1779.
63. Zhao, P.; Wang, Q.; Kaur, M.; Kim, Y.-I.; Dewald, H. D.; Mozziconacci, O.; Liu, Y.; Chen, H., Absolute quantitation of proteins by coulometric mass spectrometry. *Analytical Chemistry* 2020, 92, 7877-7883.
64. Song, X.; Chen, H.; Zare, R. N., Coulometry-assisted quantitation in spray ionization mass spectrometry. *Journal of Mass Spectrometry* 2021, 56, e4628.
65. Horn, E. J.; Rosen, B. R.; Chen, Y.; Tang, J.; Chen, K.; Eastgate, M. D.; Baran, P. S., Scalable and sustainable electrochemical allylic C–H oxidation. *Nature* 2016, 533, 77-81.
66. Badalyan, A.; Stahl, S. S., Cooperative electrocatalytic alcohol oxidation with electron-proton-transfer mediators. *Nature* 2016, 535, 406-410.
67. Wiebe, A.; Schollmeyer, D.; Dyballa, K. M.; Franke, R.; Waldvogel, S. R., Selective synthesis of partially protected nonsymmetric biphenols by reagent- and metal-free anodic cross-coupling reaction. *Angewandte Chemie International Edition* 2016, 55, 11801-11805.
68. Schulz, L.; Enders, M.; Elsler, B.; Schollmeyer, D.; Dyballa, K. M.; Franke, R.; Waldvogel, S. R., Reagent- and metal-free anodic C–C cross-coupling of aniline derivatives. *Angewandte Chemie International Edition* 2017, 56, 4877-4881.
69. Yan, M.; Kawamata, Y.; Baran, P. S., Synthetic organic electrochemical methods since 2000: on the verge of a renaissance. *Chemical Reviews* 2017, 117, 13230-13319.
70. Okada, Y.; Chiba, K., Redox-tag processes: Intramolecular electron transfer and its broad relationship to redox reactions in general. *Chemical Reviews* 2017, 118, 4592-4630.
71. Zhang, W.; Carpenter, K. L.; Lin, S., Electrochemistry broadens the scope of flavin photocatalysis: photoelectrocatalytic oxidation of unactivated alcohols. *Angewandte Chemie International Edition* 2020, 132, 417-425.
72. Moeller, K. D., Using physical organic chemistry to shape the course of electrochemical reactions. *Chemical Reviews* 2018, 118, 4817-4833.
73. Francke, R.; Little, R. D., Redox catalysis in organic electrosynthesis: basic principles and recent developments. *Chemical Society Reviews* 2014, 43, 2492-2521.
74. Fu, N.; Sauer, G. S.; Lin, S., A general, electrocatalytic approach to the synthesis of vicinal diamines. *Nature Protocols* 2018, 13, 1725-1743.

75. Leow, W. R.; Lum, Y.; Ozden, A.; Wang, Y.; Nam, D.-H.; Chen, B.; Wicks, J.; Zhuang, T.-T.; Li, F.; Sinton, D., Chloride-mediated selective electrosynthesis of ethylene and propylene oxides at high current density. *Science (New York, N.Y.)* 2020, 368, 1228-1233.
76. Hu, X.; Nie, L.; Zhang, G.; Lei, A., Electrochemical oxidative [4+ 2] annulation for the π -extension of unfunctionalized heterobiaryl compounds. *Angewandte Chemie International Edition* 2020, 59, 15238-15243.
77. Corcoran, E. B.; Pirnot, M. T.; Lin, S.; Dreher, S. D.; DiRocco, D. A.; Davies, I. W.; Buchwald, S. L.; MacMillan, D. W., Aryl amination using ligand-free Ni (II) salts and photoredox catalysis. *Science (New York, N.Y.)* 2016, 353, 279-283.
78. Murphy, J. J.; Melchiorre, P., Light opens pathways for nickel catalysis. *Nature* 2015, 524, 297-298.
79. Jeffrey, J. L.; Terrett, J. A.; MacMillan, D. W., O–H hydrogen bonding promotes H-atom transfer from α C–H bonds for C-alkylation of alcohols. *Science (New York, N.Y.)* 2015, 349, 1532-1536.
80. Zuo, Z.; Ahneman, D. T.; Chu, L.; Terrett, J. A.; Doyle, A. G.; MacMillan, D. W., Merging photoredox with nickel catalysis: Coupling of α -carboxyl sp^3 -carbons with aryl halides. *Science (New York, N.Y.)* 2014, 345, 437-440.
81. Shi, L.; Xia, W., Photoredox functionalization of C–H bonds adjacent to a nitrogen atom. *Chemical Society Reviews* 2012, 41, 7687-7697.
82. Gieshoff, T.; Kehl, A.; Schollmeyer, D.; Moeller, K. D.; Waldvogel, S. R., Insights into the mechanism of anodic N–N bond formation by dehydrogenative coupling. *Journal of the American Chemical Society* 2017, 139, 12317-12324.
83. Hayashi, R.; Shimizu, A.; Yoshida, J.-i., The stabilized cation pool method: metal-and oxidant-free benzylic C–H/aromatic C–H cross-coupling. *Journal of the American Chemical Society* 2016, 138, 8400-8403.
84. Lips, S.; Schollmeyer, D.; Franke, R.; Waldvogel, S. R., Regioselective metal-and reagent-free arylation of benzothiophenes by dehydrogenative electrosynthesis. *Angewandte Chemie International Edition* 2018, 57, 13325-13329.
85. Lips, S.; Frontana-Urbe, B. A.; Dörr, M.; Schollmeyer, D.; Franke, R.; Waldvogel, S. R., Metal-and reagent-free anodic C–C cross-coupling of phenols with benzofurans leading to a furan metathesis. *Chemistry–A European Journal* 2018, 24, 6057-6061.
86. Wiebe, A.; Lips, S.; Schollmeyer, D.; Franke, R.; Waldvogel, S. R., Single and twofold metal-and reagent-free anodic C–C cross-coupling of phenols with thiophenes. *Angewandte Chemie International Edition* 2017, 56, 14727-14731.

87. Lips, S.; Wiebe, A.; Elsler, B.; Schollmeyer, D.; Dyballa, K. M.; Franke, R.; Waldvogel, S. R., Synthesis of meta-terphenyl-2, 2''-diols by anodic C–C cross-coupling reactions. *Angewandte Chemie International Edition* 2016, 55, 10872-10876.
88. Mahanty, K.; Maiti, D.; De Sarkar, S., Regioselective C–H sulfonylation of 2 H-indazoles by electrocatalysis. *The Journal of Organic Chemistry* 2020, 85, 3699-3708.
89. Ye, X.; Zhao, P.; Zhang, S.; Zhang, Y.; Wang, Q.; Shan, C.; Wojtas, L.; Guo, H.; Chen, H.; Shi, X., Facilitating Gold Redox Catalysis with Electrochemistry: An Efficient Chemical-Oxidant-Free Approach. *Angewandte Chemie* 2019, 131, 17386-17390.
90. Xiong, P.; Long, H.; Song, J.; Wang, Y.; Li, J.-F.; Xu, H.-C., Electrochemically enabled carbohydroxylation of alkenes with H₂O and organotrifluoroborates. *Journal of the American Chemical Society* 2018, 140, 16387-16391.
91. Lennox, A. J.; Goes, S. L.; Webster, M. P.; Koolman, H. F.; Djuric, S. W.; Stahl, S. S., Electrochemical aminoxyl-mediated α -cyanation of secondary piperidines for pharmaceutical building block diversification. *Journal of the American Chemical Society* 2018, 140, 11227-11231.
92. Liang, Y.; Lin, F.; Adeli, Y.; Jin, R.; Jiao, N., Efficient electrocatalysis for the preparation of (hetero)aryl chlorides and vinyl chloride with 1,2-dichloroethane. *Angewandte Chemie International Edition* 2019, 58, 4566-4570.
93. Sperry, J. B.; Wright, D. L., The application of cathodic reductions and anodic oxidations in the synthesis of complex molecules. *Chemical Society Reviews* 2006, 35, 605-621.
94. Yoshida, J.-i.; Kataoka, K.; Horcajada, R.; Nagaki, A., Modern strategies in electroorganic synthesis. *Chemical Reviews* 2008, 108, 2265-2299.
95. Frontana-Uribe, B. A.; Little, R. D.; Ibanez, J. G.; Palma, A.; Vasquez-Medrano, R., Organic electrocatalysis: a promising green methodology in organic chemistry. *Green Chemistry* 2010, 12, 2099-2119.
96. Horn, E. J.; Rosen, B. R.; Baran, P. S., Synthetic organic electrochemistry: an enabling and innately sustainable method. *ACS Central Science* 2016, 2, 302-308.
97. Jiang, Y.; Xu, K.; Zeng, C., Use of electrochemistry in the synthesis of heterocyclic structures. *Chemical Reviews* 2018, 118, 4485-4540.
98. Kawamata, Y.; Yan, M.; Liu, Z.; Bao, D.-H.; Chen, J.; Starr, J. T.; Baran, P. S., Scalable, electrochemical oxidation of unactivated C–H bonds. *Journal of the American Chemical Society* 2017, 139, 7448-7451.

99. Möhle, S.; Zirbes, M.; Rodrigo, E.; Gieshoff, T.; Wiebe, A.; Waldvogel, S. R., Modern electrochemical aspects for the synthesis of value-added organic products. *Angewandte Chemie International Edition* 2018, 57, 6018-6041.
100. Wiebe, A.; Gieshoff, T.; Möhle, S.; Rodrigo, E.; Zirbes, M.; Waldvogel, S. R., Electrifying organic synthesis. *Angewandte Chemie International Edition* 2018, 57, 5594-5619.
101. Doobary, S.; Sedikides, A. T.; Caldora, H. P.; Poole, D. L.; Lennox, A. J. J., Electrochemical vicinal difluorination of alkenes: scalable and amenable to electron-rich substrates. *Angewandte Chemie International Edition* 2020, 59, 1155-1160.
102. Lennox, A. J. J.; Nutting, J. E.; Stahl, S. S., Selective electrochemical generation of benzylic radicals enabled by ferrocene-based electron-transfer mediators. *Chemical Science* 2018, 9, 356-361.
103. Wang, H.; Huang, H., Transition-metal-catalyzed redox-neutral and redox-green C–H bond functionalization. *The Chemical Record* 2016, 16, 1807-1818.
104. Qin, Q.; Yu, S., Visible-light-promoted redox neutral C–H amidation of heteroarenes with hydroxylamine derivatives. *Organic Letters* 2014, 16, 3504-3507.
105. Moeller, K. D.; Marzabadi, M. R.; New, D. G.; Chiang, M. Y.; Keith, S., Oxidative organic electrochemistry: a novel intramolecular coupling of electron-rich olefins. *Journal of the American Chemical Society* 1990, 112, 6123-6124.
106. Moeller, K. D.; Rutledge, L. D., Anodic amide oxidations: the synthesis of two spirocyclic L-pyroglutamide building blocks. *The Journal of Organic Chemistry* 1992, 57, 6360-6363.
107. Moeller, K. D.; Wang, P. W.; Tarazi, S.; Marzabadi, M. R.; Wong, P. L., Anodic amide oxidations in the presence of electron-rich phenyl rings: evidence for an intramolecular electron-transfer mechanism. *The Journal of Organic Chemistry* 1991, 56, 1058-1067.
108. Arata, M.; Miura, T.; Chiba, K., Electrocatalytic formal [2+2] cycloaddition reactions between anodically activated enyloxy benzene and alkenes. *Organic Letters* 2007, 9, 4347-4350.
109. Chiba, K.; Miura, T.; Kim, S.; Kitano, Y.; Tada, M., Electrocatalytic intermolecular olefin cross-coupling by anodically induced formal [2+2] cycloaddition between enol ethers and alkenes. *Journal of the American Chemical Society* 2001, 123, 11314-11315.
110. Okada, Y.; Nishimoto, A.; Akaba, R.; Chiba, K., Electron-transfer-induced intermolecular [2 + 2] cycloaddition reactions based on the aromatic “redox tag” strategy. *The Journal of Organic Chemistry* 2011, 76, 3470-3476.

111. Okada, Y.; Akaba, R.; Chiba, K., Electrocatalytic formal [2+2] cycloaddition reactions between anodically activated aliphatic enol ethers and unactivated olefins possessing an alkoxyphenyl group. *Organic Letters* 2009, 11, 1033-1035.
112. Imada, Y.; Shida, N.; Okada, Y.; Chiba, K., A novel thermomorphic system for electrocatalytic diels-alder reactions. *Chinese Journal of Chemistry* 2019, 37, 557-560.
113. Chiba, K.; Tada, M., Diels–Alder reaction of quinones generated in situ by electrochemical oxidation in lithium perchlorate–nitromethane. *Journal of the Chemical Society, Chemical Communications* 1994, 2485-2486.
114. Okada, Y.; Yamaguchi, Y.; Ozaki, A.; Chiba, K., Aromatic “redox tag”-assisted diels–alder reactions by electrocatalysis. *Chemical Science* 2016, 7, 6387-6393.
115. Ozaki, A.; Yamaguchi, Y.; Okada, Y.; Chiba, K., Bidirectional access to radical cation diels-alder reactions by electrocatalysis. *ChemElectroChem* 2017, 4, 1852-1855.
116. Okada, Y.; Chiba, K., Redox-tag processes: intramolecular electron transfer and its broad relationship to redox reactions in general. *Chemical Reviews* 2018, 118, 4592-4630.
117. Zhu, L.; Xiong, P.; Mao, Z.-Y.; Wang, Y.-H.; Yan, X.; Lu, X.; Xu, H.-C., Electrocatalytic generation of amidyl radicals for olefin hydroamidation: use of solvent effects to enable anilide oxidation. *Angewandte Chemie International Edition* 2016, 55, 2226-2229.
118. Imada, Y.; Okada, Y.; Chiba, K., Investigating radical cation chain processes in the electrocatalytic Diels–Alder reaction. *Beilstein Journal of Organic Chemistry* 2018, 14, 642-647.
119. Lorenz, K. T.; Bauld, N. L., Kinetics and mechanism of aminium salt-initiated cycloadditions. *Journal of the American Chemical Society* 1987, 109, 1157-1160.
120. Maity, S.; Zhu, M.; Shinabery, R. S.; Zheng, N., Intermolecular [3+2] cycloaddition of cyclopropylamines with olefins by visible-light photocatalysis. *Angewandte Chemie International Edition* 2012, 51, 222-226.
121. Cai, Y.; Wang, J.; Zhang, Y.; Li, Z.; Hu, D.; Zheng, N.; Chen, H., Detection of fleeting amine radical cations and elucidation of chain processes in visible-light-mediated [3 + 2] annulation by online mass spectrometric techniques. *Journal of the American Chemical Society* 2017, 139, 12259-12266.
122. Kavarnos, G. J.; Turro, N. J., Photosensitization by reversible electron transfer: theories, experimental evidence, and examples. *Chemical Reviews* 1986, 86, 401-449.
123. Slavin, J.; Carlson, J., Carbohydrates. *Advances in Nutrition* 2014, 5, 760-761.

124. Thibodeaux, C. J.; Melançon III, C. E.; Liu, H. w., Natural-product sugar biosynthesis and enzymatic glycodiversification. *Angewandte Chemie International Edition* 2008, 47, 9814-9859.
125. Duffin, K. L.; Welply, J. K.; Huang, E.; Henion, J. D., Characterization of N-linked oligosaccharides by electrospray and tandem mass spectrometry. *Analytical Chemistry* 1992, 64, 1440-1448.
126. Mock, K.; Davey, M.; Cottrell, J., The analysis of underivatized oligosaccharides by matrix-assisted laser desorption mass spectrometry. *Biochemical and Biophysical Research Communications* 1991, 177, 644-651.
127. Zhao, X.; Huang, Y.; Ma, G.; Liu, Y.; Guo, C.; He, Q.; Wang, H.; Liao, J.; Pan, Y., Parallel on-target derivatization for mass calibration and rapid profiling of N-glycans by MALDI-TOF MS. *Analytical Chemistry* 2019, 92, 991-998.
128. Lattová, E.; Skříčková, J.; Zdráhal, Z. k., Applicability of phenylhydrazine labeling for structural studies of fucosylated N-glycans. *Analytical Chemistry* 2019, 91, 7985-7990.
129. Tryfona, T.; Liang, H.-C.; Kotake, T.; Kaneko, S.; Marsh, J.; Ichinose, H.; Lovegrove, A.; Tsumuraya, Y.; Shewry, P. R.; Stephens, E., Carbohydrate structural analysis of wheat flour arabinogalactan protein. *Carbohydrate Research* 2010, 345, 2648-2656.
130. Ji, Y.; Bachschmid, M. M.; Costello, C. E.; Lin, C., S-to N-Palmitoyl transfer during proteomic sample preparation. *Journal of the American Society for Mass Spectrometry* 2016, 27, 677-685.
131. Campbell, M. P.; Abrahams, J. L.; Rapp, E.; Struwe, W. B.; Costello, C. E.; Novotny, M.; Ranzinger, R.; York, W. S.; Kolarich, D.; Rudd, P. M.; Kettner, C., The minimum information required for a glycomics experiment (MIRAGE) project: LC guidelines. *Glycobiology* 2019, 29, 349-354.
132. Xu, G.; Davis, J. C.; Goonatileke, E.; Smilowitz, J. T.; German, J. B.; Lebrilla, C. B., Absolute quantitation of human milk oligosaccharides reveals phenotypic variations during lactation. *The Journal of Nutrition* 2017, 147, 117-124.
133. Fabijanczuk, K.; Gaspar, K.; Desai, N.; Lee, J.; Thomas, D. A.; Beauchamp, J. L.; Gao, J., Resin and magnetic nanoparticle-based free radical probes for glycan capture, isolation, and structural characterization. *Analytical Chemistry* 2019, 91, 15387-15396.
134. Li, S.; Zhou, Y.; Xiao, K.; Li, J.; Tian, Z., Selective fragmentation of the N-glycan moiety and protein backbone of ribonuclease B on an Orbitrap Fusion Lumos Tribrid mass spectrometer. *Rapid Communications in Mass Spectrometry* 2018, 32, 2031-2039.
135. Alley Jr, W. R.; Mann, B. F.; Novotny, M. V., High-sensitivity analytical approaches for the structural characterization of glycoproteins. *Chemical Reviews* 2013, 113, 2668-2732.

136. Iavarone, A. T.; Udekwu, O. A.; Williams, E. R., Buffer loading for counteracting metal salt-induced signal suppression in electrospray ionization. *Analytical Chemistry* 2004, 76, 3944-3950.
137. El Rassi, Z., Recent progress in reversed-phase and hydrophobic interaction chromatography of carbohydrate species. *Journal of Chromatography A* 1996, 720, 93-118.
138. Churms, S. C., Recent progress in carbohydrate separation by high-performance liquid chromatography based on size exclusion. *Journal of Chromatography A* 1996, 720, 151-166.
139. Lee, Y.-C., Carbohydrate analyses with high-performance anion-exchange chromatography. *Journal of Chromatography A* 1996, 720, 137-149.
140. Maier, M.; Reusch, D.; Bruggink, C.; Bulau, P.; Wuhler, M.; Mølhøj, M., Applying mini-bore HPAEC-MS/MS for the characterization and quantification of Fc N-glycans from heterogeneously glycosylated IgGs. *Journal of Chromatography B* 2016, 1033, 342-352.
141. Wunschel, D.; Fox, K.; Fox, A.; Nagpal, M.; Kim, K.; Stewart, G.; Shahgholi, M., Quantitative analysis of neutral and acidic sugars in whole bacterial cell hydrolysates using high-performance anion-exchange liquid chromatography–electrospray ionization tandem mass spectrometry. *Journal of Chromatography A* 1997, 776, 205-219.
142. Zielinska, D. F.; Gnad, F.; Wiśniewski, J. R.; Mann, M., Precision mapping of an in vivo N-glycoproteome reveals rigid topological and sequence constraints. *Cell* 2010, 141, 897-907.
143. Vandenborre, G.; Van Damme, E. J.; Ghesquiere, B.; Menschaert, G.; Hamshou, M.; Rao, R. N.; Gevaert, K.; Smagghe, G., Glycosylation signatures in *Drosophila*: fishing with lectins. *Journal of Proteome Research* 2010, 9, 3235-3242.
144. Rudd, P. M.; Guile, G. R.; Kuster, B.; Harvey, D. J., Oligosaccharide sequencing technology. *Nature* 1997, 388, 205-207.
145. Cao, C.; Yu, L.; Yan, J.; Fu, D.; Yuan, J.; Liang, X., Purification of natural neutral N-glycans by using two-dimensional hydrophilic interaction liquid chromatography× porous graphitized carbon chromatography for glycan-microarray assay. *Talanta* 2021, 221, 121382.
146. Juvonen, M.; Kotiranta, M.; Jokela, J.; Tuomainen, P.; Tenkanen, M., Identification and structural analysis of cereal arabinoxylan-derived oligosaccharides by negative ionization HILIC-MS/MS. *Food Chemistry* 2019, 275, 176-185.
147. Yong-Gang, X.; Rong-Jian, Z.; Yu, S.; Liang, J.; Kuang, H.-X., A high methyl ester pectin polysaccharide from the root bark of *Aralia elata*: Structural identification and biological activity. *International Journal of Biological Macromolecules* 2020, 159, 1206-1217.

148. Bereman, M. S.; Williams, T. I.; Muddiman, D. C., Development of a nanoLC LTQ orbitrap mass spectrometric method for profiling glycans derived from plasma from healthy, benign tumor control, and epithelial ovarian cancer patients. *Analytical Chemistry* 2009, 81, 1130-1136.
149. Liu, Y.; Wang, C.; Wang, R.; Wu, Y.; Zhang, L.; Liu, B.-F.; Cheng, L.; Liu, X., Isomer-specific profiling of N-glycans derived from human serum for potential biomarker discovery in pancreatic cancer. *Journal of Proteomics* 2018, 181, 160-169.
150. Hua, S.; Saunders, M.; Dimapasoc, L. M.; Jeong, S. H.; Kim, B. J.; Kim, S.; So, M.; Lee, K.-S.; Kim, J. H.; Lam, K. S., Differentiation of cancer cell origin and molecular subtype by plasma membrane N-glycan profiling. *Journal of Proteome Research* 2014, 13, 961-968.
151. Xu, G.; Goonatilleke, E.; Wongkham, S.; Lebrilla, C. B., Deep structural analysis and quantitation of O-linked glycans on cell membrane reveal high abundances and distinct glycomic profiles associated with cell type and stages of differentiation. *Analytical Chemistry* 2020, 92, 3758-3768.
152. Li, Q.; Li, G.; Zhou, Y.; Zhang, X.; Sun, M.; Jiang, H.; Yu, G., Comprehensive N-glycome profiling of cells and tissues for breast cancer diagnosis. *Journal of Proteome Research* 2019, 18, 2559-2570.
153. Papac, D. I.; Wong, A.; Jones, A. J., Analysis of acidic oligosaccharides and glycopeptides by matrix-assisted laser desorption/ionization time-of-flight mass spectrometry. *Analytical Chemistry* 1996, 68, 3215-3223.
154. Harvey, D. J., Electrospray mass spectrometry and fragmentation of N-linked carbohydrates derivatized at the reducing terminus. *Journal of the American Society for Mass Spectrometry* 2000, 11, 900-915.
155. Yang, Q.; Wang, H.; Maas, J. D.; Chappell, W. J.; Manicke, N. E.; Cooks, R. G.; Ouyang, Z., Paper spray ionization devices for direct, biomedical analysis using mass spectrometry. *International Journal of Mass Spectrometry* 2012, 312, 201-207.
156. Ishikawa, M.; Kuroyama, H.; Takeuchi, Y.; Tsumuraya, Y., Characterization of pectin methyltransferase from soybean hypocotyls. *Planta* 2000, 210, 782-791.
157. Selman, M. H.; Hemayatkar, M.; Deelder, A. M.; Wührer, M., Cotton HILIC SPE microtips for microscale purification and enrichment of glycans and glycopeptides. *Analytical Chemistry* 2011, 83, 2492-2499.
158. Mortimer, J. C.; Miles, G. P.; Brown, D. M.; Zhang, Z.; Segura, M. P.; Weimar, T.; Yu, X.; Seffen, K. A.; Stephens, E.; Turner, S. R., Absence of branches from xylan in *Arabidopsis gux* mutants reveals potential for simplification of lignocellulosic biomass. *Proceedings of the National Academy of Sciences* 2010, 107, 17409-17414.

159. Faik, A.; Held, M., Plant cell wall biochemical omics: The high-throughput biochemistry for polysaccharide biosynthesis. *Plant Science* 2019, 286, 49-56.
160. Perrin, R. M.; DeRocher, A. E.; Bar-Peled, M.; Zeng, W.; Norambuena, L.; Orellana, A.; Raikhel, N. V.; Keegstra, K., Xyloglucan fucosyltransferase, an enzyme involved in plant cell wall biosynthesis. *Science (New York, N.Y.)* 1999, 284, 1976-1979.
161. Faik, A.; Price, N. J.; Raikhel, N. V.; Keegstra, K., An Arabidopsis gene encoding an α -xylosyltransferase involved in xyloglucan biosynthesis. *Proceedings of the National Academy of Sciences* 2002, 99, 7797-7802.
162. Liepman, A. H.; Wilkerson, C. G.; Keegstra, K., Expression of cellulose synthase-like (Csl) genes in insect cells reveals that (CslA) family members encode mannan synthases. *Proceedings of the National Academy of Sciences* 2005, 102, 2221-2226.
163. Cocuron, J.-C.; Lerouxel, O.; Drakakaki, G.; Alonso, A. P.; Liepman, A. H.; Keegstra, K.; Raikhel, N.; Wilkerson, C. G., A gene from the cellulose synthase-like C family encodes a β -1,4 glucan synthase. *Proceedings of the National Academy of Sciences* 2007, 104, 8550-8555.
164. Wu, Y.; Williams, M.; Bernard, S.; Driouich, A.; Showalter, A. M.; Faik, A., Functional identification of two nonredundant Arabidopsis (1,2) fucosyltransferases specific to Arabinogalactan proteins *Journal of Biological Chemistry* 2010, 285, 13638-13645.
165. Nanda, K. K.; Tignor, S.; Clancy, J.; Marota, M. J.; Allain, L. R.; D'Addio, S. M., Inhibition of N-nitrosamine formation in drug products: a model study. *Journal of Pharmaceutical Sciences* 2021, 110, 3773-3775.
166. Ashworth, I. W.; Dirat, O.; Teasdale, A.; Whiting, M., Potential for the formation of N-nitrosamines during the manufacture of active pharmaceutical ingredients: an assessment of the risk posed by trace nitrite in water. *Organic Process Research and Development* 2020, 24, 1629-1646.
167. Beard, J. C.; Swager, T. M., An organic chemist's guide to N-nitrosamines: their structure, reactivity, and role as contaminants. *The Journal of Organic Chemistry* 2021, 86, 2037-2057.
168. Mao, D.; Ding, C.; Douglas, D. J., Hydrogen/deuterium exchange of myoglobin ions in a linear quadrupole ion trap. *Rapid Communications in Mass Spectrometry* 2002, 16, 1941-1945.

169. European Medicines Agency. Amsterdam, Netherlands. In ICH guideline M7(R1) on assessment and control of DNA reactive (mutagenic) impurities in pharmaceuticals to limit potential carcinogenic risk. , 2013; Vol. EMA/CHMP/ICH/83812/2013., pp https://www.ema.europa.eu/en/documents/scientific-guideline/guideline-assessment-control-dna-reactivemutagenic-impurities-pharmaceuticals-limitpotential_en.pdf. retrieved on 01/07/2022
170. Lu, J.; Li, M.; Huang, Y.; Xie, J.; Shen, M.; Xie, M., A comprehensive review of advanced glycosylation end products and N- Nitrosamines in thermally processed meat products. *Food Control* 2022, 131, 108449.
171. Bharate, S. S., Critical analysis of drug product recalls due to nitrosamine impurities. *Journal of Medicinal Chemistry* 2021, 64, 2923-2936.
172. Krietsch Boerner, L., The lurking contaminant. *C&EN* 2020, 98, 27-31.
173. Kadmi, Y.; Favier, L.; Soutrel, I.; Lemasle, M.; Wolbert, D., Ultratrace-level determination of N-nitrosodimethylamine, N-nitrosodiethylamine, and N-nitrosomorpholine in waters by solid-phase extraction followed by liquid chromatography-tandem mass spectrometry. *Central European Journal of Chemistry* 2014, 12, 928-936.
174. Herrmann, S. S.; Duedahl-Olesen, L.; Granby, K., Simultaneous determination of volatile and non-volatile nitrosamines in processed meat products by liquid chromatography tandem mass spectrometry using atmospheric pressure chemical ionisation and electrospray ionisation. *Journal of Chromatography A* 2014, 1330, 20-29.
175. Ngongang, A. D.; Duy, S. V.; Sauv e, S., Analysis of nine N-nitrosamines using liquid chromatography-accurate mass high resolution-mass spectrometry on a Q-Exactive instrument. *Analytical Methods* 2015, 7, 5748-5759.
176. Krauss, M.; Hollender, J., Analysis of nitrosamines in wastewater: exploring the trace level quantification capabilities of a hybrid linear ion trap/Orbitrap mass spectrometer. *Analytical Chemistry* 2008, 80, 834-842.
177. FDA, Combined N-nitrosodimethylamine (NDMA) and N-nitrosodiethylamine (NDEA) impurity assay by GC/MS-Headspace. 2019, 1-7.
178. Zheng, J.; Kirkpatrick, C. L.; Lee, D.; Han, X.; Martinez, A. I.; Gallagher, K.; Evans, R. K.; Mudur, S. V.; Liang, X.; Drake, J.; Buhler, L. A.; Mowery, M. D., A full evaporation static headspace gas chromatography method with nitrogen phosphorous detection for ultrasensitive analysis of semi-volatile nitrosamines in pharmaceutical Products. *The AAPS Journal* 2022, 24, 23.
179. Moradi, S.; Shariatifar, N.; Akbari-adergani, B.; Molaee Aghaee, E.; Arbameri, M., Analysis and health risk assessment of nitrosamines in meat products collected from markets, Iran: with the approach of chemometric. *Journal of Environmental Health Science and Engineering* 2021, 19, 1361-1371.

180. Jurado-Sánchez, B.; Ballesteros, E.; Gallego, M., Comparison of the sensitivities of seven N-nitrosamines in pre-screened waters using an automated preconcentration system and gas chromatography with different detectors. *Journal of Chromatography A* 2007, 1154, 66-73.
181. Wichitnithad, W.; Sudtanon, O.; Srisunak, P.; Cheewatanakornkool, K.; Nantaphol, S.; Rojsitthisak, P., Development of a sensitive headspace gas chromatography–mass spectrometry method for the simultaneous determination of nitrosamines in losartan active pharmaceutical ingredients. *ACS Omega* 2021, 6, 11048-11058.
182. Li, W.; Chen, N.; Zhao, Y.; Guo, W.; Muhammd, N.; Zhu, Y.; Huang, Z., Online coupling of tandem liquid-phase extraction with HPLC-UV for the determination of trace N-nitrosamines in food products. *Analytical Methods* 2018, 10, 1733-1739.
183. Boczar, D.; Wyszomirska, E.; Zabrzewska, B.; Chyła, A.; Michalska, K., Development and validation of a method for the semi-quantitative determination of N-nitrosamines in active pharmaceutical ingredient enalapril maleate by means of derivatisation and detection by HPLC with fluorimetric detector. *Applied Sciences* 2021, 1-16.
184. Cetó, X.; Saint, C. P.; Chow, C. W. K.; Voelcker, N. H.; Prieto-Simón, B., Electrochemical detection of N-nitrosodimethylamine using a molecular imprinted polymer. *Sensors and Actuators B Chemical* 2016, 237, 613-620.
185. Majumdar, S.; Thakur, D.; Chowdhury, D., DNA carbon-nanodots based electrochemical biosensor for detection of mutagenic nitrosamines. *ACS Applied Bio Materials* 2020, 3, 1796-1803.
186. Coffacci, L.; Codognoto, L.; Fleuri, L. F.; Lima, G. P. P.; Pedrosa, V. A., Determination of total nitrosamines in vegetables cultivated organic and conventional using diamond electrode. *Food Analytical Methods* 2013, 6, 1122-1127.
187. Breider, F.; von Gunten, U., Quantification of total N-nitrosamine concentrations in aqueous samples via UV-Photolysis and chemiluminescence detection of nitric oxide. *Analytical Chemistry* 2017, 89, 1574-1582.
188. Zhao, P.; Wang, Q.; Kaur, M.; Kim, Y.-I.; Dewald, H. D.; Mozziconacci, O.; Liu, Y.; Chen, H., Absolute Quantitation of Proteins by Coulometric Mass Spectrometry. *Analytical Chemistry*. 2020, 92, 7877-7883.
189. Kinlen, P. J.; Evans, D. H.; Nelsen, S. F., Electrochemical oxidation of tetramethylhydrazine, 1,1-dimethyl-2,2-dibenzylhydrazine and tetrabenzyl-hydrazine. *Journal of Electroanalytical Chemistry and Interfacial Electrochemistry* 1979, 97, 265-281.

190. Masui, M.; Nose, K.; Terauchi, S.; Yamakawa, E.; Jeong, J.; Ueda, C.; Ohmori, H., Electrochemical oxidation of N-nitrosodialkylamines : mechanism of N-nitramine and beta-Ketonitrosamine Formation. *Chemical and Pharmaceutical Bulletin* 1985, 33, 2721-2730.
191. de Oliveira, R. T. S.; Salazar-Banda, G. R.; Machado, S. A. S.; Avaca, L. A., Electroanalytical determination of N-nitrosamines in aqueous solution using a boron-doped diamond electrode. *Electroanalysis* 2008, 20, 396-401.
192. Gorski, W.; Cox, J. A., Oxidation of N-nitrosamines at a ruthenium-based modified electrode in aqueous solutions. *Journal of Electroanalytical Chemistry* 1995, 389, 123-128.
193. Chai, Y.; Sun, H.; Wan, J.; Pan, Y.; Sun, C., Hydride abstraction in positive-ion electrospray interface: oxidation of 1,4-dihydropyridines in electrospray ionization mass spectrometry. *Analyst* 2011, 136, 4667-4669.
194. Chen, M.; Cook, K. D., Oxidation artifacts in the electrospray mass spectrometry of A β Peptide. *Analytical Chemistry* 2007, 79, 2031-2036.
195. Limanto, J.; Shultz, C. S.; Dorner, B.; Desmond, R. A.; Devine, P. N.; Krska, S. W., Synthesis of a tertiary carbinamide via a novel Rh-catalyzed asymmetric hydrogenation. *The Journal of Organic Chemistry* 2008, 73, 1639-1642.
196. Hunter, E. P. L.; Lias, S. G., Evaluated gas phase basicities and proton affinities of molecules: an update. *Journal of Physical and Chemical Reference Data* 1998, 27, 413-656.